**Super-resolution imaging of cardiac immuno-markers: Defining quality criteria for use in dual colour STORM and DNA-PAINT single molecule localisation microscopy**

Submitted by
**Carl Lee Harrison**
to the University of Exeter
as a thesis for the degree of
**Doctor of Philosophy in Physics**
In January 2019



I certify that all material in this thesis which is not my own work has been identified and that no material has previously been submitted and approved for the award of a degree by this or any other University.

Signature: ……..

UNIVERSITY OF EXETER | LIVING SYSTEMS INSTITUTE

# Abstract

Aberrant Ryanodine receptor behaviour is highly implicated in cardiovascular disease. Post-translational modifications are used widely in the body to control the dynamics of proteins to respond to acute and chronic demands. Phosphorylation is a key, highly tuneable modification used by cells by the reversible enzymatic addition of a phosphate group to single amino acids within protein structures. Common cardiac diseases such as arrhythmia, hypertension, and heart failure have been linked to excessive ryanodine receptor phosphorylation and transgenic constitutive phosphorylation has shown disease aetiology in disease models.

Phosphorylation is typically measured *en masse* by use of Western blots, or more recently phosphoproteomics, however the spatial distribution has remained a mystery. Ryanodine receptors are found in clusters and their influence tightly controlled spatially. As phosphorylation increases their range of influence, it is of great interest to observe the pattern of phosphorylation within and between ryanodine receptor clusters.

Ryanodine receptor clusters have been well characterised in electron microscopy and the fluorescence based super-resolution microscopy, achieving single receptor resolution. This thesis details the validation pipeline for translation phosphorylation-state specific antibodies from Western blot through to super-resolution microscopy. The phosphorylation distribution was compared between isolated ventricular cardiomyocytes and ventricular tissue sections for Ser-2808 and Ser-2814 phosphorylation. Strong reductions in basal phosphorylation caused by the isolation procedure were observed for

Ser-2808 but not Ser-2814. These differences in Ser-2808 phosphorylation were then investigated in dual channel STORM super-resolution microscopy, highlighting stark contracts in colocalisation between the confocal and STORM techniques.

This population and sub-population experiment was then translated into the new DNA-PAINT technology and a direct comparison of performance between STORM and DNA-PAINT was discussed. The data described in this thesis shows a methodological approach to enabling other biophysicists to perform quantitative super-resolution microscopy to determine the extent and spatial distribution pattern of phosphorylation of a protein of interest at the nanoscale. Important differences were observed in the phosphorylation state due to cardiomyocyte isolation procedures that are of interest to a wide audience of cardiovascular researchers.

DNA-PAINT is emerging as the progression of SMLM from STORM microscopy due to the greater control of imaging parameters it affords. Parallel experiments of Ryanodine receptor Ser-2808 phosphorylation were performed in tissue sections. Comparisons between dual channel STORM and DNA-PAINT were evaluated. Open questions about DNA-PAINT are also highlighted and discussed.

# Acknowledgements

This thesis has taken significant effort and would not have been possible without the support of many academics, colleagues, and friends. Firstly, I wish to extend my sincere gratitude to my academic supervisor Professor Christian Soeller for giving me the opportunity to study for a PhD, the latitude to explore my scientific interests and extensive training and support to transform me from a physiologist into a biophysicist. I would like to thank my second supervisor Professor Michael Schrader for his support, guidance, and patience. I also wish to thank my colleagues, especially Dr Ruisheng Lin and Dr Izzy Jayasinghe for their endless support and training. I would also like to thank my colleagues Tobias Lutz and Dr Alex Clowsley for support with experiments

I wish to thank Professor John Colyer for his extensive support and readiness to speak at distance about the project, the wider cardiac physiology, and the academic career. Additionally, I wish to thank him as part of Badrilla Ltd and their support and funding for the project. Thank you to the academics I met during my time at Badrilla Ltd and the University of Leeds for their kindness and support.

Thank you to Dr Ellen Green, Professor Peter Winlove, Dr Francesca Palombo, Dr Tim Etheridge, Dr Yolanda Hill, Nick Gaunt, Dr Tara Craggs, Dr Ross Jones, and Dr Cynthia Andoniadou and my family for the emotional support, proofreading, endless cups of tea, grumbles, laughs, and generally helping me to get over the line. An extra special mention for Westwood Shadow Harrison, for keeping my sane. A constant companion and many of my breakthroughs were formulated during our runs along the South West Coastal Path and through the Dartmoor Tors. Finally, I wish to thank my examiners for kindly donating their time to facilitate this process.

# Contents

# Abbreviations

| | |
|---|---|
| **BP** | Blood Pressure |
| **$Ca^{2+}$** | Calcium ion |
| **CaMKII** | Calcium/calmodulin kinase II |
| **cAMP** | Cyclic adenosine monophosphate |
| **CM** | Cardiomyocyte |
| **DNA-PAINT** | DNA Point Accumulation for Imaging in Nanoscale Topography |
| **HF** | Heart Failure |
| **HR** | Heart Rate |
| **LTCC** | L-type calcium channels |
| **PKA** | Protein kinase A |
| **PKG** | Protein kinase G |
| **PLN** | Phospholamban |
| **$P_o$** | Open probability |
| **PTM** | Post-translational modification |
| **RyR2** | Ryanodine receptor type 2 |
| **SERCA2a** | Sarco(endo)plasmic reticulum calcium ATPase type 2a |
| **SMLM** | Single molecule localisation microscopy |
| **SR** | Sarcoplasmic reticulum |
| **STORM** | Stochastic Optical Recontruction Microscopy |
| **T-Tubule** | Transverse tubule |

# Chapter 1

## Introduction

Cardiovascular disease is one of the main causes of premature death and disability in the UK. Cardiovascular research has a broad motivation; from heart disease to renal failure, diabetes, stroke, and vascular dementia. This gives a strong motivation for basic research in cardiovascular physiology. Whilst much is known about gross mechanisms of cardiac physiology and pathologies, knowledge at the molecular scale remains incomplete.

Innovative technologies, including genetics, magnetic resonance imaging, electron microscopy and polymerase chain reaction, have transformed our understanding of biological concepts in unforeseen ways. In 2014 the Nobel prize in Chemistry was awarded for super-resolution microscopy, citing the ability surpass the light microscopy resolution limit of 200 nm. This technology allows single molecules to be observed and quantified in previously unseen detail.

Physiological function is modulated by chemical modifications of the proteins involved. A common post-translational modification (PTM) is phosphorylation of a protein. Excessive phosphorylation of associated proteins (especially the cardiac Ryanodine receptor; RyR2) has been implicated in many common cardiovascular diseases by biochemical assays. Currently, spatial information of protein phosphorylation is not well understood. This project utilised the power of super-resolution microscopy to investigate the spatial distribution of phosphorylation of the RyR2. These data are of use to cardiac physiologists whom perform functional experiments, as well as having wider implications for

biophysicists to investigate cell biology mechanisms that rely on PTM as a whole.

**The Heartbeat**

The heart beats rhythmically in order to maintain a consistent blood supply to the body. At rest, blood passively fills into the atria and then through into the ventricles. This period, where the heart is at rest both electrically and mechanically, is termed diastole. Diastole accounts for two thirds of the heartbeat duration. The sino-atrial node is a population of specialised cells that spontaneously generate a depolarising current, termed the action potential (AP). This is due to the pacemaker, or funny current ($I_f$), which can be modulated by the second messenger molecule cAMP, a downstream effector of adrenergic stimulation (Brown *et al.*, 1979; Baruscotti *et al.,* 1979).

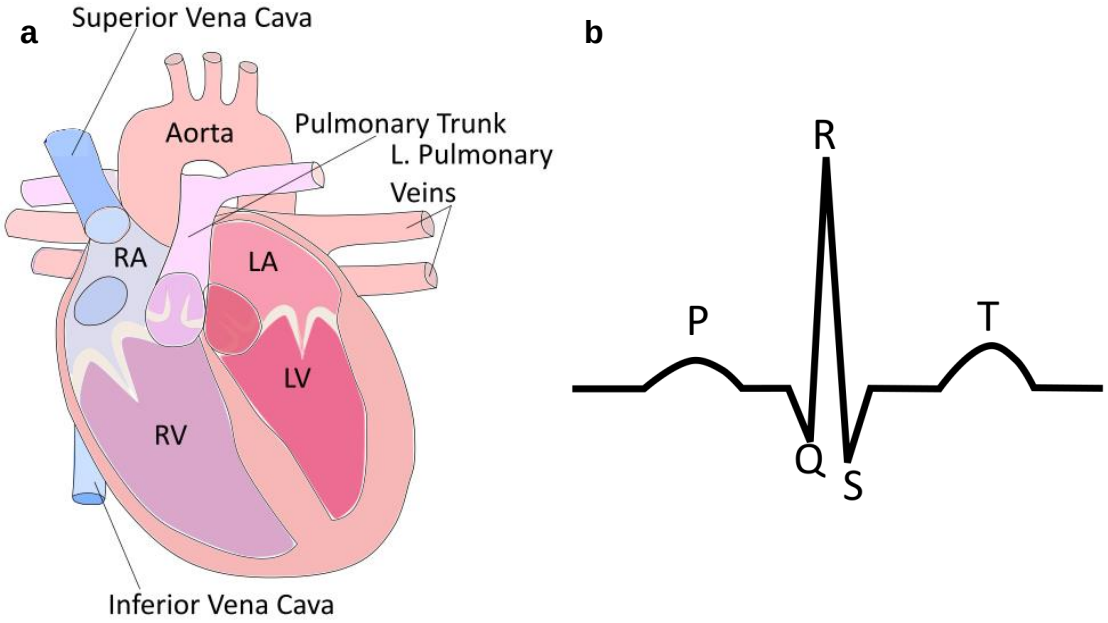


**Figure 1.1 (a) Schematic of the heart chambers and associated vessels. Deoxygenated blood enters the right atrium (RA) from the inferior and superior venae cavae. Then passes into the right ventricle (RV) before being ejected into the pulmonary trunk. Oxygenated blood returns via the left and right pulmonary veins into the left atrium (LA). The blood then passes into the left ventricle (LV) before being ejected into the aorta to supply the body. (b) Example ECG trace. The P-wave represents atrial depolarisation. The QRS complex represents the ventricular depolarisation, whilst the T-wave represents the ventricular repolarisation.**

The AP spreads through and depolarises the atria, leading to atrial contraction. This serves to 'top up' the blood volume in the ventricle. Pressure within the ventricle increases slightly as a result, thus causing the atrioventricular valves to close. After a brief delay, the AP reaches the ventricles via the conducting system and the ventricles contract to propel one stroke volume of blood into the great vessels. The atria and ventricles then relax, and blood can passively refill in the phase termed diastole, before another contraction (or systole). In this way blood is sent to the lungs from the right side of the heart, returned to the left side of the heart oxygenated, and then sent out to supply the bodily tissues with $O_2$ and remove waste products (i.e. $CO_2$) to be sent to the lungs for expiration (Levick, 2003).

Cardiac function is modulated by neuronal and endocrine inputs to increase or decrease heart rate (HR) according to metabolic demand, or to prepare the body for activity due to external stimuli (such as during the 'fight or flight' response). The sinoatrial node, atrioventricular node, and Purkinje fibres form the conduction system of the heart (figure 1.2). The atria are electrically insulated from the ventricles and the heartbeat is delayed slightly as it passes through the atrioventricular node before spreading across the ventricles via the Purkinje fibres. This delay allows the atria to contract and 'top-up' the blood volume of the ventricles, and the atrioventricular valves to close before contraction of the ventricles (Levick, 2003).

**Cardiovascular Physiology and Pathology**

Every cell in the body requires a constant supply of $O_2$, nutrients, water, endocrine signals, and the removal of waste products such as $CO_2$. The cardiovascular system performs this function in a highly efficient manner. The heart is a strong muscular pump at the centre of an approximate figure-8 vascular system. One loop (systemic system; left) supplies blood to the body, whilst the second loop (respiratory system; right) sends blood to the lungs to resupply with $O_2$ and remove $CO_2$.

Whilst each side of the heart handles the same volume of blood per heartbeat, the two systems are not identical. The left side services the body and is termed the systemic circulation. The left ventricle wall is approximately 3-fold thicker than the right side and produces a systolic pressure of approximately 120 mmHg at rest in a healthy adult (Weber and Lackland, 2016). The right ventricle is much thinner and produces a systolic pressure of approximately 14 mmHg (Hoeper *et al.,* 2013). These differences are reflected in the lower

volume of the respiratory circulation from the right side of the heart, and the lower resistance against which it must pump.

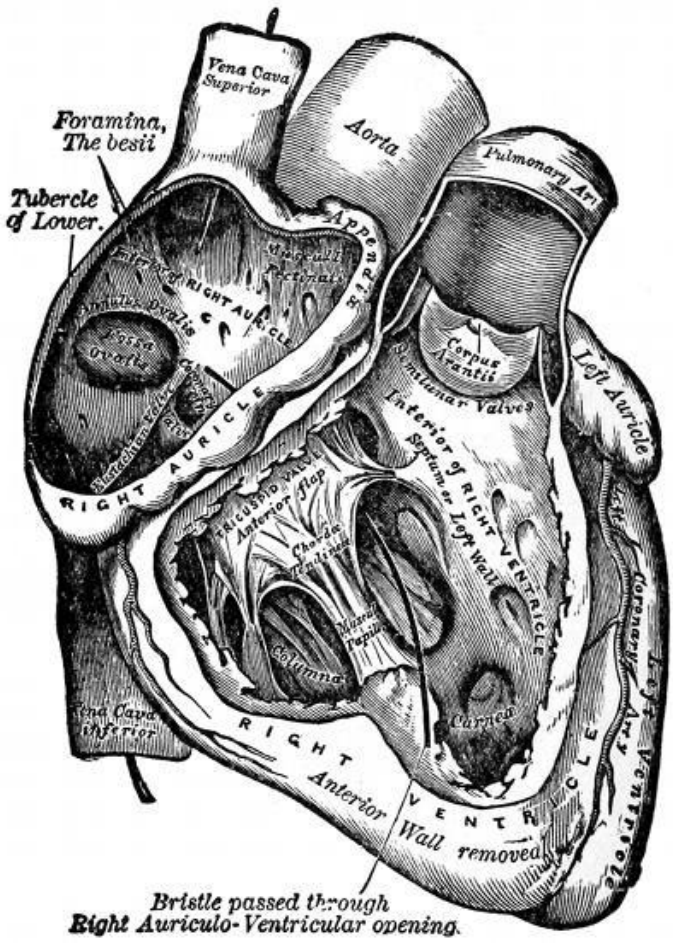


**Figure 1.2. Wood block etching of the major anatomical features found in the right atrium and ventricle (dissected). Adopted from (Gray and Carter, 1858)**

The contractility of the whole heart is represented well by the single cardiomyocyte (CM), and so an understanding of the clinical measures and symptoms educates the interpretation of isolated CM experiments. Cardiac function can be measured clinically as the volume of blood pumped from one side of the heart per minute, termed cardiac output. Cardiac output represents the flow across a vascular bed, and volume of venous return of a healthy heart and is approximately 5 $L.min^{-1}$ at rest in a 70 kg adult human male. The ejection fraction is the proportion of ventricular volume that is expelled per heartbeat. Typical ejection fraction values for healthy adult are 55-75% of the

total ventricular blood volume. Failure of CM contraction results in lower cardiac output and lower ejection fraction, ultimately resulting in an inability to sufficiently perfuse the body and brain with oxygenated blood.

Blood pumped out of the heart must travel through the circulatory system under sufficient pressure to overcome the resistance from the muscular arterial vessels. The blood pressure (BP) measured clinically is stated as the systolic pressure over the diastolic pressure, reflecting the differential pulsatile flow of blood through the arteries. Measurement of BP is an indirect measure of the pressure created by cardiac contraction. It will vary depending on the artery measured, but typically the brachial artery is measured as it is approximately at the same level as the heart and so there are no large influences of gravity. BP lies within an optimal range; high enough to sufficiently perfuse the entire body, whilst not too high to damage the vessel walls through sheer stress. This can lead to atherosclerotic plaques, and so serious disease. This resistance is termed total peripheral resistance.

The mean arterial pressure is the weighted average of these pressures. It is important to maintain mean arterial pressure as these pressures - within a normal HR - produce the required perfusion rate of key organs, such as the bran, lungs, and kidneys. Total peripheral resistance, and therefore diastole, can be affected by blood viscosity, vasoconstriction (a result of adrenergic stimulation), or on some cases stenosis – a pathological narrowing of major arteries (Siddiqui, 2011).

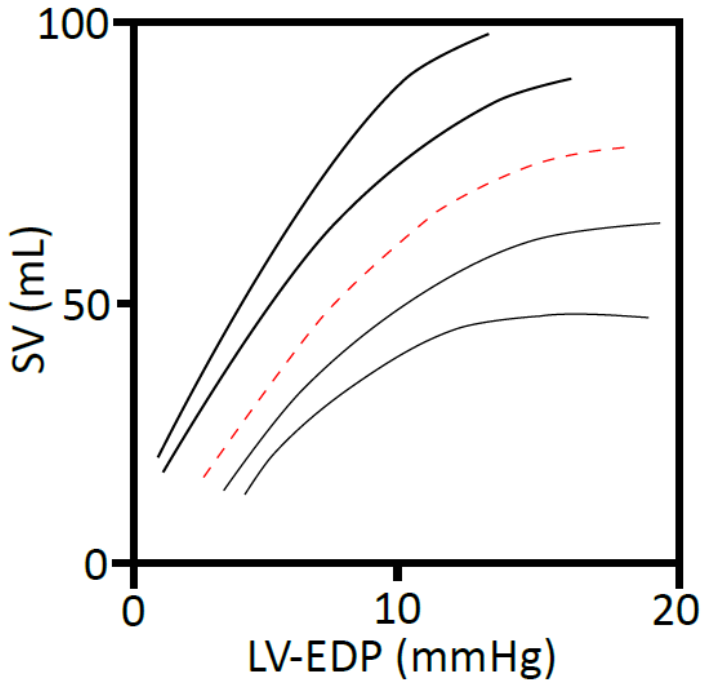


**Figure 1.3. A range of example Frank-Starling curves. As left ventricular end diastolic pressure (LV-EDP) increases, stroke volume (SV) increases. Increased afterload or decreased contractility shifts the curve to the right and down. Decreased afterload and increased contractility (such as during exercise) shift the curve up and to the left. Red dashed line represents a normal state (Summarised in Levick, 2003).**

HR is increased in response to greater demand, such as during exercise, partially accounting for observed increases in cardiac output. The ejection fraction also increases, via a process known as the Frank-Starling mechanism resulting in increased force of contraction due to increased stretch. Frank-Starling curves describe the relationship between venous return and stroke volume (figure 1.3). Points along the curve are dependent upon the venous return, whereas each different curve is true for a fixed total peripheral resistance (or afterload) and contractility (also termed inotropy). Assuming these constant starting conditions, increased venous return translates into increased filling of the ventricle (and so increased preload).

Contraction in this instance results in a larger stroke volume to return to the same end systolic volume in the healthy heart. This does not hold true for ventricles in failure however. This is proposed to be due to stretching of

individual sarcomeres within the CM. This occurs by a combination of sensitisation of the contractile machinery to $Ca^{2+}$ and varying degrees of overlap of the contractile fibres.

Hypertension results in an increased afterload against which the heart must pump more forcefully to maintain the same rate of perfusion. Causes are variable and complex but simplified into primary or secondary hypertension (Levy, 1996). Primary hypertension is caused by both genetic and environmental factors, such as obesity, high salt intake, or smoking. Secondary hypertension is a result of another illness, such as kidney disease, atherosclerosis, or endocrine disorders (i.e. hypothyroidism).

$$\sigma \propto \frac{P \cdot r}{h}$$

**Equation 1.1. Adaptation of the Law of Laplace states ventricular wall stress (σ) is proportional to the product of ventricular pressure (*P*) and ventricular radius (r), divided by ventricular wall thickness (h).**

According to the law of Laplace, that wall tension (T) in thin walled sphere or cylinders is proportional to the pressure (*P*) times radius (r). This law holds true when adapted to the ventricle (equation 1.1). This law shows how dilated cardiomyopathies result in a reduced ability to perfuse the body sufficiently, as for a given aortic diastolic pressure to overcome, the ventricular wall stress (σ) increases as the radius increases and wall thickness decreases in dilated cardiomyopathy. As such, the ventricular CM are required to contract more forcefully to maintain the same mean arterial pressure (Levick, 2003).

## The Cardiac Action Potential

The cardiac AP is the result of temporally distinct electrical conductance of a range of physiologically common ions. Each channel is activated or

deactivated in a voltage-dependent manner, and so the activation of one channel will lead to the activation and/or deactivation of itself and others. This ensures the AP will be completed in the same manner every time and will complete once it has been initiated.

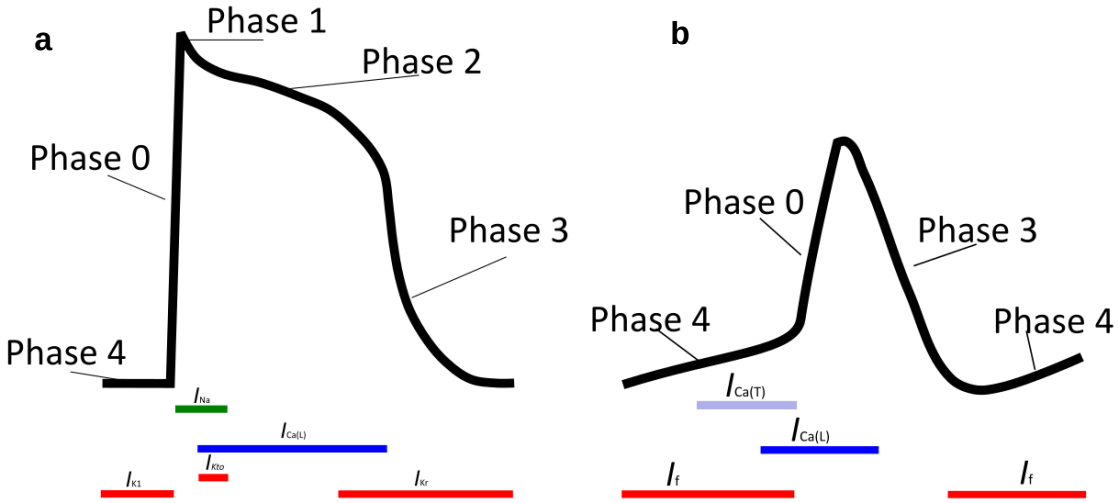


**Figure 1.4 Single CM action potentials. (a) Isolated ventricular CM AP. (b) Isolated SA-node pacemaker AP. Phase 0 represents sarcolemmal depolarisation due to $Na^+$ influx. Phase 1 represents the overshoot and a transient $K^+$ corrects it. Phase 2 is termed the plateau and is caused by $Ca^{2+}$ influx after $Na^+$ channels deactivate. Phase 3 represents repolarisation and due to deactivation of $Ca^{2+}$ channels and activation of $K^+$ channels.**

Diastole is reflected in phase 4 of the ventricular cardiomyocyte action potential, where the resting membrane potential is stable at approximately -90mV (Woodbury, *et al.,* 1950). Entry of cations through gap junctions of neighbouring myocytes or pacemaker cells takes the membrane potential to threshold (~-70mV). This opens voltage-gated fast $Na^+$ channels and is termed phase 0. Phase 0 signifies the start of systole and results in a rapid upstroke in membrane potential to approximately +50mV. These $Na^+$ channels are inactivated rapidly and must cycle through to the closed but active state at very low membrane potentials. As such, they cannot be re-activated until the cell returns to phase 4.

Phase 1 represents a brief overshoot, often referred to as the cardiac notch. Depolarisation transiently opens $K^+$ channels that lower the membrane

potential for the plateau, phase 2. During phase 2 the L-type calcium channels (LTCC) located in the T-tubules open for a relatively long period, resulting in the plateau. This calcium intrusion initiates contraction. LTCC slowly deactivate at positive membrane potentials and as they close, $K^+$ currents dominate, and the AP enters phase 3. This repolarises the sarcolemma and the AP re-enters phase 4 until a new AP arrives (Levick, 2003).

The phases have an element of flexibility, but the ratio of time lengths of each phase is retained even if the HR increases. For example, during exercise, adrenergic stimulation results in phosphorylation of multiple channels involved. This increases the kinetic properties and open probability ($P_O$) of various channels resulting in a faster AP, and therefore increased HR. Alterations to physiologic concentrations of key ions can also affect the AP. Hyperkalaemia increases the $I_{Na}$ during phase 0, whilst increasing the rate of LTCC inactivation and intrusion of $K^+$ during phase 3 (Bers *et al.,* 2003). The short-term effect of this is an increased hear rate (tachycardia).

The CM resting membrane potential typically settles near the $K^+$ equilibrium ($E_K$). $E_K$ is elevated in hyperkalaemia, which if increased sufficiently, will set the resting potential above the $I_{Na}$ activation threshold. The $Na^+$ channels required for the phase 0 upstroke are reactivated at negative membrane potentials, and so fewer will be available to initiate the AP in hyperkalaemia, ultimately leading to long term decreased HR (bradycardia).

The opposite effects are observed in hypokalaemia, which is associated with worsened clinical outcomes due to an increased risk of ventricular tachyarrhythmias. This is mainly due to the use of diuretics and activation of the renin-angiotensin-aldosterone system, resulting in the loss of $K^+$ in urine

(Skogestad and Aronsen, 2018). With regards to the AP, hypokalaemia results in hyperpolarisation, longer AP durations, and risk of early or delayed (i.e. uncoupled) depolarisations, which may result in $Ca^{2+}$ waves in single cells, or arrhythmia across the tissue (Weiss and Zhilin, *2017*).

**Cardiomyocyte Ultrastructure**

The heart comprises several types of muscle cell, each providing a specialised function. CM are the contractile units of the heart muscle. Healthy CM are typically uni- or binucleated and have either a rod-like or forked morphology. CM are approximately 80-100 µm long and connected to one another via intercalated discs at each pole of the cell. They have highly repeating structures called sarcomeres chained together to form individual myofibrils and bundled together to form myofibres. The myofibres, in turn, are arranged in a longitudinal manner throughout the volume of the CM, minus the nucleus.

The cardiac AP needs to be able to reach all sarcomeres near simultaneously to allow for a coordinated contraction of the cell. There are specialist structures that penetrate through the myofibres and run along the surface of individual fibrils across the cell. These structures are 200-400 nm tubes of extracellular membrane that penetrate through the CM located at each Z-line of the sarcomeres, bringing the extracellular space into close proximity with the inner depths of the CM (Soeller and Cannell, 1999). In transverse view they are less dense and more spoke like inward projections in larger mammals, when compared with rat and mouse (Jayasinghe *et al.,* 2012). Axial tubules are a significant minority of the membranous network and join two corresponding transverse tubules (commonly referred to as T-tubules),

perpendicular to their trajectory. T-tubules and their regular and parallel repeating pattern are lost in many disease states. Under these conditions, T-tubules are often visualised at oblique angles, with an overall loss of T-tubules density (Ibrahim *et al.,* 2011).

Without T-tubules, current would diffuse through the sarcomeres of a myocyte from outside to inside. The result of this is the loss of coordination of contraction between the different contractile units within the cell and in an overall loss of force generation (Ibrahim, 2011). Hill (1949) showed that the rate of contraction initiation was too rapid across a muscle cell to be due to diffusion. A structural feature was required to transmit the AP into the entire volume of the CM without delay.

T-tubules are highly heterogenous in terms of orientation, diameter, and whether they are close-ended inward projections or continuous tubulations of the sarcolemma that penetrate the CM, as observed via electron microscope studies (Soeller and Cannell, 1999; Ibrahim et al., 2011; Porter and Palade, 1957). T-tubules come into proximity with the sarco(endo)plasmic reticulum (SR) at regular intervals, bringing the channels on the T-tubules close enough to form a nanodomain with the channels on the opposing SR (figure 1.5).

T-tubules have been observed in all mammalian tissues that have been investigated, but not in avian, reptile, or amphibious tissue and are consistently found within ventricular CM (Brette and Richard, 2003). Recent data has challenged the previously held belief that they were only sparse or absent in mouse and rat atrial CM (Smymias *et al.*, 2010). T-tubules have recently been observed in atrial CM of large mammals, such as human, pig, and sheep (Richards *et al.*, 2011; Gadeberg *et al.*, 2016).

Approximately 60% of ventricular T-tubules are found in the traditional context of a transverse tubule adjacent to the Z-line, though 40% occurs between these z-lines. The T-tubules connect the extracellular spaces on either side, via an intricate meshwork, or rete (Soeller and Cannell, 1999). Thus, the extracellular space is expanded into the T-tubules (in their study, T-tubules accounted for 3.6% of the cellular volume).

This is vital for excitation-contraction coupling as it allows extracellular signals to reach the contractile machinery more quickly. The T-tubules contain LTCC that are near the Ryanodine receptor (RyR2) calcium channels found on directly opposing the SR. This space, termed the dyad, brings the SR in to close proximity (~15 nm) of the sarcolemma, creating a calcium nanodomain, as these signals are physically compartmentalised (Franzini-Armstrong, Protasi and Ramesh, 1999; Vega *et al.*, 2011).

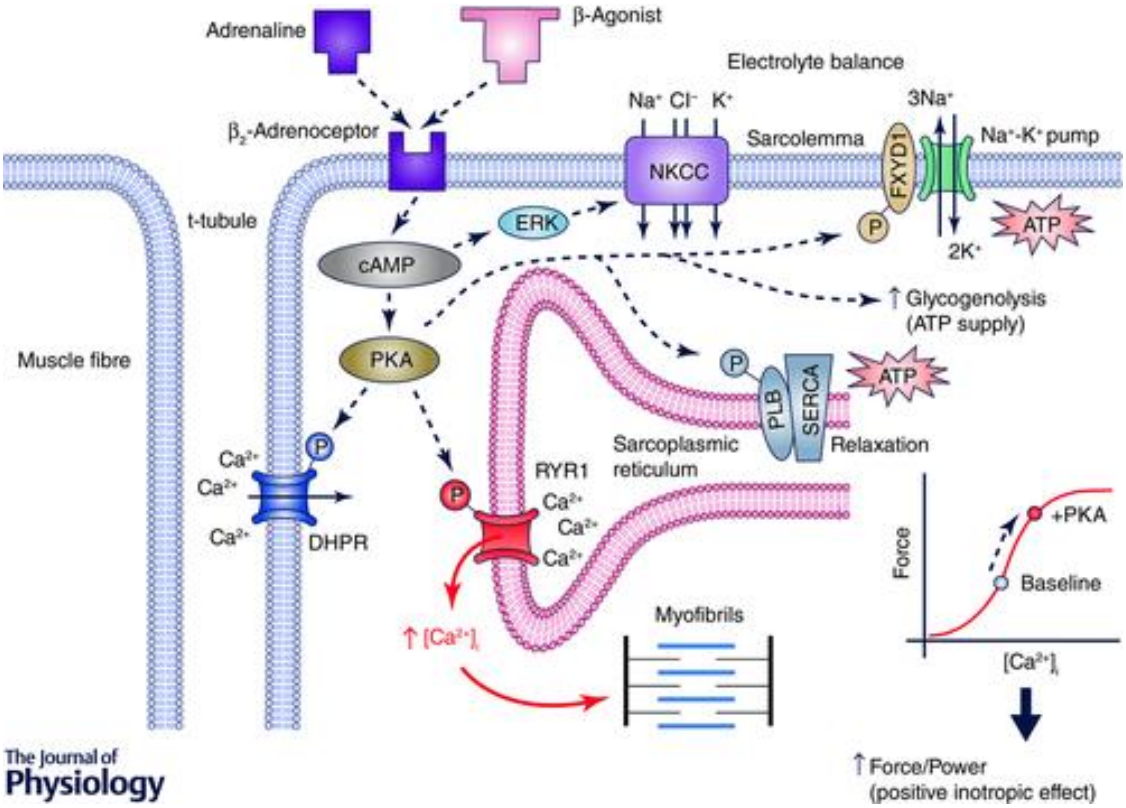


**Figure 1.5. Schematic diagram of excitation-contraction coupling proteins within the cardiomyocyte. $Ca^{2+}$ ions are cycled between the sarcoplasmic reticulum $Ca^{2+}$ store and cytosol to go onto activate contraction. Approximately 20% of the $Ca^{2+}$ is also cycled between the extracellular space and the cytosol during depolarisation and repolarisation of the sarcolemma. These processes can all be modulated by external stimuli, such as the activation of PKA via β-adrenergic receptors as shown here. Reproduced with permission from Cairns and Borrani (2015).**

LTCC activation caused by the AP arrival onto the T-tubules leads to a small but significant influx of $Ca^{2+}$ ions. These are enough to activate the RyR2 in a process called calcium-induced calcium release (CICR). RyR2 clusters are considered binary as the $Ca^{2+}$ released from the SR through RyR2 will activate all RyR2 within that cluster. Additionally, clusters within approximately 150 nm of each other are functionally coupled into calcium release units (CRU), sometimes referred to as superclusters (Franzini-Armstrong, Protasi and Ramesh, 1999; Baddeley *et al.*, 2009; Hou *et al.*, 2015). This is because the neighbouring cluster is sufficiently close to always be activated by the $Ca^{2+}$ released from the activated cluster.

$Ca^{2+}$ released through RyR2 goes on to activate the contractile machine in excitation-contraction coupling (Figure 1.6). During AP phase 3 RyR2 close. At this time the sarco(endo)plasmic reticulum calcium ATPase (SERCA2a) in the SR membrane pumps approximately 90% of the $Ca^{2+}$ back out of the cytosol and into the SR, with the remaining 9% being extruded through the sarcolemma by the sodium-calcium exchanger (NCX) (Li *et al.*, 1998). This system effectively resets the internal workings of the cell. $Ca^{2+}$ will diffuse away from the contractile machinery resulting in relaxation of the muscle and cellular diastole as the AP enters phase 4.

SERCA2a is partially inhibited, predominantly by phospholamban (PLN), amongst other regulatory proteins (Tada *et al.*, 1974; Tada, Kirchberger and Katz, 1975). PLN can be phosphorylated at Ser-16 and Thr-17 through the PKA and CamKII pathways respectively, resulting in release of this inhibition (Hagemann and RP, 2002; Mattiazzi *et al.*, 2005). This process is required to maintain the ratio of the heartbeat. When LTCC and RyR2 kinetics are increased due to adrenergic stimulation, SERCA2a and PLN activity must compensate too so that the heartbeat and AP shorten relative to their constituent parts.

**Excitation-Contraction Coupling**

$Ca^{2+}$ ions released from RyR2 during phase 2 of the AP diffuse to the nearby contractile machine in a time-synced manner. Here the $Ca^{2+}$ ions activate the contractile machinery and initiate contraction. As the $Ca^{2+}$ ions are removed from the intracellular space (sarcoplasm) and pumped into the SR, the local

concentration drops. This results in a loss of contraction. As such this is known as excitation-contraction coupling.

Excitation-contraction coupling happens at each sarcomere along a myofibril and across the CM at approximately the same time. As such, RyR-mediated $Ca^{2+}$ release must be uniform and even across the CM to result in an even, coordinated contraction. This event relies on interweaved protein strands (actin and myosin filaments) interacting and pulling together, like the teeth of two combs sliding together. This is an energetic process and so requires ATP to catalyse the reaction, whilst the presence of $Ca^{2+}$ ion uncovers the actin filaments to allow the ATP-mediated contraction. As such both intracellular calcium concentration ($[Ca^{2+}]_i$) and ATP are required for contraction to occur (Cheng *et al.,* 1993).

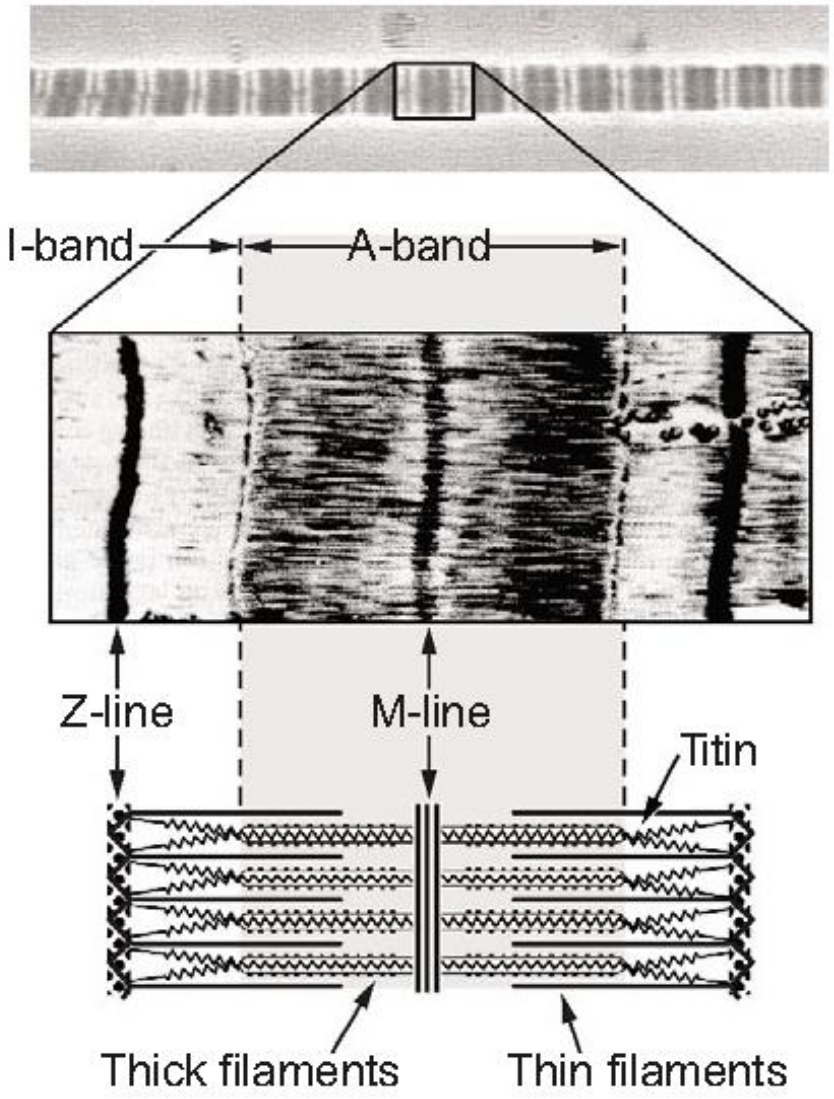


**Figure 1.6. The highly ordered striated structure of actin myosin filaments used for contraction in striated muscle. An Electron micrograph of a single myofibril is shown (top panel) with an individual sarcomere highlighted (centre panel). A diagrammatic representation shows the interleaved nature of actin and myosin. Titin anchors myosin to the Z line (bottom panel). Figure adapted from Herzog (2014).**

Contraction is dependent upon ATP as well as $Ca^{2+}$. The troponin-tropomyosin complex is a filament that runs the length of the actin filaments lying in a helical groove. When $Ca^{2+}$ binds, the troponin complex undergoes a conformational change, pulling the tropomyosin filament out of the groove and so revealing the myosin binding sites on the actin filament. Next, the myosin head with ADP + $P_i$ bound separately attaches to actin filament. Upon actin-myosin binding, ADP + $P_i$ are released, the head pivots, and a power stroke is

generated. This physically pulls the actin molecule past the myosin filament towards the M-line by 10 nm. At this point the contraction has occurred but the actin and myosin are still bound together. A new ATP molecule binds to the myosin head causing it to release from the actin filament. The myosin head will then hydrolyse the ATP to ADP + $P_i$ to 'cock' the unbound myosin head back ready to repeat the cycle further along the actin filament (Cheng *et al.,* 1993; Levick, 2003).

**Ryanodine Receptor Cluster Physiology and Phosphorylation**

RyR2 are homotetramers made up of 565 kDa proteins that form a $Ca^{2+}$ release channel through the SR. Low concentrations of Ryanodine locks the RyR into a sub-conductance state, where the RyR channel intermittently allows single $Ca^{2+}$ ions across the membrane. This results in tetanic muscle contraction as the SR $Ca^{2+}$ slowly leaks uncontrollably into the cytosol. Ryanodine completely blocks this current at higher concentrations (>100μM) (Meissner *et al.*, 1986; Zalk and Marks, 2017). This discussion focuses on the cardiac RyR2 isomer, but it should be noted that all of the 3 RyR isomers are expressed in a wide range of tissue other than muscle, including the brain, liver, lungs, and pancreas.

RyR2 are found in clusters of varying sizes that typically follow a near exponential distribution in frequency as size increases and consistent with stochastic cluster assembly. (Franzini-Armstrong, Protasi and Ramesh, 1999; Baddeley *et al.*, 2009). Co-immunoprecipitation experiments of RyR2 showed it has a microenvironment of functional proteins intimately surrounding it, such as calstabin (FKBP12.6), mAKAP anchoring protein, PKA, CaMKII, and

protein phosphatases 1 (PP1) and 2 (PP2a) (Marx *et al.*, 2000; Kushnir *et al.*, 2010). Recent studies have also shown that there are interacting partners within RyR2 clusters such as IP3 (Taylor and Tovey, 2010) and junctophillin-2 (Jayasinghe *et al.*, 2018b).

RyR2 clusters and CRUs function is to release $Ca^{2+}$ in localised bursts. There is a $10^4$ difference in sarcoplasmic versus $[Ca^{2+}]_{SR}$ and so the spark diffuses rapidly away from the CRU, before being extruded from the cytosol by either NCX or SERCA2a. This release from a single CRU is termed a $Ca^{2+}$ spark in part due to their appearance when observed with fluo-3 (that fluoresces when bound by $Ca^{2+}$), and partly because the event is what 'sparks' E-C coupling into action (Cheng *et al.*, 1993). As such, the physiology of RyR2 can be thought of in terms of $Ca^{2+}$ spark behaviour.

Resting CM displayed $Ca^{2+}$ sparks are local events of approximately 2 µm in diameter and last for around 30 ms using confocal microscopy. Upon stimulation, these summate to produce a calcium transient. Transients are of non-uniform activation due in part to the heterogeneity of CRU size and RyR clusters' stochastic activation within them. As such a $Ca^{2+}$ transient activation pattern is similar to $Ca^{2+}$ sparks (Cannell *et al.,* 1994). Under normal physiological conditions, the volume engulfed by a single $Ca^{2+}$ spark contains several CRU but none are activated by the spark. In conditions with high extracellular concentrations ($[Ca^{2+}]_O$), sparks can activate nearby CRUs. These sparks have an increased amplitude (4,1x), spatial size (1.7x), and frequency (4x) when $[Ca^{2+}]_O$ is increased 10-fold (Cheng *et al.,* 1996). This activity can then propagate CRU activation in a spatially and temporally synchronised manner, creating a $Ca^{2+}$ wave. Though there is some evidence

that $Ca^{2+}$ waves perform a function in developing CM, in the adult they are considered pathological. RyR2 are sensitised by SR $Ca^{2+}$ concentrations ($[Ca^{2+}]_{SR}$) and by agonists, such as caffeine, plus other mechanisms that increase the RyR2 $P_O$, lower the SR $Ca^{2+}$ threshold (Venetucci *et al.,* 2007). A $Ca^{2+}$ wave will slightly depolarise the sarcolemma and can also induce a transient inward current through the NCX (Weir and Beuckelmann, 1989). Combined, these may be sufficient to produce an AP in the single cell. Whilst it requires the concerted aberrant firing of approximately 10,000 cells to produce an ectopic beat, the underlying causes are often global and so calcium sparks and waves of single cells are of strong interest in pathology. Clinically, ectopic beats can develop into full fibrillation – a complete loss of contractile coordination and so loss of ejection fraction and ultimately, death.

The contraction and systolic $Ca^{2+}$ transient reduce in amplitude and rate of decay in heart failure (HF). RyR2 are thought to play a significant role in this, along with altered SERCA2a activity, typically due to phosphorylated PLN releasing its inhibition. It has been proposed that FKBP12.6 stabilises RyR2 and is released upon phosphorylation of RyR2 at Ser-2808. The removal of this stabilisation is thought to increase diastolic $Ca^{2+}$ leak from RyR2 and decrease the number of RyR2 that open during CICR, reducing contractility (Marx *et al.*, 2000). Marx and coworkers showed that human RyR2 receptors were hyperphosphorylated in HF, and coimmunoprecipitated with the molecules responsible for local phosphorylation control (PP1, PP2a, FKBP12.6, PKA).

Others however, argue that this is only a brief, transient effect and when caffeine was applied to single cells SR load quickly equilibrated and took on a

new steady state (Venetucci *et al.,* 2007). As sensitivity to $[Ca^{2+}]_{SR}$ increased due to caffeine treatment, the RyR2 $Ca^{2+}$ transient amplitude increased, leading to more $Ca^{2+}$ leaving the SR. This extra luminal $Ca^{2+}$ would be extruded from the sarcoplasm until the system equilibrated. In contrast, the Marx hypothesis states that the RyR2 channel when phosphorylated takes on a sub-conductance state, that allows a constant trickle of $Ca^{2+}$ ions. This would result in a depletion of SR $Ca^{2+}$ and so inadequate contraction. It would also result in aberrant RyR2 cluster activation from the $Ca^{2+}$ leak, coupled with increased RyR2-$P_O$ due to PKA phosphorylation.

**Ryanodine Receptor Phosphorylation in Health and Disease**

RyR2 function is modulated by various PTMs, in particular, phosphorylation by protein kinase A (PKA) and $Ca^{2+}$/calmodulin protein kinase K (CaMKII) at (at least) three sites, Ser-2030, Ser-2808, and Ser-2814 (Huke and Bers, 2009; Xiao *et al.,* 2006, Witcher *et al.,* 1991; Wherens *et al.,* 2004). Currently, the field is conflicted with regards to the role of these phosphorylation sites in causing heart disease, though it is agreed that phosphorylation is increased across these sites. The entire April 2014 edition of Circulation Research was dedicated to this question (see Dobrev and Wehrens *et al.,* (2014) and Houser, (2014) for extensive reviews). This demonstrated the difficulty in these experiments and the differences in data and observation. Herein I summarise my reading of the literature as what is (somewhat) held as consensus. Disputed evidence is highlighted but it is beyond the scope of this summary to settle the dispute.

**Ser-2030 Phosphorylation**

Ser-2030 phosphorylation is the most recent site to have been described as a target for PKA phosphorylation due to β-adrenergic stimulation (Xiao *et al.,* 2006). Ser-2030 was observed to be lowly phosphorylated in independent studies and highly phosphorylated in response to isoproterenol treatment on isolated CM. Ser-2030 was not seen to be hyperphosphorylated in failing rat hearts. In an important study to compare different sources of pssAb across Ser-2030, Ser-2808, and Ser-2814 epitopes, they found no (Chen pssAb) or very faint (Valdivia pssAb) signal at rest and a strong signal after isoproterenol treatment. However, the authors noted that a strong dose of isoproterenol (1 μM for 15 mins) was required to illicit the response. Whilst this could be a product of low affinity of the two antibodies, it is at contrast to the Chen lab's claim that Ser-2030 is a key modulator of physiological RyR2 activity upon adrenergic stimulation (Xiao *et al.,* 2006).

Wehrens and colleagues (2006) tested recombinant human RyR2 channel that had replaced the serine with an alanine to result in a constitutively unphosphorylatable site (RyR2-S2031A, corresponding to Ser-2030 in mice and rat). They found that with the addition of a specific PKA inhibitor ($PKI_{5-24}$) parallel protein from RyR2-S2808A mice were not phosphorylated by PKA, whilst wild type RyR2 were. Those data together cast doubt on the importance of Ser-2030 as a phosphorylation site and the specificity of PKA to it. Whether recombinant RyR2-S2031A can be appropriately compared with murine RyR2-S2808A is also a potential source of confusion in interpreting these studies. Currently, there is limited experimental evidence on the role of Ser-2030 as a phosphorylation site, with consensus tipping towards Ser-2030

is not PKA specific and does not appear to have any correlation to disease progression (Wehrens *et al.,* 2006; Bovo *et al.,* 2017).

**Ser-2814 Phosphorylation**

Ser-2814 was the first described RyR2 phosphorylation site due to CaMKII action, not PKA. Ser-2814 phosphorylation and/or increased CaMKII activity is currently considered the prime suspect of RyR2 related disorder.

Ser-2814 phosphorylation was shown to increase RyR2-$P_O$ and $Ca^{2+}$ sensitivity, as evidenced in single channels in lipid bilayers, and $Ca^{2+}$ spark frequency in isolated CM (Wehrens *et al.,* 2004; van Oort *et al.,* 2010). Ai and coworkers (2005) used an arrhythmogenic, non-ischaemic rabbit model to investigate the role of RyR2 phosphorylation in HF progression. It was found that RyR2 and FK-506 binding protein 12.6 (FKBP12.6) expression were decreased, whereas CaMKII and inositol triphosphate receptors ($IP_3R$; a different SR $Ca^{2+}$ release channel) were increased 50 – 100%. CaMKII inhibition, but not PKA inhibition, reduced the pathologically heightened SR $Ca^{2+}$ leak in HF isolated CM, suggesting CaMKII phosphorylation at Ser-2814 is responsible for increased diastolic SR $Ca^{2+}$ leak and so lead to arrhythmias and contractile dysfunction in HF.

Further evidence showed that increased CaMKII activation led to increased $Ca^{2+}$ sparks and waves (uncontrolled spread of excitation; arrhythmogenic phenomena in single CM). In constitutively pseudophosphorylated mice (RyR2-S2814D) inhibition of CamKII had no effect on the pathological signs, whereas it did reduce them in wild type mice (van Oort *et al.,* 2010).

Soliman and colleagues (2019) recently showed that the propensity for diabetic mice to progress into HF was linked to increased Ser-2814 phosphorylation. This study focused on the role of the RhoA/ROCK system. Rho-associated protein kinase (ROCK) is a PKA/PKG/PKC like serine-threonine kinase and has downstream effects of the GTPase-like RhoA kinase. ROCK +/- mice attenuated CaMKII phosphorylation, which leads to Ser-2814 phosphorylation. Spontaneous $Ca^{2+}$ leak was increased in diabetic HF mice, whilst ROCK +/- diabetic HF mice had attenuated levels of spontaneous $Ca^{2+}$ (Soliman *et al.,* 2019).

Supporting evidence was published recently that showed PLN ablation increased SR $Ca^{2+}$ uptake, and so reduced Ser-2814 induced diastolic $Ca^{2+}$ leak (Valverde *et al.,* 2019). Removing Ser-2814 hyperphosphorylation by use of RyR2-S2814A mice was shown to protect against non-ischaemic causes of HF, whereas HF progression due to ischaemic incidents (surgical myocardial infaction) were not protected (Respress *et al.,* 2012).

Likewise, human induced pluripotent stem cell-derived CM were engineered into tissue-like states by Park and colleagues (2019). They modelled the genetic arrhythmogenic disorder catecholaminergic polymorphic ventricular tachycardia (CPVT). CPVT is a genetic disorder, most commonly due to a point mutation in RyR2 that leads to ventricular tachycardia and can result in cardiac arrest and sudden death. As the name suggests, CPVT is triggered by catecholamines, such as adrenaline i.e. during physical activity or emotional stress. CRISPR Cas9 gene editing of Ser-2814 showed this phosphorylation event was required to generate re-entrant arrhythmia in engineered tissue (Park *et al.,* 2019). A mutant RyR2-P2328S mouse model of CPVT with atrial

fibrillation. This mouse model reported no difference in phosphorylation state of Ser-2814 or Ser-2808 site between RyR2P2328S mice and wild type in the absence of adrenergic stimulation, suggesting that CPVT does not cause Ser-2814 phosphorylation but is summative (Salvage *et al.,* 2019).

It is accepted that diastolic SR $Ca^{2+}$ leak due to Ser-2814 is a true factor in HF progression. Ser-2814 is consistently reported to be lowly phosphorylated at basal levels and increases substantially in disease states (Walweel *et al.,* 2019; Salvage *et al.,* 2019; Dobrev and Wehrens, 2014; Huke and Bers, 2009). More recent studies have found that hyperphosphorylation of Ser-2814 can result in disease progression, typically through arrhythmias. Ser-2814 Whether Ser-2814 phosphorylation or increased activation of CaMKII are responsible is yet to be dissected. (Wehrens *et al.,* 2004; Dobrev and Wehrens, 2014; Bers, 2012).

**Ser-2808 Phosphorylation**

Ser-2808 was the first RyR2 phosphorylation site reported. Whilst initially reported as being phosphorylated by CaMKII, it is now broadly accepted as a PKA specific phosphorylation site, though there have been reports of CaMKII and protein kinase G (PKG) being responsible for Ser-2808 phosphorylation (Witcher *et al.,* 1991; Huke and Bers, 2009; Bers, 2012; Camors and Valdivia, 2014). Addition of PKA to RyR2 in lipid bilayers increased the RyR2-$P_O$ and this was prevented with constitutively dephosphorylated RyR2-S2808A (Wehrens *et al.,* 2004). Further circumstantial evidence came from application of PKA to isolated wild type CM, which resulted in increased Ser-2808 phosphorylation. However, PKA only increased the $Ca^{2+}$ transient at systolic

$Ca^{2+}$ concentrations, but not diastolic, where the leak occurs (Bers *et al.,* 2003).

Constitutive phosphorylation of RyR2-S2808D replicated in some, but not all subsequent studies, setting the tone for the future Ser-2808 debate (Wehrens *et al.,* 2004; Wehrens *et al.,* 2006; Stange *et al.,* 2003). RyR2-S2808A transgenic mice were created by several groups independently and studies on these mice fuelled the controversy. Initial, seminal results published by the Marks group showed that RyR2 was hyperphosphorylated by PKA in-vitro using kinasing reactions, with maximal phosphorylation resulting in a stoichiometry of 3.8±0.1 moles [$\gamma^{32}P$] ATP detected per mole of RyR2, indicating that PKA phosphorylates one site per RyR monomer. As PKA is downstream activated by increased system adrenergic stimulation in response to acute or chronic stress, they then looked at PKA phosphorylation of RyR2 from human HF and a canine model of non-ischaemic HF. They found that RyR2 were PKA hyperphosphorylated and proposed a model where RyR2, FKBP12.6, PKA, and the phosphatases PP! and PP2a, plus anchoring protein mAKAP formed a macromolecular complex (Marx *et al.,* 2000).

This work created an initial excitement in the field that turned into controversy lasting the next decade or so (Bers, 2012). Subsequent studies showed that FKBP12.6 is expressed at much lower levels than RyR2, casting doubt of the model that Ser-2808 phosphorylation leads to dissociation of FKBP12.6 and so loss of receptor stability and increased diastolic $Ca^{2+}$ leak (Dobrev and Wehrens, 2014; Camors and Valdivia, 2014; Xiao *et al.,* 2004; Zissimopoulos *et al.,* 2011). The Marks group demonstrated that RyR2-S2808A mutant mice showed reduced responses in HR and contractile responses in isolated CM as

well as protection from catecholaminergic-induced cardiac dysfunction, suggesting that prevention of Ser-2808 phosphorylation could protect against heart disease (Marx *et al.,* 2000). The Marks group also created a RyR2-S2808D mouse line that resulted in an increased diastolic $Ca^{2+}$ leak, increased mortality after myocardial infaction and no improvement with β-adrenergic receptor blockers, unlike wild type mice (Shan *et al.,* 2010).

The Valdivia and Houser groups also created RyR2-S2808A mice. These studies failed to replicate those of the Marks group. The $Ca^{2+}$ transient amplitude and contraction were increased in both wild type and RyR2-S2808A mice, with no difference in response to isoproterenol between them (MacDonnell *et al.,* 2008). The Valdivia group, using the same RyR2-S2808A mouse strain as the Houser group failed to observe any protection from a chronic stress model of HF and minimal pathological changes in whole heart or isolated CM experiments. They concluded that as the constitutive deletion of the Ser-2808 phosphorylation site failed to protect against HF progression, then it is unlikely to be play a major role in the underlying mechanisms of HF (Benkusky *et al.,* 2007).

Each of these conflicting studies used different metrics in different mouse strains. Whilst one can argue that touted disease mechanisms should be conserved across mouse strains, let alone to be translated into clinic, it still makes interpreting the data and potential experimental error harder. Overall, it is mostly agreed by the majority of the field that Ser-2030 is basally dephosphorylated by PKA, and the role of this site in physiology or pathology is not clear. Ser-2808 has controversial and conflicting experimental data surrounding it. Ser-2808 basal phosphorylation is quite high, at around 50-

75% and is predominantly phosphorylated by PKA, though the exclusivity has been questioned. Ser-2814 is lowly phosphorylated at baseline and phosphorylated by CaMKII. Ser-2814 has the most consistent evidence of contributing to disease progression, though the controversy is far from settled.

**Imaging RyR Clusters Requires Super-Resolution Microscopy**

The purpose of T-tubules has been of interest to the field since their visualisation by light microscopy in the late 19$^{th}$ Century (see Huxley, 1971). The structures of these T-tubules and the surrounding junctional SR (forming a couplon) was observed first in EM by Linder and colleagues (1956). Further EM studies revealed that these T-tubules were extensions of the sarcolemma, and axial T-tubules observed 15 years later (Franzini-Armstrong and Porter, 1964; Sperelakis and Rubio, 1971). These findings explained earlier observations that excitation can penetrate into the centre of the cell in approximately 40 ms, a speed not possible by diffusion alone (Hill, 1949).

The 3-dimensional t-tubule network was visualised using two-photon microscopy and revealed an intricate network of interconnected tubules of diameters between 200 – 450 nm (Soeller and Cannell, 1999). The $Ca^{2+}$ current inhibitor, ryanodine, was found to specifically bind to the SR that were nearest T-tubules (Fleischer *et al.,* 1985). Functional studies eventually identified the RyR2 receptor as key to $Ca^{2+}$ release and the formulation of the theory of CICR (Fabiato, 1985). From these initial EM images of couplons, RyRs were imaged using confocal microscopy and deconvolution image analysis. RyR labelling was seen in striations with unequal fluorescence

intensities, suggesting unequal distributions of the underlying RyR receptors into puncta (Jayasinghe *et al.,* 2009).

**Underlying Mechanisms of STORM SMLM Microscopy**

Super-resolution microscopy techniques that were demonstrated in 2006 based on the localisation at nanometre scale of single fluorescence emitters, termed single molecule localisation microscopy (SMLM) provided a method to visualise RyR clusters at the single receptor resolution within intact CM for the first time, using immunofluorescence approaches (Betzig *et al.,* 2006; Hess *et al.,* 2006; Rust *et al.,* 2006).

Thousands of imaging frames are recorded where only a sparse subset of fluorophores emit at any one time. These are sufficiently sparse that the diffraction limited spot of light emitted by one emitter does not overlap with any others within the same frame. This allows for successive localisations to be summed and create a super-resolved map of emitter positions, composed into an SMLM image.

Reversible saturable optical fluorescence transitions (RESOLFT) is the generic principle underlying the more popular technique known as stimulated emission depletion (STED) microscopy (Bossi *et al.*, 2006; Sahl, Hell and Jakobs, 2017). STED microscopy utilised a second laser at a much higher wavelength to de-excite fluorophores when the excitation laser in a laser scanning set up excites a diffraction limited spot. The depletion laser has a ring shape and the diameter of the hole inside it can be tuned, thus physically limited the area excited below the diffraction limit of the excitation laser power.

$$\sigma = \sqrt{\left(\frac{s_i^2 + \frac{a^2}{12}}{N}\right) \cdot \left(\frac{16}{9} + \frac{8\pi s_i^2 b^2}{a^2 N}\right)}$$

**Equation 1.2. Localisation precision of a PSF. Localisation precision (σ) is a function of the number of photons collected (*N*), the pixel size (*a*), the standard deviation of PSF ($S_i$), and mean background signal (*b*).**

Photoactivatable localisation microscopy (PALM) activates endogenous or genetically tagged fluorescent proteins and is proving useful in live cell super-resolution microscopy (Betzig *et al.*, 2006). Stochastic optical reconstruction microscopy (STORM) was developed to produce the same result as PALM only using fluorescent dyes as commonly used in antibody-based labelling systems and was demonstrated independently at the same time as PALM. Initial experiments used fluorescence energy transfer between acceptor and donor molecules conjugated together, and shortly after direct excitation (dSTORM) was achieved with the use of oxygen scavenging buffers (Rust *et al*., 2006; Heilemann *et al.*, 2008). For simplicity, STORM herein refers to direct STORM.

## Resolution

$$d = \frac{\lambda}{2[n \cdot sin(a)]}$$

**Equation 1.3. The Abbe resolution limit of a light microscope. The resolution (*d*) is a function of the emission wavelength (*λ*) divided by twice the numerical aperture (NA) calculated from the refractive index of the medium being imaged (*n*) and the sine of the half angle of the light collection cone of the objective (*a*)**

Visible light is comprised of a range of wavelengths of electromagnetic radiation that the human eye can sense. Photons travel as a wave in straight lines and become diffracted as they pass through media or a slit, similar to an ocean wave through a harbour entrance. Other related biophysical techniques such as spectroscopy and EM are also limited by the diffraction of light.

Transmission EM is not a light microscopy technique, however the still present diffraction of electrons through the media and microscope materials limits the resolution of the observed image to approximately 0.1 nm (Williams and Carter, 1996). Spectroscopy and EM are both label-free, however are not suitable for investigating the distributions of specific proteins.

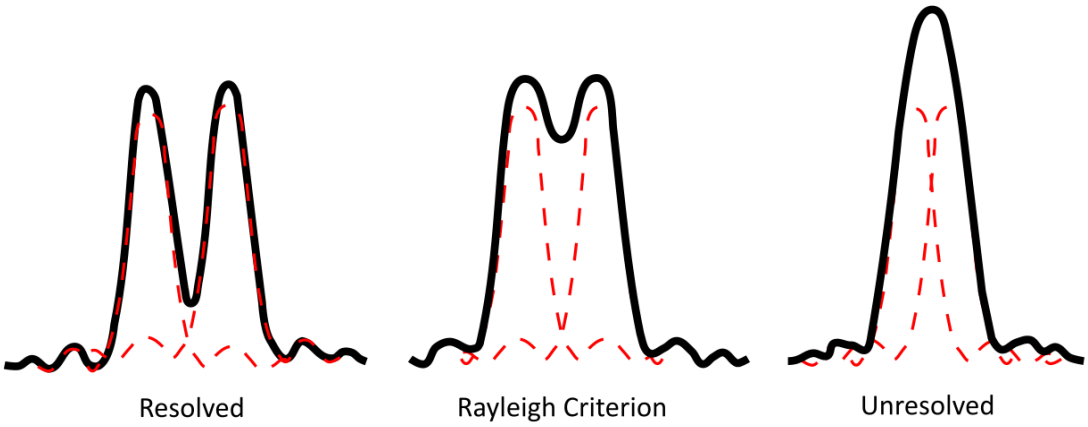


**Figure 1.7. The Rayleigh criterion. The PSF intensity profiles of two-point sources. Their separation dictates whether they can be resolved in a light microscope.**

Light microscopy resolution lies between these values. The shortest wavelength of light the human eye can observe is near 400 nm and so the minimum achievable resolution is near 200 nm in x,y. These wavelength-specific differences arise from the diffraction of light. Ernst Abbe, Lord Rayleigh, and C.M. Sparrow have all described the resolution limit of light approximately equally (Abbe, 1873; Rayleigh F.R.S, 1879; Sparrow, 1916). During diffraction, the light wave emitted from an effectively dimensionless singular point source and is broadened and bent into a point spread function (PSF) on contact with an obstacle. As shown in figure 1.7, the PSF maxima peak is far greater than its width, resulting in a z resolution of approximately 500 nm (equation 1.4).

$$d_z = \frac{2\lambda}{[n \cdot sin(a)]^2}$$

**Equation 1.4. Axial resolution limit. The axial resolution ($d_z$) is a function of twice the emission wavelength ($\lambda$) divided by the square of the NA, calculated as the refractive index of the medium image ($n$) multiplied by the sine of the angle of collection of the objective lens ($a$).**

The PSF is the result of constructive and destructive interference caused by light diffraction. If one considers each point of a wave of light to be emitting Huygen's wavelets, the sum of the interferences results in peaks and troughs of decaying intensity with a periodicity defined by the wavelength of light. The Rayleigh criterion defines the minimum distance separation between two-point sources that allow for them to be resolved. This is the distance at which the first minima of the PSF A coincide with the maxima of PSF B (figure 1.7). For over a century, light microscopy has been fundamentally limited by the intrinsic nature of light.

## Fluorescence

Fluorophores are molecules whose chemical structure allow for absorption of energy in the form of photons to transiently excite an electron from a singlet ground state ($S_0$) to an excited state ($S_1$). This energy is then released as a photon with lower energy as the electron relaxes back to $S_0$. The precise chemical structure of the molecule dictates the precise wavelengths of light required to excite them. These explain why there are a range of different fluorophores that cover different portions of the visible spectrum and the red shift between excitation and emission spectra.

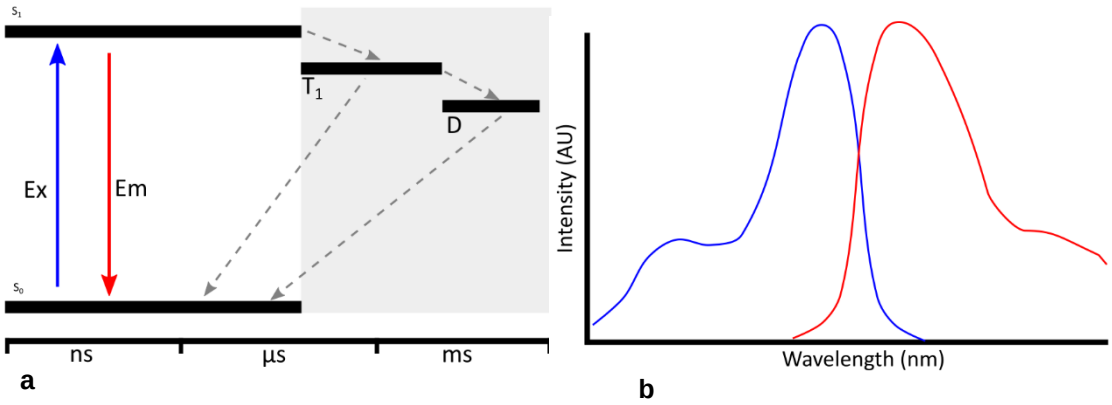


**Figure 1.8. Underlying mechanisms of fluorescence excitation and emission. (a) Jablonski diagram showing the electron energy levels and corresponding fluorescence states. Fluorophores are excited from $S_0$ to $S_1$ by the absorption of a photon (blue arrow). A red Stokes' shifted photon is released upon radiative relaxation back to $S_0$ (red arrow). In some instances, electrons enter the triplet state ($T_1$) and are held there for longer. Eventually a photon may be released during relaxation to the ground state $S_0$. Fluorophores may instead enter the dark state and the resulting relaxation is much slower and occurs at lower intensity (phosphorescence). Typical time scales are shown. The grey region depicts the dark state (b) Schematic excitation and emission spectra of a given fluorophore. Each fluorophore has an excitation maximum that lasers are typically selected for (blue line) and emit fluorescence at lower energy in a red Stokes' shifted spectrum (red line).**

In traditional widefield or confocal fluorescence microscopy, it is desirable to maintain a constant behaviour across all fluorophores to allow the sample to be imaged. This is achieved by balancing excitation intensity to excite the fluorophores, whilst being insufficient to cause irreversible chemical reactions that fundamentally alter the fluorophore's structure and prevent the absorption of photons (photobleaching). Chemical mountants such as Prolong Gold (ThermoFisher, USA), Vectashield (Vectorlabs, USA), and Mowiol (Sigma-Aldrich, USA) include anti-fade agents that aim to prevent these reactions so that samples can be kept in storage and re-imaged over months or years.

Switching buffers act in a counter-intuitive manner. Whilst traditional mounting media contain anti-fade agents, switching buffers encourage molecules into the triplet state (figure 1.6). By containing either thiols or oxygen scavenging systems, they also reduce the likelihood of oxidation, a key mechanism of photobleaching. When coupled with high laser powers, the net result is rapid

cycling of fluorescence from individual fluorophores that stochastically enter the dark state. The dark state is an intermediate excited triplet state that is non-radiative and the probability of relaxation via radiative or non-radiative pathways is low. The result of this is a long (milliseconds) excited, non-fluorescing state of the fluorophore and so it is effectively dark and non-excitable. STORM requires the majority of fluorophores to be in this state at any one time to ensure only a subset are fluorescing and so can be adequately distinguished from each other and localised.

These appear like a brief 'blink' of light from a mostly darkened sample (herein termed 'events'). When these are imaged over time, each fluorophore is imaged and localised (equation 1.2) to typically less than 20 nm in x,y and less than 50 nm in z (Hell *et al.*, 2015). Then the underlying points are then reconstructed into a pseudu-image of the underlying structure of interest.

Common buffers can be aqueous based, such as a glucose oxidase-based scavenger. This requires the presence of glucose to deplete oxygen from the switching buffer. These buffers are particularly useful for live cell PALM microscopy as they can be made into physiological saline buffers and compatible with STORM. Fixed samples do not require this and so 90% glycerol switching buffers are also commonly used (Baddeley *et al.*, 2009, 2011; Hou *et al.*, 2015; Tam and Merino, 2015). Glycerol based buffers have a better refractive index match between the objective oil, glass coverslip, and media (NA = 1.47). This reduces the refraction of the samples, especially in optically thick specimens that can occur when imaging through an oil immersion objective and into an aqueous based switching buffer.

**Super-resolved RyR clusters and phosphorylation distribution**

The first use of SMLM imaging in CM investigated the peripheral RyR clusters of isolated CM (Baddeley *et al.,* 2009). This study employed the use of a Highly Incluned and Laminated Optical Sheet (HILO) illumination methodology, which allows SMLM to be performed in relatively thick samples (i.e. thicker than 10 µm, Tokunaga *et al.,* 2008; Jayasinghe *et al.,* 2018). Subsequent studies have employed HILO SMLM imaging of RyRs within tissue sections and isolated CM to image RyR (amongst other related proteins). These studies have shown that interior RyR clusters are ~4 times larger than peripheral and demonstrated the ability to observe single RyRs (Baddeley *et al.,* 2009; Hou *et al.,* 2015). Although the majority of clusters observed contained <5 RyRs, around 80% of the RyR population were found to reside within a few large clusters (>100 RyRs; Hou *et al.,* 2015). Nearest neighbour measurements between RyR clusters were also reduced in SMLM (~140 nm) compared with confocal (~670 nm) microscopy, due to the capability to resolve single RyR receptors between the large puncta.

Building on earlier work that estimated local $Ca^{2+}$ concentrations would reach micromolar concentrations within 100 nm of RyR couplons, it was modelled that RyR clusters within this distance are likely to be functionally coupled, so the release of one cluster will activate the neighbouring cluster. This forms effectively functional ‘super-clusters’ and the SMLM data suggest that RyR clusters regularly form super-clusters (2-6, mean ~3.4; Hou *et al.,* 2015; MacQuaide *et al.,* 2015).

RyR cluster data is firmly linked to t-tubule morphology data. The diameters and degree of tubule branching (axial tubules) were different between

mammalian species. As a general principle, larger mammals ie human or pig, had much less t-tubule density than smaller mammals, i.e. rat or mouse (Jayasinghe *et al.,* 2015).

Whilst STORM SMLM relies on manipulating the photophysical properties of fluorescent dyes, a new approach has recently been developed to overcome the intrinsic limitations of STORM microscopy, i.e. photobleaching of fluorophores and limited number of photons produced, resulting in a limit in achievable resolution. DNA Point Accumulation Imaging in Nanoscale Topography (DNA-PAINT) was recently developed to overcome these limitations (Jungmann *et al.,* 2016). DNA-PAINT utilises the transient binding of short single stranded DNA oligos (approximately 10 bases). One strand, termed the docking strand, is conjugated to an antibody or other appropriate marker, whilst the complimentary, or imager strand is free in solution with a fluorophore conjugated to it. As the imager strand diffuses free in solution, it contributes near no fluorescence to the image on the camera. Once it is temporarily bound to the docking strand, it strongly emits fluorescence from a fixed point. This DNA-PAINT fluorescence is an SMLM event that can be localised in an identical fashion to a photoswitching event in STORM.

DNA-PAINT has recently been deployed to visualise RyRs within isolated CM (Jayasinghe *et al.,* 2018). RyRs were localised to within 10 nm and RyR clusters were observed to be incompletely packed, as had previously been believed due to in-vitro reconstitution of RyR clusters within bilayers to approximately a third of the maximal packing density (Jayasinghe *et al.,* 2018; Asghari *et al.,* 2009)

Atrial T-tubules appeared disordered when visualised with super-resolution STED microscopy in both mouse and human (Brandenburg *et al.,* 2016). The visualisation of pssAb using diffraction limited confocal microscopy in atrial T-tubules in the same study showed RyR hyperphosphorylation hubs within axial-transverse tubule junctions. This finding displayed the non-uniform distribution of phosphorylation. This suggests there may be complications in the definition of a super-cluster inclusion criteria, as phosphorylation increases the amount of $Ca^{2+}$ released from RyR and decreases the threshold $Ca^{2+}$ concentration required to activate RyR clusters. Confocal microscopy data that used pssAb against Ser-2808 and Ser-2814 intimated that RyR clusters found on axio-transverse junctions are hyperphosphorylated hubs, which propagate excitation along the non-junctional tubules, and appeared to be unphosphorylated (Brandenburg *et al.,* 2016).

Most recently, a wholly different method of achieving similar resolution to SMLM microscopy, expansion microscopy, was used to investigate the distribution of RyR phosphorylation of peripheral clusters in control isolated CM and a pulmonary hypertension (PH) model in rat (Sheard *et al.,* 2019). Expansion microscopy works with diffraction limited confocal microscopy. Instead of breaking the diffraction limit, this protocol binds markers to an acrylamide gel, break down the cellular material, and then isotropically swell the gel. This physically separates the proteins of interest by up to 10 times their native distances (for further information see Tillberg *et al.,* 2016; Chen *et al.,* 2015). Sheard and colleagues (2019) showed that peripheral RyR clusters were heterogeneously phosphorylated. Importantly, it was shown that the effect of physiological adrenergic agonists produced a different pattern of

increased phosphorylation to that observed in PH rat, as too were the distribution of RyRs in peripheral clusters. This suggests that it is not only the amount of RyRs that are phosphorylated that could cause disease, but also their distribution within RyR clusters.

**Summary**

These recent findings highlight the importance of investigating the spatial distribution of RyR phosphorylation sites in health and disease. This thesis investigates the spatial distribution of RyR phosphorylation in deep RyR clusters for the first time, and the effects of the CM isolation procedure on RyR phosphorylation distribution compared with tissue sections. These findings represent important implications for experimental design and interpretation of functional isolated CM experiments and the wider understanding RyR physiology. Super-resolution imaging of RyR2 and pssAb bridge the knowledge gap between traditional confocal microscopy of RyR2 and biochemical assays relating to channel phosphorylation. Furthermore, this thesis represents a robust method for quantifying sub-populations within a larger population, as compared to a more traditional protein A versus protein B quantification.

This thesis covers the development and deployment of quantitative approaches to study the spatial distribution of RyR2 phosphorylation sites at the nanoscale.

- Chapter 2 provides an overview of the methodological approaches used and quantitative strategies.

- Chapter 3 provides experimental evidence of pssAb translation from traditional Western blot analysis to immunohistochemistry. Contained in this chapter are qualitative assessments of a range of PssAb, and quantitative results for pRyR2-S2808 and pRyR2-S2814 using confocal microscopy and pRyR2-S2808 using single channel STORM microscopy.
- Chapter 4 quantifies the spatial distribution of pRyR2-S2808 within the context of total RyR2 distribution using dual channel STORM super-resolution microscopy. Further, these data provide detailed quantification of a redistribution of pRyR2-S2808 due to the CM isolation procedure, as compared to tissue sections.
- Chapter 5 develops and deploys DNA-PAINT to observe pRyR2-S2808 in relation to RyR2. This chapter develops important experimental strategies when using DNA-PAINT and compares the performance and limitations of this with STORM modality of SMLM microscopy in biological samples. These are discussed together in chapter 6.

# Chapter 2

## General Methods: Western blots, IHC, confocal microscopy, SMLM, image processing and data analysis

### Summary

Biological molecules, such as proteins, can be modified by the addition of a small chemical group to a specific site. These modifications lead to changes in the biophysical properties of the protein, such as kinetics or opening and closing mechanisms of channels. These modifications, termed post-translational modifications (PTM) are employed widely within biological systems to elicit fine control of the system. As such there are undesired consequences if this mechanism is disturbed. Dysregulation of phosphorylation levels have been strongly linked to pathology in cardiovascular disease, typically seen as hyperphosphorylation. It is known that phosphorylation alters channel kinetics, open probabilities, and disinhibits accessory proteins, such as PLN. The spatial distribution of these alterations is of importance, yet it has not been interrogated in cardiovascular calcium handling proteins, such as RyR at the nanoscale. Antibody based immunofluorescence labelling produces high specificity to visualise individual proteins of interest. More recently, phosphorylation state specific antibodies (pssAb) have been developed that are specific to an epitope site only when it has been phosphorylated. Phosphorylation is a key physiological mechanism to tune the behaviour of proteins and its spatial distribution is of increasing interest. Protein distribution has traditionally been imaged using antibodies for

immunofluorescence microscopy experiments, whilst mass phosphorylation levels have been assayed with pssAb, typically by Western blot.

Badrilla UK develop, validate, and manufacture pssAb for common cardiovascular proteins. These antibodies have been extensively validated by the company and the literature in Western blot applications. This thesis details the validation of using pssAb for microscopy experiments. The Soeller lab has extensive experience in imaging these proteins of interest, such as RyR2 and SERCA2a using SMLM based super-resolution microscopy. These previously validated total protein antibodies were employed as a known standard in dual labelled experiments.

Previously validated cardiac Western blot prepared samples that were supplied by Badrilla UK Ltd. Pharmacological intervention on CM was used to test antibody performance by comparing Western blot data with confocal and stochastic optical reconstruction microscopy (STORM) super-resolution microscopy experiments from the same antibody batches. Robust methods of employing confocal, STORM and DNA-PAINT microscopy have been developed to investigate the spatial distribution of phosphorylation within super-resolved RyR2 receptor clusters. This methodology can be applied to any question where a sub-species of a total population is to be investigated. PTMs, differing isoforms, and functionally similar proteins are all prime candidates and have relevance across a wide range of questions, from developmental biology to degenerative disease.

**Rat Sample Preparation for Tissue Sections and CM**

All animal experiments were performed under Schedule 1 procedures in accordance to the University of Exeter's Animal Ethics Committee. Cardiac myocytes were isolated from a Langendorff reverse perfusion set up. 250-350 g, 7-8 weeks old male Wistar rats were terminally anaesthetised via 100 $mg.kg^{-1}$ pentobarbitone sodium intraperitoneal injection. Animals were dispatched via cervical dislocation followed by exsanguination in accordance with the 1986 Animals (Scientific Procedures) Act, approved by the Animal Ethics Approval Committee of the University of Exeter. Once observed reflexes were lost (as a proxy for consciousness) rats underwent cervical dislocation. The chest cavity was immediately opened, and the heart resected, thus confirming death via exsanguination. The heart was briefly placed in $Ca^{2+}$-free Tyrode's solution before the aorta was cannulated and the heart retroperfused (Hou *et al.*, 2015).

The heart was perfused at 37°C on a Langendorff apparatus at a constant flow rate for a period of 4 minutes with $Ca^{2+}$-free Tyrode's solution. Finally, the heart was exposed to isolation solution (containing 1 mg/mL collagenase (Worthington, USA), and 1mg/mL protease (Sigma, USA) and 200 µM $CaCl_2$), for 15 mins. The heart was then dissected at the atrio-ventricular septum. The ventricles were diced and triturated to liberate individual CM in 150 µM $CaCl_2$ containing modified Tyrode's solution (Robert M Bell, 2011).

Only isolations with a yield >70% rod-shaped cells were accepted for experimental use. For attached cell experiments, CM settled for 2 hours at 37°C onto cleaned number 1.5 laminin coated coverslips mounted into open chambers prior to pharmacology and fixation. Either 1 µM Calyculin A (Sigma,

UK) or 1 µL vehicle (DMSO) was applied to CM for 15 minutes. CM were immediately fixed in 2% formaldehyde for 10 mins by 1:1 addition of 4% formaldehyde in PBS to Tyrode's containing CM at the end of the pharmacological incubation period. CM were pelleted and washed for 15 mins in PBS before being pelleted and re-suspended in storage solution (75 µM Bovine serum albumen (BSA), 15 mM $NaN_3$, in 1 x PBS).

Hearts destined for tissue sectioning were fixed in 2% formaldehyde (PFA) in PBS for 1 hour. Whole hearts were then washed for 15 mins before being incubated in 10% (1 hour), 20% (2 hours), and 30% (overnight) sucrose containing PBS (w/v) and subsequently flash frozen in methyl butane cooled liquid nitrogen. Tissue was then placed at -80°C for long term storage. Sectioning was performed at -16°C on a cryostat (ThermoFisher Scientific, UK) at a thickness of 10 µm. Sections were oriented to either longitudinal or cross-sectional views and attached to 0.05% poly-L-lysine cleaned number 1.5 coverslips. Coverslips had previously been cleaned by a brief wash in saturated NaOH in methanol and extensive washing in MilliQ filtered $dH_2O$ (Merck-Millipore).

Cells destined for Western blot assay were counted before pharmacological treatment and volumes adjusted if required to a minimum of 500,000 rod-shaped cells per mL by sedimentation/resuspension in the same buffer. 2x sample buffer [10% (w/v) sodium dodecyl sulfate (SDS), 20% glycerol (v/v), 120 mM Tris-HCl (pH 6.8), 0.02%] was added and cells were homogenised on ice immediately after drug treatment. Samples were then spun, and the supernatant retained to remove debris. 4% (v/v) β-mercaptoethanol with 0.02% (w/v) final concentration bromophenol blue was added to create a

Laemmli buffer environment and samples were stored at -80°C (Sigma-Aldrich, 2004).

## Antibody validation by Western blot

### SDS-PAGE

Sodium dodecyl sulfate (SDS) denatures proteins into long polypeptide chains, whilst also giving the molecule a uniform net negative charge. When the SDS variant of polyacrylamide gel electrophoresis (PAGE) is performed, the protein will migrate at a rate inversely proportional to its molecular weight, as the influence of tertiary structure or individual amino acid charge contributions have been removed. This method is important for investigating novel proteins, confirming the presence of known proteins, and confirming the specificity of antibodies. SDS-PAGE results in a gel with clearly denoted bands of proteins all the same molecular weight. To confirm whether the proteins of a specific band are the protein of interest, immunohistochemistry is required. The whole process is known as a Western blot.

SDS-PAGE electrophoresis was performed with a 6% cast gel for RyR or 12% gel for PLN. All samples were loaded with either 10,000 mouse CM or 10 µg total protein canine cardiac SR vesicles (cSR) in Laemmli buffer containing bromophenol blue for visualisation. A protein standard with molecular weights from 5 kbp to 250 kbp was added to an adjacent well. Electrophoresis was performed with vertical plates at 100 V and 250 mAmps for 3 hours at 4°C in the presence of running buffer using Biorad apparatus (Carter *et al.*, 2011).

**Western blot**

The resolving gel was washed briefly in $dH_2O$ and placed in transfer buffer (20% MeOH, 4°C) to equilibrate. A PVDF membrane was activated in MeOH and placed onto the gel and rolled for a firm contact. The 'transfer sandwich' for wet transfer was assembled as shown with care taken to remove any air bubbles. The gel was placed on the cathode (negative) side and the PVDF membrane on the anode (positive) side to ensure protein migration into the membrane. Transfer was performed at 10 V and 100 mAmps overnight.

After transfer, the protein standard was visible on the PVDF and the gel stained with Coomassie blue stain to confirm protein was no longer present before disposal. Stock 10x Tris-buffered saline (TBS) was freshly prepared and adjusted to pH 7.4. 1x TBS was made with $dH_2O$, some of which had 0.1% (v/v) Tween-20 (TBST). 5% (w/v) milk powder was added to 100 mL TBST and stirred thoroughly. PVDF was cut into appropriate experiments and each was blocked separately with 1 cm covering of blocking solution and placed on the shaker for 30 mins.

**Figure 2.1. Apparatus for the use in Western blot transfer assembly. The Cassette consists of the electrophoresis gel (blue) in pressed contact with PVDF or nitrocellulose membrane (white). These are sandwiched by transfer buffer-soaked sponge pads and then blotting paper and held together firmly. An electric current is applied to drive the negatively coated proteins towards the anode and so firmly attaches them into the blotting membrane.**

| Antibody | Dilution | Species | Manufacturer |
|---|---|---|---|
| pPLN-S16 | 1:5000 | Rabbit | Badrilla Ltd |
| RyR2 C3-33 | 1:2000 | Mouse | ThermoFisher |
| pRyR2-S2808 | 1:5000 | Rabbit | Badrilla Ltd |
| pRyR2-S2814 | 1:5000 | Rabbit | Badrilla Ltd |
| HRP Secondary Antibodies | 1:2500 | Donkey | Badrilla Ltd |

**Table 2.1. Antibody dilutions, species, and manufacturer for Western blots.**

Primary antibody was diluted into 5 mL blocking solution and placed into a 50 mL falcon tube. Membrane was placed inside, and the tube was rolled for 3 hours. Membranes were washed four times for 5 mins with TBST on the orbital shaker and returned to 50 mL falcon tubes and incubated for 90 mins in horseradish peroxidase (HRP) linked secondary antibodies. Membranes were then rinsed briefly, and then washed three times for 5 mins in TBST on an

orbital shaker with a minimum depth of 1 cm. Samples were incubated with an enhanced chemiluminescent detection kit (Amersham Biosciences) then underwent immediate immuno-detection using a CCD camera and Compass software (ProteinSimple). Images were exported as TIFF files.

**Immunofluorescence Immunohistochemistry Labelling**

Immunohistochemistry utilises antibodies; proteins created by the immune system to target and identify specific epitopes. Primary antibodies bind specifically to one protein epitope, whilst secondary antibodies will bind to any protein in a species-specific manner. Here, mouse derived anti-RyR or anti-PLN (ie total antibody) were used as primary antibodies, alongside rabbit derived pssAb. Then a goat derived anti-mouse or anti-rabbit antibody was applied as a secondary antibody. These secondary antibodies have a fluorophore attached to them. This combination allows different proteins to be visualised with different coloured fluorophores attached to different classes of secondary antibody, and so multiple targets can be observed at the same time and is termed immunofluorescence (IF). To aid the specificity of these antibodies, samples are regularly ‘blocked’ by bathing in a normal goat serum (NGS) or bovine serum albumin (BSA) solution. These bind to offsite targets and so reduce non-specific binding of the antibodies to be used.

Fixed CM in storage solution were centrifuged and once re-suspended were permeabilised in PBS + 1% Triton X-100 for 10 min at room temperature (RT). CM were then blocked in 1 % normal goat serum (NGS) in PBS for 1 hour. Tissue sections were briefly rehydrated in PBS and blocked in Image-iT FX ThermoFisher, UK) signal enhancer for 1 hour. If Badrilla Ltd pssAb were

used, blocking consisted of 1% NGS and 1% BSA (w/v) in PBS overnight. Primary antibody incubation was performed overnight at 4°C in a PBS solution with 1% BSA, 0.05% $NaN_3$ and 0.1% Triton-X100. Cells were washed by centrifugation and re-suspension in PBS three times for 20 mins each before secondary antibody incubation for 2 hours at RT. Cells were washed a further three times for 20 mins and then immediately mounted. Attached cells and tissue sections were stained identically using an aspirator in lieu of centrifugation. Table 2.2 details blocking conditions and dilutions per antibody (Jayasinghe *et al.*, 2018; Hou *et al.*, 2015).

| Antibody | Block | Duration |
|---|---|---|
| PLN* | 1 % NGS in PBS | Overnight |
| pPLN-S16 † | 1 % BSA, 1 % NGS in PBS | Overnight |
| pPLN-T17 † | 1 % BSA, 1 % NGS in PBS | Overnight |
| RyR2 (C3-33)* | 1 % BSA, 1 % NGS in PBS | 1 hour |
| pRyR2-S2808 † | 1 % BSA, 1 % NGS in PBS | Overnight |
| pRyR2-S2814 † | 1 % BSA, 1 % NGS in PBS | Overnight |
| RyR2 (34C) † | 1 % NGS in PBS | 1 hour |
| SERCA* | 1 % NGS in PBS | 1 hour |

**Table 2.2. Details of blocking conditions for various primary antibodies. For tissue experiments, Image-iT FX was used in lieu of the blocking solution for the same duration. * denotes mouse monoclonal antibodies. † denotes rabbit polyclonal antibodies raised against a known peptide.**

Selection of secondary antibody and mountant was matched to the intended experimental use (see Table 2.3). For confocal microscopy and STORM microscopy on CM cells were re-suspended into buffer and 10 µL was placed between a 1.5 glass coverslip and slide. Slides for STORM were sealed immediately with nail varnish to limit oxygenation of the media. Prolong Gold was sealed fully 48 hours after mounting to allow it to set fully before imaging. STORM microscopy and DNA-PAINT experiments on tissue sections were

performed in an open chamber. 1,5 glass coverslips were attached to the underside of a custom cut Perspex slide of approximately 6 mm depth. A central 15mm hole drilled through the slides meant that the samples were exposed within the well formed by the chamber and the affixed coverslip (Jayasinghe *et al.*, 2018). This allowed ready access for switching buffers, performing washes, introducing DNA-PAINT imagers or quenchers, etc (Lutz *et al.*, 2018**).**

| Technique | Mountant | Mode | Dyes |
|---|---|---|---|
| Confocal Microscopy | Prolong Gold | Enclosed slide | Alexa 488, Alexa 594, Alexa 647 |
| STORM Microscopy | 100mM MEA in 90% glycerol and 1x PBS | Enclosed slide or open chamber | Alexa 647, Alexa 680, Alexa 700 |
| DNA-PAINT | Buffer C (1xPBS + 500mM NaCl) | Open chamber | ATTO655, ATTO700 |

**Table 2.3. Mounting conditions and mode varied dependent upon technique. Detailed are the mountant used and fluorophores selected, relative to the specified imaging modality.**

## Confocal Microscopy

Laser scanning confocal microscopy (herein referred to as confocal microscopy) utilises a spatial pinhole to block out of focus light, increasing the image contrast and slightly increasing the image resolution. The laser is scanned across the sample and an image built up pixel by pixel. By changing the focal plane, 3-dimensional images can be reconstructed from stacking multiple 2-dimensional images, assuming appropriate sampling frequencies. The use of the spatial pinhole in an optically conjugate plane that reduces the sample exposure as only a small focused laser beam is sent into the sample during acquisition.

Samples (whether CM or tissue sections) were imaged on a Leica SP5 or SP8 laser scanning confocal microscope with a 63x Lambda blue 1.4 NA oil immersion objective. For the three fluorophores used (Alexa-488, Alexa-594, Alexa-647) an $Ar^+$ 488 nm, HeNe 594 nm, or HeNe 633 nm laser was used, respectively. Image pixel size were less than 90 nm in x,y to achieve adequate Nyquist sampling.

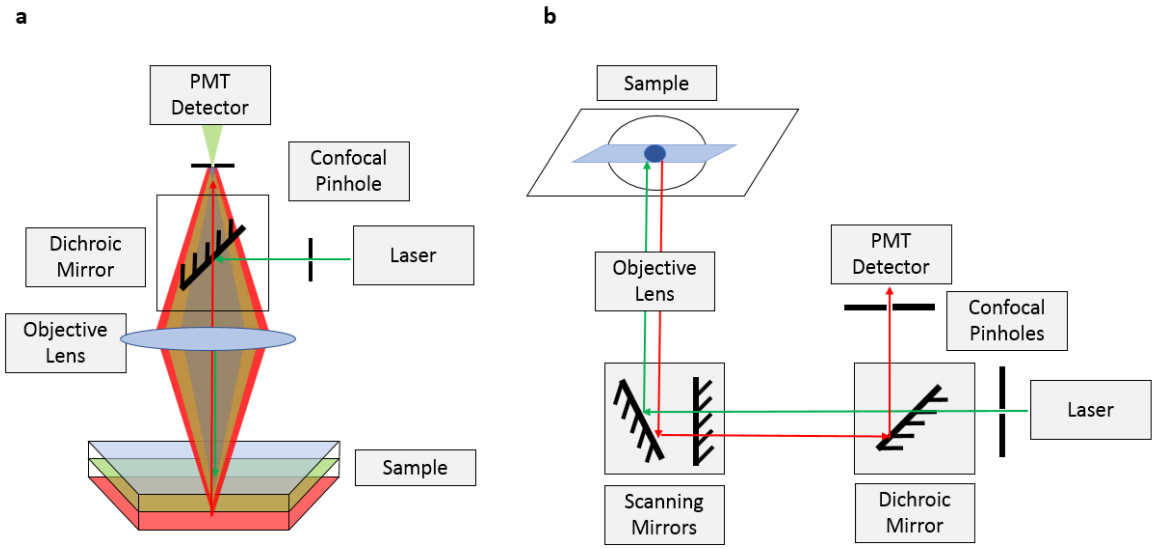


**Figure 2.2. Principles of confocal microscopy. (a) Emitted fluorescence from different z-positions within a sample focus at different focal planes (blue, green, and red). Pinholes confocal to each other and the sample at the light source and at the detector ensures the illumination is only focused onto one z-position. Out of focus emitted light (blue, red) are blocked by the pinhole at the detector and only in focus light (green) is observed. (b) Schematic of a confocal microscope layout. Excitation light (green arrows) passes through a confocal pinhole and through a dichroic mirror onto scanning mirrors. These move the excitation beam across an image row by row, one-pixel width at a time. In this way the laser scanning confocal microscopy image is built up voxel by voxel.**

Tissue section images were taken at least 1 µm deep into the tissue to reduce the effect of mechanical distortion during sectioning. CM were imaged either at the periphery or 1-2 µm (deep) into the cells. All imaging was performed sequentially. This allowed for each channel to be optimised (i.e. maintaining the same optical slice, confirming no bleed through). All files were saved as 8-bit RGB TIFF files.

## Image Processing

Image channels were normalised to RyR2 peak intensity using FIJI(IsJustImageJ) using 8-bit images per channel. Firstly, the mean background was subtracted from each channel and the RyR2 channel was scaled to 255. This multiplication factor was then applied to the pssAb. The pssAb signal did not appear to be stronger than the RyR2 signal. Channels were then combined as composite images and saved as RGB-type TIFF files.

$$P_n = (P - B) \cdot \left(\frac{255}{P_{max}}\right)$$

**Equation 2.1. Equation for the normalisation of signal intensities. The scaling factor calculated for total protein channel was applied to both total and PSSA channels. The new pixel intensity ($P_n$) is equal to the original pixel value (P) minus background (B), multiplied by the scaling factor. This was calculated by dividing 255 by the maximum pixel value in the original image, once the background was subtracted ($P_{max}$).**

## Confocal Microscopy Quantification

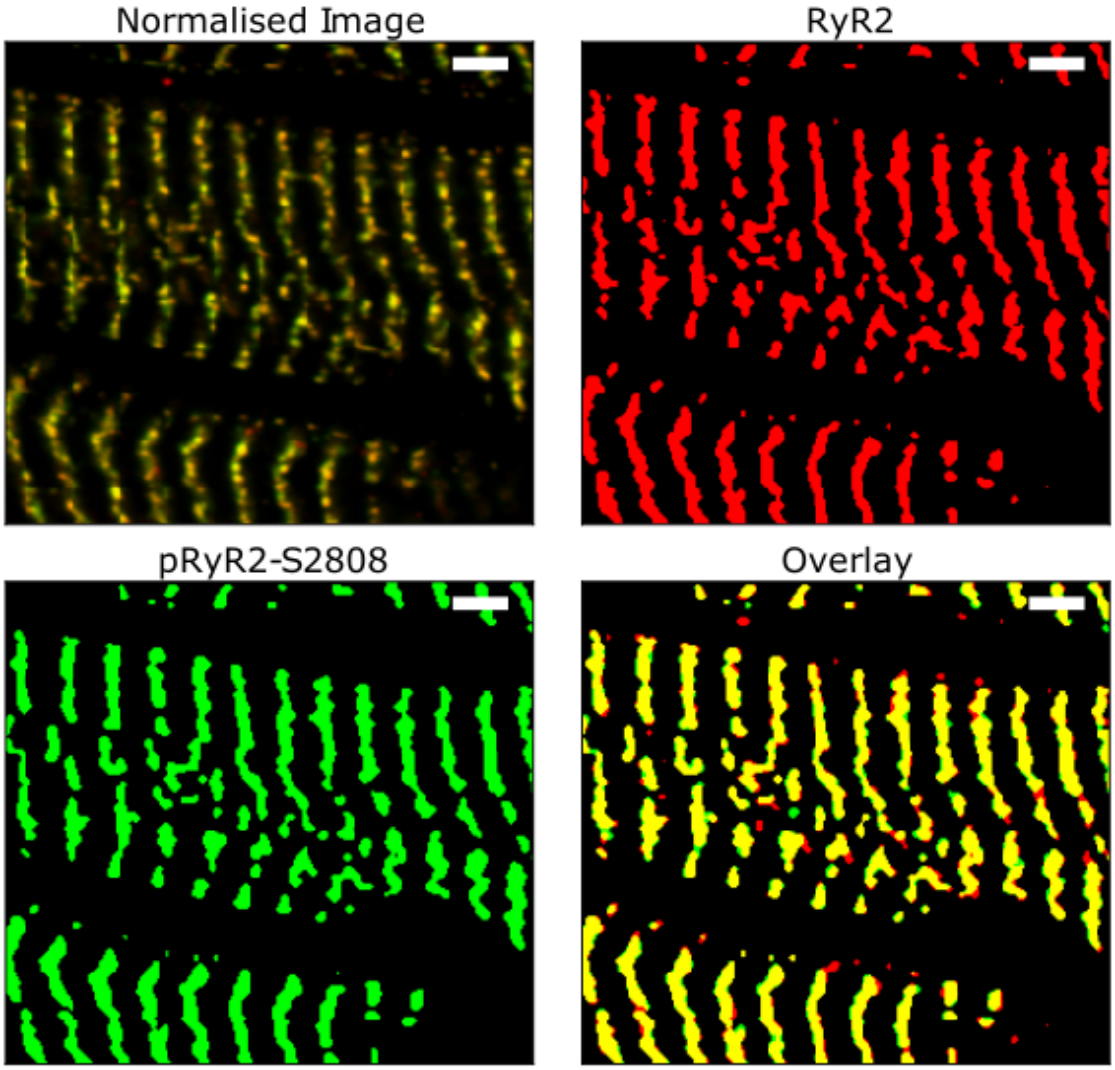


**Figure 2.3. Representative image of control CM stained for pRyR2-S2808 (green) and RyR2 (red), corresponding binarised channels and binarised colocalisation mask (yellow). Scale bar =2 µm.**

Figure 2.3 shows the image processing pipeline for area colocalisation measures used to estimate the spatial coverage of pssAb on total antibody images in confocal microscopy. A novel Python Notebook programme was written for semi-automated quantification of colocalisation for whole data sets. Colocalisation was quantified by creating binary masks from a percentage of 80% relative intensity-based threshold. Figure 2.3 depicts the image processing pipeline with a normalised image (left) and then the binarised

mask images resulting from the 80% threshold of pixel intensities. The pssAb (green), total RyR2 (red), and colocalised pixels (yellow) are displayed.

**Single Molecule Localisation Microscopy**

The direct STORM variant of SMLM was used for super-resolution imaging of phosphorylation distribution within total protein clusters, for example the distribution of phosphorylation at Ser-2808 on all observable RyR2 clusters. 2-dimensional STORM microscopy allows an approximately 10x improvement in x,y resolution over widefield or confocal imaging, whilst maintaining an optical sectioning similar to diffraction limited microscopy (Rust, Bates and Zhuang, 2006).

STORM microscopy was performed on a Nikon Ti-E inverted fluorescence microscope with a Nikon 60x 1.49 NA oil-immersion TIRF objective (Baddeley *et al.*, 2010; Jayasinghe *et al.*, 2018). Illumination was limited to a highly inclined light sheet (hilo) by adjusting the beam angle to be slightly less than required for total internal reflection fluorescence (TIRF) microscopy. Hilo illumination allows for greater contrast than widefield illumination, whilst allowing regions deep into sections to be imaged, which TIRF illumination would not allow. Hilo illumination resulted in approximately 20 μm diameter region of excitation. This was typically enough to excite the entire width of a CM. SMLM image acquisition was performed using a 642 nm laser at a laser power of ~150 $mW.cm^{-1}$.

## STORM Microscopy

Fluorophores are excited from a ground state to a bright state according to the excitation spectra. In the presence of the imaging buffer and sufficient energy, the majority of fluorophores enter a meta-stable dark (or triplet) state. These either return to the bright state and result in the release of a photon by radiative decay to the ground state, or non-radiative decay to the ground state by other mechanisms. Fluorophores cycle between bright and ground state rapidly under intense illumination. This results in the fluorophore releasing many photons in a brief amount of time. As entry to the triplet state is probabilistic, more, faster cycles result in relatively fast entry to the triplet state and a brief, bright period when many photons are released by excitation state cycling. The reducing conditions of the imaging buffer help to prolong the triplet state, resulting in a minority subset of fluorophores only ever being excited during any one frame (figure 2.7). Due to the stochastic nature, these blinking events are sufficiently spread out spatially and temporally to allow each individual fluorophore to be seen as a diffraction limited spot, that was then be localised.

Alexa 647 and/or Alexa 700 fluorophores blink when excited at this intensity of laser power and in the presence of the STORM imaging buffer. The buffer used here was a 90% glycerol, 10% 10x PBS, 100 mM mercaptoethanol amine (MEA). MEA acts as a reducing agent, encouraging blinking behaviour, whilst a 90% glycerol mix allows a 1x PBS environment whilst reducing refractive index mismatches between the coverslip and imaging media.

Ellman's assay was used to test the activity of our imaging buffer immediately before mounting and imaging. Ellman's reagent utilises

5,5'-dithiobis(2-nitrobenzoic acid) (DTNB) to estimate the amount of free thiol groups in a test solution. The thiol (MEA in our buffer) reacts with DTNB, creating a mixed disulphide and 2-nitro-5-thiobenzoic acid. The result of this reaction is a yellow colour forming. Absorbance of $TNB^{2-}$ can be quantified at 412 nm. From validation experiments performed by the lab previously a colour chart with corresponding 1-8 scores was provided. Ellman's assay results with a score of at least 4 were required for mounting. Although buffers were nominally produced at 100 mM, the Ellman's test was required to account for any loss of activity in the MEA stock over time (Aitken A, 2009).

Approximately 20-25 thousand frames were acquired at 50 ms integration times with an electron multiplying gain of 0 onto an Andor Zyla sCMOS camera. Dual colour STORM utilised a 50 ms integration time with an electron multiplying gain of 85 on an Andor Ixon EM-CCD camera. Emitted light from dual colour experiments was directed through a custom splitter device. Here, the light was split by a high flatness DC T710 LPXXR-U43 dichroic mirror (Chroma Scientific) before each channel was recorded on two 512 x 256 halves of an EM-CCD camera (Andor, Japan). Events were detected from each frame using an algorithm developed within the PYME Acquire software (Baddeley *et al.*, 2009; Baddeley *et al.*, 2010).

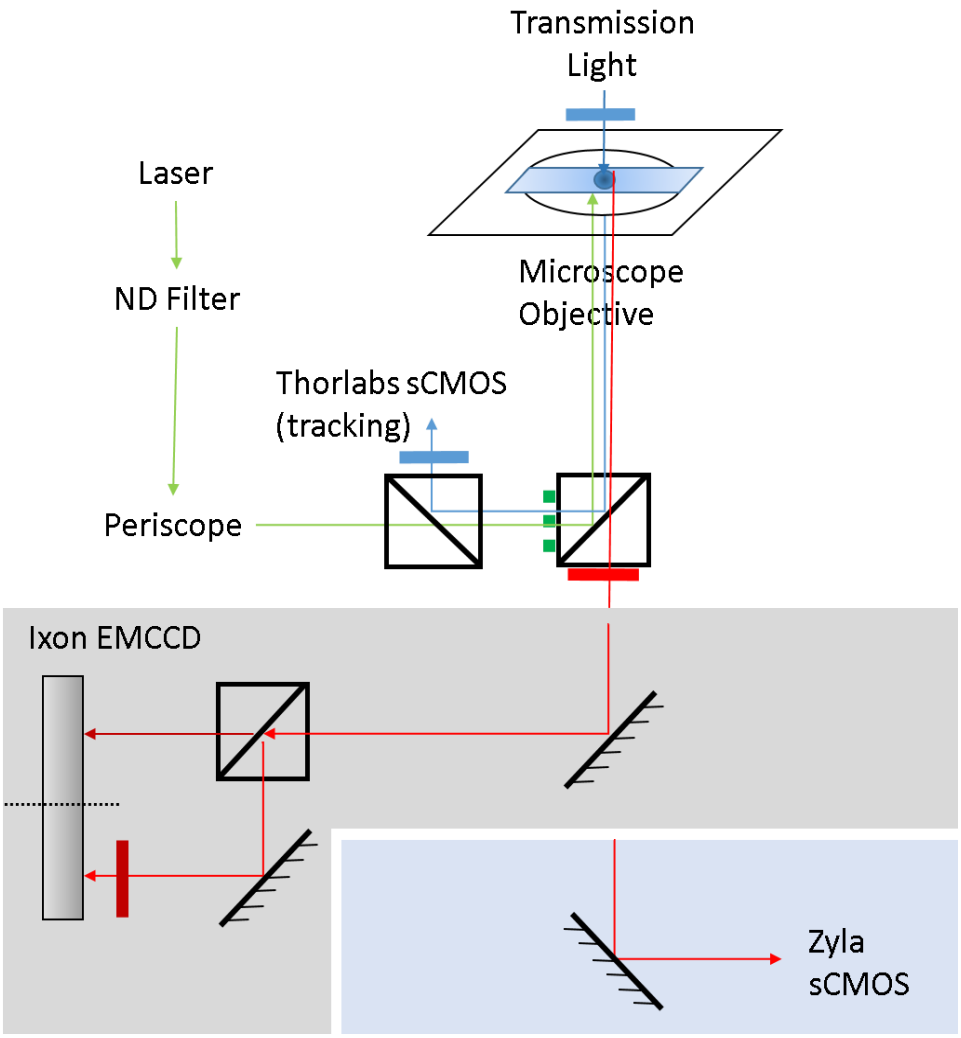


**Figure 2.4. Schematic of the custom microscope layout. Samples were mounted on a custom slide holder mounted on a Nikon Ti-2000. The stage was controlled by a piezo stage controller and controlled via PYME acquire software. The 63x Nikon 1.49NA objective was mounted to a PiFoc piezo controller with a travel of 300nm. 642nm or 671nm laser illumination was directed into the rear of the microscope via a filter wheel containing ND0.5, ND1, ND2, ND3, and ND4 neutral density filters and through a custom-built periscope. Adjustment to mirrors in this periscope allowed for hilo or TIRF illumination conditions to be achieved. Filter cubes within the microscope contained the relevant dichroic mirror (see table). Emitted fluorescence returns through the objective, through the dichroic mirror and appropriate emission filter. Single colour STORM and DNA-PAINT experiments were performed on the Zyla sCMOS camera (light blue box). Dual colour experiments were imaged onto an Ixon EMCCD via a splitter device (gray box). The filter cube used for dual-colour experiments had its own excitation (dotted green line) and emission filter (red line). Short and long channels were split and imaged onto two halves of the camera (denoted by dotted line) with a clean-up filter in front of the long channel (dark red line). Transmitted light passed through a short-pass blue filter into the objective and was sent to a third camera, via a polarising beam splitter, used by the tracking software.**

Figure 2.4 shows the microscope layout used for all SMLM experiments. This dual camera system used a splitter device to separate the emission spectra of two fluorophores excited by the same laser source. The experimental set up also allowed transmitted light to be sent to a further camera to enable z-tracking via custom software within the PYME operating system (Baddeley *et al.*, 2011).

| Illumination | Dye | Dichroic | Excitation Filter | Emission Filter |
|---|---|---|---|---|
| CoolLED | Transmitted | - | - | Semrock FF02-447/60 |
| CoolLED pE-4000 | FITC | DM505 | Chroma D480/30 X 233 743 | Chroma D535/40 M 230459 |
| CoolLED pE-4000 | Cy3 | Semrock FF593-D103 | Semrock 562/40 | Nikon BA590 |
| Omicron 642 nm 140 mW | Alexa-647 | Semrock FF660-Di02 | Semrock 628/40 | Semrock 692/40 |
| Omicron 642 nm 140 mW | ATTO-655 | Semrock FF660-Di02 | Semrock 628/40 | Semrock 692/40 |
| Viasho VA-11-N 671 nm 800 mW | Alexa-660 | Chroma Q680LP | Semrock 655/40 | Omega Optical XF3104 690ALP |
| Viasho VA-11-N 671 nm 800 mW | Alexa-680 | Chroma Q680LP | Semrock 655/40 | Omega Optical XF3104 690ALP |
| Omicron 642 nm 140 mW | Alexa-700 | Semrock FF660-Di02 | Semrock 628/40 | Semrock 692/40 |
| Omicron 642 nm 140 mW | ATTO-700 | Semrock FF660-Di02 | Semrock 628/40 | Semrock 692/40 |
| **Omicron 642 nm 140 mW** | **Alexa-647 and Alexa-700** | **Chroma DC T710 LPXXR-U43** | **-** | **-** |
| **Omicron 642 nm 140 mW** | **ATTO-655 and ATTO-700** | **Chroma DC T710 LPXXR-U43** | **-** | **-** |

**Table 2.4. Filters required for the relevant dyes used. Bold denotes the filters used via the splitter device. The LED light went through the same dichroic and excitation filters that were relevant to the dyes. Filter in bold relevant for dual colour experiments.**

## Dual channel STORM Microscopy

Dual channel experiments utilised a splitter device as shown in figure 2.4. A dichroic mirror (DC T710 LPXXR-U43, Chroma Scientific) was inserted into the splitter device that split the emitted light at 710 nm. Wavelengths above this passed into the long channel, and wavelengths below this were reflected to the short channel. These light paths were reflected in such a way that they each occupied a separate half of the camera chip. Each event detected by PYMEAcquire measured the maximum intensity of the event and the correlating region on the other half of the camera chip (Baddeley *et al.*, 2011).

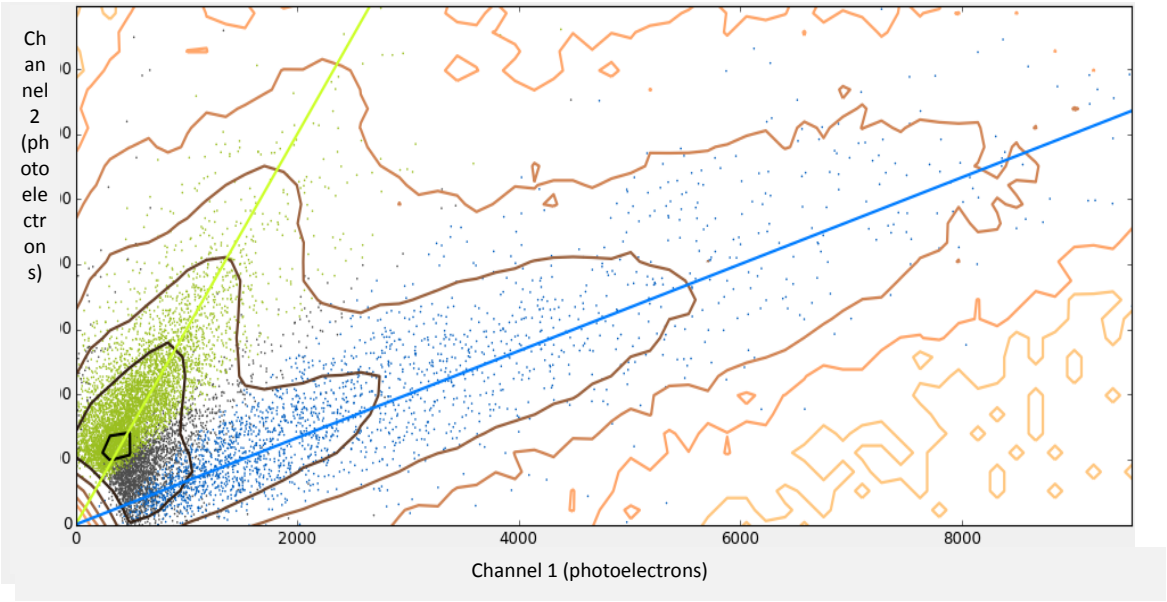


**Figure 2.5. Ratiometric channel assignment of event photoelectron intensity in dual channel STORM microscopy data. Maximum intensities of paired Gaussian fitted coordinates. Events were assigned to either channel 1 (long channel, blue line and dots), channel 2 (short channel, green lines and dots), or excluded (gray dots). Units are photoelectrons.**

The experimental pathway shown in figure 2.4 explains how the emitted light of both fluorophores is separated through a splitter device onto two halves of the acquisition camera. These two halves will eventually be overlaid to produce the final image, and so in order to determine which fluorophore it is most likely to have originated from, a ratiometric analysis is performed on

pairwise regions of interest. For example, one localisation event on one half of the camera was compared to the corresponding region on the other half, in case of bleed through. These coupled intensities were then plotted against each other. Lines of best fit applied from modelling experiments for individual dyes were applied onto these plots with defined limits of inclusion. Points were then assigned to channel 1, channel 2, or excluded. Events were assigned to each channel based on a probabilistic fitting as predicted by the spectra of each dye through the dichroic mirror (Baddeley *et al.*, 2011). Here, the green line of best fit accounts for the short channel (Alexa 647) and the blue line accounts for the long channel (Alexa 700). The points close to the relative lines of best fit are also colour-coded. These are then assigned to the respective channel. Gray points are not easily distinguishable and so excluded from the channel assignment and not used for the image rendering.

**Calibration of the Splitter Device**

Shiftfield maps were recorded for calibration of dual colour imaging when the emitted light was split using the splitter device (above) and recorded on the two 512 x 256 halves of an EM-CCD camera (Andor, Japan). A sample containing sparse Tetraspeck or ThermoFisher fluorospheres in Prolong Gold (NA 1.47) were used and the piezo stage stepped through a grid like pattern. The resulting series ensured beads had been imaged across the entirety of the camera chip. Overlap was first approximated manually by moving the mirrors in the splitter device, using the PYME software for real time

visualisation. Correction vectors were then calculated in a shiftmap protocol and these corrections applied immediately before experiments began.

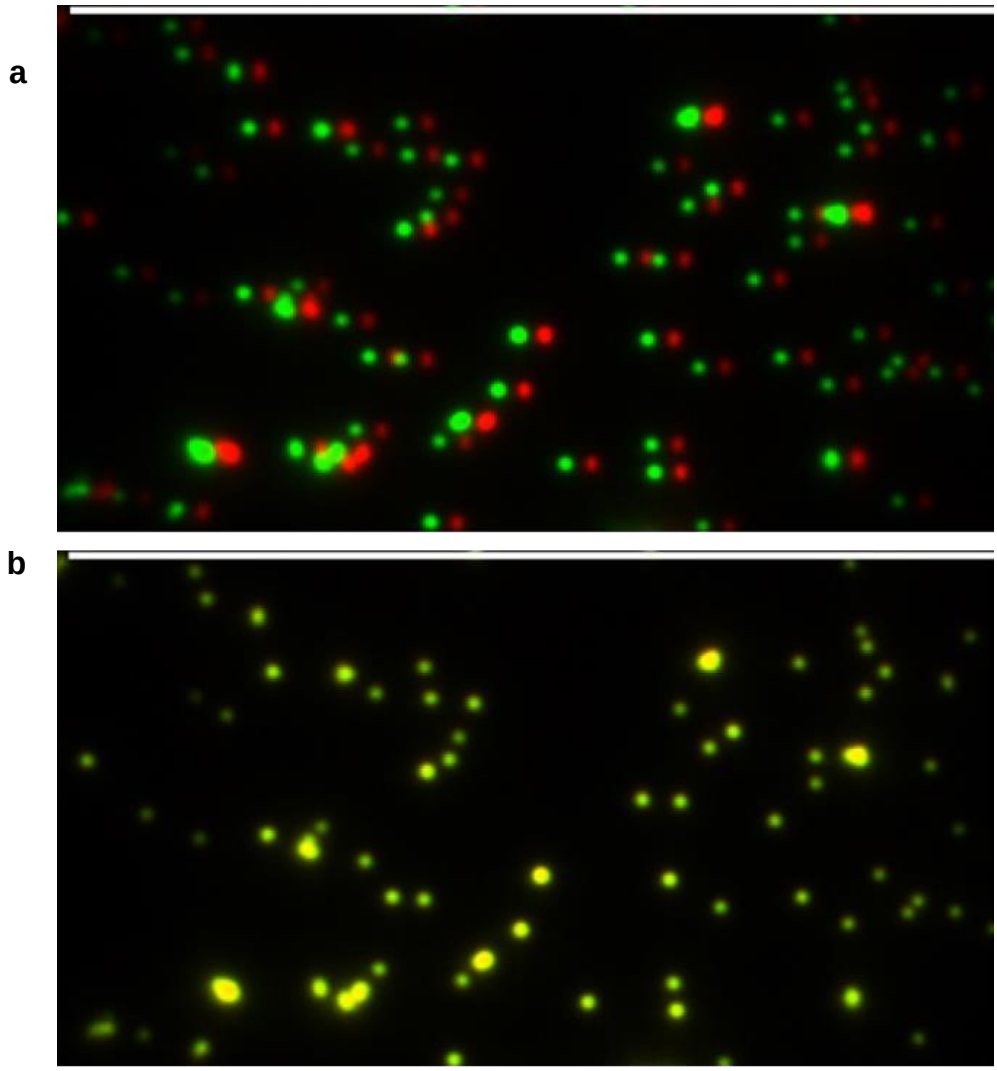


**Figure 2.6. Calibration of dual channel imaging. (a) Short (green) and long (red) channels were coarsely aligned manually using 100 nm Red (Tetraspeck) or 200 nm dark red (ThermoFisher) fluorescent bead samples mounted in Prolong Gold. Beads were imaged as the stage moved across a pre-defined grid pattern. (b) The calculated correction aligned the channels. (c) PYME allowed for shiftfield correction vectors to be calculated and were applied immediately prior to imaging.**

Initial exposure to the excitation laser resulted in global excitation of all fluorophores in the illuminated region. The fluorophores rapidly began to photoswitch and the event rates decay as more enter the dark state until a stead quasi-equilibrium was reached. The event rate was typically stable but slowly decaying over the course of the entire imaging experiment. This is

because a subset of fluorophores was being photobleached and so reducing the population of excitable fluorophores. The bleaching effect was cumulative and if an experiment was run long enough, would result in all fluorophores being permanently photobleached.

Series acquisition was set to start analysis after 200 frames in order to avoid this initial period of mass excitation, which resulted in many overlapping events. Beyond this brief period, the region of interest was sufficiently dark to allow single molecule events to be observed. Efforts were taken to reduce background fluorescence to enhance the single molecule's contrast as much as possible, such as using HiLO illumination, image-iT FX treatment, and avoiding over-fixation. The intensity of the blinks however, was limited by the intrinsic properties of the fluorophore. The resulting image of a sample imaged with identical conditions and duration yields only very sparse events.

**Drift Tracking in the Z-Dimension**

Z-tracking calibration was performed prior to series acquisition. Blue transmitted light was shone through the sample and detected on a separate tracking camera (Thorlabs DCC3240N). Once the sample region was identified the x,y stage controllers were disabled and Z-tracking calibration protocol was performed. This performed 200 nm steps above and below the imaging plane at 1 s integration time intervals, recording an image in each focal plane. A cross correlation analysis was performed on the transmitted light frames (1000 ms integration) and any focus plane shifts that were detected were then compared to the calibration stack. Mechanical adjustments were made in near-real time using a Piezo focuser (Physik

Instrumente, Germany) that the objective was mounted directly onto, with a tolerance of <30 nm. Data from this system was used to computationally correct for drift in x,y by correcting event coordinates.

**DNA-PAINT SMLM Microscopy**

STORM (and variants such as PALM) has resulted in a paradigm shift in the data obtained from fluorescence microscopy experiments. This is allowing scientists to observe proteins of interest at the molecular scale to compliment EM studies, and increasingly to observe their behaviour in live cell experiments (Sahl *et al.*, 2017; Jayasinghe *et al.*, 2018). STORM based SMLM dual channel imaging has several limitations. It requires multiple labels each with distinct or lowly overlapping emission spectra in order to unmix the signals and determine which event has originated from which label. Not every fluorescent dye is well suited to STORM microscopy as they may have a low quantum yield, may not ready excite into the dark state, or photobleach quickly even in the presence of switching buffers.

The ideal dual colour experiment would use two dyes with high quantum yield, the ability to photoswitch, and have well separated emission spectra. Imaging buffer composition is often unique to each dye, and so a compromise must be found. As such, finding compatible dyes that can both perform optimally or near optimally in the same imaging buffer is challenging.

Whilst this is possible, such as using Alexa 647 and Alexa 750 (Baddeley *et al.*, 2011), Alexa 680 and Alexa 750 (Munro *et al.*, 2016), or Alexa 647 and Alexa 700 (shown in this thesis), it is difficult to achieve maximum performance from both dyes (Vogelsang *et al.*, 2010).

DNA point accumulation for imaging in nanoscale topography (DNA-PAINT) is a technically distinct method for achieving single molecule localisations (Jungmann *et al.*, 2014). Whereas in STORM the aim is to achieve temporally separated, spatially resolvable fluorescent events via photoswitching, DNA-PAINT effectively achieves this by only having the fluorophore localise for a transient, but tuneable time. The kinetics of DNA-PAINT experiments no longer depend on the dye property (in fact preferring a stably fluorescent, non-blinking dye), rather than the control of binding on and off rates of the imager strand to the docking strand. This opened up the possibility of sequential imaging of distinct targets using the same buffer conditions and dye (Jungmann *et al.*, 2014). Removing the differences in chromatic aberration inherent to all other fluorescence IHC based experiments and is termed Exchange-PAINT.

Recently, other tools have been developed to compliment this experimental approach, such as quenchers (Lutz *et al.*, 2018). Quenchers are essentially docking strand-like oligomers that bind to the imager whilst free in solution. This effectively prevents imager strands from binding to docking strands. Quenchers allow an exchange to occur without the imaging solution being exchanged completely. This allows for x,y,z tracking solutions to remain constant and so helps with registration of the channels. Alternatively, DNA-PAINT can be used in a dual colour format, termed ratio-PAINT. Whilst chromatic aberrations remain, the issue of buffer compatibility is removed. This also helps with channel registration, particularly if the experiment focuses on direct interactions, physical couplings, or subsets within

populations (such as phosphorylation on RyR), as the sample drift between imager exchanges is not perturbed.

To make markers for DNA-PAINT, single stranded DNA oligomers, termed docking strands, of specific length and sequence (~10 bases) were directly conjugated to IgG secondary antibodies. Multiple sequences denoted by a P (P1, P3, P5, etc) were produced (Eurofins Genomics, Germany) and the complimentary 'imager' strands were ordered with a stable fluorophore attached, such as ATTO 655 or ATTO 700 (Lutz *et al.*, 2018).

| DNA Oligo | Sequence (3' --- 5') |
|---|---|
| P1 Docking | **A-T-C-T-A-C-A-T-A-T-T** |
| P1 Imager | **G-T-A-G-A-T-G-T-A-T** |
| Q1 Quencher | **C-A-T-C-T-A-C-A-T-A** |
| P3 Docking | **A-T-T-A-C-T-T- C- T-T-T** |
| P3 Imager | **G-T-A-A-T-G-A-A-G-A** |
| Q3 Quencher | **C-A-T-T-A-C-T -T-C-T** |
| P5 Docking | **A-A-A-T-G-G-A-T-T-T-T** |
| P5 Imager | **C-T-T-T-A-C-C-T- A-A** |
| Q5 Quencher | **G-A-A-A-T-G-G-A-T-T** |

**Table 2.5. DNA sequences for imager, docking, and quencher strands of type 1,3, and 5.**

The imager strand was sufficiently diluted into Buffer C (a PBS like buffer with additional NaCl 500 mM, pH 7.2 Jungmann et al., 2014). Imager strands transiently bind to the docking strands for sufficient time (>100 ms) that result in the appearance of an event. When the dilution is sufficient (0.1-1 nM) these blinks were adequately sparse to allow for single event detection using the same PYME software as is detailed above. These events were captured at 100 ms integration time and a detection threshold of 2.0 in PYME, and otherwise processed in an identical manner.

DNA-PAINT imagers give a low, diffuse background fluorescence in HiLO illumination mode. Due to their rapidly diffusing behaviour this is less than

what would come from bright out of focus STORM photoswitching blinks. Additionally, whereas STORM has an intrinsic limit of the photobleaching and so finite number of events from one fluorophore, imager strands can be thought of as infinitely available. This is because if photobleaching was to occur, further imager strands will arrive from the diffuse imaging medium, to replace photobleached imagers.

DNA-PAINT represents the removal of two key limitations in STORM microscopy. Each version has its own limitations, such as increased drift for exchange-PAINT or the potential for chromatic issues and unequal illumination intensity of the two fluorophores in ratio-PAINT. However, each also represents a marked improvement on their corresponding STORM modalities. The implementation of either PAINT variant is dependent upon the aim of the experiment. As such, both modalities are valid going forward and their use was dictated by the experimental aim. Extensive validation has been performed and published recently (Jayasinghe *et al.*, 2018).

To further expedite the process, quenchers were added free to solution approximately 2-10x the concentration of imager. These bind to the imager strand and effectively reduce the concentration of free imager in solution (Lutz *et al.*, 2018). The next imager sequence could then be added. Quenchers have also proved very useful in tuning the number of events to achieve ideal conditions.

DNA-PAINT provides a robust alternative to the STORM SMLM modality. The use of multiple colour imager strands akin to a dual channel STORM experiment is more robust as they can both fluoresce reliably in the same buffer, whereas optimal buffer conditions for fluorophores in STORM are often

unique per fluorophore. This results in a compromise between the two channels in STORM. DNA-PAINT also allows more events to arise from the same point, as they are not limited by the photophysics or photobleaching inherent in STORM. However, DNA-PAINT takes longer to image and so drift becomes more of a concern, especially in an Exchange-PAINT scenario. Whilst it was initially thought that DNA-PAINT could be imaged indefinitely, but it was found by Blumhardt and colleagues (2018) that the docking strand conjugation does suffer slightly from photodamage, albeit to a much lesser extent than the photobleaching effects observed in STORM.

**Acquisition, Event Detection and Localisation**

The python-based application Launchworkers.py was initiated during experimental setup. Launchworkers.py manages the 10-core processor of the machine and assigns subsets of frames to each processor during the analysis phase initiated in the PYMEAcquire software. Series of raw data TIFF images were saved into a H5 file. Each processor performs the localisation one frame at a time. Once the Analysis function in PYMEAcquire was started, a near-real time visualisation of localisations results was obtained. These data were then recorded into a .H5R file for further analysis. These events were then reconstructed into a pseudo-image using Delauney triangulation as previously reported (Baddeley *et al.*, 2010).

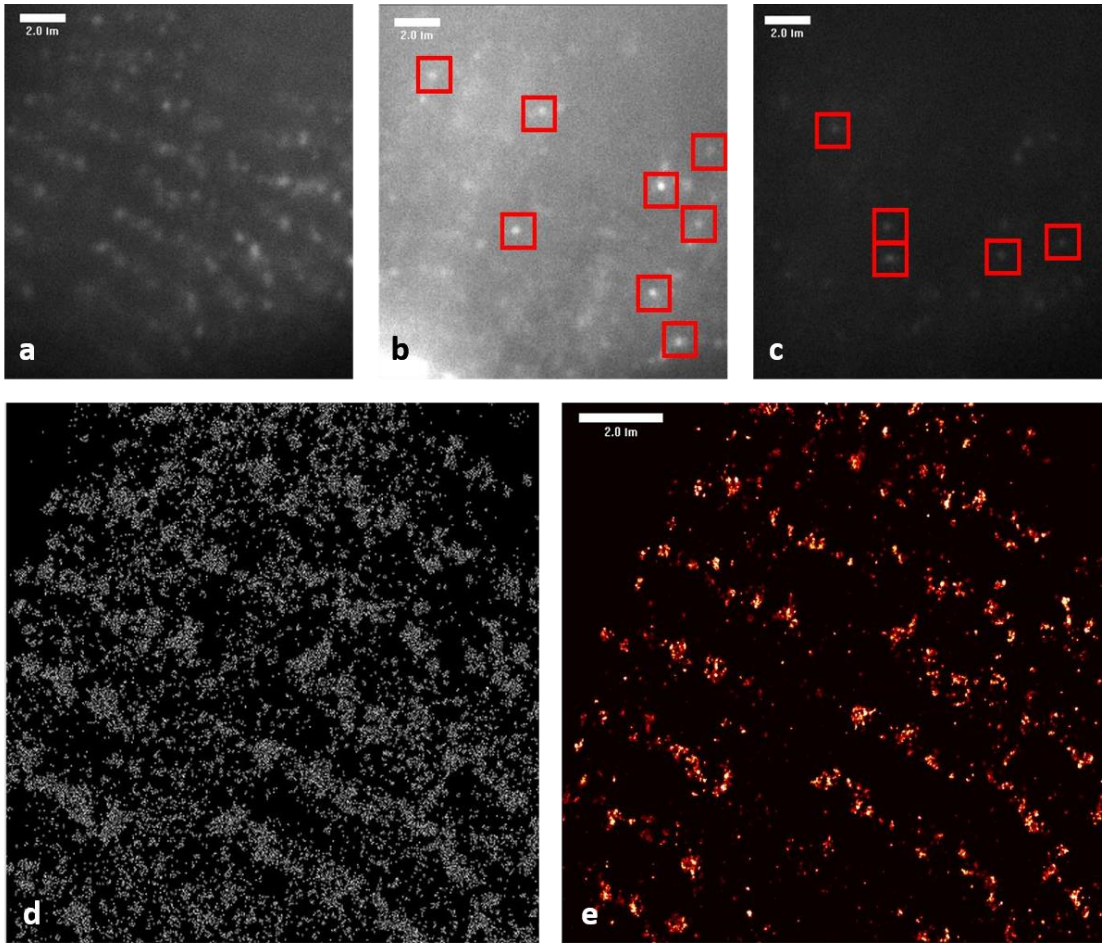


**Figure 2.7. Image acquisition, localisation, and rendering pipeline. Top panels are representative frames through the duration of the acquisition process. (a) An initial widefield image was captured during the pre-bleach protocol. (b) Full laser power results in a brief saturation due to intense excitation as seen in the bottom left of frame before fluorophores began to transition into the dark state and blinks were seen. (c) Steady state photoconversion achieved after approximately 200 frames. Red boxes indicate ROI where events were detected and localised. (d) Each event was localised to a point. (e) Points were rendered using a Delauney triangulation method to create the super-resolved image (bottom right).**

The event detection and localisation occurred within the .H5 file during PYMEAcquire analysis. The various parameter settings for STORM and DNA-PAINT are shown in table 2.4. Firstly, the images were passed through a bandpass filter, to remove high band and very low band components. Next, the background (averaged) values were estimated from the previous 30 frames and subtracted. The analysis procedure then estimated a threshold level from the estimated pixel signal to noise ratio (SNR). The value set here

was a scaling factor applied to this threshold and was typically fixed. After thresholding, components that conform to a circular shape (i.e. fairly non-eccentric, no single pixels, within a maximum diameter, etc) had their centroid plotted, with a small ROI (typically 15 x 15 pixels), placed around it. Localisation was then performed on each ROI and the localised point was then plotted (figure 2.7d). These points were then joined by Delauney triangulation to produce a rendered image (figure 2.7e). The intensity of the triangle is inversely proportional to its area. This results in triangle created from 3 very close points being white, whilst 3 very sparse points are near black. To avoid sharp triangular patterns in the rendered image, these triangulations were jittered randomly from the localisation points, with an average being taken (40 iterations). This smoothing effect creates a visually smoother image and allows thresholding to be performed without the influence of the triangulation vertices. This method results in some loss of resolution, but unlike a Gaussian blurring, the jitter is relative to the local effective resolution per triangle (Baddeley *et al.,* 2010).

This process was also performed for dual channel experiments. Event localisations were assigned to each channel based on the ratiometric fit (Baddeley *et al.*, 2011). These data were then mapped on top of each other in a composite image using the shiftmaps created at the calibration stage. Data could be analysed either on a per channel basis or as a dual channel image.

## Negative Staining Experiments

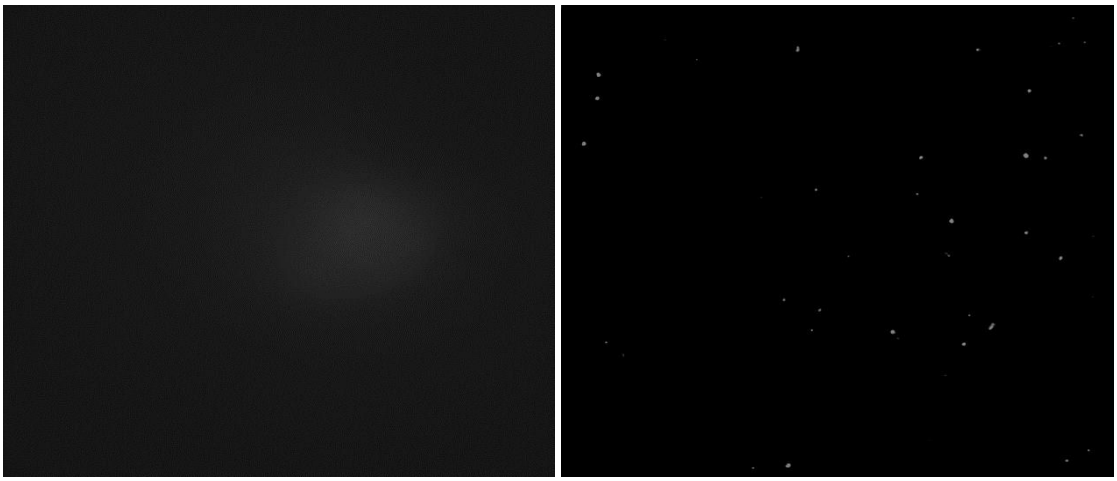

**Figure 2.8. Widefield typical frame of tissue treated with Image-iT FX only (left) during acquisition using the same STORM imaging protocol. Final rendered image after ~25,000 frames with contrast increased 10x compared to a representative STORM image (right). Scale bar = 2 µm.**

There are some endogenous biomolecules that can 'blink' resulting in detected events. These properties are often utilised to perform spectroscopic studies, on live cell metabolism. Although it is not possible to completely remove these molecules, they were assessed to be very minor in comparison to the signal intensity and distribution observed in immunofluorescence stained samples. Maximum intensity of these images remained below 5% intensity of a typical RyR2 STORM image. Results shown in figure 2.8 demonstrate the low amount of non-specific SMLM events that may arise from the tissue itself or the chemicals used during the IHC processing of the same. As these data show approximately empty images, one has high confidence in the specificity of the results from SMLM experiments and that observed events are from the labelled proteins of interest.

## Core Analysis Functions

Key functions, written in python by Professor Christian Soeller (University of Exeter), were used for the analysis of single and dual channel SMLM data sets. With support from Dr Ruisheng Lin (University of Exeter), python scripts were written to automate these functions and expand on them in order to perform data analysis on whole datasets. Statistics were performed and figures generation in python using the *scipy, numpy, pandas,* and *matplotlib* modules. Minor adjustments were made for specific analyses, such as those detailed for the colocalisation criteria in chapter 4 versus chapter 5. These analysis functions combined to best measure the cluster areas per channel, the amount of colocalisation per cluster, the fraction of clusters that were colocalised, and the distance of the remaining non-colocalised signals for context.

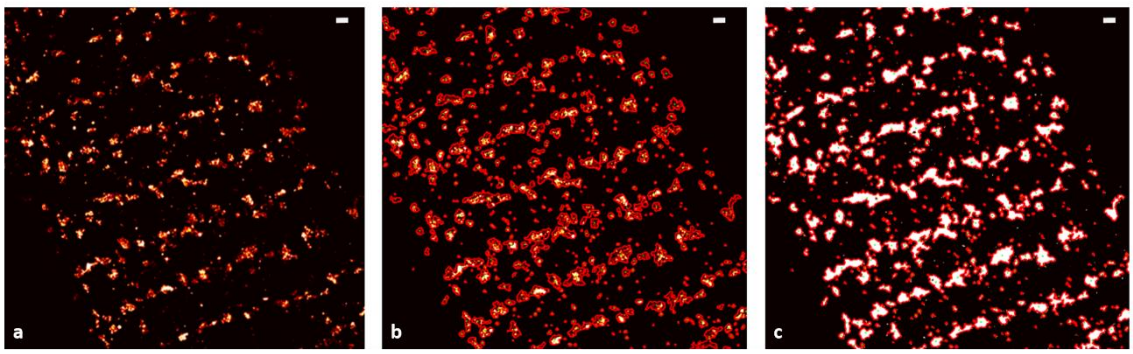


**Figure 2.9. Image analysis pipeline for identification and quantification of RyR clusters. (a) Rendered STORM image of peripheral RyR2 in Control CM. (b) Threshold isobars (red) at 80% fractional threshold. (c) Corresponding highly contrasted generated. Scale bar = 500 µm.**

RyR clusters have been analysed using SMLM techniques by the Soeller group and others. Analysis was based on EM data of RyRs in lipid bilayers. These stochastically formed into RyR clusters where receptors adopted a quasi-crystalline pattern. As such the clusters sizes were expressed as the

number of RyR that could fit into the area of the cluster if arranged in this packed crystalline-like array.

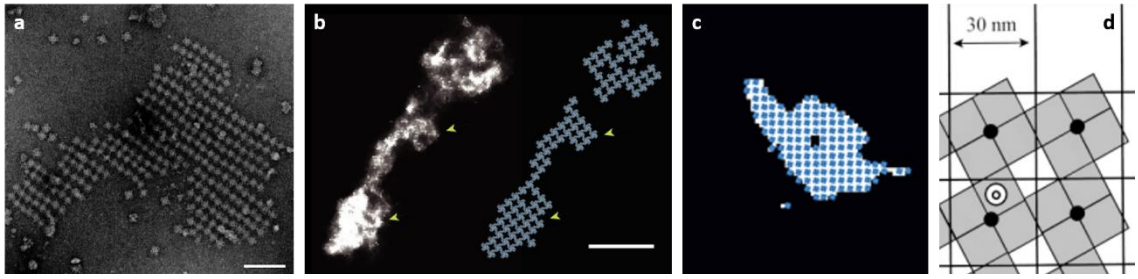


**Figure 2.10. Examples of RyR packing from different study types. (a) Direct EM evidence of RyR lattice-like clustering in lipid bilayers. Scale bar 150 nm (Yin and Lai, 2000). RyR clustering lattice applied to analysis of super-resolution STORM microscopy images in ventricular CM (b, Baddeley *et al.*, 2009) and atrial CM (c, MacQuaide *et al.*, 2015). RyR clustering pattern as the basis of computer simulation studies (d, Stern *et al.*, 1999). Figures adapted from relevant references.**

This was based on the known size in x, y of the ~30 x 30 nm RyR channel (Wagenknecht *et al.*, 1989; Yin and Lai, 2000) and has been used widely in the literature (Baddeley *et al.*, 2009; MacQuaide *et al.*, 2015; Munro *et al.*, 2016). This approach gives a good approximation of cluster size, though it is recognised that deep RyR clusters are 3-dimensional. Nevertheless these measures provide a reproducible measure across experiments appropriate to the resolution achieved with STORM (Baddeley *et al.*, 2009, 2011; Hou *et al.*, 2015; Munro *et al.*, 2016).

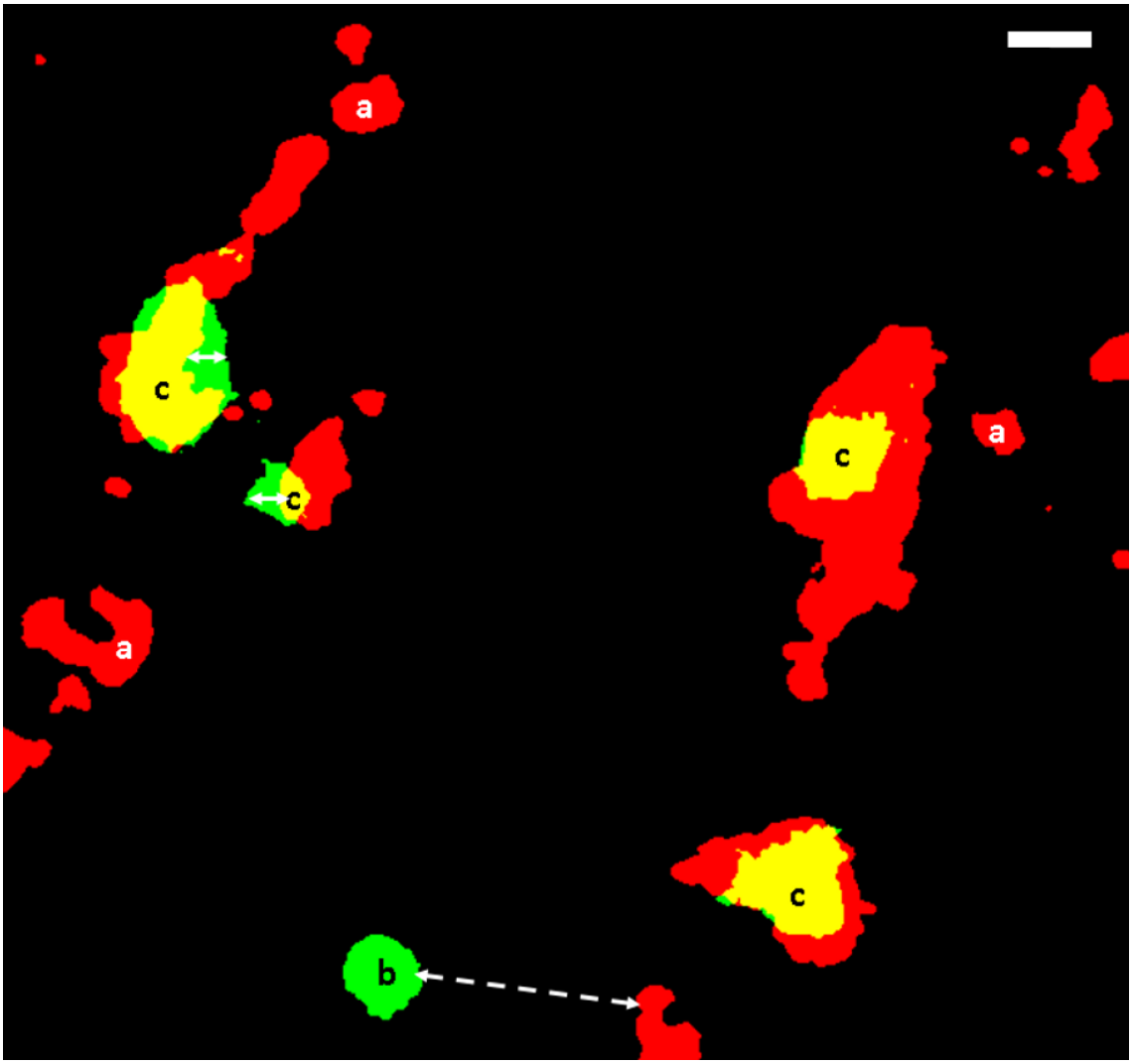


**Figure 2.11. Representative dual channel STORM mask data from Control CM depicting quantification strategies. (a) RyR2 clusters (red). (b) pRyR2-S2808 clusters (green). (c) Colocalised (phosphorylated, yellow) RyR clusters. Median distance measures illustrated by double-headed arrows. Euclidean pixel distances from the edge of reference mask (shown here as RyR2, red) to each pixel of the opposing channel (pRyR2-S2808, green). Solid lined arrows denote inclusion criteria for measurement of phosphorylated clusters (results chapter 2). Dashed line arrow denotes additionally included measures for comparison of channel performance (results chapter 3). Scale bar = 250 nm.**

Two functions were written to capture two aspects of colocalisation; the fraction of the total RyR cluster population colocalised, and the average amount of colocalisation in a cluster-wise manner, based on similar previous work (Jayasinghe *et al.*, 2012; Hou *et al.*, 2015; Munro *et al.*, 2016). This can be thought of as 'how many clusters were colocalised and by how much?'.

Results chapter 4 investigates the amount of phosphorylation signal and so the fraction was calculated only for those that contained signal. This removed bias from unphosphorylated (non-colocalised) clusters. Results chapter 5 measured the mean fraction across all clusters including those with no colocalisation. This allowed the performance of Ratio--PAINT to be assessed from either channel as the reference point. These measures are analogous to the approach used in confocal microscopy detailed above. The SMLM analysis is different however, in that the total fraction includes clusters in a binary manner, regardless of the degree of colocalisation, and the clusterwise fraction is similar to the percentage area colocalisation measure on a cluster to cluster basis.

Binarised image masks produce hard borders between signals. For colocalisation measurements this is a requirement, however for a fuller understanding of the data the distances from the edge of the reference mask were measured to each pixel of the opposite channel (figure 2.5). These measures were based on previous experiments and inform the confidence of the experiment (Goodman *et al.*, 2017; Baddeley *et al.*, 2011; Hou *et al.*, 2015; Munro *et al.*, 2016). The assumption is that the closer these pixels are to the opposing channel, the more likely they are to have originated from the colocalised cluster signal and thus from the target protein (i.e. the green pRyR2-S2808 signal denoted by solid double headed lines belongs to the same population that contributed to the yellow in figure 2.10c above).

# Chapter 3

## Validation from Western blots to SMLM microscopy: Modulation and detection of phosphorylation on the cardiac Ryanodine receptor

### Introduction

The isolated ventricular cardiomyocyte (CM) is an intricate and finely balanced system. This balance is maintained when the heart rate changes, such as during exercise. Primarily, proteins undergo post-translational modifications (PTM) that alter their biophysical properties. One prominent PTM is phosphorylation, a readily reversible modification that alters protein behaviour (Ardito *et al.*, 2017). A general principle of protein phosphorylation is that there is a constant turnover maintained in a steady state of protein kinase and protein phosphatase activity, until external stimuli occur (Hunter, 1995). RyR2 and other CICR related proteins undergo phosphorylation in a complimentary manner to shorten the overall heartbeat, whilst maintaining the relative ratios of each phase of the ventricular action potential in normal conditions, such as during exercise or the fight or flight response (Shan *et al.*, 2010). RyR2 releases $Ca^{2+}$ ions from the internal SR store that go on to initiate contraction. The sarco(endo)plasmic reticulum $Ca^{2+}$ ATPase cardiac isoform 2a (SERCA2a) works in an opposing fashion to remove this free cytosolic $Ca^{2+}$ and pump it back into the SR, in essence resetting the system for the next heartbeat. Phospholamban (PLN) inhibits SERCA2a, but releases its inhibition upon phosphorylation, allowing more $Ca^{2+}$ to be taken up into the SR faster.

In disease, aberrant phosphorylation is generally observed, and RyR2 hyper-phosphorylation in particular (Carter *et al.*, 2011; Mattiazzi and Kranias, 2014). At least three sites are currently well characterised on the RyR2 and phosphorylated at Ser-2808, Ser-2814, and Ser-2030 at rest. The basal phosphorylation levels were reported to be most abundant for Ser-2808, then Ser-2814, and the least for Ser-2030 (Huke and Bers, 2008). Though there is evidence for cross-talk, it is approximated that protein Kinase A (PKA) is the predominant phosphorylation mechanism at pRyR2-S2808, and calcium-calmodulin kinase II (CaMKII) is predominant at pRyR2-S2814. pRyR2-S2030 is less well understood, having only been discovered relatively recently, but it is thought to be phosphorylated by PKA to a lesser extent at rest and is reportedly not hyper-phosphorylated in disease (Xiao *et al.*, 2005; Huke and Bers, 2008).

RyR2 mediated $Ca^{2+}$ release begins the cycle excitation-contraction (EC) coupling, which initiates contraction. $Ca^{2+}$ induced RyR2 $Ca^{2+}$ release (CICR) is the phenomenon whereby a small influx of $Ca^{2+}$ ions result in the activation of the RyR clusters, which release a large amount of $Ca^{2+}$ from the sarcoplasmic reticulum (SR). This $Ca^{2+}$ then rapidly diffuses through the sarcoplasm and interacts with the contractile machinery, initiating contraction. CICR is initiated by depolarisation of the sarcolemma due to an AP. If left in this state, the contraction would become tetanic (maximal and sustained). $Ca^{2+}$ must be removed from the cytosol to relax the muscle back to the starting state. SERCA2a pumps $Ca^{2+}$ out of the cytosol and into the SR, which can be thought of as a $Ca^{2+}$ store in relation to EC coupling.

The rate at which SERCA2a transports $Ca^{2+}$ into the SR is dependent on being partially inhibited by the binding of PLN. This mechanism appears to be the reduced affinity of SERCA2a for $Ca^{2+}$ ions due to the physical interaction from PLN (Kranias, 1985; Colyer and Wang, 1991). Phosphorylation of PLN removes this physical interaction, resulting in the disinhibition of SERCA2a. Increased PKA and CaMKII signalling results in PLN relinquishing its inhibitory effect on SERCA2a, and so more $Ca^{2+}$ can be transported into the SR faster. SERCA2a has become a prime target of modulation to improve contractility in heart failure (HF) (Park and Oh, 2013). As such, phosphorylation of PLN is coordinated with RyR2 phosphorylation and both have been deemed to be of strong interest to the field (Aoyama *et al.*, 2011).

Phosphorylation affects the biophysical properties of proteins. Ser-2808 phosphorytion of RyR2 for example, increases the open probability of the channel. SERCA2a can be phosphorylated at Ser-38, however this has been shown to be absent in physiological states (Rodriguez *et al.*, 2004). Measurement of phosphorylation has traditionally been performed in Western blot experiments. Whilst Western blot data are incredibly useful and informative, these data represent an average over the total cell population and any spatial information has been lost. Great lengths have already been taken to create and validate phosphorylation-state specific antibodies for individual sites, such as pRyR2-S2808. Whilst these antibodies have been used successfully by several groups in Western blot analyses, they have not been used widely in microscopy studies. This thesis outlines the first quantification of the spatial distribution of phosphorylation within individual cells at the diffraction limited level, and within protein clusters using the super-resolution

microscopy methods STORM and DNA-PAINT. This chapter discusses the validation steps of a wide catalogue of relevant novel cardiac immuno-markers from Badrilla Ltd.

**Aims**

This chapter describes the validation pipeline for the use of phosphorylation-state specific antibodies in combination with a total protein antibody for the same protein (i.e. RyR2) and their applicability to fluorescence microscopy experiments. Phosphorylation-state specific antibodies were first used in dual colour diffraction limited experiments using confocal microscopy in combination with matched total protein antibodies that had been previously validated for imaging experiments (i.e. pRyR2-S2808 with RyR2). Positive Western blot results were obtained for several phosphorylation state specific antibodies (pssAb) supplied by Badrilla Ltd as part of the industrial collaboration of this project. pssAb showed appropriate bands for the 22 kDa PLN or 565kDa RyR2 in canine SR vesicles (cSR) preparations supplied by Badrilla Ltd with no observable secondary bands. Whilst there is no guarantee or strong correlation of performance for antibodies used in Western blots and immunofluorescence (IF) microscopy experiments, these provide the best case scenario for candidate pssAb. The pssAb were tested for suitability in immunofluorescence microscopy experiments for both PLN and RyR2 at multiple phosphorylation sites.

Of the initial screens, pRyR2-S2808 was deemed the most appropriate target based on reliability and high basal levels of fluorescence signal in a RyR2-like distribution that reduced the chance of false positive experiments in control

experiments. The basal level of fluorescence signal against the pRyR2-S2808 primary antibody was high enough to be confident that it was not non-specific labelling (as may be observed in the low basal phosphorylation of RyR2-S2030 (Xiao *et al.*, 2005)) and it is robust and reliable across CM and rat tissue sections using IHC in confocal microscopy.

Phosphorylation-state specific and total RyR2 antibodies were used in Western blot to confirm sensitivity under pharmacological perturbations of protein phosphatase activity. The same production batch of antibody were used in subsequent confocal and super-resolution microscopy experiments detailed in this chapter. Here, fluorescence signals from pRyR2-S2808 and pRyR2-S2814 have been quantified for its spatial distribution in relation to total RyR2 using dual colour fluorescence IHC and confocal microscopy.

The aims of this chapter are:

1. Current data is mostly derived from biochemical assays, with the exception of a single confocal microscopy and a single expansion microscopy-based studies (Brandenburg *et al.,* 2016; Sheard *et al.,* 2019). The first aim was to translate results from Western blot analysis of pssAb relevant to EC Coupling i.e. RyR2 and PLN related pssAb into reliable immunohistochemistry protocols. This will allow a further dimension of information to be obtained versus the current capabilities demonstrated in the literature.
2. Immunohistochemistry and image analysis protocols will be developed, immunofluorescence confocal microscopy experiments of dual labelled samples for pssAb and total protein antibody pairs were performed. A

panel of pssAb will be assessed and those with strong agreement to total antibody will be progressed to quantification.

3. Response to pharmacological intervention will be assessed using confocal microscopy. The pssAb(s) with demonstrable differences between pharmacological states will provide the greatest level of confidence in the technique and will be progressed to SMLM experiments.

**Contributions**

I have performed each aspect of these experiments; however, I wish to acknowledge the substantial help I have received in obtaining and analysing the data contained in this chapter. All Schedule 1 procedures, cell isolation, and cell fixation or tissue cryoprotection and sectioning were performed by Dr Izzy Jayasinghe (University of Leeds), Dr Alex Clowsley (University of Exeter), Dr Ellen Green (University of Exeter), and I.

All Western blots and BCA analysis were performed by myself. Schedule 1 procedures, cell isolation, Western blot sample preparation at Badrilla Ltd were all performed by myself and Dr Eleftheria Pervolaraki (University of Leeds), with help and guidance Mr Lewis Jolly (University of Leeds), and Professor John Colyer Badrilla Ltd, University of Leeds).

All confocal microscopy experiments were performed by myself. Python scripts for analysis were written and developed by myself with extensive support from Dr Ruisheng Lin (University of Exeter), with guidance from Professor Christian Soeller (University of Exeter).

**Confirmatory Western blot experiments for RyR2 and PLN pssAb**

Western blots are a widely used tool to assess the presence, and relative abundance of proteins detected using antibody labelling. They are a multi-step process with common points of failure. Samples are loaded as uniformly negatively charged, denatured linear proteins (Kurien and Scofield, 2006; Mahmood and Yang, 2012). Longer polypeptides have higher molecular weights and migrate slower than shorter, lighter proteins during electrophoresis. Then once the electrophoresis is complete the proteins are transferred onto a blotting membrane with an even and firm contact. Membranes then undergo antibody based imaging for specific proteins (Kurien and Scofield, 2006).

For validation purposes, Badrilla Ltd provided samples they had created and validated previously. Canine SR (cSR) vesicles in the control state or stimulated with either PKA or CaMKII with electrical stimulation to ensure $Ca^{2+}$ cycling. cSR vesicles were created from homogenised canine ventricular tissue that was then fractionated and SR vesicles obtained. cSR vesicles enrich the samples for SR related proteins and remove unwanted total protein and so can be thought of as a crudely purified SR sample. Mouse CM were also used either isolated from control hearts or hearts that were perfused with 10 µM isoprenaline for 3 mins prior to undergoing the isolation procedure. These samples will be referred to as cSR, PKA cSR, CaMKII cSR, mouse CM, or 100 nM isoprenaline mouse CM in the remainder of this chapter. When dealing with large proteins, such as RyR2 (565 kDa) sample preparation can be difficult (MacPhee, 2010). Known samples produced by Badrilla Ltd were an important resource for validation steps.

cSR and mouse CM samples were Western blotted for phosphorylation at Ser-16 or Thr-17. Ser-16 phosphorylation is mediated by PKA, whereas Thr-17 phosphorylation is mediated by CaMKII in a frequency dependent manner (Schwinger *et al.*, 1999; Zhao *et al.*, 2004)

The pPLN-S16 pssAb was available in two forms, serum-derived and affinity purified (AP). Both were blotted (1:5000) and showed positive staining for a 25 kDa band in PKA cSR (figure 3.1a and 3.1b, lane 2), which is compatible with expected PKA mediated ser-16 phosphorylation. pPLN-S16AP did not detect the 5 kDa monomer of PLN that can often be present near the 10 kDa band in Western blots in PKA cSR and did not detect any observable signal in 100 nM isoprenaline mouse CM (figure 3.1b, lane 5), whereas pPLN-S16 serum based pssAb did (figure 3.1a, lane 5).

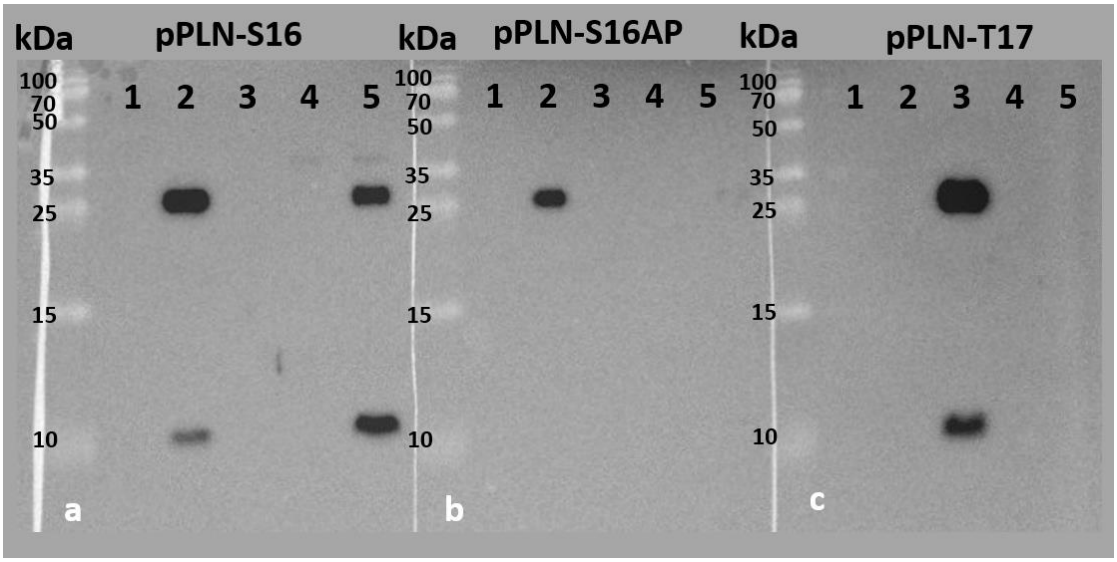


**Figure 3.1. Western blot analysis using pPLN-S16 (a), pPLN-S16AP (b), and pPLN-T17 (c). Samples: cSR (lane 1), PKA cSR (lane 2), CaMKII cSR (lane 3), mouse CM (lane 4), 100 nM isoprenaline CM (lane 5). cSR samples contained 4 µg. Mouse CM contained approximately 10,000 CM.**

The pPLN-T17 pssAb detected signal at the same level of the pPLN-S16 antibodies with both approximately 25 kDa and approximately 10 kDa bands present in the CaMKII cSR sample (figure 3.1c, lane 3). Based on these data, pPLN-S16 and pPLN-T17 showed that they were sensitive to their respective

phosphorylation states, when PLN was pharmacologically phosphorylated at Ser-16 and Thr-17.

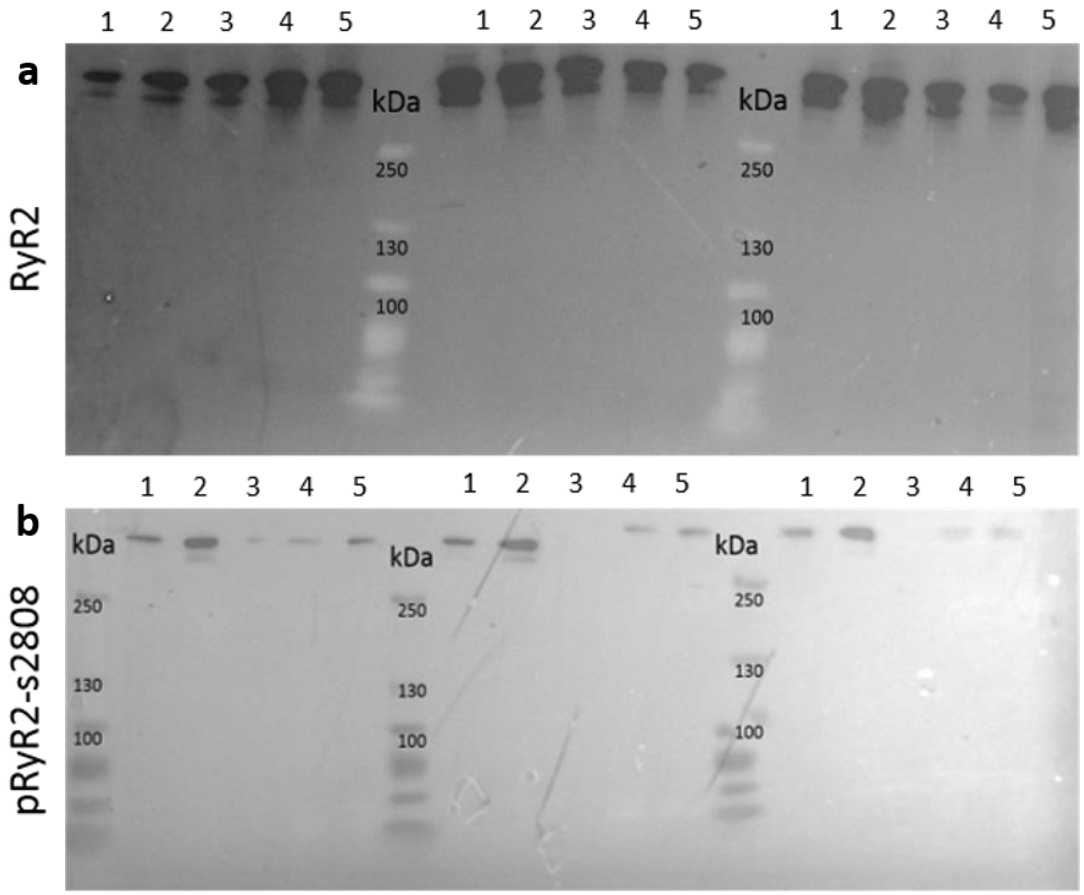


**Figure 3.2. Western blot triplicates analysis using RyR2 (a) and pRyR2-S2808 (b). Samples loaded were mouse CM (lane 1), 100 nM isoprenaline mouse CM (lane 2), cSR (lane 3), CaMKII cSR (4), PKA cSR (5). All sample volumes contained approximately to 10,000 cells or 10 µg of cSR vesicles.**

The mouse monoclonal C3-33 anti-RyR2 (MA3-916, Thermofisher) primary antibody used previously by our lab for super-resolution experiments gave a strong signal for RyR2 in all samples and across triplicate panels (figure 3.2a). RyR2 blots confirmed approximately even starting material for consideration of pRyR2-S2808 labelled blots (figure 3.2b). Lane 2 in each panel of figure 2b contains 100 nM isoprenaline mouse CM. When compared to mouse control CM in lane 1, the signal is stronger in each triplicate. This is also observed for the PKA cSR in lane 5 compared with control cSR in lane 3 of the left panel,

and even CaMKII cSR in lane 4, which would be expected as Ser-2808 phosphorylation is PKA mediated. These data show that pRyR2-S2808 is sensitive to phosphorylation level at ser-2808. As with the pPLN-S16 antibody, pRyR2-S2808 and pRyR2-S2814 had a serum and affinity purified product available to test (See chapter 2 for further details).

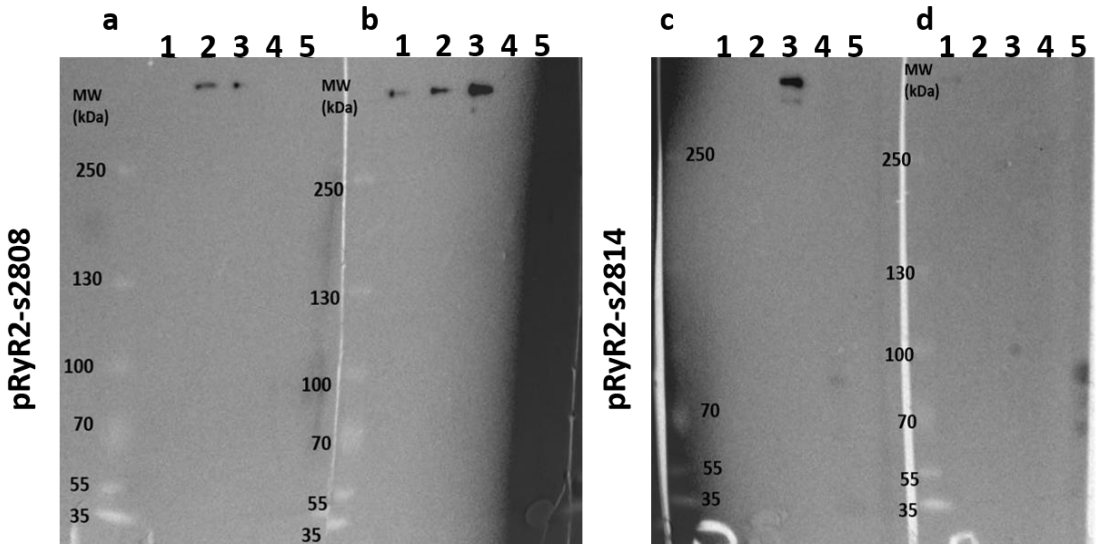


**Figure 3.3. Western blots of pRyR2-S2808 and pRyR2-S2814 serum and affinity purified pssAb. pRyR2-S2808 serum (a) and affinity purified (b). Samples loaded in panels a and b were: cSR (lane 1), PKA cSR (lane 2), CaMKII cSR (lane 3), rat CM (4) 1 µM Calyculin A CM (5). pRyR2-S2808 serum (c) and AP (d). Samples loaded in panels c and d were cSR (lane 1), CaMKII cSR (lane 2), PKA cSR (lane 3), rat CM (4) 1 µM Calyculin A CM (5). All sample volumes approximated to 10,000 cells or 4 µg total protein.**

pRyR2-S2808 (1:5000) serum (figure 3.3a) and affinity purified (figure 3.3b) increased intensity in the PKA cSR (lane 2) and CaMKII cSR (lane 3) compared with control cSR (lane 1). pRyR2-S2814 serum and affinity purified pssAb Western blot signals had the opposite relationship. Only pRyR2-S2814 (1:5000) serum (figure 3.3c) showed a positive signal for Ser-2814 phosphorylation in cSR CaMKII (lane 3).

The strong pRyR2-S2814 signal in CaMKII cSR (figure 3.3c) reflects the specificity of the pRyR2-S2814 antibody. The band in lane 3 is of the correct molecular weight and of any, lane 3 would be expected to have the strongest

signal. Lanes 4 and 5 were rat control CM and CM treated with the PP2a phosphatase inhibitor 1 µM Calyculin A that I prepared. These sample preparations appear to have been unsuccessful.

In summary, all pssAb that showed positive staining had bands of an appropriate size and with no observable secondary staining. pPLN-S16 serum, pPLN-T17 serum, pRyR2-S2808AP and pRyR2-S2814 serum were deemed to have the best signal to noise ratio in Western blot, with little observable cross reaction in both cSR and total CM preparations. These antibodies progressed to immunofluorescence confocal microscopy experiments.

**Immunofluorescence Validation and Optimisation of PLN pssAb**

Whilst Western blot data was encouraging, antibodies do not necessarily perform equally in different applications. As such, their performance needed to be tested in immunofluorescence confocal microscopy prior to progression into super-resolution experiments. A standard IHC protocol within our lab was used when labelling CM or tissue sections and amended as appropriate. This protocol is based on a 1% normal goat serum (NGS) block for 1 hour, overnight primary incubation, and 2 hrs secondary antibody incubation, with appropriate washes.

Iterative troubleshooting established that the pPLN-T17 required 24hrs blocking with 1% bovine serum albumen (BSA) and 1% NGS at a 1:200 dilution. The PLN antibody seemed consistent with either method of blocking and gives a consistent signal in the longer block (figure 3.4). These

parameters were adopted as the new starting point for the other pssAb and appeared to work reliably for all other Badrilla Ltd pssAb tested (figure 3.5).

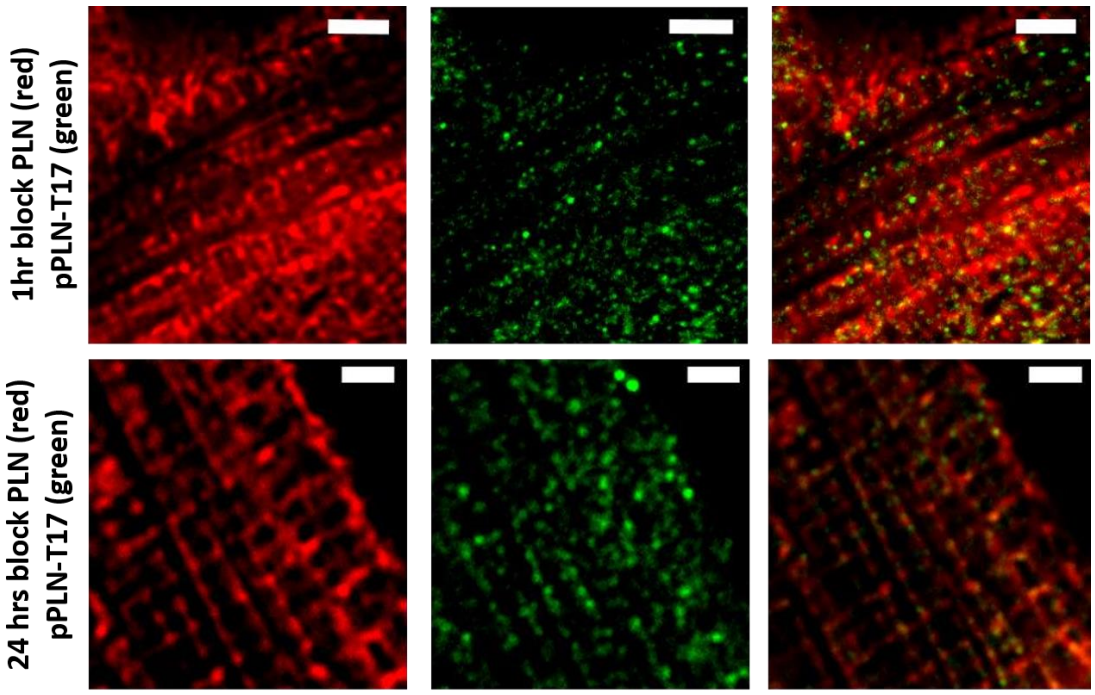


**Figure 3.4. Representative immunofluorescence confocal microscopy images of control CM. Total anti-PLN (red, left), pPLN-T17 (green, centre), and corresponding overlay images are shown. 1 hour (row 1) and overnight (row 2) blocking protocols were performed for each of control CM. Scale bar = 2 µm.**

Figure 3.4 shows results of immunohistochemistry optimisation experiments for PLN (red) and pPLN-T17 (green). 24 hrs incubation with blocking buffer produced greater specificity of pPLN-T17 pssAb.Next, pPLN-T17 and pPLN-S16 were used along with the total PLN antibody in immunofluorescence confocal microscopy experiments on control CM and 1 µM Calyculin A CM. Both pPLN-T17 and pPLN-S16 produced a recognisable SR-like pattern that agreed well with PLN. Qualitatively, both pssAb increased their signal coverage in 1 µM Calyculin A CM. Across all samples, PLN phosphorylation appeared to be nodal, often localised to the junctions where axial and transverse PLN signal cross (figure 3.5).

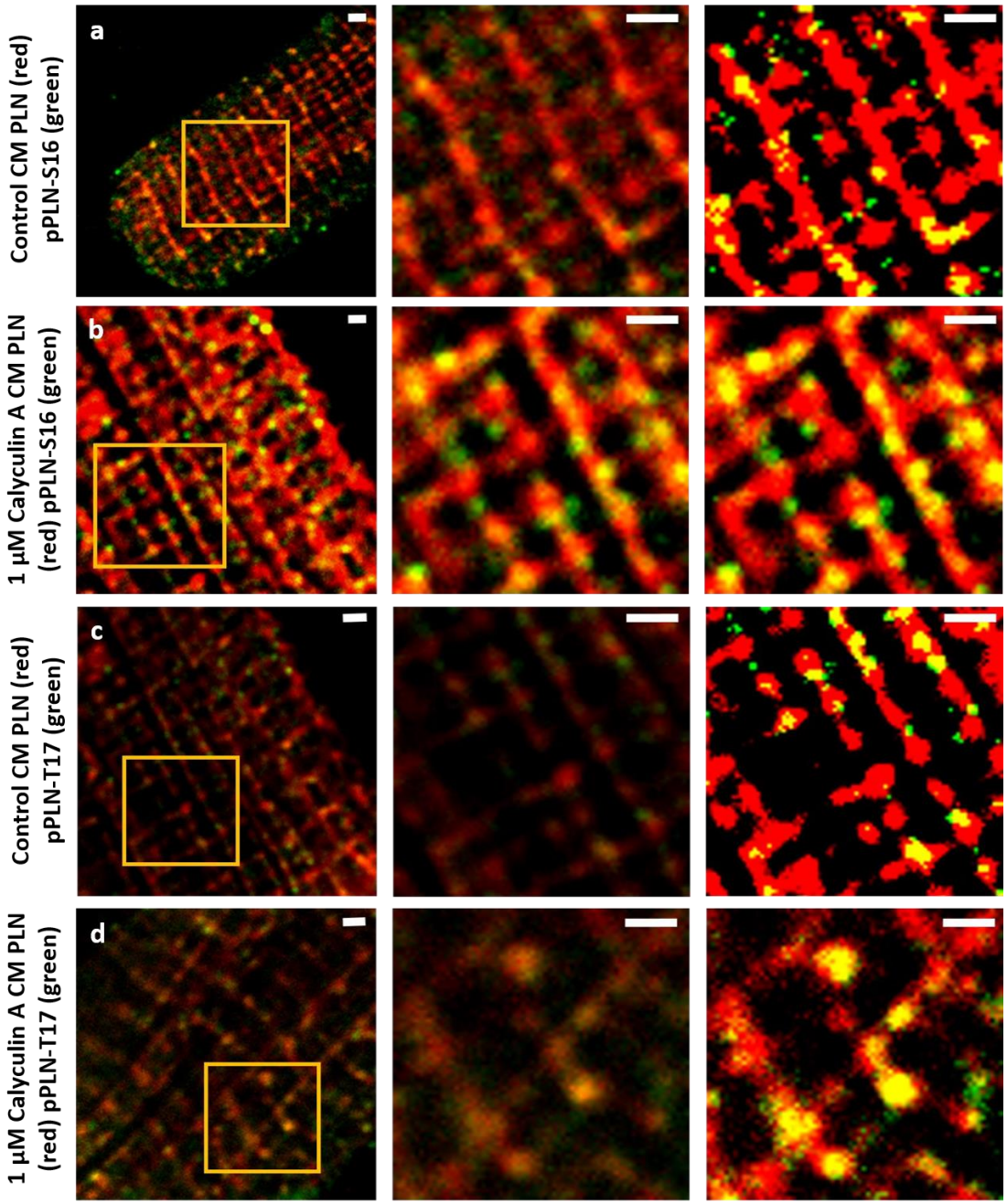


**Figure 3.5. Representative immunofluorescence confocal microscopy images of CM for antibodies against total PLN or PLN pssAb under pharmacological conditions. Total anti-PLN (red) was dual labelled with either pPLN-S16 (a and b, green) or pPLN-T17 (c and d, green) in control CM (a and c) and 1 µM Calyculin A CM (b and d). Scale bar = 1 µm. Regions of interest (ROI) in images were enlarged in the centre column. ROI images were reproduced with enhanced contrast for display purposes (right column).**

PLN related pssAb were then assessed under pharmacological conditions, as shown in figure 3.5. 1 µM Calyculin A CM had more nodes phosphorylated than control CM for both Ser-16 and Thr-17. This suggests that there is a certain level of cellular coordination of the relevant kinases and phosphatases

involved in PLN phosphorylation, as evidenced by the non-uniform, but not completely random pattern of PLN phosphorylation (figure 3.5). Both PLN pssAb signals colocalised well with PLN and produced this nodal behaviour. This distribution would be most interesting to observe in the context of SERCA2a due to PLN's phosphorylation-dependent interaction with SERCA2a.

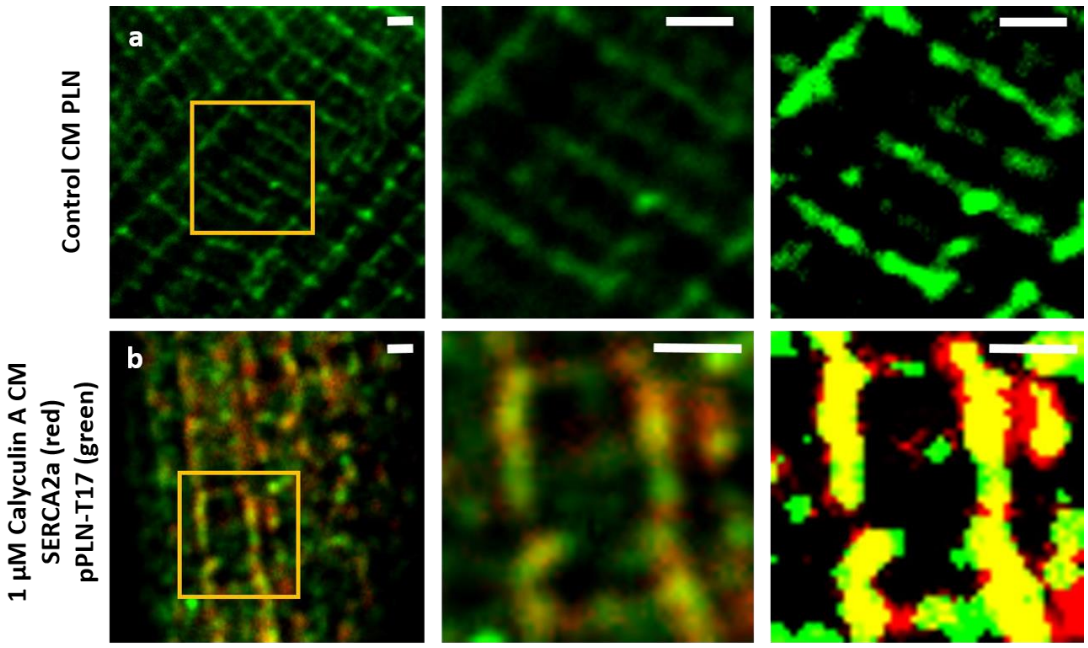


**Figure 3.6. Representative immunofluorescence confocal microscopy images of SR related antibodies. (a) anti-PLN in control CM. (b) SERCA2a (red) and pPLN-T17 (red, bottom row) in 1 µM Calyculin A CM. Scale bar = 1 µm. ROI in images were enlarged in the centre column. ROI images were reproduced with enhanced contrast for display purposes (right column).**

In order to assess the rabbit raised SERCA2a related pssAb, a suitable counter marker was required. Our only reliable SERCA2a total antibody was also rabbit raised, and so the mouse raised anti-PLN was used instead, as it should colocalise with SERCA2a. Despite the modest amount of immunohistochemistry based fluorescence microscopy data on PLN, much is known about PLN and it is mostly distributed within the SR in a pattern very similar to the SERCA2a channel that it inhibits physiologically, plus notably highly concentrated around the nuclear envelope (Vangheluwe *et al.*, 2003;

Wu *et al.*, 2016). The mouse monoclonal anti-PLN (clone A1, product number A010-14, Badrilla Ltd, UK) was used in a 1:100 dilution, as per our standard protocol (figure 3.6). PLN gave a strong SR-like signal when imaged alone (figures 3.4, 3.5) and agrees with previous confocal microscopy images of PLN (Wu *et al.*, 2016). pPLN-S16 or pPLN-T17 were imaged along with PLN. A SERCA2a-like pattern was observed with the pPLN-S16 and pPLN-T17 using the standard protocol (figure 1, left column. 1:100 dilution incubations were performed after an overnight block that produced a SR-like pattern. Low phosphorylation was detectable in control CM using both antibodies, which agrees with physiological data, whereas 1 μM Calyculin A CM produced a nodal pattern that colocalised well with PLN and was stronger at the axio-lateral junctions in the SR. This pattern appeared for both pPLN-S16 and pPLN-T17. Ser-16 is phosphorylated by PKA, whilst Thr-17 is phosphorylated by CaMKII. This suggests that PLN phosphorylation control is spatially coordinated across multiple signalling cascades (Zhao *et al.*, 2004).

Unlike the other phospho-state specific antibodies, where there was a total RyR2 protein antibody previously validated in immunofluorescence experiments, super-resolution microscopy data for anti-PLN was lacking. pssAb PLN were imaged with both the mouse anti-SERCA2a (Invitrogen, UK) and Badrilla Ltd mouse anti-PLN, showing good agreement in gross structure between SERCA2a and PLN (figure 3.2 and 3.3). Dual channel experiments are required in the future to fully validate this.

It was hoped that a rabbit anti-SERCA2a antibody could be found to image with the Badrilla Ltd mouse anti-PLN for dual colour imaging. Unfortunately, the rabbit anti-SERCA2a antibodies we had available to us showed poorer

labelling than our mouse anti-SERCA2a that has previously been validated. Comparisons between the mouse anti-SERCA2a and PLN stains in parallel experiments showed suitable distributions, and so we have confidence in the accuracy of Badrilla Ltd's PLN antibody (figure 3.3). In order to fully validate phospho-specific PLN antibodies, the mouse anti-PLN antibody should ideally be validated against its physiological partner, SERCA2a. I decided that without an appropriate rabbit anti-SERCA2a antibody, the validation process would be incomplete, and so attention was instead focused onto the RyR2 set of antibodies. It is hoped that the mouse anti-PLN images here motivate others to perform further work on the spatial distribution of SERCA2a and PLN using immunofluorescence and super-resolution techniques.

**Immunofluorescence Validation and Optimisation of RyR2 pssAb**

RyR2 related pssAb were tested using 1% BSA and 1% NGS blocking solution for 24 hrs. These were tested in dual labelled immunofluorescence confocal microscopy experiments with the same total RyR2 antibody as used for Western blot analysis (figure 3.2).Total RyR2 labelled was consistent with other confocal data using 1 hr 1% NGS block (Chen-Izu *et al.*, 2006). RyR2-S2808 is predominantly phosphorylated by PKA and dephosphorylated by PP2a (Rodriguez *et al.,* 2003; Shan *et al.*, 2010). Ser-2808 was therefore the most easily modulated phosphorylation site with our 1 μM Calyculin A or 20 μM H-89 incubations of quiescent cells and without the requirement of field stimulation devices. As such, pRyR2-S2808 and dephoRyR2-S2808, which is sensitive only to the dephosphorylated Ser-2808 site were tested in control CM and tissue sections. These experiments were aimed to characterise how

well the pssAb agreed with the total RyR2 antibody, and whether they responded in the expected way to pharmacological intervention. This is analogous to the aims of the PLN experiments detailed in figures 3.4, 3.5.

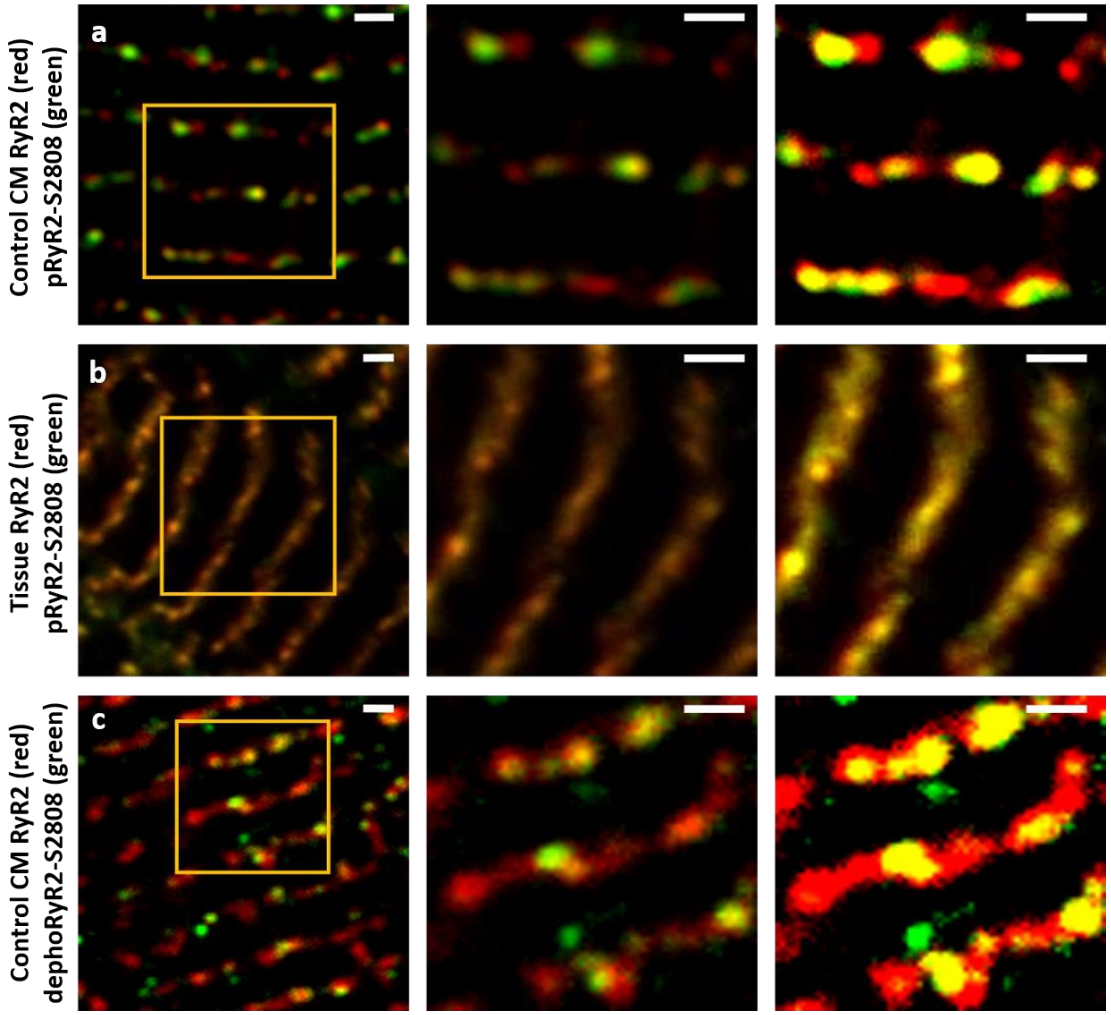


**Figure 3.7. Representative immunofluorescence confocal microscopy images of RyR2 and Ser-2808 related pssAb. (a) Control CM labelled for RyR2 (red) and pRyR2-S2808 (green). (b) Tissue sections labelled for RyR2 (red) and pRyR2-S2808 (green). (c) Control CM labelled for RyR2 (red) and dephoRyR2-S2808 (green). Scale bar = 1 µm. ROI in images were enlarged in the centre column. ROI images were reproduced (centre column) with enhanced contrast for display purposes (right column).**

Next, similar experiments were performed for total RyR2 (red) and RyR2-related pssAb (green) as shown in figure 3.7. Three RyR2 related pssAb were available; pRyR2-S2808, dephoRyR2-S2808, and pRyR2-S2814. The Ser-2808 site has been widely reported to have a high resting phosphorylation level and is easily manipulated in-vitro via the adrenaline

mediated PKA signalling pathway (Huke and Bers, 2008; Shan *et al.*, 2010). pRyR2-S2808 signal consistently agreed well with RyR2 co-labelling, in both CM and tissue sections (figure 3.7). dephoRyR2-S2808 showed good specificity compared to the RyR2 labelling (figure 3.7c) and the amount of colocalisation was consistent with the amount of phosphorylation from the pRyR2-S2808 labelled control CM. Both pRyR2-S2808 and dephoRyR2-S2808 immunofluorescence experiments displayed punctate labelling in CM, whereas pRyR2-S2808 produced a more even and widespread signal in tissue sections.

RyR2 related phosphorylation state-specific antibodies showed promise and our lab has extensive experience in RyR2 super-resolution microscopy experiments (Baddeley *et al.*, 2009; Baddeley *et al. ,* 2010; Jayasinghe *et al.*, 2018). Next these RyR2 related pssAb were used in immunofluorescence confocal microscopy experiments to test their response after pharmacological perturbation of RyR2 phosphorylation. Western blots have shown that the anti-pRyR2-S2808 antibody detects the phosphomimetic peptide that it was raised against in a denatured linear form (Carter *et al.*, 2011). The pRyR2-S2808 affinity for this sequence was tested in the native form with IHC in non-denatured proteins in-situ in tissue sections and CM preparations.

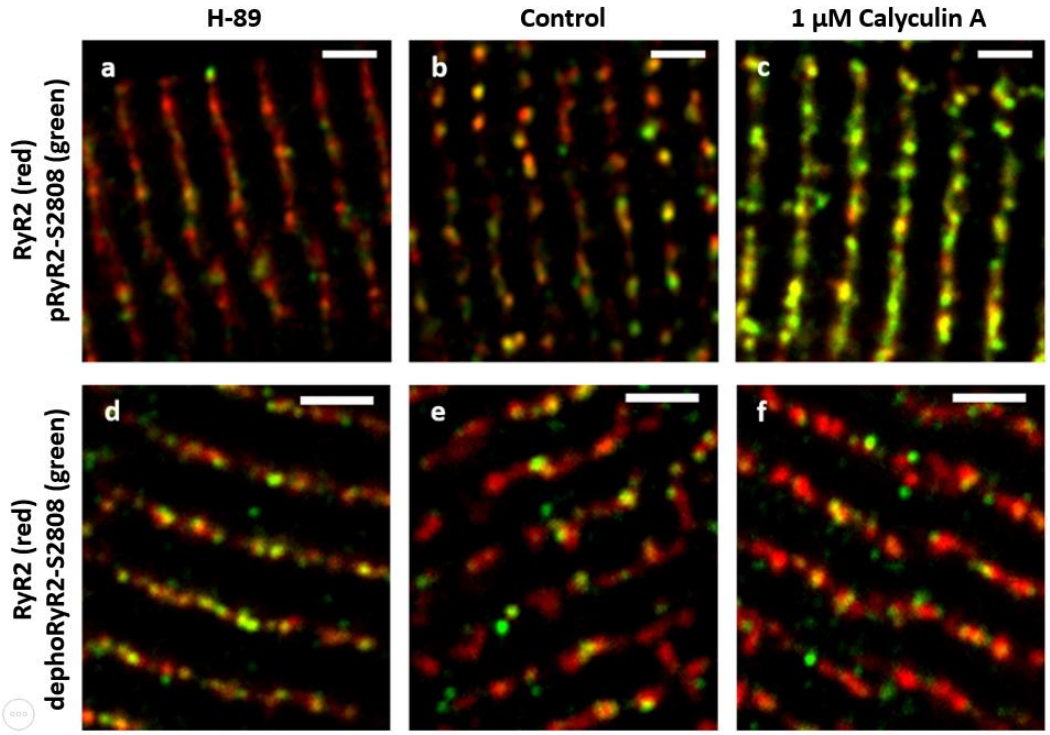


**Figure 3.8. Representative immunofluorescence confocal microscopy images of RyR2 and Ser-2808 related RyR2 pssAb under different pharmacological states. (a-c) RyR2 (red) and pRyR2-S2808 (green) in CM. (d-f) RyR2 (red) and dephoRyR2-S2808 (green) in CM. 20 µM H-89 CM (a, d), control CM (b, e), and 1 µM Calyculin A CM (c, f) are shown. Scale bar = 2 µm.**

The pharmacological intervention was used on isolated CM to modulate phosphorylation levels of Ser-2808 to assess the sensitivity of related pssAb (figure 3.8). When considering data from experiments using pssAb, it is useful to consider the entire population as being in one of two states at any one time. As such, the protein is either phosphorylated at a specific site, or it is not. The pssAb will report if it is in the state that it recognises. For example, pRyR2-S2808 will report phosphorylated Ser-2808, whilst dephoRyR2-S2808 reports dephosphorylated Ser-2808.

Phosphorylation was increased by phosphatase inhibition with 1 µM Calyculin A (Rodriguez *et al.*, 2003; Belevych *et al.*, 2011), or decreased with 20 µM H-89 (Sigma, UK), a PKA inhibitor (Rodriguez *et al.*, 2003; Terentyev *et al.*, 2003; Curran *et al.*, 2007). I decided to focus on 1 µM Calyculin A

treatments compared to control as enhanced signal is better for validation purposes, and hyperphosphorylation is an application motivation. As such the ability to validate hyperphosphorylation in a model state is of most relevance to future applications in disease states.

DephoRyR2-S2808 did show a relative increase after incubation with 20 μM H-89 (figure 3.7d), however, in both control and 1 μM Calyculin A samples the spatial agreement appeared variable in relation to RyR2. The dephoRyR2-S2808 signal pattern agreed well with RyR2, however in a subset of experiments there was a noticeable amount of signal that had no corresponding coincident RyR2 signal (figure 3.7d-f). Additionally, dephoRyR2-S2808 signal increased in at least one experiment after Calyculin A treatment, as did pRyR2-S2808 where only pRyR2-S2808 would be expected to increase. I judged that dephoRyR2-S2808 required further development of the experimental conditions.

The pRyR2-S2808 antibody signal increased in Western blots (figure 3.2) and initial confocal microscopy experiments of 1 μM Calyculin A CM (figure 3.10). Incubation with the phosphomimetic peptide before secondary antibody incubation would allow assessment of the antibody's antigen binding in non-denatured protein samples. This co-labelled with a total RyR2 antibody (figure 3.9). A sample was prepared without primary antibody incubation to confirm there was no staining artefact from the use of both anti-mouse and anti-rabbit secondary antibodies.

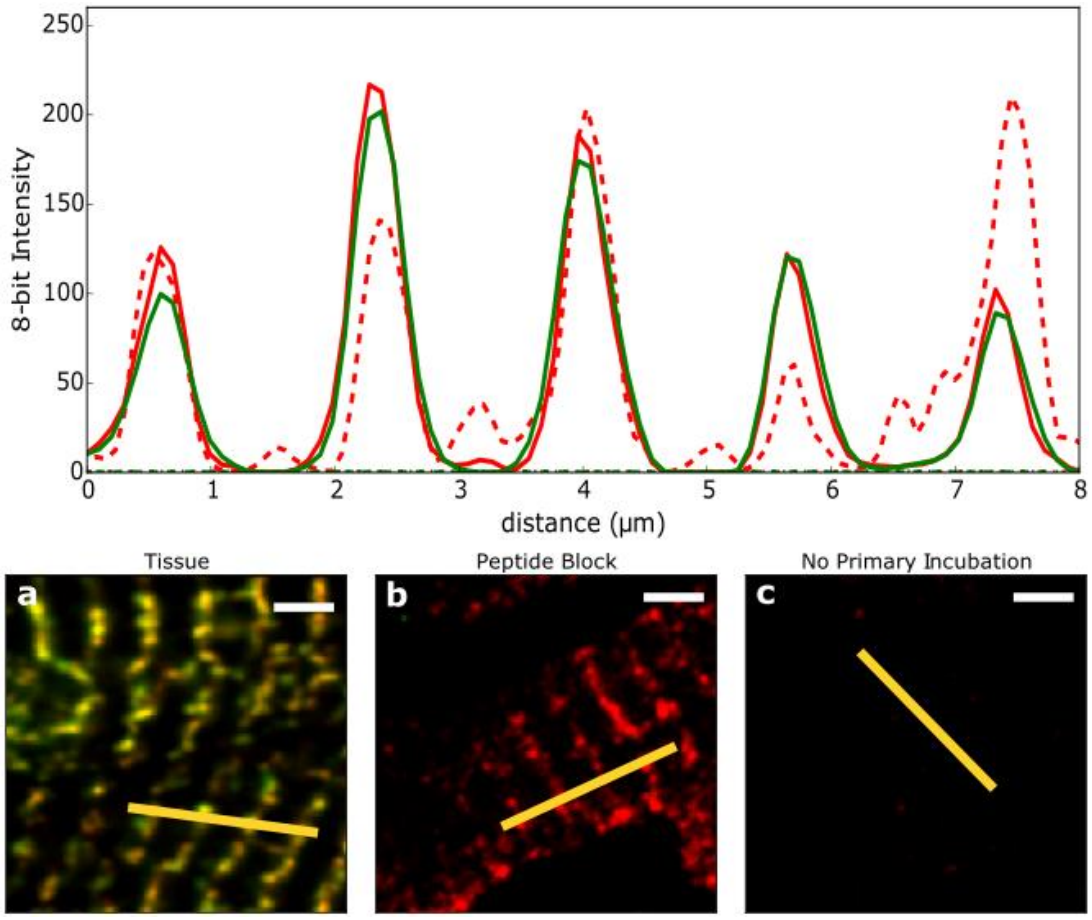


**Figure 3.9. Immunohistochemistry confocal microscopy analysis of secondary antibody labelling in different primary antibody label states for RyR2 (red) and pRyR2-S2808 (green). Intensity traces corresponding to 5-pixel averaged line measures (yellow lines). (a, solid line) Tissue sections immunolabelled with RyR2 and pRyR2-S2808. (b, dashed line) Tissue sections immunolabelled with RyR2 and pRyR2-S2808 that was incubated with the phosphomimetic peptide for the Ser-2808 epitope. (c, dot-dashed line) Tissue sections immunolabelled with anti-mouse and anti-rabbit secondary antibodies.**

Five pixel averaged linear intensity profiles were measured across the peptide inhibition experiment samples and compared (figure 3.9). The periodicity of peaks for RyR2 and pRyR2-S2808 in figure 8a reflect the periodicity of sarcomeres or T-tubules (Soeller and Cannell, 1999). The traces agree well with each other and reaffirms the visual conclusions that pRyR2-S2808 signal has a coincidental spatial distribution to RyR2 signal and very little elsewhere. The pssAb were incubated in a 5:1 solution with the peptide strand to which they were raised (provided by Badrilla Ltd (Leeds, UK)).

There was no observable difference between the pRyR2-S2808 channels in the peptide inhibition sample (figure 3.8a green dashed line) and the no primary antibody sample (figure 3.8 green dot dashed line). This indicated that the pRyR2-S2808 antibody specifically recognised this sequence, which is required for the phospho-site sensitivity (Rodriguez *et al.*, 2003). The pRyR2-S2808 was selected to continue further immunofluorescence microscopy-based quantification.

**pRyR2-S2808 Validation Summary**

The pRyR2-S2808 and pRyR2-S2814 pssAb were assessed in Western blots and for performance in immunofluorescence when co-labelled with a previously validated RyR2 antibody. Confocal microscopy was used to assess the pattern of pssAb distribution qualitatively and later quantified. Visual summaries for the validation of both pssAb are outlined in figure 3.10 and 3.11 and discussed.

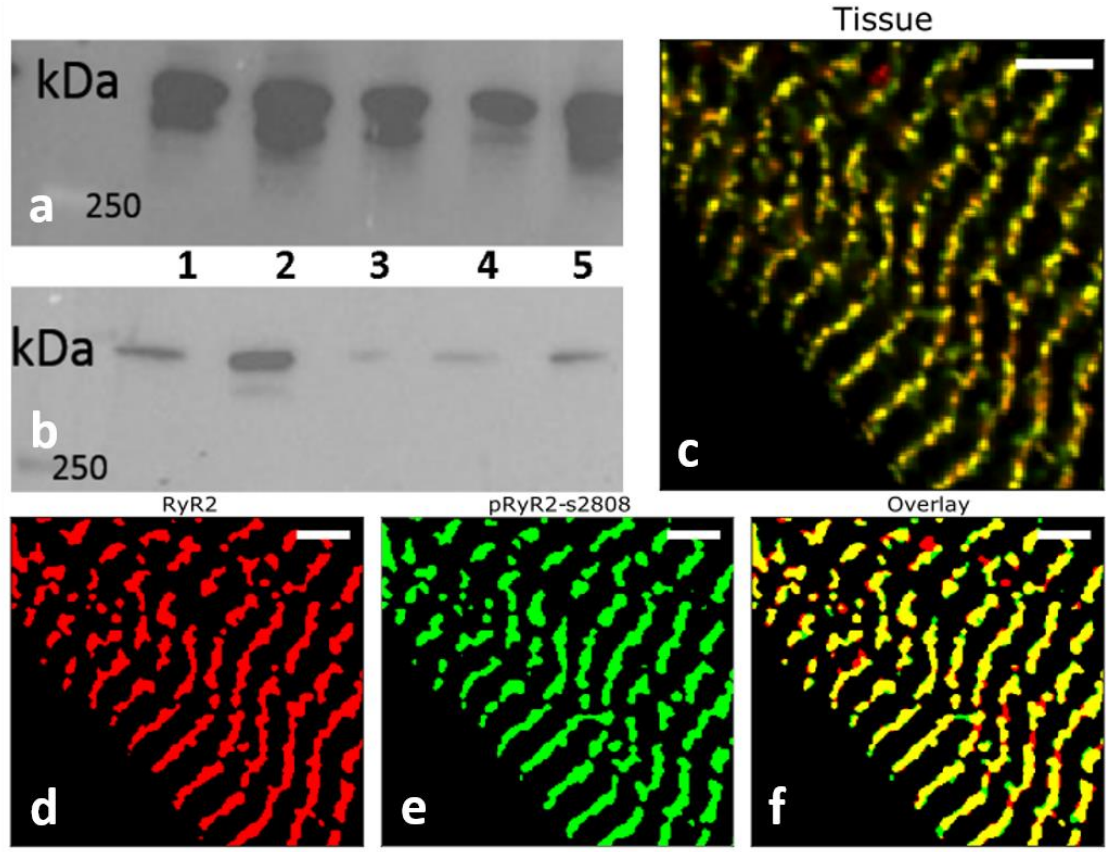


**Figure 3.10. Validation of pRyR2-S2808 for confocal microscopy imaging. Western blots reproduced from figure 2 show (a) RyR2 and (b) pRyR2-S2808. Samples loaded were isolated mouse CM (1), 10 µM isoprenaline perfused mouse heart CM (2), control cSR (3), CaMKII cSR (4), PKA cSR (5). All sample volumes approximated to 10,000 cells or 10 µg total protein cSR. (c) Representative normalised image of dual labelled RyR2 (red) and pRyR2-S2808 (green) in tissue sections. (d-f) Resulting images of median filtering and 80% intensity fractional threshold that were then binarised. RyR2 (red, d), pRyR2-S2808 (green, e), overlay (colocalisation appears as yellow, f). Scale bar = 2 µm.**

The pRyR2-S2808 Western blots (figure 3.1; lower blot) showed an increased signal under pharmacological stimulation (lanes 2, 4, 5). This Badrilla Ltd pRyR2-S2808 antibody has been widely verified in previous studies, most notably in the Huke and Bers (2006) paper that concluded this antibody is the most responsive to pharmacological intervention. These data in figure 3.10 show dual labelled RyR2/pRyR2-S2808 CM and tissue sections can be appropriately used for confocal microscopy. The RyR2 has been well documented at this scale previously (Baddeley *et al.*, 2009). The pRyR2-S2808 consistently showed a similar distribution and colocalised with

RyR2. These data show good agreement of pRyR2-s2808 with observed RyR2 counter-stain.

**pRyR2-S2814 Validation Summary**

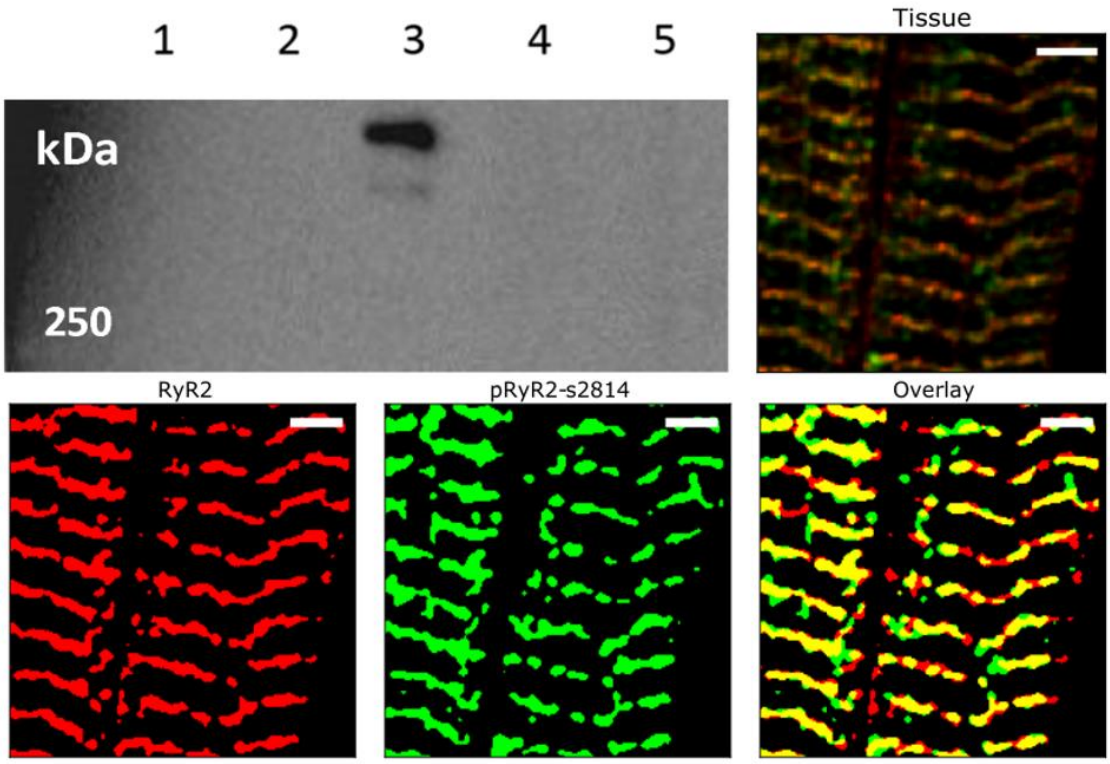


**Figure 3.11. Validation of pRyR2-S2814 for confocal microscopy imaging. Western blots reproduced from figure 3 show (a) pRyR2-S2814. Samples loaded control cSR (1), PKA cSR (2), CaMKII cSR (3), isolated mouse CM (4), 10 µM isoprenaline perfused mouse heart CM (5). All sample volumes approximated to 10,000 cells or 10 µg total protein cSR. (c) Representative normalised image of dual labelled RyR2 (red) and pRyR2-S2814 (green) in tissue sections. (c-e) Resulting images of median filtering and 80% intensity fractional threshold that were then binarised. RyR2 (red, c), pRyR2-S2814 (green, d), overlay (colocalisation appears as yellow, e). Scale bar 2 µm.**

The pRyR2-S2814 pssAb underwent the same quality checkpoints as pRyR2-S2808. Western blots were performed with the batch matched antibody used for confocal microscopy experiments (see figure 3.6). Binary masks representing RyR2 (red), pRyR2-S2814 (green), and the multiplication of these masks representing the colocalisation (yellow) consistently agreed

well with the RyR2 channel similar to Ser-2808 phosphorylation shown in figure 3.11.

**Conclusion**

A range of antibody markers generally gave good IHC results given the expected distributions of either RyR2 striations or of PLN SERCA-like meshwork. Phospho-specific antibodies agreed well with their total antibody counterparts and the signal was sensitive to pharmacological manipulation of phosphorylation. PLN and phospho-PLN require other partner antibodies, such as SERCA2a to fully validate their distribution, and the importance of these relationships. It is hoped that these PLN data encourage future studies dedicated to this highly pathologically relevant protein.

Phospho-specific RyR2 generally agreed well with the distribution of total RyR2 signal. The dephoRyR2-S2808 unfortunately did not react in the expected way to pharmacological intervention as reliably as one would have hoped for. In light of all of these factors, I decided pRyR2-S2808 was the best candidate to progress to super-resolution imaging and quantification within a biological context. pRyR2-S2814 was also deemed reliable. As pRyR2-S2808 levels are highest, it was decided that reliable comparisons to RyR2 would be the most beneficial for validation into quantitative super-resolution microscopy. Taken together with the consistent and high-quality Western blot data, the pRyR2-S2808 and pRyR2-S2814 passed the specificity validation steps and progressed to confocal quantification. These results show that pRyR2-S2808 and pRyR2-S2814 can be used for quantification of resting phosphorylation levels in control CM and tissue sections when co-immuno-labelled with total

RyR2 primary antibody for dual colour confocal microscopy experiments. pRyR2-S2808 is also a strong candidate to advance into super-resolution microscopy validation experiments.

The final aim of this series of experiments is to perform dual colour STORM super-resolution microscopy of RyR2 and pRyR2-S2808 in CM and tissue sections. This will allow the intracluster distribution of RyR2 phosphorylation to be assessed on a scale compatible with the physiological nanodomain in which it influences $Ca^{2+}$ handling and sub-cellular physiology. These results show that a range of pssAb were successful in immunofluorescence confocal microscopy experiments, including pPLN-S16, pPLN-T17, pRyR2-S2808, pRyR2-S2814, and the never previously imaged PLN total antibody. The pRyR2-S2808 pssAb represents the most appropriate candidate for super-resolution validation, as it had the greatest observable change due to pharmacological intervention. As such, chapter 4 details the quantification of pRyR2-S2808 in confocal microscopy data sets, along with the validation and quantification of pRyR2-S2808 distribution within RyR2 clusters using STORM super-resolution microscopy.

# Chapter 4

## Quantification of Ser-2808 phosphorylation distribution: Confocal and dual channel STORM super-resolution microscopy

### Introduction

RyR2 phosphorylation has been thoroughly researched, with hyperphosphorylation consistently observed in the diseased state. Whether the phosphorylation found on Ser-2808 or Ser-2814 (or the newly discovered Ser-2030) was causative or correlative, is hotly debated and discussed further in the introduction (Huke and Bers, 2008; Dobrev and Wehrens, 2014). All work has predominantly been reliant on Western blot data, often in parallel with functional isolated cardiomyocyte experiments. These data provide a rich background of information, but the spatial distribution of phosphorylation has not been investigated within RyR clusters. These data will help to educate the analysis of $Ca^{2+}$ handling experiments such as $Ca^{2+}$ sparks imaging, or in patch-clamp electrophysiology experiments on other membrane channels. Patch-clamp electrophysiology and $Ca^{2+}$ spark experiments provide valuable information.

Whilst techniques such as $Ca^{2+}$ sparks imaging and electrophysiology can test different pharmacological or disease states, they do not measure the phosphorylation status across a single cluster. Single receptor experiments have shown the changes in channel properties due to phosphorylation, but at a loss of spatial information. As such, the spatial distribution of phosphorylation on the cluster scale will be useful to provide a more detailed

context in which to assess functional data. Indeed Brandenburg and colleagues (2016) performed thorough investigations using confocal microscopy that Ser-2808 increased primarily at nodes of axial and transversely oriented T-tubules after atrial hypertrophy in isolated mouse atrial CM. Their study utilised the same pRyR2-S2808 and pRyR2-S2814 Badrilla Ltd pssAb as were used here. The experiments detailed in this chapter focus on the more widely studied ventricular CM and quantify the spatial distribution, not only using confocal microscopy but also with optical super-resolution imaging.

Huke and Bers (2008) demonstrated the potential limitations in pssAb based research. Their thorough and comprehensive comparison of three manufacturers' antibodies for serine-2808 and serine-2814 in various pharmacological conditions confirmed the reliability of the Badrilla Ltd antibodies used in this study. The motivation for this thesis was in part to help the field progress through the conflicting Western blot data published on RyR2 phosphorylation and potential mechanistic consequences (see chapter 1).

RyR2 cluster sizes vary widely, following an approximately exponentially decaying frequency RyR cluster sizes. The ever growing literature on cardiac RyR2 super-resolution data have helped to educate mathematical modelling principles and refined understanding of $Ca^{2+}$ spark experimental data (Wescott *et al.*, 2016; Galice *et al.*, 2018). Super-resolution methods have been able to measure RyR2 clusters in relation to other proteins within the clusters, such as junctophilin-2 (Munro *et al.*, 2016) . The Munro (2016) paper quantified the degree of colocalisation to show that junctophilin-2 presence inside RyR2 clusters correlated with effective stabilisation of the RyR2 cluster

behaviour in live cell recordings. Wang and colleagues (2014) used similar methods to investigate the influence of junctophilin-2 knockdown on the relative distribution of RyR2 and NCX in a tamoxifen-induced conditional junctophilin-2 knockdown mouse model. Wang *et al.,* (2014) measured the distances between RyR2 and NCX and found that the knockdown junctophilin-2 model resulted in an increased and more variable distance separation between RyR2 and NCX. Isolated rat control CM, 1 µM Calyculin A treated CM, and rat ventricular tissue sections (referred to as tissue herein) were fixed and immune-labelled for confocal microscopy in an identical manner as shown in Chapter 3.

For confocal microscopy quantification in this chapter, the images were separated by channel and each channel was converted to a 32-bit image. Firstly, each channel was normalised by subtracting the background intensity per channel and the RyR2 signal was then scaled to fil the 8-bit range (0 - 255). The scaling factor for RyR2 was then applied to the pssAb channel. The pssAb channel maximum intensities were lower than maximum RyR2 channel and so saturation was avoided, then the channels converted to 8-bit and recombined into a single RGB image. An 80% fractional threshold was used to generate binary images from normalised and median filtered images. This approach maintains the ability to compare across different cells that may have different absolute values, in a similar manner to what has been used previously (Sage *et al.,* 2005). The phosphorylation is stated as percentage of total RyR2 signal area colocalised with signal from the pssAb.

The data presented in this chapter have varied statistical properties and handled in a case dependent manner. Data presented in immunofluorescence

confocal microscopy data were approximately normally distributed between experiments. One-way Levine's univariate test of variances and hierarchical statistics were performed between animal data sets of the same type (i.e. all myocytes from animals $CM_1$ compared with all myocytes from $CM_2$ and $CM_n$) by Dr David Crossman (University of Auckland). These showed significant differences between animal experiments of all experimental types for Ser-2808 in confocal microscopy. This meant that with animal to animal variation, a hierarchical statistical test was required. The intra-class correlation coefficients (ICC) analysis was identified as an appropriate method that accounts for data sets from multiple animals having naturally differing means. ICC significance testing was performed, and p-values calculated. Null hypotheses were rejected when $p < 0.05$ (*) and differences less than $p < 0.001$ annotated (***).

The data presented in this chapter quantify RyR2 Ser-2808 and Ser-2814 phosphorylation in the context of single cell using confocal microscopy and individual RyR2 clusters using STORM super-resolution microscopy in CM and ventricular tissue sections for Ser-2808.

**Aims**

This chapter describes quantification of the spatial distribution of two pssAb in the context of the total RyR2 population. Chapter 3 outlined the methodological approaches to apply these in confocal microscopy, which was performed for RyR2 with either pRyR2-S2814 or pRyR2-S2808 for tissue sections and isolated CM. Dramatic changes were observed in in pRyR2-S2808 and so this was selected for further investigation in STORM

super-resolution microscopy. Control experiments accounts for potential differences in RyR2 clusters between tissue and control experiments along with demonstrations of limitations associated with the use of secondary antibody systems. Finally, pRyR2-S2808 was imaged with RyR2 in dual channel STORM microscopy experiments.

The aims of this chapter are:

1. RyR2 phosphorylation is of strong interest to the field and the lab. Quantitative confocal microscopy will be performed on pRyR2-S2808 and pRyR2-S2814. Initial screens showed that pRyR2-S2814 had a qualitatively larger response to pharmacological intervention and so this will progress to single channel SMLM experiments to test whether this difference is observable at the nanoscale.
2. Create custom python scripts to quantify the area and distribution of RyR2 phosphorylation. Protein cluster areas, and amount of colocalisation will be calculated based on threshold masked image analysis (see figure 2.8). This quantitation will describe how much of the RyR2 clusters are phosphorylated at Ser-2808, and how many clusters overall include a phosphorylation signal.
3. These methods will be applied to dual channel STORM microscopy of RyR2 and pRyR2-S2808 to assess any differences in Ser-2808 distribution as a result of the CM isolation procedure. This is a previously unpublished observation, yet of strong importance to those physiologists whom study the single isolated CM.

## Contributions

I performed all experiments detailed in this chapter with the assistance of others that I wish to acknowledge. All Schedule 1 procedures, cell isolation, and cell fixation or tissue cryoprotection and sectioning were performed by myself and Dr Izzy Jayasinghe (University of Leeds), Dr Alex Clowsley (University of Exeter), and Dr Ellen Green (University of Exeter). Image processing and quantification, and statistical analysis was performed by myself with the aid of Dr Ruisheng Lin (University of Exeter) and Professor Christian Soeller (University of Exeter). Advanced hierarchical statistical testing was performed by Dr David Crossman (University of Auckland).

## Immunofluorescence Based Quantification Using Confocal Microscopy

As detailed in the previous chapter, the pRyR2-S2808 and pRyR2-S2814 antibodies showed the most promise in initial testing and were progressed to confocal microscopy quantification. The immunofluorescence protocols outlined here were initially optimised for the PKA mediated Ser-2808 phosphorylation site but were also appropriate for the CaMKII mediated Ser-2814 phosphorylation site. Both pssAb were assessed across three samples; control CM, 1 µM Calyculin A CM, and tissue sections using immunofluorescence confocal microscopy. The percentage of colocalisation was quantified and the pattern of distribution assessed. I describe the distribution along T-tubules across the width of the myocyte.

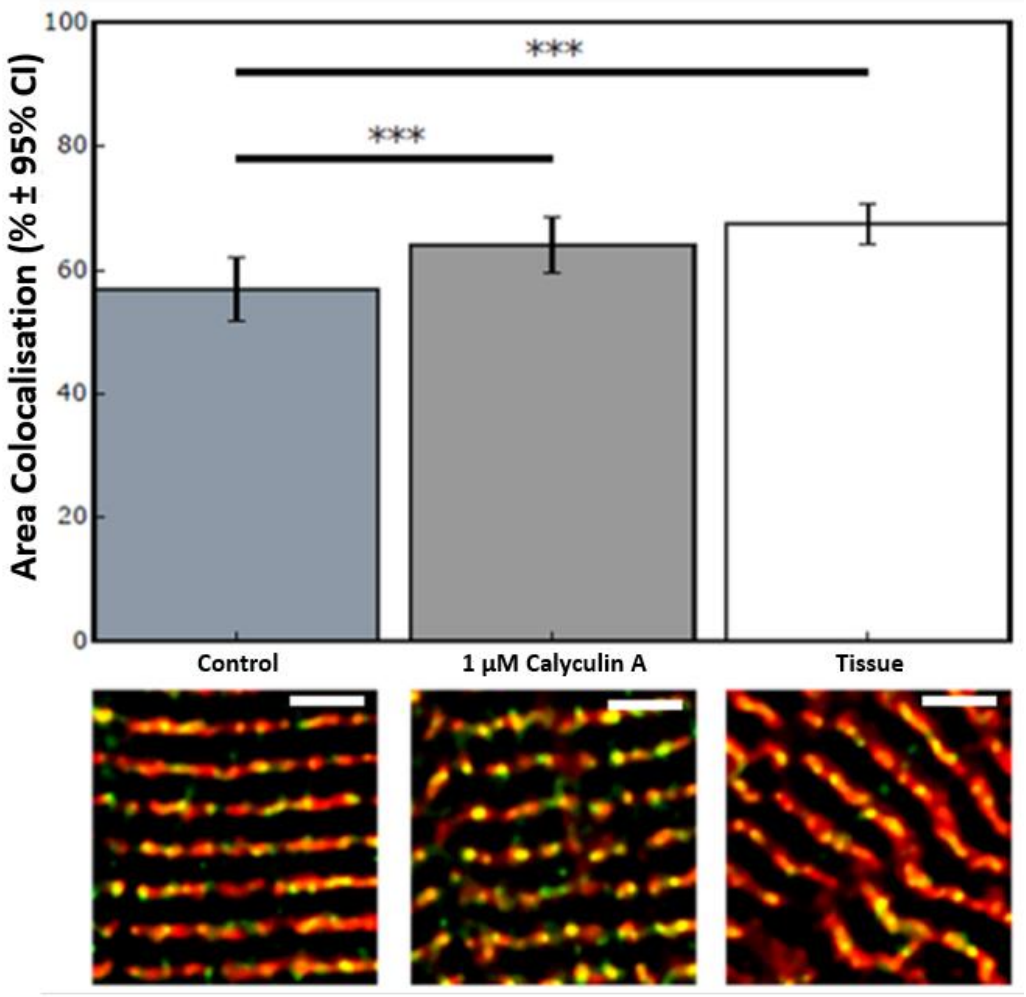


**Figure 4.1. Quantification of pRyR2-S2814 coverage by area. Bars indicate mean percentage of RyR2 area colocalised with pRyR2-S2814 (95% CI) for control CM (slate; n = 27(from 3 animals)), 1 µM Calyculin A CM (gray; n = 32(3)), tissue sections (white; n = 32(3)). Horizontal bars indicate significant differences (*** p<0.001). Representative confocal images of RyR2 (red) and pRyR2-S2814 (green) in control CM, 1 µM Calyculin A CM, and tissue sections are shown. Scale bar = 2 µm.**

The spatial distribution of pRyR2-S2814 was assessed in ventricular CM and tissue sections. Immunofluorescence confocal microscopy experiments showed a variable distribution of pRyR2-S2814 in comparison to the dual labelled RyR2. Qualitatively, the colocalisation appeared punctate in both CM and tissue sections, similar to that observed in atrial CM (Brandenburg *et al.*, 2016). Signal from pRyR2-S2814 occupied 56.8 ± 5.1% (95% CI) of total RyR2 signal area in control CM. 1 µM Calyculin A CM Ser-2814 phosphorylation significantly increased phosphorylation percentage area of

64.1 ± 4.4% (95% CI). Tissue sections had a similar pattern of colocalisation of Ser-2814 phosphorylation at 67.4 ± 3.2% (95% CI) (figure 4.1). All samples had a similar pattern of distribution. Ser-2814 phosphorylation was found in a punctate distribution spread fairly evenly along the T-tubules and throughout the cells imaged. Some portions of the RyR2 signal lacked colocalised pRyR2-S2814 signal. There was no pattern to this absence and likely reflects the probability of occurred due to the overall average of colocalised area.

The data shown in figure 4.1 suggest that RyR2 phosphorylation at Ser-2814 is modestly reduced ( -12.7%) as a result of the CM isolation procedure used in these experiments. Ser-2814 colocalisation data suggest that the reduction from CM isolation compares to tissue sections was restored by treatment with 1 µM Calyculin A.

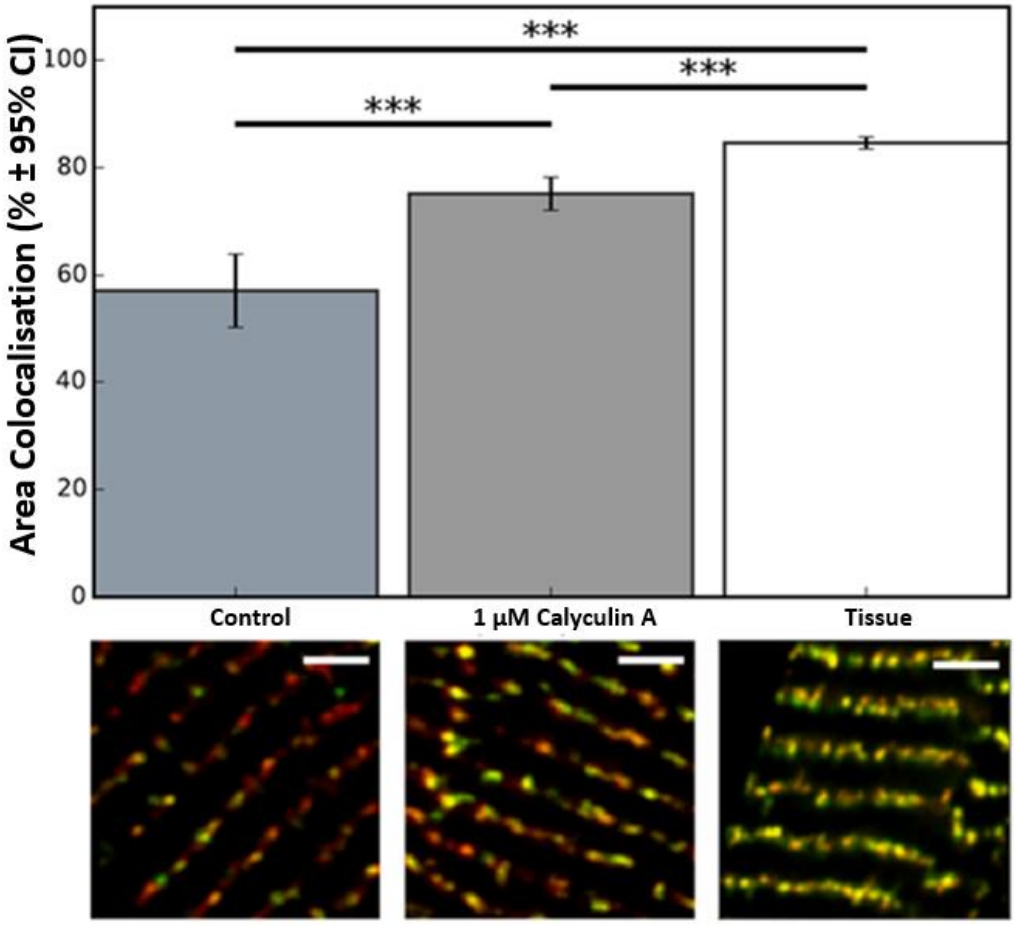


**Figure 4.2. Quantification of pRyR2-S2808 coverage by area. Bars indicate percentage of RyR2 area colocalised with pRyR2-s2808 (95% CI). For control CM (slate; n = 34(6)), 1 µM Calyculin A CM (gray; n = 40(6)), tissue sections (white; n = 47(4)). Horizontal bars indicate significant differences (*** p<0.001). Representative confocal images of RyR2 (red) and pRyR2-S2808 (green) in control CM, 1 µM Calyculin A CM, and tissue sections are shown. Scale bar = 2 µm.**

The distribution of pRyR2-S2808 was then assessed in an identical manner. There were qualitatively obvious differences between each set of samples. Control CM had a similar punctate colocalisation pattern to that observed in figure 4.1, albeit with more variability. 1 µM Calyculin A CM had a punctate pattern with more overall signal, whilst tissue sections had a near continuous colocalisation pattern. Signal from pRyR2-S2808 pssAb occupied 57.1 ± 6.9% (95% CI) of RyR2 signal area for control CM. 1 µM Calyculin A CM had an increased coverage of Ser-2808 phosphorylation to 75.0 ± 3.0% (95% CI).

Tissue sections showed an even higher percentage coverage of Ser-2808 phosphorylation at 85.6 ± 1.2% (95% CI).

These data (figure 4.2) show a more pronounced effect on phosphorylation levels and distribution pattern for Ser-2808 phosphorylation coverage (-27.5%) as compared to Ser-2814 (-10.6%). Tissue sections have a continuous or rarely broken pattern of colocalised signal. This is altered to a punctate pattern similar to that observed in Ser-2814 experiments (figure 4.1) in control CM. 1 µM Calyculin A treatment increased the area of colocalisation. The area of colocalisation below that of tissue sections and was still punctate, but to a lesser extent.

Unlike Ser-2808, when the area of colocalisation from Ser-2814 was fully restored to the levels observed in tissue sections by treatment with the phosphatase PP2a inhibitor 1 µM Calyculin A. Recent immunofluorescence confocal microscopy of pRyR2-S2808 and pRyR2-S2814 in isolated atrial CM show a punctate phosphorylation distribution similar to that reported in figures 3.1 and 3.2 (Brandenburg *et al.*, 2016). The colocalisation areas reported here are focused on the spatial distribution. One must remember that the stoichiometry of phosphorylation may vary from zero to four per RyR. Nevertheless, these data represent a global view of phosphorylation distribution in the t-tubule regime and provide insights into EC coupling physiology and show that Ser-2808 and Ser-2814 are non-uniformly phosphorylated in CM. Additionally, Ser-2808 and Ser-2814 phosphorylation had different patterns of distribution (continuous versus discrete, respectively) in tissue sections.

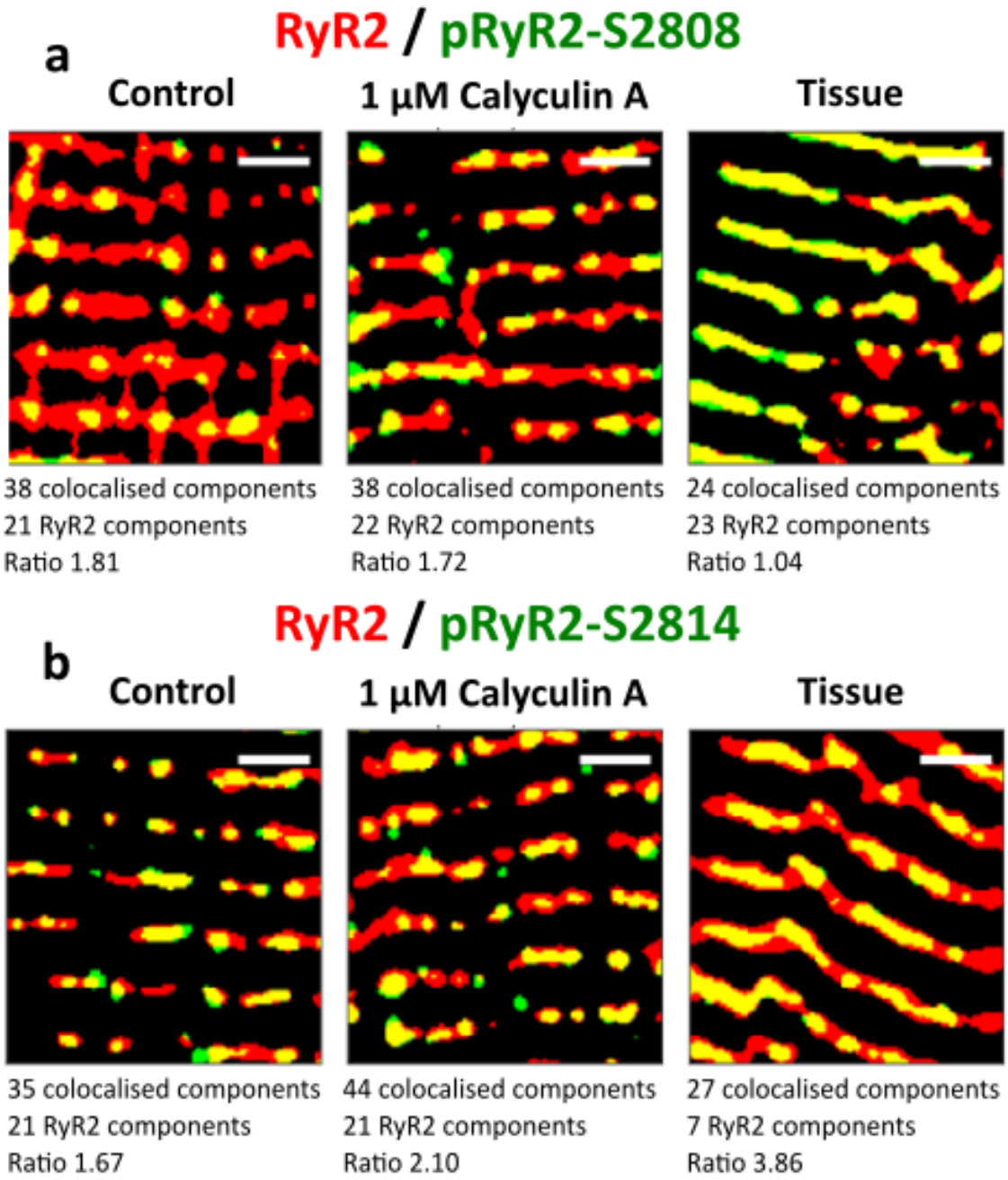


**Figure 4.3. Example binarised images of RyR2 (red), pssAb (green), and colocalised phosphorylation (yellow) of pRyR2-S2808 (a) or pRyR2-S2814 (b) in Control CM, 1 µM Calyculin A CM, or tissue sections. Scale bar = 2 µm.**

On inspection of the binarised masks of RyR2 and pRyR2-S2808 there was an observed difference in the pattern of signal colocalisation. Control CM and 1 µM Calyculin A CM had a punctate, discrete distribution of phosphorylation, whereas tissue sections had a continuous colocalisation pattern. Distribution

of pRyR2-S2814 signal had a similar discrete, broken pattern of phosphorylation across all sample types.

A ratio was calculated of the number of colocalised (yellow) clusters to number of RyR2 clusters, where pssAb clusters with no colocalisation were not counted. A ratio above 1 reflects a one-to-many relationship of RyR2 clusters to pssAb colocalisation. A ratio close to 1 reflects an even, continuous colocalisation distribution. This observation is also consistent with the observations of another study using the same antibodies to measure phosphorylation in atrial CM (Brandenburg *et al.*, 2016). Significant differences were found between all pRyR2-S2808, reflecting significant differences between overall percentage area colocalisation. No significant differences were detected between any of the pRyR2-S2814 samples. As changes in this ratio for pRyR2-S2808 reflected the total area colocalisation, these two metrics were plotted against each other to assess whether there was any relationship between them.

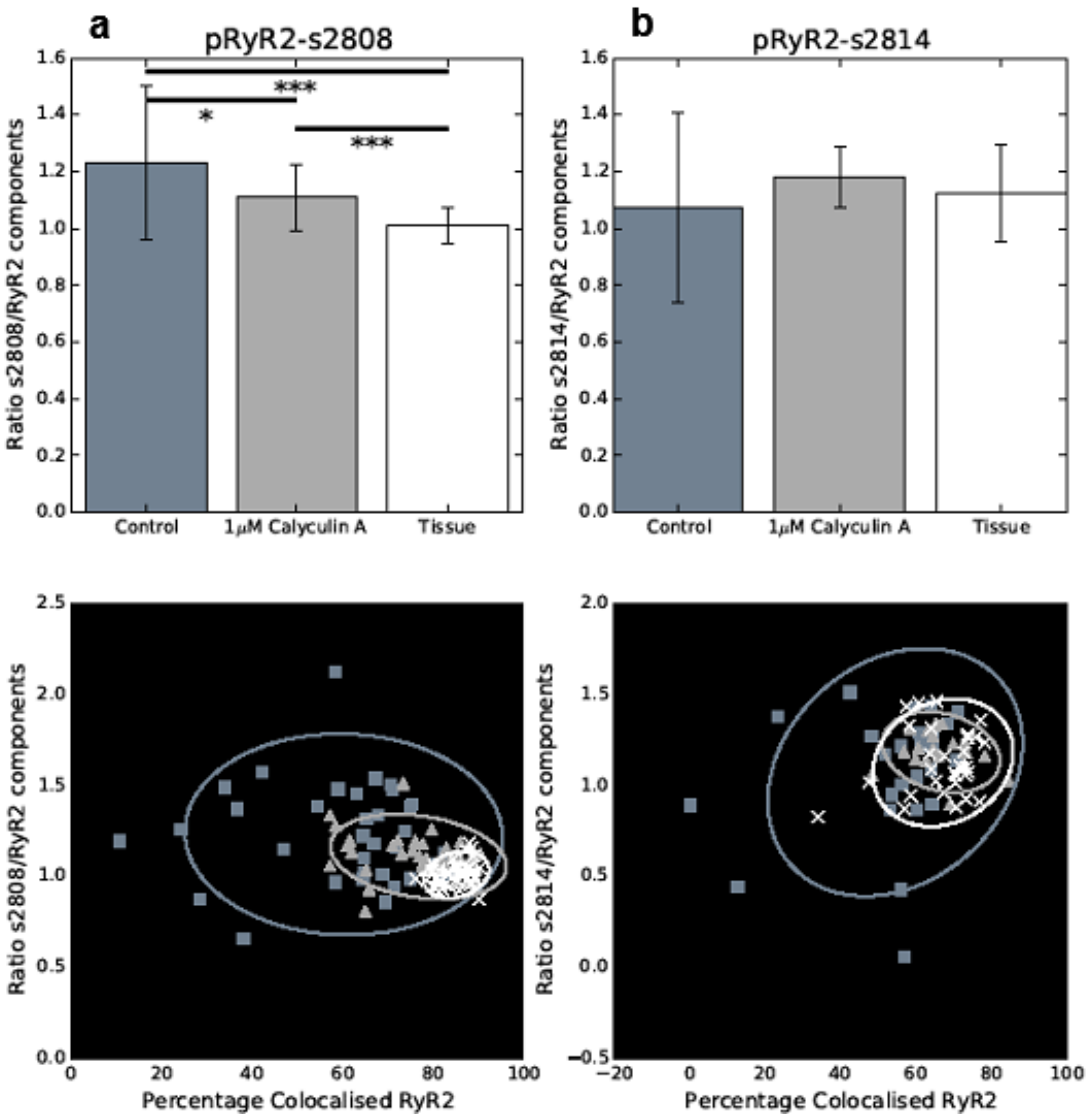


**Figure 4.4. Comparison of total phosphorylation and pattern of distribution. Bar charts show the ratio of discrete colocalised components to RyR2 components (control CM (slate), 1 µM Calyculin A CM (gray), and tissue sections (white) from pRyR2-S2808 (a) and pRyR2-S2814 (b) of data shown in figures 3.1 and 3.2. Horizontal bars indicate significant differences (* p<0.05, *** p<0.001). Scatter plots show results of each individual image with the percentage colocalisation versus component ratio for control CM (slate squares), 1 µM Calyculin A CM (gray triangles), and tissue sections (white crosses). Ellipses represent 95% confidence intervals.**

The pattern of distribution described in figure 4.3 was quantified by calculating the ratio of colocalised clusters to RyR2 clusters. In a theoretical case of 100% colocalisation, this ratio would be 1.0. If the phosphorylation was uniform, and effectively represented an erosion of the colocalised mask, then this ratio would be conserved. Ratios above 1 indicate at RyR2 have on

average have more than one colocalised component. A single RyR2 striatum with two discrete areas of colocalisation would have a ratio of 2.0, etc. Data in figure 4.4 shows a significant difference in component ratios between all three pRyR2-S2808 samples, similar to the differences in area of Ser-2808 colocalisation (unpaired two-way T-test). No significant difference was found between any of the pRyR2-S2814 samples.

Taken together, figures 4.1-4.4 show that the Ser-2808 is more dramatically affected by the isolation procedure. The amount of Ser-2808 phosphorylation reduced by -27.5% of total RyR2 compared with tissue sections. This can be considered as the effect of the isolation procedure when considered as an intervention. The pattern is significantly altered from continuous and even phosphorylation to discrete puncta. Ser-2814 phosphorylation was reduced by 12% of total RyR2. Ser-2814 retained the same level of punctate phosphorylation distribution, evidenced by no significant difference between ratios. These data suggest that PKA mediated Ser-2808 phosphorylation is more affected by the isolation procedure compared to Ser-2814.

**Super-Resolution STORM Microscopy**

STORM super-resolution microscopy is one type of SMLM microscopy. SMLM relies on the activation of only a subset of fluorophores per image, and many images taken in quick succession. These data can be projected to produce a widefield microscopy image. SMLM takes advantage of the fact that a diffraction limited spot of light originating from a single fluorophore follows a Gaussian distribution of intensity. By fitting a Gaussian function to the fluorophore's signal (event) the true position of the fluorophore can be

estimated. STORM requires high signal intensity with as low background as possible. High signal-to-noise ratio results in a higher precision in estimating the localisation. STORM gives an approximately 10-fold increase in resolution, dependent upon sample optical thickness and experimental performance.

RyR2 have been studied rather extensively in super-resolution using SMLM techniques and other super-resolution microscopy techniques, such as stimulated emission depletion microscopy (STED). STED can be considered as a super-resolution confocal microscope. RyR2 has been shown to assemble into clusters with an exponential decay size-frequency distribution and can be found in 'super-clusters', or calcium release units (CRU) (Baddeley *et al.*, 2009; Hou *et al.*, 2015). CRU are functionally coupled RyR2 clusters that are of interest in terms of CICR. The ability to resolve cluster architecture will provide new insights into $Ca^{2+}$ cycling behaviours. Additional studies have quantified the relative distribution of RyR2 with other targets of interest, such as actin bundles, caveolin-3, and junctophilin-2 (Jayasinghe *et al.*, 2012; Wong *et al.*, 2013; Hou *et al.*, 2015; Munro *et al.*, 2016).

Confocal microscopy experiments pRyR2-S2808 resulted in a wider range of colocalisation by area between samples, from 57.1% control CM to 87.6% in tissue. This range provided a test case to show that the pRyR2-S2808 pssAb reports the coverage of Ser-2808 phosphorylation at the super-resolution level, like that shown in the confocal microscopy data (figure 4.1-4.4).

STORM super-resolution microscopy results in many measures per image, rather than one per image for the confocal microscopy experiments. Each image underwent similar image processing with a fractional threshold applied (80% for RyR2, 65% for pRyR2-S2808) and then binary image masks

produced per channel (Baddeley *et al.*, 2009; Baddeley *et al.*, 2010). Binary image masks underwent a connected components labelling step. This applies an unique identifying label to each discrete area of binary signal, reflecting individual clusters. Four metrics were measured per component using a PYME based *recipes* protocol to perform measurements (see www.python-microscopy.org for further information). Python scripts were used to analyse whole data sets based on the *recipes* outputs as a series of measures per cluster for each individual image. Initial single channel STORM microscopy image analysis focused on RyR cluster sizes, with the remaining measures developed for analysis of dual channel experiments. The measures reported here are:

1. Median RyR cluster size was based on the assumed lattice-like arrangement of RyR2 receptors observed by electron microscopy experiments in clusters from purified RyR2 in lipid bilayers and its approximate size of 30 by 30 nm in x,y (Wagenknecht *et al.*, 1989; Yin and Lai, 2000). Cluster sizes follow a highly right skewed distribution. As such the median is the most appropriate metric for comparing RyR cluster size.
2. Total fraction of colocalisation measured what fraction of the population of clusters appeared to have signal above the relevant thresholds from both channels. The lower limit of this was set at 5%. This is not equivocal to the confocal microscopy data's mean total coverage, as the total fraction includes any cluster that has more than 5%. In theory, if every cluster was colocalised by 6% area, the total fraction would equal 1. This measure describes the proportion of RyR2 clusters that

undergo phosphorylation events in the given biological states. As such this is a key descriptor of the spatial distribution of RyR2 phosphorylation events on Ser-2808. These data were not skewed and so a mean was reported.

3. The clusterwise fraction of colocalisation measure is complementary to the total fraction. It measures the mean percentage of colocalisation in a similar fashion to that performed on the confocal microscopy data, on a per component/cluster basis. These data were then averaged (mean) to give the mean amount of colocalisation within those clusters that had colocalised signal. For the purposes of this chapter, these measures did not include RyR2 clusters. This removed the influence on the mean of non-colocalised clusters, as their fraction is equal to 0 and the total fraction showed this was a considerable proportion. These data were not skewed and so a mean was reported.
4. Median distance from reference masks. Thresholding to binary image masks may appear as an all-or-none descriptor of colocalisation, for signal from 5 nm (one-pixel size) outside of that boundary is classed as non-colocalised. The signal from pRyR2-S2808 outside of this mask could either have come from the same cluster, or elsewhere. The distance metric measured the distance of every pixel in the colocalised channel from the edge of the reference channel mask. All pixels within the boundary were set to 0 nm to prevent negative distances of pixels within the cluster. The lower the value, the closer the non-colocalised pRyR2-S2808 is from the RyR2 channel. Low values would support the working assumption that the antibodies report Ser-2808

phosphorylation and that the pRyR2-S2808 signal is most likely coming from the same cluster. Very large distances would suggest pRyR2-S2808 signal far away from RyR2 signal, and more likely reflect pRyR2-S2808 signal coming from either antibody binding to other structures, or RyRs without the RyR2 co-label. This measure when pRyR2-S2808 was the reference mask gleans insight into the pattern of phosphorylation within the RyR2 cluster. For example, fully phosphorylated RyR2 clusters would give a value close to zero, whereas a central core of phosphorylation would have a distance of the radius of RyR2 cluster minus radius of pRyR2-S2808 cluster. These distances followed a highly right skewed distribution and so median was reported.

**Single Channel STORM Super-Resolution Microscopy**

Prior to progressing to dual channel STORM super-resolution microscopy experiments, the RyR2 and pRyR2-S2808 were first validated and quantified in single channel STORM experiments. These were performed in peripheral clusters in control and 1 µM Calyculin A CM. Peripheral clusters are essentially 2-dimensional and the closest RyR2 to the coverslip, resulting in minimal refraction of the signal as it passes through the media to the objective (Hou *et al.*, 2015). Additionally, peripheral clusters directly oppose the sarcolemma by approximately 10 nm and so are also indirectly of interest to the patch-clamp electrophysiology field (Fawcett and McNutt, 1969; Soeller and Cannell, 1997). Single channel STORM experiments were used to test

whether 1 µM Calyculin A treatment altered the cluster size distribution of pRyR2-S2808 compared to control CM.

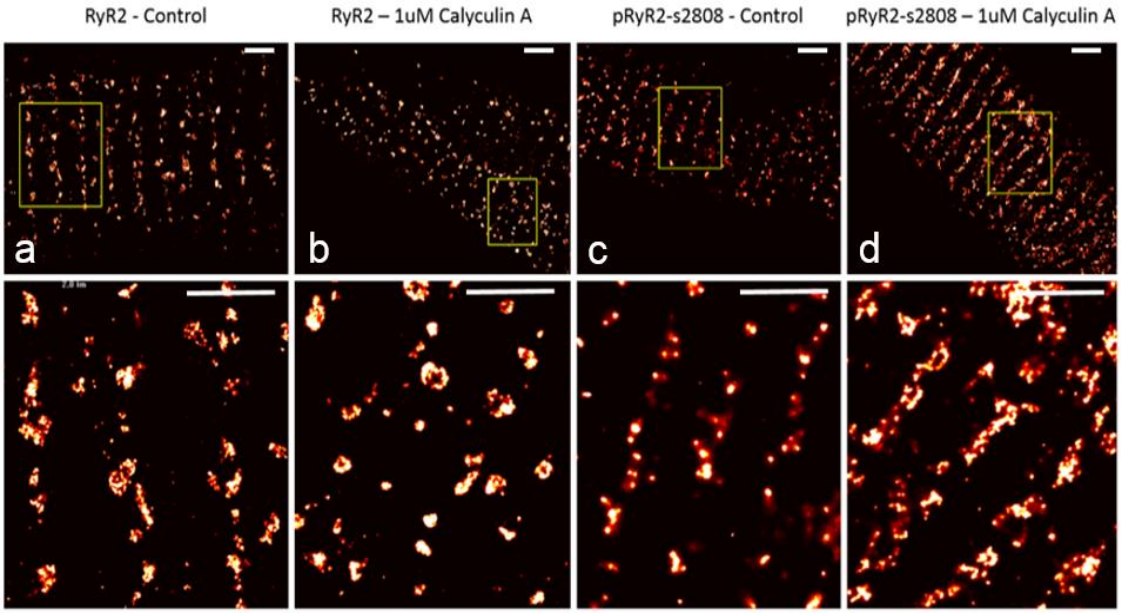


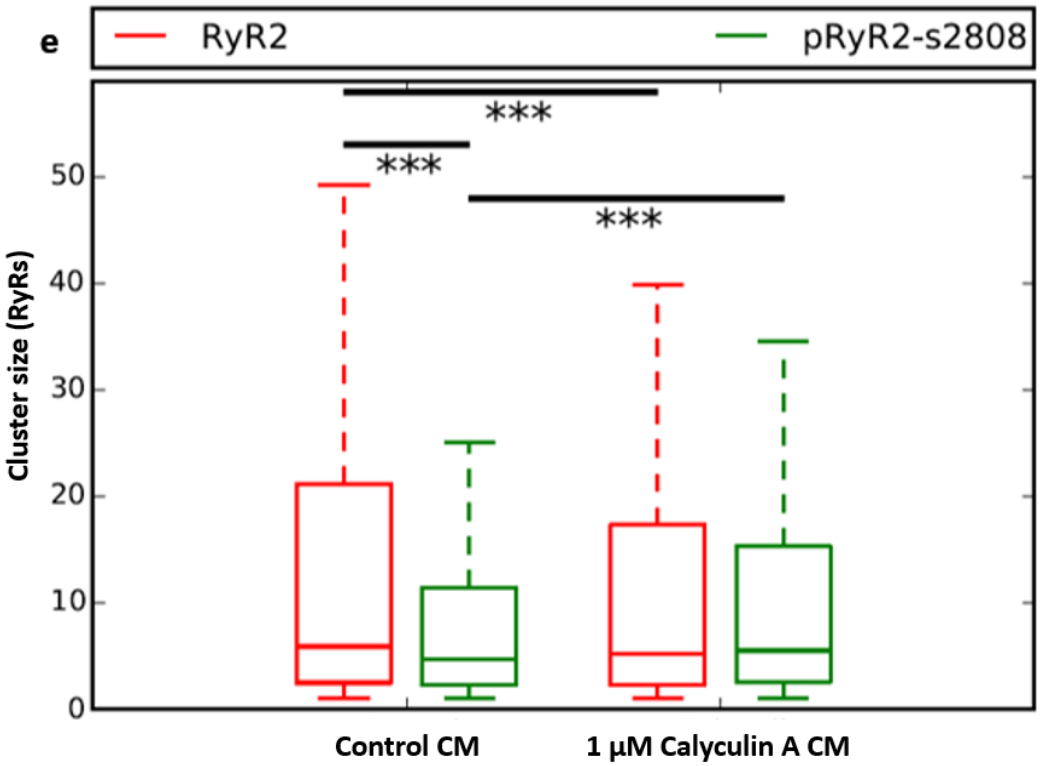


**Figure 4.5. Representative single channel STORM super-resolution images of peripheral RyR2 in control CM (a, n = 33(4)) and 1 µM Calyculin A CM (b, n = 34(4)). Peripheral pRyR2-S2808 clusters in control CM (c, n = 24(4)) and 1 µM Calyculin A CM (d, n = 34(4)). Scale bar = 2 µm. Box plots (e) represent the median (horizontal), interquartile range (box) and flyers of cluster sizes for RyR2 (red) and pRyR2-S2808 (green) in control CM and 1 µM Calyculin A CM (right). Horizontal bars indicate significant differences (*** $p < 0.001$) tested using a Mann-Whitney-U test.**

Peripheral RyR2 have consistency with previously published data from our group (mean of medians were control CM = 5.9 RyRs, 1 µM Calyculin A CM = 5.2 RyRs $p < 0.05$) whether these differences are physiologically relevant is not determinable by these experiments. There is very limited emerging data suggested RyR2 phosphorylation re-organises RyR2 channels within clusters using correlative $Ca^{2+}$ Spark line scan confocal microscopy and EM tomography (Asghari *et al.*, 2018). This emerging question will need further experimentation, and these data should not be used to draw strong conclusions on this.

Peripheral clusters labelled with pRyR2-S2808 were smaller in control CM (median = 4.75 RyRs) and increased in size in 1 µM Calyculin A CM (median = 5.5 RyRs) $p < 0.05$. Peripheral 1 µM Calyculin A CM pRyR2-S2808 clusters sizes were not significantly different to 1 µM Calyculin A CM RyR2 cluster sizes, suggesting they had maximal, or near maximal coverage of phosphorylation.

These data show a highly right skewed distribution of data for both RyR2 previously published (Baddeley *et al.*, 2009). The cluster sizes for pRyR2-S2808 followed the same pattern of distribution. As such the medians and inter-quartile ranges were measured. These measures are appropriate for this distribution (Krzywinski and Altman, 2014). Measures in the literature are often reported as means, making comparisons to the literature inaccurate. However, these RyR2 images were consistent with previous data published by this lab. Data presented in figure 3.6 has been clipped to show 95 % of the cluster sizes, but it should be noted that the vast majority of individual images had clusters in excess of 1000 RyRs. This extreme skew may also explain

why the means cited in literature are often closer to 60 – 100 RyRs as the median is unaffected by the higher values (Baddeley *et al.*, 2009; Hou *et al.*, 2015).

I have elected not to supply the mean alongside this to allow direct comparison as I do not want to tempt the reader to focus on the mean and discard the median values. Whilst medians appear to be similar in these data (figure 4.5e), ranges reflect the significant differences, especially in control CM versus 1 µM Calyculin A CM pRyR2-S2808.

Comparisons using medians alone may prove subtle, and so ranges, inter-quartile range, or confidence intervals are recommended (Wulllschleger *et al.*, 2014). Indeed, undue focus on single measures should be avoided by the inclusion of a range. There is a shift in the biomedical field to this practice, which is more widespread in clinical research (Hazra, 2017). The pRyR2-S2808 gave clear RyR2-like patterns of labelling and were judged to be consistent with the total RyR2 images for quality of labelling and so could progress further to two-channel STORM super-resolution microscopy.

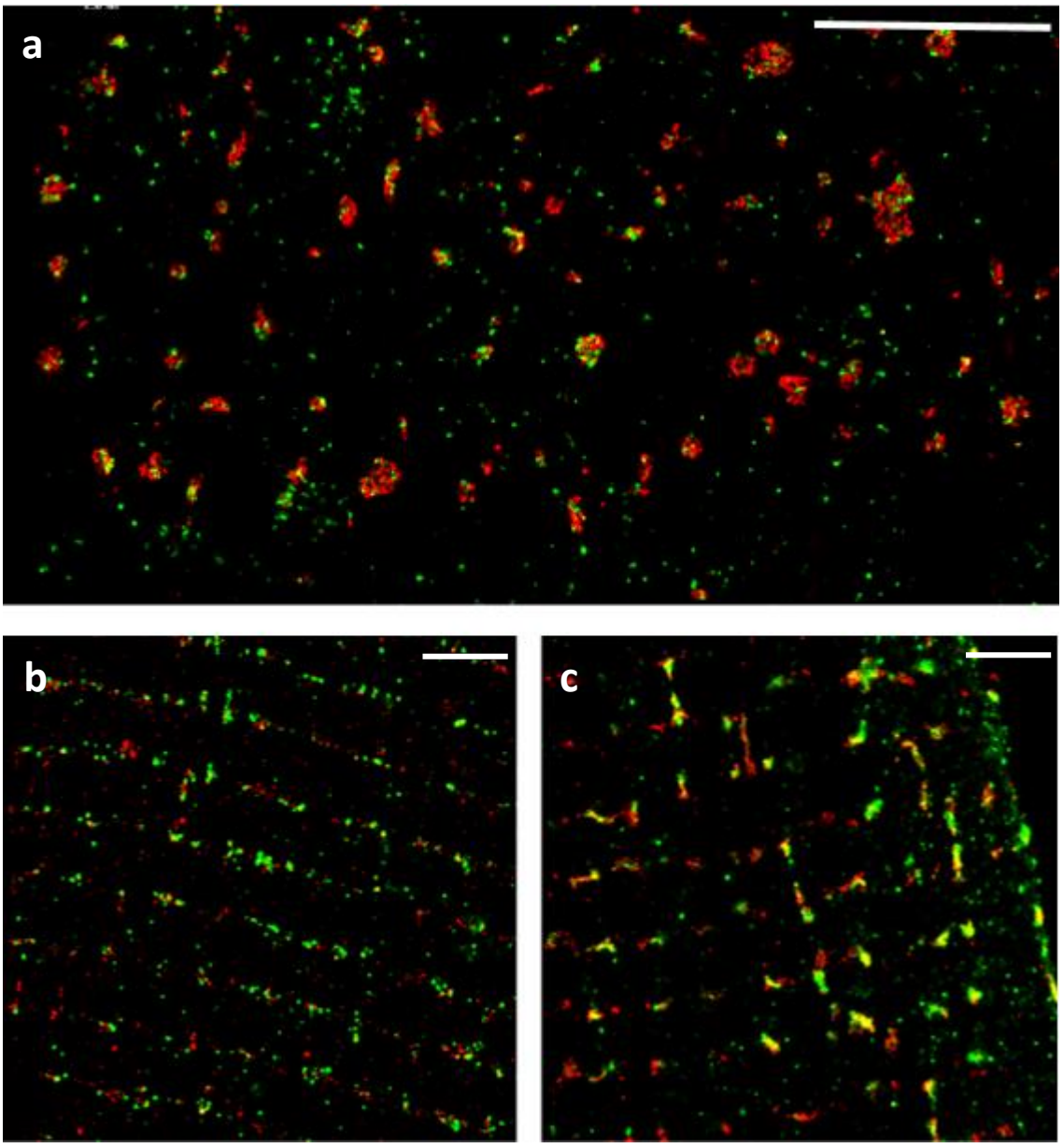


**Figure 4.6. Example images showing limitations in the dual channel STORM approach. (a) Dual channel STORM super-resolution microscopy image of peripheral RyR clusters. RyR2 (red) labelled with Alexa-647 and pRyR2-S2808 (green) labelled with Alexa-700. (b) RyR2 anti-mouse 700 (red) pRyR2-S2808 anti-rabbit Alexa 647 (green) imaged deep into 1 µM Calyculin A CM. (c) RyR2 anti-mouse Alexa 647 (red) and pRyR2-s2808 anti-rabbit Alexa 700 (green) imaged deep into control CM with edge of cell visible. Scale bars = 2 µm.**

The next experiments combined the mouse anti-RyR2 and rabbit pRyR2-2808 antibodies to perform dual channel STORM experiments. Our methods utilise two sets of fluorophores for each primary antibody that can be excited with the same 642 nm laser, in this case Alexa 647 and Alexa 700. A beam splitter device separated the emitted light at approximately 710 nm and these were

imaged onto separate parts of the same camera chip. The emitted light pathway was calibrated with fluorescent beads prior to each experiment to correct for this physical separation of the light. The reconstructed image could then be created. Near cross-talk free reconstruction of the two channels was achieved by assignment of events to one of the two dye species and subsequently rendered with the standard methods used for single channel image (for further details see Methods).

Peripheral RyR clusters were labelled for RyR2 (anti-mouse Alexa 647, red) and pRyR2-S2808 (anti-rabbit Alexa 700, green). Green pRyR2-S2808 puncta appeared distal to total RyR2 more frequently than colocalised with RyR2 (red) signal. The pRyR2-S2808 clusters distal to RyR2 were indistinguishable in shape and size compared with those colocalised with RyR2 (figure 4.6a). Additionally, they did not appear like the single channel pRyR2-S2808 images (figure 4.5) using the anti-rabbit Alexa 647 secondary antibody. A second batch of secondary anti-rabbit Alexa 700 antibody was tested and produced similar results.

Figure 4.6b shows the unsatisfactory experimental results in testing a new anti-mouse Alexa 700 conjugated secondary antibody. In these experiments the RyR2 signal was poor, most likely due to a failure of that particular batch of secondary antibody. This was repeated on several samples. Parallel experiments were performed with the mouse anti-RyR2 and rabbit pRyR2-S2808 been applied from a common stock, before the two colours (Alexa 647 and Alexa 700) being applied for both combinations. The Alexa 647 anti-mouse gave a strong signal (figure 4.6c) deep into CM whilst this was absent with Alexa 700 anti-mouse (figure 4.6b). These experiments were

performed on CM from the same isolation with a common primary antibody solution, indicating a fault with the Alexa 700 anti-mouse and not the primary antibodies.

Imaging deep into the cells in dual channel STORM showed that the fidelity was greatly improved in deep optical sections, compared with peripheral clusters. It was noted that the membranes often have some pRyR2-S2808 Alexa 700 signal distal to the RyR2 Alexa 647 signal. This can be seen on the right edge of the cell in figure 4.6c. These results show a difficulty in dual labelling of peripheral RyR clusters, when compared with the deep RyR clusters. Additionally, tissue sections do not have the peripheral clusters accessible due to the random level of sectioning and their encasement into the extracellular matrix. As such, deep RyR clusters were measured for confidence of labelling and to allow even comparison between CM and tissue sections.

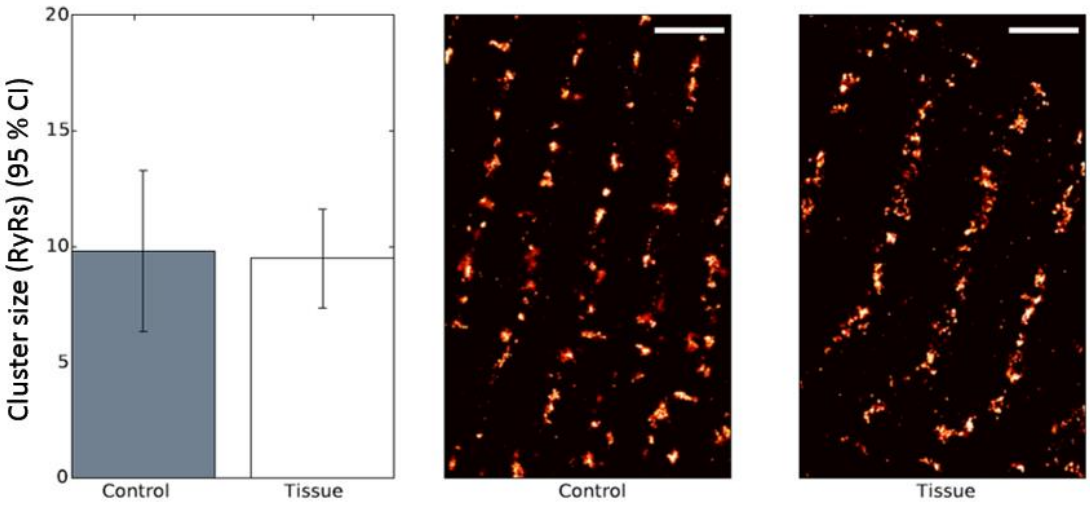


**Figure 4.7. Super-resolution STORM area based size analysis of deep RyR2 clusters of control CM compared to tissue sections. Bars show average median (95% CI) RyR2 cluster size for control CM (n = 19(4)) and tissue sections (n = 24(4)). Example STORM super-resolution images of RyR2 clusters for control CM and tissue sections are shown. Scale bar 2 µm.**

Before progressing to dual channel STORM experiments in deep RyR clusters, single channel RyR2 STORM experiments were performed using Alexa-647. These experiments had a similar motivation to the single channel peripheral clusters. These experiments also allowed for a comparison between isolated CM and tissue sections and whether the RyR2 cluster morphology was different. Control CM (average median = 9.9 RyRs) and tissue sections (average medians = 9.8 RyRs) had no significant difference in RyR2 cluster sizes (figure 4.7). This experiment showed that the isolation procedure does not alter RyR2 morphology when compared to tissue sections. Prior measurements of RyR2 cluster sizes have been used interchangeably between tissue sections and CM. These data show that this is an acceptable approach for the future.

**Dual Channel STORM Super-Resolution Microscopy**

The results detailed in the chapter so far have demonstrated the gross distribution of pRyR2-S2808 signal appears continuous for tissue sections, and discrete in control CM and 1 µM Calyculin A CM, when imaged with confocal microscopy (figure 4.2-4.4). RyR2 and pRyR2-S2808 antibodies were shown to give a consistent RyR-like signal with the previously categorised shape of cluster size distribution (figure 4.6). A sampling method was developed to allow comparisons between confocal data and to avoid aberrant labelling on CM cell surfaces by imaging the deep RyR clusters. A dye pair of Alexa 647 and Alexa 700 were shown to work well together to produce a dual channel super resolution image (figure 4.6). Deep RyR clusters were shown to be comparable between control CM and tissue (figure 4.7). This allowed for direct comparisons between the spatial distribution of pRyR2-S2808 in deep RyR clusters. The four key measures outlined in this chapter were taken for control CM, 1 µM Calyculin A CM, and tissue sections from dual channel STORM images (figures 4.8 – 4.11).

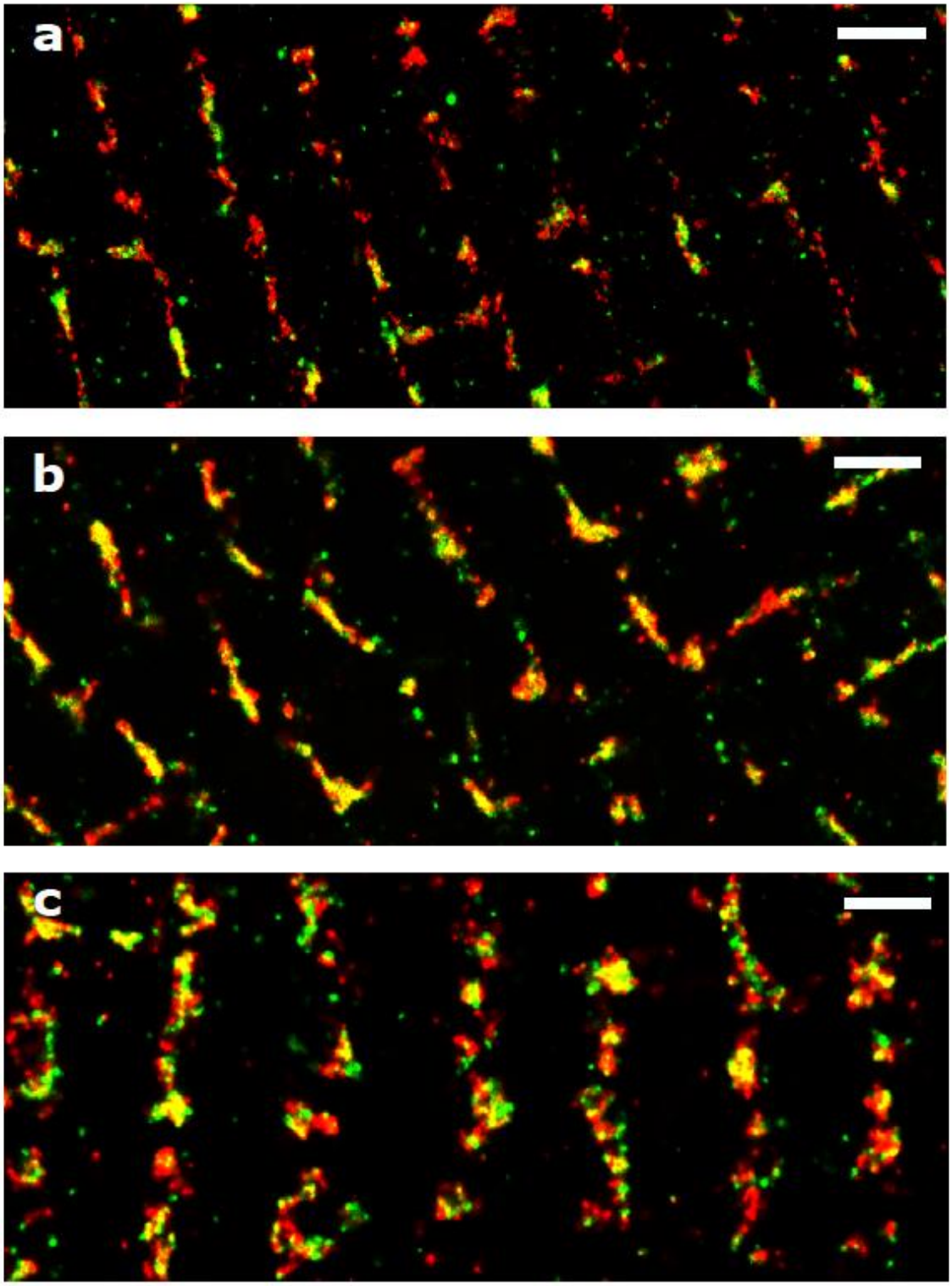


**Figure 4.8. Representative dual channel STORM super-resolution microscopy images for control CM (a), 1 µM Calyculin A CM (b), and tissue sections (c). RyR2 (red) was labelled with Alea-647 and pRyR2-S2808 (green) was labelled with Alexa-700. Scale bar = 2 µm.**

Dual channel STORM images of deep RyRs labelled with RyR2 and pRyR2-S2808 showed an RyR-like distribution of both signals similar to the single channel deep RyR images shown in figure 4.7. On visual inspection,

signal from pRyR2-S2808 agreed well with RyR2 (figure 4.8). Signal from pRyR2-S2808 was observed across a subset of RyR2 clusters. Visually, the pattern of colocalisation appeared varied between clusters in each set of samples. Qualitative assessment of control CM appeared to have noticeably less colocalisation than 1 µM Calyculin A CM and tissue sections.

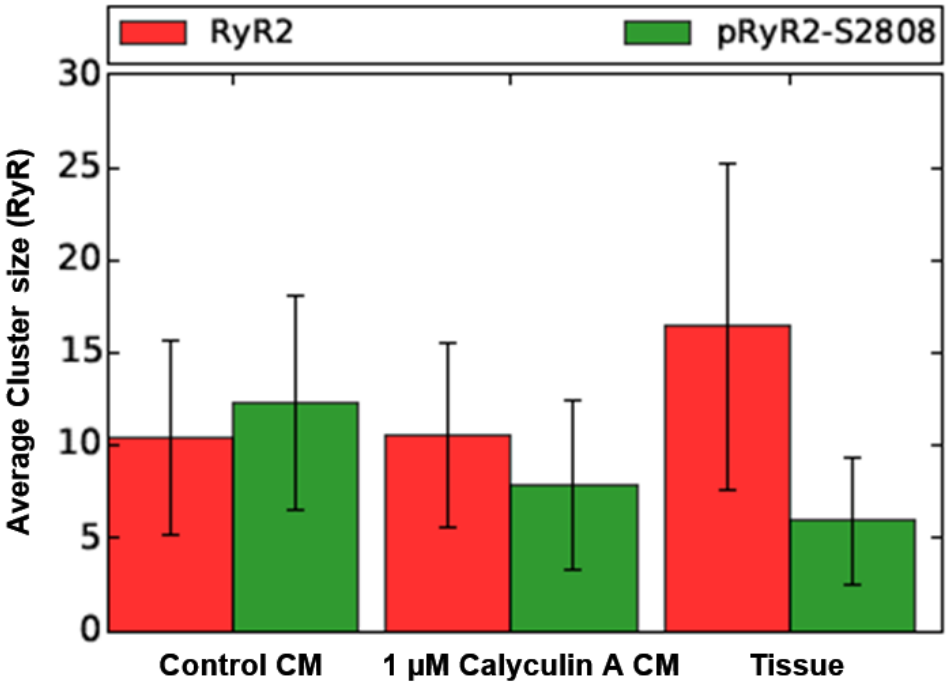


**Figure 4.8. Quantification of RyR cluster sizes using STORM microscopy of Control CM (n = 25(4)), 1 µM Calyculin A CM (n = 23(4)), and tissue sections (n = 29(4)). Average median (SD) RyR2 (red) and pRyR2-S2808 (green) cluster size (RyRs).**

Median cluster sizes were measured and the mean of these medians was calculated (termed average median) with standard deviation (SD) to reflect the variability between images and animals. There is currently no statistical consensus on pooling medians. Some studies transform the medians to estimates of means for pooling, whilst others discount medians from meta-analyses. Median values were not skewed per sample and so SD of the medians was used appropriately to describe the average median RyR cluster size.

Average median (SD) RyR2 cluster sizes were similar between Control CM (10.4 ± 5.2 (RyRs (SD)) and 1 μM Calyculin A CM (10.5 ± 5.0 (RyRs (SD)). Average median RyR2 cluster sizes for tissue sections were increased, at 16.4 ± 8.8 (RyRs (SD)). This increase was not observed in single channel experiments (figure 4.7) and is not readily explained. This is an experiment that requires some more development to rule out possible causes of bias, such as off-parallel tissue section preparation, day to day differences in switching buffer performance, and differences in imaging set ups between single channel and dual channel.

Cluster sizes of pRyR2-S2808 were markedly different for each sample. Despite the observably lower amount of pRyR2-S2808 clusters in Control CM samples, their average median cluster size was 12.3 ± 5.8 (RyRs (SD)). On inspection of the data, Control CM images appeared to agree with these data. Cluster sizes for pRyR2-S2808 in 1 μM Calyculin A CM were 7.9 ± 4.5 (RyRs (SD)) and tissue sections was 6.0 ± 3.4 (RyRs (SD)).

These data for pRyR2-S2808 cluster sizes broadly agree with either RyR-like clusters or subsets of RyR2 clusters. However, these measures did not describe the influence of RyR2 clusters that were totally non-phosphorylated. For readers more familiar with Western blot data that expresses the amount of phosphorylation at Ser-2808 as a fraction of all of total RyR protein, the total fraction metric is not analogous. Cluster size is an informative metric, but to contextualise it, the fraction of clusters that had colocalised signal denoting phosphorylated clusters, and the average fraction area of each cluster that was colocalised were calculated.

The reduction in 1 µM Calyculin A clusters in both RyR2 and pRyR2-S2808 was interesting. Recent findings have suggested that isoproterenol rearranges the RyRs within a cluster (Asghari *et al.,* 2018). This could result in differences in segmentation of RyRs and so observed smaller clusters. The reduction of phosphorylation in these samples would reflect this but mean that a smaller pRyR2-S2808 cluster could account for a higher fraction of colocalisation. Additionally, the measurement here is an averaged median. As such, the emergence of many single phosphorylated RyRs plus decreased total RyR2 cluster sizes would shift this value smaller, despite more overall phosphorylation. An analogy for this is if the median size of the 8 major islands in Hawaii is between 673.4 $km^2$ of Moloka and 1430.5 $km^2$ of Kaua'i. If we were to include the remaining 129 small islands however, the median would be much smaller, despite a larger land mass in total being studied. In the same way, control CM with fewer, but larger pRyR2-S2808 clusters being compared to 1 µM Calyculin A CM with more overall phosphorylation but including many smaller clusters.

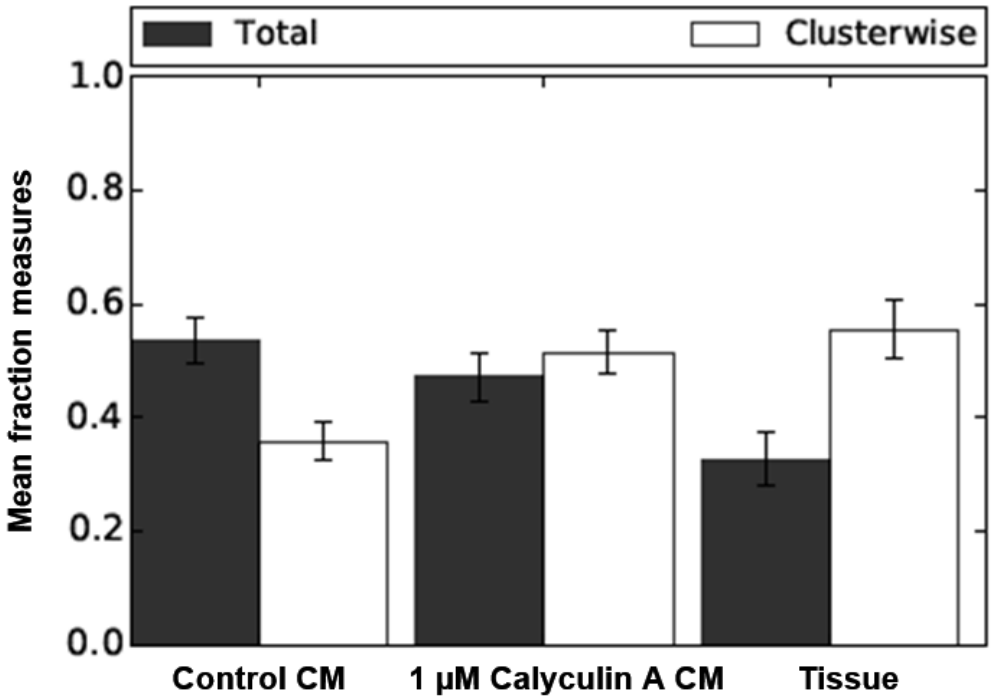


**Figure 4.9. Fraction colocalisation measures using STORM microscopy of Control CM (n = 25(4)), 1 µM Calyculin A CM (n = 23(4)), and tissue sections (n = 29(4)). Mean (95% CI) total fraction of RyR2 clusters that were phosphorylated (>5%, black bar) and the mean (95% CI) cluster-wise fraction of colocalised clusters (white bar) are shown.**

These cluster size data were placed into context by measuring what fraction of the total RyR2 cluster area was colocalised, termed clusterwise fraction. Clusters with more than 5% area colocalisation were included in this analysis and shown as black bars in figure 4.9. For example, the full population of RyR2 (fraction = 1.0) have a median cluster size of 10.4 ± 5.2 (RyRs (SD)). The fraction of RyR2 deemed to be phosphorylated was 0.54 ± 0.04 (95% CI). The median pRyR2-S2808 cluster size of 12.3 ± 5.8 (RyRs (SD)) is only applicable to this 0.54, and the remaining 0.46 were considered as 0 and discounted from the calculation. The mean clusterwise area of colocalisation was calculated as 54%. For Control CM the mean fraction of clusterwise area of colocalisation was 0.33 ± 0.05 (95% CI). The fractions calculated here were not skewed and so 95% confidence intervals (95% CI) were calculated. 95%

CI reflect the range of values that means would be expected to fall in 95% of the time if these experiments were repeated.

Control CM had a mean total fraction of 0.56 ± 0.04 RyR clusters phosphorylated. The Control CM clusterwise fraction measure showed that these clusters were phosphorylated on average by 0.33 ± 0.05 of the area of the clusters. The mean total fraction of RyR clusters phosphorylated in was increased by the treatment with 1 µM Calyculin A to 0.47 ± 0.04 (95% CI). The mean fraction of clusterwise colocalisation was increased by treatment with 1 µM Calyculin A to 0.51 ± 0.04 (95% CI). Whilst the total fraction of RyR clusters that were phosphorylated in tissue sections was lower compared to CM, amount by which these clusters were phosphorylated increased tissue sections. 0.33 ± 0.05 (95% CI) of RyR clusters contained phosphorylation in tissue sections. Of these clusters, the mean fraction of clusterwise area increased to 0.55 ± 0.05 (95% CI).

These experiments found distinct patterns of phosphorylation between samples. The pattern of phosphorylation in 1 µM Calyculin A CM was expected to be altered when compared to Control CM based on the known action of Calyculin A and the differences observed in confocal data (figure 4.2), and peripheral RyR clusters (figure 4.5). The additional differences between both CM samples and tissue sections reflect the ability of STORM super-resolution microscopy to find differences in phosphorylation states of within individual sub-diffraction limit sized RyR clusters.

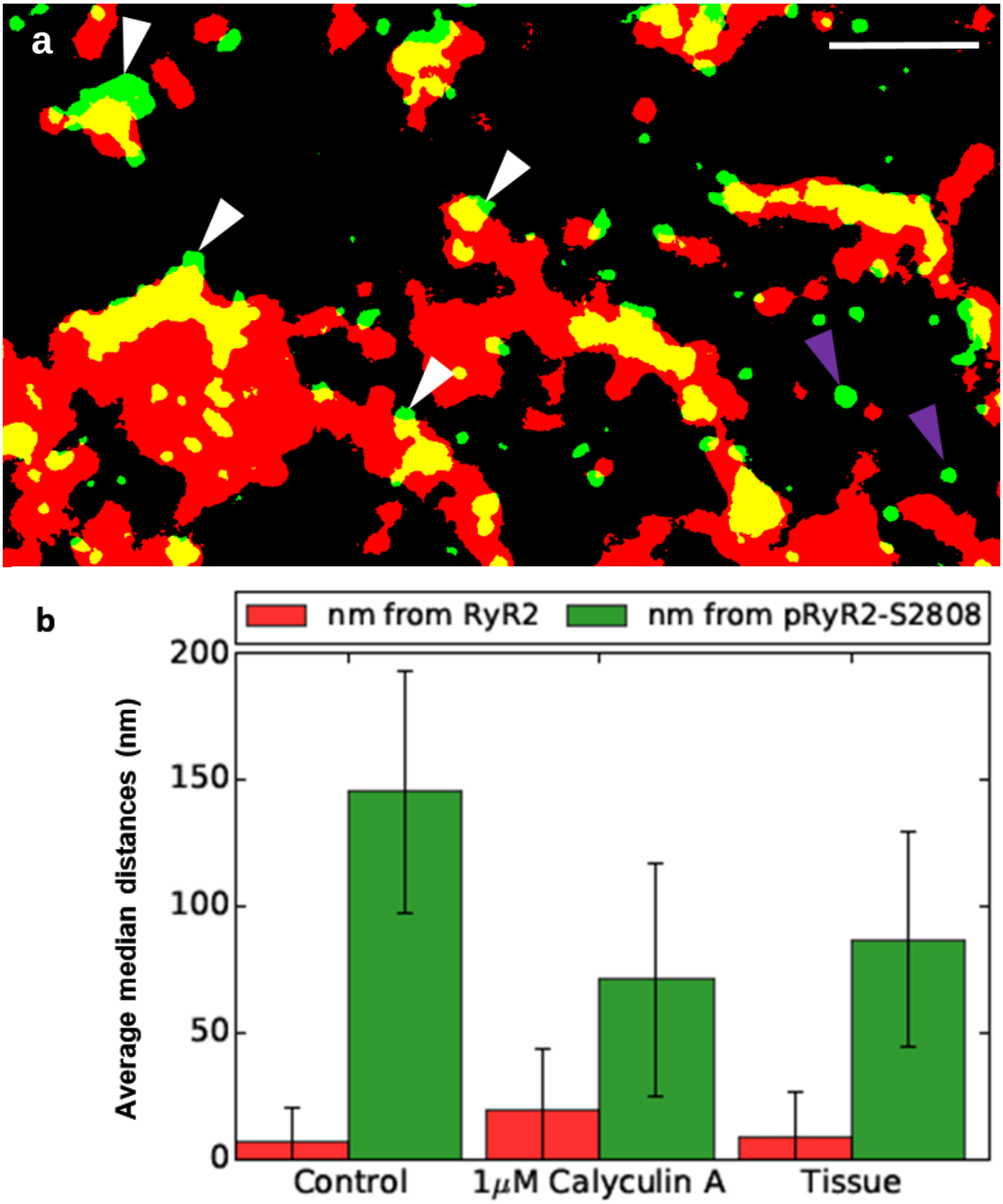


**Figure 4.10. Distance from mask measures using STORM microscopy of Control CM (n = 25(4)), 1 µM Calyculin A CM (n = 23(4)), and tissue sections (n = 29(4)). (a) Example post-processed dual channel STORM image from a tissue section showing RyR2 (red) and pRyR2-S2808 (green) binary masks. Overspill signal (white arrows) and non-colocalised signal (purple arrows) from pRyR2-S2808 are highlighted. (b) Mean (95% CI) median distance from RyR2 (red bars) and pRyR2-S2808 (green bar) are shown.**

The fractional colocalisation measures described in figure 4.9 quantified the colocalised area only from pRyR2-S2808 seen as yellow in figure 4.10a. Less than 100% of the pRyR2-S2808 signal was colocalised. On visual inspection the amount of non-colocalised pRyR2-S2808 (visible as green in figure 4.10a)

was minor and appeared to be in two types of distribution. Some is described as overspill pRyR2-S2808 signal (figure 4.10a). This overspill signal likely originated from the same cluster as the adjoining colocalised signal (figure 4.10a). Small non-colocalised puncta appear with no obvious neighbouring RyR2 (red) signal. More information about the distribution of pRyR2-S2808 signal was obtained by measuring the distance from the edge of the RyR2 (red) masks out to this non-colocalised signal (green). Low median values indicate that 50% of the signal is very close to the RyR2 signal, and likely to be from overspill pRyR2-S2808 signal (figure 4.10a). High values would indicate large contributions from non-colocalised puncta (purple arrows, figure 4.10a).

The calculated distances of pRyR2-S2808 signal from RyR2 (figure 4.10b) were similar across samples. Average median distance from RyR2 were 6.3 ± 14.2 nm (SD) for Control CM, 19.2 ± 24.3 nm (SD) for 1 µM Calyculin A CM, and 8.9 ± 17.2 nm (SD) for tissue sections. These measures mean that half of the pRyR2-S2808 signal not counted into the fraction measures is highly likely to be overspill signal and originate from the colocalised clusters, given the 30 nm diameter of a single RyR2 and the refraction of signal on the nano-scale in such optically thick specimens. These measures also suggest that non-colocalised pRyR2-S2808 (figure 4.10a) are only a minor contribution to the total pRyR2-S2808 signal. This supports the measurement of pRyR2-S2808 colocalisation and that this likely represents the true distribution of Ser-2808 phosphorylation across all samples.

Distances from pRyR2-S2808 (figure 4.10b) can be thought of as a measure from the pRyR2-S2808 clusters, primarily out to the edge of the RyR2 (figure

4.10a) mask cluster. Control CM had the highest clusterwise colocalisation fraction (0.56 ± 0.04) and the highest average median distance from pRyR2-S2808 of 145.4 ± 47.8 nm (SD). These data combine to suggest a general pattern of low phosphorylation within the cluster. Whilst it is difficult to draw firm conclusions, it would be consistent with a small central core of phosphorylation, or several puncta towards the centre of RyR2 clusters.

The fraction of RyRs phosphorylated increased in 1 µM Calyculin A CM (0.47 ± 0.04). The average median distance from pRyR2-S2808 decreased to 71.0 ± 46.1 nm (SD). If the fraction of a cluster that is colocalised increases, the remaining area of red only signal is reduced. As such, the distance measures from the now larger yellow cluster out to the edge of a reduced red cluster size in 1 µM Calyculin A CM or same sized in tissue. This suggests that if less area is red only, then fewer RyRs are now still dephosphorylated, meaning some have become phosphorylated. This reduction in the number of dephosphorylated RyRs means there were fewer dephosphorylated RyR2 (figure 4.10a) to measure across, so reducing the distance measure.

Average median distances of 86.8 ± 17.9 nm (SD) from pRyR2-S2808 in tissue sections were slightly higher than 1 µM Calyculin A CM, despite a decreased fraction of clusterwise colocalisation (~0.36). Median cluster values were increased in tissue sections compared to both CM samples (figure 4.8). This would make the distance measure proportionally less in tissue sections. These measures do not comment on the pattern of the colocalised components. These data are consistent with a bimodal distribution of either completely dephosphorylated or substantial amounts of phosphorylation within phosphorylated RyR clusters. Visual inspection of the intra RyR2 distribution

of pRyR2-S2808 signal confirmed that they appeared randomly patterned, with a central tendency. There did not appear to be a defining pattern of phosphorylation (i.e. central core, peripheral ring, chequered).

## Conclusion

This chapter detailed the application and quantitation of the cardiac RyR2 related pssAb in ventricular cardiac myocytes. This was performed for phosphorylation events at Ser-2808 and Ser-2814 using immunofluorescence confocal microscopy initially. This was performed in control CM, 1 µM Calyculin A CM, and tissue sections. There were marked differences between the two pssAb in each sample type, with pRyR2-S2808 being modulated more strongly than pRyR2-S2814. pRyR2-S2808 was then selected to progress to SMLM super-resolution experiments in order to assess the differences observed using diffraction limited confocal microscopy at the single RyR cluster scale.

| | Control CM | 1 µM Calyculin A CM | Tissue |
|---|---|---|---|
| pRyR2-S2814 | 56.6 ± 5.1% | 64.1 ± 4.6% | 67.4 ± 3.2% |
| pRyR2-S2808 | 57.1 ± 6.9% | 75.0 ± 3.0% | 85.6 ± 1.2% |

**Table 4.1. Mean percentage areas (95% CI) quantified from immunofluorescence confocal microscopy for pRyR2-S2814 and pRyR2-S2808 normalised to the area of RyR2 signal within each image.**

The CM isolation procedure appeared to alter the pattern of phosphorylation when compared to tissue sections. In effect, the CM isolation procedure can be considered as an intervention. The tissue sections represent a time close to $t = 0$ with no isolation manoeuvre performed, and so as close as it practicable to the native state. The phosphorylation levels for Ser-2814 and Ser-2808 are similar in control CM, however respond less to non-stimulated

1 µM Calyculin A than Ser-2808 did and was considerably lower in tissue sections. Ser-2808 phosphorylation by area was reduced by -27.5% by the isolation procedure, whereas Ser-2814 was only reduced by -10.6% (See figures 4.1 and 4.2). Importantly, the pattern of this distribution also changed for Ser-2808 but not for Ser-2814 (figures 4.3, 4.4). Ser-2808 pattern of phosphorylation changed from continuous in tissue sections to discrete in control and 1 µM Calyculin A CM, whereas Ser-2814 phosphorylation had a discrete pattern of phosphorylation across all three sample types.

The literature is conflicted regarding RyR phosphorylation and its relevance to disease. In many cases, Ser-2808 hyper-phosphorylation has been described as increasing towards 90%, with inconsistent correlations drawn between Ser-2808 phosphorylation and disease aetiology, whereas Ser-2814 hyper-phosphorylation has been more consistently attributed to disease aetiology, but not globally. I consider the findings detailed in this chapter about the differences between isolated CM and tissue sections to have a high relevance to such studies, as hyper-phosphorylation of Ser-2808 in isolated CM studies may only return the levels to the physiological level observed in tissue sections. Increases to the same level (i.e. approximately 85%) for Ser-2814 is grossly larger than that observed in tissue sections and so becomes an unequal comparison, previously not appreciated. I hope that these types of experiments become a standard control experiment to inform interpretation of single CM experiments regarding phosphorylation. It may also help to explain the conflicting reports of Ser-2808 phosphorylation in the literature as experimenters may inadvertently be returning the phosphorylation to baseline

rather than truly hyper-phosphorylating them to the same extent as is feasible from Ser-2814.

The changes readily observed in Ser-2808 phosphorylation amount and distribution pattern were chosen for further investigation by super-resolution STORM microscopy. Single channel experiments were performed on either RyR2 or pRyR2-S2808 labelled with Alexa 647 individually in the peripheral clusters of isolated CM. Peripheral clusters are flattened against the sarcolemma and so effectively 2 dimensional for imaging purposes (Franzini-Armstrong *et al.*, 1999). These peripheral clusters have been imaged using the same system by other members of the group and these images were assessed to be of a consistent quality (Baddeley *et al.*, 2009; Hou *et al.*, 2015; Jayasinghe *et al.*, 2018). These experiments showed that application of 1 µM Calyculin A increased the median and range of pRyR2-S2808 puncta approaching but less than the RyR2 cluster sizes, in line with what would be expected.

To allow for a replication of the imaging situation applied using immunofluorescence confocal microscopy, and equal comparisons between CM and tissue sections, deep RyRs (approximately 1 µm from the coverslip) were imaged. This accounted for possible mechanical deformation due to tissue sectioning, and ensured no peripheral clusters were included in the analysis as they have a fundamentally different structure (Baddeley *et al.*, 2011). Single channel RyR2 STORM experiments compared deep RyRs in control CM and tissue sections and found no differences in cluster sizes. This

finding allowed direct comparison between deep RyR clusters and their Ser-2808 phosphorylation states between CM and tissue sections.

Dual channel labelling of peripheral clusters was technically limiting, though was achieved in deep RyRs. Quantitative analysis was performed to assess the cluster sizes, distribution of phosphorylated clusters within the population (total fraction), amount of phosphorylation observed within clusters (clusterwise fraction), and an assessment of the non-overlapping signal and its proximity to RyR2 (median distances). Together, these measures describe how much Ser-2808 phosphorylation is distributed across the RyR2 cluster population.

| | Control CM | 1 µM Calyculin A CM | Tissue |
|---|---|---|---|
| Total fraction | 0.56 ± 0.04 | 0.47 ± 0.04 | 0.36 ± 0.03 |
| Clusterwise fraction | 0.33 ± 0.05 | 0.51 ± 0.04 | 0.55 ± 0.05 |
| Median distance from pRyR2-S2808 (nm) | 145.4 ± 47.8 | 71.0 ± 46.1 | 86.8 ± 17.9 |

**Table 4.2. Summary of all measured values using dual channel STORM microscopy for control CM, 1 µM Calyculin A CM, and tissue sections.**

Contrary to the quantification from confocal microscopy (summarised in table 4.1) where the area of colocalisation was greatest in tissue compared with CM, Control CM had the greatest total fraction of phosphorylated clusters (0.56 ± 0.04). These clusters however, had the lowest clusterwise fraction of colocalisation by area at 0.33 ± 0.05. Tissue had an effectively inverse of this, where only 0.36 ± 0.03 of all clusters were phosphorylated, but to a much higher level (0.55 ± 0.05). 1 µM Calyculin A fractions lay in between, with 0.47 ± 0.04 clusters being phosphorylated by a mean coverage of 0.51 ± 0.04. This suggests that PKA signalling is reduced during the isolation procedure,

but it is not fully recoverable, and so there are likely other pathways being altered too.

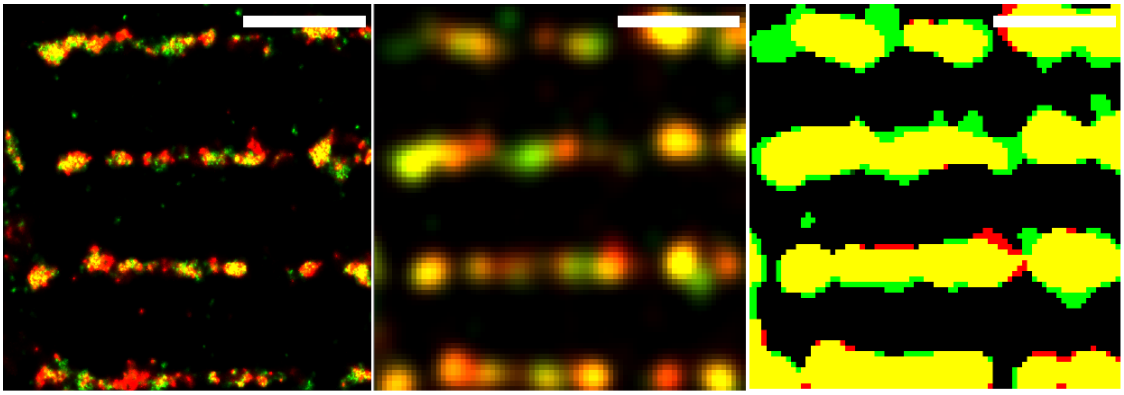

**Figure 4.11. Resolution improvement from STORM microscopy. (a) Dual channel STORM rendered image. (b) Corresponding Gaussian blurred diffraction limited approximation. (c) 80% fractional threshold applied to image (b) of RyR2 (red) and pRyR2-S2808 (green) in tissue section. Scale bar = 2 µm**

Tissue sections have a relatively lower amount of RyRs phosphorylated but to a higher level when compared to control CM. These data were surprising considering the immunofluorescence confocal microscopy data. A Gaussian rendered image blurred to recreate true pixel size (80 nm) showed an image of continuous colocalisation, similar to those observed in immunofluorescence confocal microscopy (figure 4.11).

The pattern of phosphorylation was fundamentally different in isolated CM with more clusters displaying colocalisation but to a lesser extent. 1 µM Calyculin A CM represent a partial recovery, with a similar fraction to control CM of clusters being phosphorylated, at levels more similar to tissue. Median cluster sizes of pRyR2-S2808 were smaller in tissue, despite them covering a larger mean clusterwise fraction of colocalisation. This suggests the RyR clusters in tissue sections contained multiple discrete phosphorylation puncta and was confirmed on visual inspection. This pattern was altered in both CM samples to fuller colocalisation and the median pRyR2-S2808 cluster sizes were increased in both CM samples compared to tissue. RyR2 cluster sizes were larger in tissue sections to both CM, however whether this was an

imaging or section artefact would require further investigation. Single labelled experiments, which are subject to fewer labelling issues and no potential for crosstalk showed no differences between median cluster sizes.

Data were summarised here as means of medians in order to communicate the data as the median values were not skewed. However, there is currently no standard statistical approach to pooling median data. Image analysis on SMLM data will require more refined statistical approaches compared to that traditionally applied to immunofluorescence confocal microscopy due to the increase in measures that result in non-normal data distributions. This is reflected here in the median measures applied to RyR cluster sizes and median pixel distances. Hierarchical statistics has been deployed to further aid in the complications that arise from multi-animal experiments in confocal microscopy. Current deliberations are ongoing as to how best test the data produced from STORM microscopy data.

The phosphorylation state of the cardiac RyR has been imaged and its spatial distribution quantified for Ser-2808 and Ser-2814 in rat ventricular myocytes. The distribution and intra-cluster levels of Ser-2808 phosphorylation have been imaged and quantified in rat ventricular myocytes using dual channel STORM microscopy. These methods have been demonstrated to be sensitive enough to glean new information about RyR physiology at the molecular scale. Furthermore, important differences in the amount and also patterning of Ser-2808 phosphorylation have been revealed between tissue and isolated CM samples. Equally importantly, it was found that Ser-2814 and Ser-2808 phosphorylation were unequally perturbed by the isolation procedure, which is

of profound importance to the experimental approaches currently used in the field of RyR phosphorylation and ryanodinopathies.

# Chapter 5

## Towards observing RyR2 Ser-2808 phosphorylation at sub-cluster resolution: Comparison of dual channel STORM versus DNA-PAINT and methods to improve experimental performance

### Introduction

Chapter 2 detailed the type of information about the distribution of RyR2 phosphorylation on Ser-2808 using dual channel STORM super-resolution microscopy. These data provide new insights into the molecular composition of RyR clustering and towards an understanding of molecular physiology. STORM microscopy has revealed incredible detail in recent years, however still has its own intrinsic limitations (Hell *et al.*, 2015; Tam and Merino, 2015). STORM microscopy replies on the manipulation of fluorescent dyes due to their photophysical properties in certain excitation powers and buffer conditions, typically by oxygen scavenging enzymes or the use of thiol based reducing agents (Vogelsang *et al.*, 2008; Swoboda *et al.*, 2012; Glushonkov *et al.*, 2018). There are no patterns to which buffers work for which fluorescent molecule. Photobleaching is an eventuality within this system. As such the dyes are an intrinsic limit on the resolution gained, despite their manipulation also being the key to gaining super-resolved images.

Two channel STORM requires two dyes that are spectrally distinct and have buffer conditions that are compatible with mounting for simultaneous imaging. This is typically a compromise. The dual colour pair presented in this thesis represent an improvement in performance compared with the previously used

Alexa 680 and Alexa 750 dye pair (evaluated in the thesis of Dr Alex Clowsley, University of Exeter 2017). Additional optical considerations must be taken into account too. For instance, complete spectral separation in the case of Alexa 647 and Alexa 750 would require either dual laser excitation and appropriate optics to separate the two emission spectra onto two cameras, or the use of a splitter device and compromised excitation of the two dyes (Baddeley *et al.*, 2011; Bates *et al.*, 2012).

This means that whilst STORM based SMLM has enabled vast insights to be reported, this progress has been incomplete (Jayasinghe, *et al.*, 2018). Jungmann and colleagues (2014) recently described the use of a new tool to acquire the same type of SMLM image data. DNA points accumulation for imaging in nanoscale topography (DNA-PAINT) uses DNA oligonucleotides (oligos) conjugated to secondary antibody labels, in an analogous manner to standard immunofluorescence (IF) microscopy. These DNA oligos are termed docking strands. The complimentary (imager) strand has a photostable dye conjugated to it and is injected free in solution in the imaging buffer. This buffer is a PBS based buffer with additional salts (referred to as Buffer C), as the purpose of the DNA-PAINT buffer is no longer to control photoswitching, rather to control the on and off rates of the transient binding of the DNA oligo strands (Jungmann *et al.*, 2014; Lutz *et al.*, 2018).

The imager strand stochastically and transiently binds to the docking strand for timescales on the order of tens to hundreds of milliseconds. The freely diffusing imager strands are constantly fluorescing whilst in the illumination field. However, they transit so fast that the net result is a low homogenous field of out of focus light, analogous to a defocused homogenous background

signal. When ‘docked’, the imager strand strongly fluoresces for an appropriate amount of time to be imaged as an ‘event’. The resulting data can then be localised in an identical manner to STORM based SMLM data.

DNA-PAINT offers several distinct advantages. As was first demonstrated, different oligo sequences can be used to image epitopes sequentially. This multiplexing can be achieved using the same dye molecule, thus removing chromatic aberrations inherent in all other multi-colour immunofluorescence microscopy (Jungmann *et al.*, 2014). Multi-channel DNA-PAINT (ratio-PAINT) can also be performed. This maintains a similar experimental speed as multi-channel STORM microscopy compared with exchange-PAINT, whilst retaining the chromatic aberrations. The additional improvement from ratio-PAINT compared with multi-channel STORM is that there is no requirement for buffer compatibility compromises. Two stably fluorescent dyes should respond predictably to the illumination methods used.

DNA-PAINT imager strands represent a limitless pool of potential events, and so bleaching is not a concern. The longer binding times and the fact that the dyes selected do not readily go into the dark state, results in brighter events, and so better localisation. These facts combined have been used recently by our laboratory to improve on the imaging of RyR and junctophilin-2 dual-channel STORM imaging previously published with exchange-PAINT to resolve individual peripheral RyRs for the first time in immunofluorescence based SMLM (Munro *et al.*, 2016; Jayasinghe *et al.*, 2018). This technology was adapted to further the investigation of RyR2 and pRyR2-S2808 dual channel imaging within this thesis and technical comparisons were performed to evaluate the two approaches for a population and sub-population style of

experimental design. The flexibility of DNA-PAINT was hijacked to investigate the performance of our microscope system more precisely than is possible in STORM.

**Aims**

DNA-PAINT is an alternative approach to SMLM microscopy that proposes to be more consistent and more likely to achieve full sampling of the antibodies due to a lack of reliance on fluorophore photoswitching and compatible imaging buffers (Jayasinghe *et al.,* 2018).

This chapter compares the performance of two labelling strategies to perform SMLM experiments. STORM microscopy has enabled unprecedented detail to be observed in biological systems. STORM manipulates the photophysical properties of dyes in order to be able to localise them individually. This information is then used to estimate the true positions of the markers and effectively cast aside the emitted light to build up an image of the likely underlying structure. However, this is limited by the brightness of the fluorophores and their propensity for photobleaching. As such, the sampling rate is limited by the dye molecules themselves and thus so too is the achievable resolution.

DNA-PAINT provides a new labelling strategy which allows for infinite replenishment of the fluorophore. This is achieved by taking advantage of transient binding of two short single stranded DNA oligos; one conjugated to an antibody, and the second conjugated to a fluorophores free in solution. As the concentration of imager strands free in solution can be tuned, so too can the event rates. If photobleaching occurs, further imager strands can be

added to act as an infinite pool of localisation events. The advent of quencher strands (Lutz *et al.*, 2018) also allows for multiple targets to be imaged using the same fluorophore, removing a further complication of dual channel imaging. As these experiments matured, key strategies were developed in order to best assess whether ratio-PAINT or exchange-PAINT were most appropriate. These methods now allow computer scientists and microscopists to experimentally assess localisation algorithms by way of a constant source of localisation events over a STORM sample. A novel protocol in matrix-PAINT was developed that allows assessment of an individual microscope set up, and to determine adequate event rate and number of frames to achieve full event sampling.

The aims of this chapter are:

1. The RyR2 and pRyR2-S2808 dual channel sub-population experiments detailed in chapter 4 will be performed on tissue sections using DNA-PAINT. This is to enable direct comparisons between the two techniques on a biologically interesting question, in an optically challenging sample (thick tissue section, imaged away from the cover slip).
2. Important guidelines on how to set DNA-PAINT experimental design parameters will be developed and demonstrated with suitable control experiments. With any new technology, the risk of incorrect experimental design is increased with the first application in a new sample. This chapter will address these concerns and compare the performance to the known standard of dual channel STORM microscopy.

## Contributions

I have performed each of these experiments, however I wish to acknowledge the substantial help I have received in obtaining and analysing the data contained in this chapter. All Schedule 1 procedures, cell isolation, and cell fixation or tissue cryoprotection and sectioning were performed by myself and Dr Izzy Jayasinghe (University of Leeds), Dr Alex Clowsley (University of Exeter), and Dr Ellen Green (University of Exeter). Data analysis was performed using core functions written by Professor Christian Soeller (University of Exeter). Data analysis was performed in custom python scripts I wrote with help from Dr Ruisheng Lin (University of Exeter). Quencher-PAINT experiments were assisted by Mr Tobias Lutz (University of Exeter).

## Dual Channel SMLM Experiments in STORM and DNA-PAINT

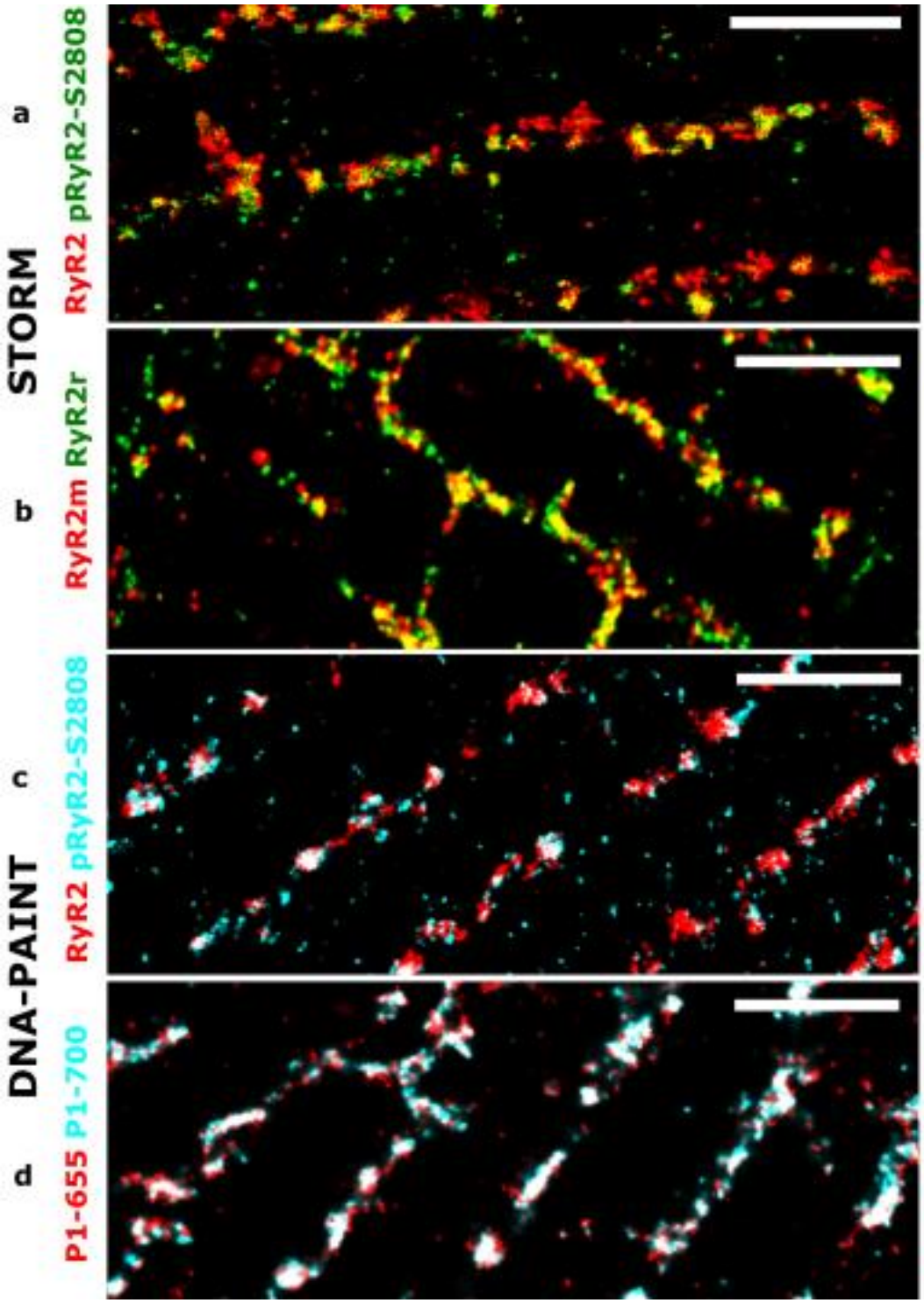


**Figure 5.1. Example images of SMLM experiments. (a) Dual channel STORM image of RyR2 (Alexa 647, red) and pRyR2-S2808 (Alexa 700, green). (b) Dual channel STORM image of mouse anti-RyR2 (Alexa 647, red) and rabbit anti-RyR2 (Alexa 700, green). (c) Dual channel ratio-PAINT image of RyR2 (ATTO 700, red) and pRyR2-S2808 (ATTO 655, cyan). Dual channel ratio-PAINT image of RyR2 with P1 imager sequence conjugated with ATTO 700 (red), and ATTO 655 (cyan). Scale bars = 2 μm.**

Data from dual channel STORM experimental data in tissue analysed in chapter 4 are reproduced and re-analysed in this chapter. Dual labelling of RyR was performed to compare to the pssAb data in order to test whether epitope competition could result in a population and subpopulation distribution, rather than true Ser-2808 phosphorylation patterning. However, the differences consistently observed between tissue and CM (chapter 4) show this is likely to be due to the real Ser-2808 distribution. Then the RyR and pssAb experiments were reproduced using ratio-PAINT in order to accurately compare imaging modalities with identical illumination and fluorescence conditions (figure 5.1). Ratio-PAINT allowed the chromatic aberration of the system to be assessed, by applying both ATTO 655 and ATTO 700 variants of the same P1 imager strand at the same time. The events should therefore have occurred at the same sites on the docking strands and so the remaining differences were expected to be due to the remaining uncorrected chromatic aberration in the system (figure 5.1d).

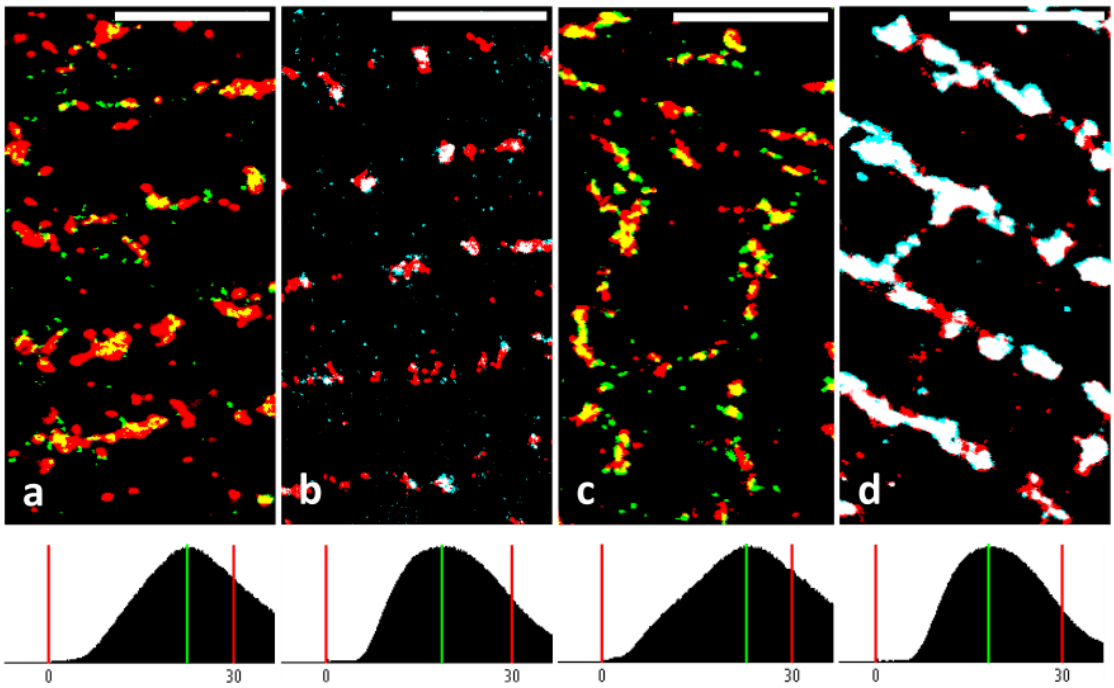


**Figure 5.2. Localisation precision estimates for each SMLM experiment type. Example binarised images with corresponding localisation precision histograms per event (nm) and the mode localisation precision highlighted (green line). (a) Dual channel STORM image of RyR2 (Alexa 647, red) and pRyR2-S2808 (Alexa 700, green). (b) Dual channel STORM image of mouse anti-RyR2 (Alexa 647, red) and rabbit anti-RyR2 (Alexa 700, green). (c) Dual channel ratio-PAINT image of RyR2 (ATTO 700, red) and pRyR2-S2808 (ATTO 655, cyan). Dual channel ratio-PAINT image of RyR2 with P1 imager sequence conjugated with ATTO 700 (red), and ATTO 655 (cyan). Scale bars = 2 µm.**

The PYME software calculated the localisation precision per event and this was plotted as a frequency histogram (figure 5.2e). The mode of this histogram was taken as an estimate of the localisation precision (green bars, figure 5.2). The red bars (figure 5.3) denote the limits that were accepted as viable events for the rendered image, i.e. with a localisation precision of less than 30 nm.

The localisation precision distributions had internal consistency within experimental types. STORM experiments (figure 5.2a, 5.2c) displayed a unimodal distribution with a mode of approximately 23 nm. Figure 5.2 shows representative binarised images and histograms of localisation precision for STORM RyR2 and pRyR2-S2808 (Figure 2a, mode = 22.6 nm) and

selfSTORM mouse anti-RyR2 and rabbit anti-RyR2 (Figure 2c, mode = 22.9 nm). Ratio-PAINT displayed a slightly right skewed unimodal distribution with a mode of approximately 18 nm. The localisation precision for a typical ratio-PAINT experiment (figure 5.2b) had a mode of 17.6 nm, whilst figure 5.2d shows a self-PAINT image had a modal localisation precision of 17.8 nm. These data represent an approximate 20% improvement in localisation precision on the same markers and a spectrally similar dye pair for image of RyR2 phosphorylation deep into tissue sections. This improvement and the change in shape of the distribution so that relatively more of the events have a lower localisation precision reflect the benefits of DNA-PAINT based approaches, even still using two colours. These data show that STORM and ratio-PAINT produce a consistent localisation precision across different IHC targets, on different experimental days, in optically thick tissue sections. Although a 20% improvement may seem modest in comparison to the 10-fold improvement SMLM experiments give on diffraction limited microscopy, it reflects the difficulty in improving resolution in biological samples when imaging at the nanoscale.

Importantly, this localisation precision estimate of less than 18 nm is approaching that required to observe single RyRs. If the packing density observed in peripheral clusters where RyRs have a mean spacing of 40 nm, this would be sufficient resolution to resolve phosphorylation on neighbouring RyRs in 2D. The case for 3D is still more difficult at present, with significant challenging to performing dual channel 3D imaging, though this performance supports the case for ratio-PAINT 3D imaging in the future. Clusters were

analysed in an identical manner to chapter 4 and the differences in these measures due to the improvement in localisation precision were described.

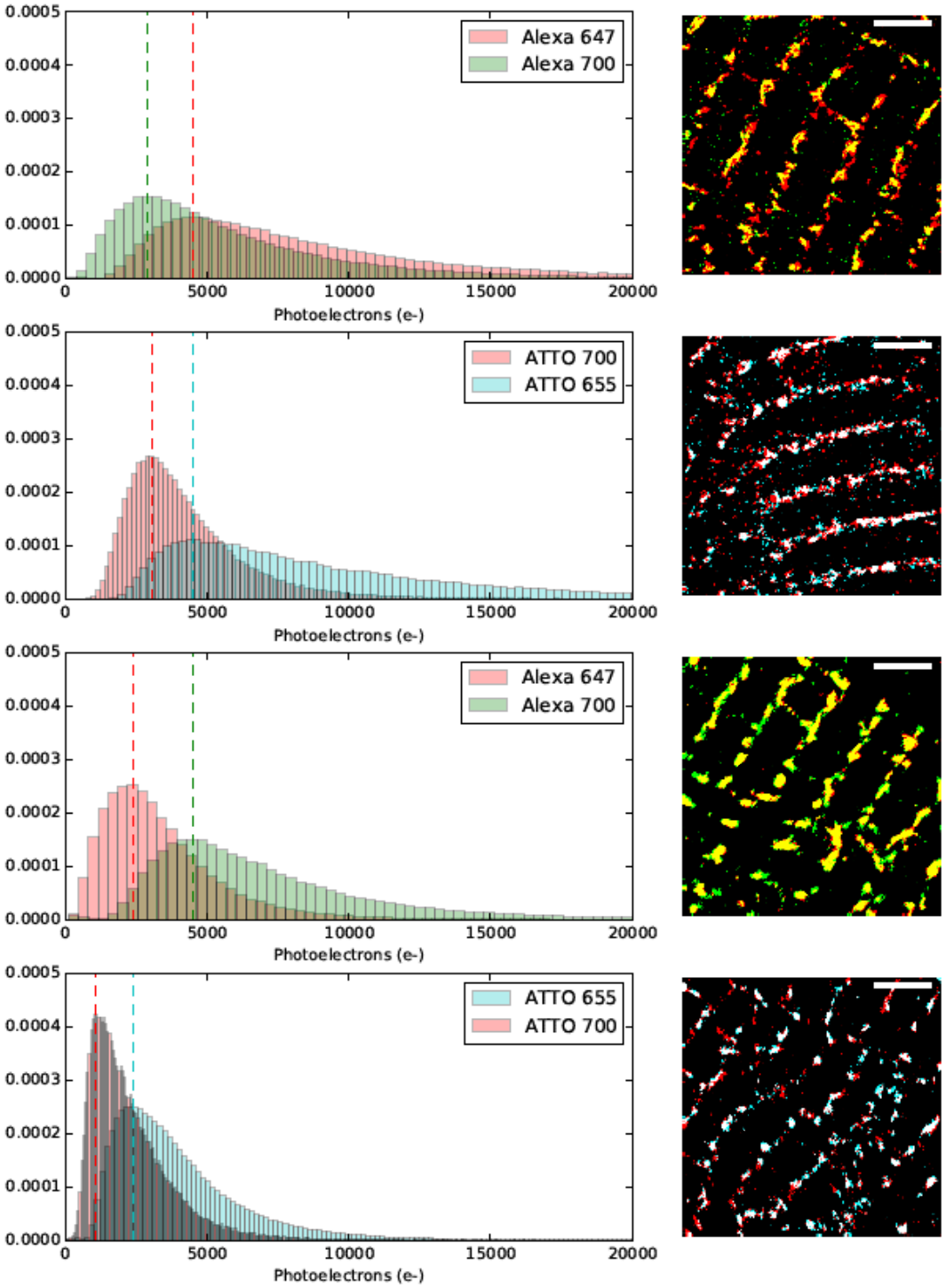


**Figure 5.3. Normalised histograms of photoelectron count per event detected and corresponding image. (a) Dual STORM image of RyR2 Alexa 647 (red) and pRyR2-S2808 Alexa 700 (green). (b) Ratio-PAINT image of RyR2 ATTO 655 (red) and pRyR2-S2808 (cyan). (c) Self STORM image of mouse anti-RyR2 Alexa 647 (red) and rabbit anti-RyR2 Alexa 700 (green). (d) Self-PAINT image of mouse anti-RyR2 P1 with both ATTO 655 and ATTO 700. Scale bars = 2 µm.**

SMLM techniques rely heavily on bright events and low background signals. Events localised to the same position can be summated, effectively producing a much strong signal. As the background increases with the square root of the signal intensity, this is an efficient way of increasing localisation precision. Normalised frequency histograms of event photoelectron count (figure 5.3) show the variability between samples and experiments. This can be due to different thicknesses or labelling of tissue sections, exact laser illumination angle, or precise local imager concentrations. Additional variability in STORM images may be as a result of varying MEA buffer activity; as the MEA buffer loses activity, it may shift from the optimal effective concentration of Alexa 647 (100 mM MEA) down towards the optimal effective concentration of Alexa 700 (50 mM MEA) and could explain the reversal of mode event brightness between these two fluorophores in a dualSTORM image and selfSTORM image (figure 5.3a, 5.3c). The relationship between modes of ATTO 655 and ATTO 700 was retained between ratio-PAINT and self-PAINT (figures 5.3b, 5.3d), despite a shift, most likely due to illumination conditions on the day being not quite identical. The endless replenishment of DNA-PAINT events will also help to minimise the effect of illumination conditions required for optically thick and sub-optimal preparations on localisation precision. The net result of these benefits from DNA-PAINT is that samples can be imaged for longer and each subsequent image will be more equally than compared with sequential STORM imaging due to buffer activity decay. An effectively limitless event pool also affords the experimentalist control of sampling rates for the first time.

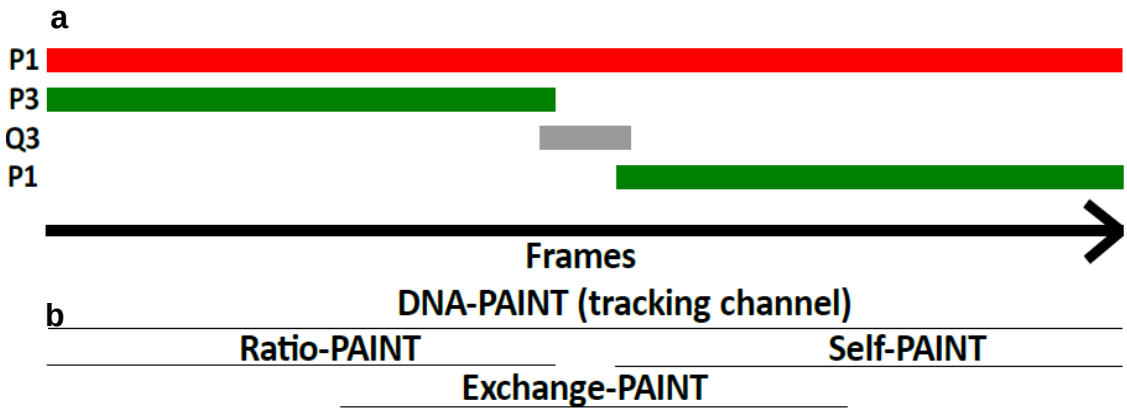


**Figure 5.4. Matrix-PAINT protocol. (a) ATTO 700 (red) P1 imager reference channel complimented by ATTO 655 (green) channel. First, a P1 and P3 ratio-PAINT image (first half) is obtained. P3 quencher strands (Q3) remove the P3 signal without the need to wash. P1 ATTO 655 is then added to obtain a P1 self-PAINT image. P1 ATTO 700 remains uninterrupted and so acts as a reference channel for tracking or drift purposes. (b) Four possible types of image are obtained from the Matrix-PAINT protocol; ratio-PAINT, self-PAINT, exchange-PAINT, and tracking channel.**

The matrix-PAINT protocol allowed for an unrivalled internal control experiment compared with the capabilities of STORM based SMLM. This protocol produces four types of image. On initial inspection, the ratio-PAINT and exchange-PAINT images are of the most interest to applied experiments. However, the self-PAINT and tracking channel images produced hold vital information for the microscopist, and so also the biologist interpreting ratio-PAINT and self-PAINT data.

Self-PAINT experiments illustrate the chromatic differences between the two dyes within the system. Moreover, this experiment could be performed sequentially in an exchange-PAINT fashion to assess how the post-processing and event detection thresholds act on both dyes independently and through the splitter. Eventually, these types of experiments will help to allow for dye-specific detection settings through a splitter device for ratio-PAINT imaging. The tracking channel acts as an internal reference when broken up into sub-sections (i.e. halves in this example). Any observable differences between the image as a result of unbroken application of the same

imager strand is likely to be due to; either insufficient sampling per half, and so the images of each half represent different randomly sampled subsets, or changes in focal plane due to drift in x,y or z. The quencher phase can be observed and the number of P3 ATTO 655 events assessed to confirm post-hoc that the quenching worked successfully. The flexibility afforded by ratio-PAINT and the quencher systems that allowed for matrix-PAINT to be utilised holds a lot of potential for users to calibrate their own systems, and ultimately improve SMLM performance and reproducibility across laboratories.

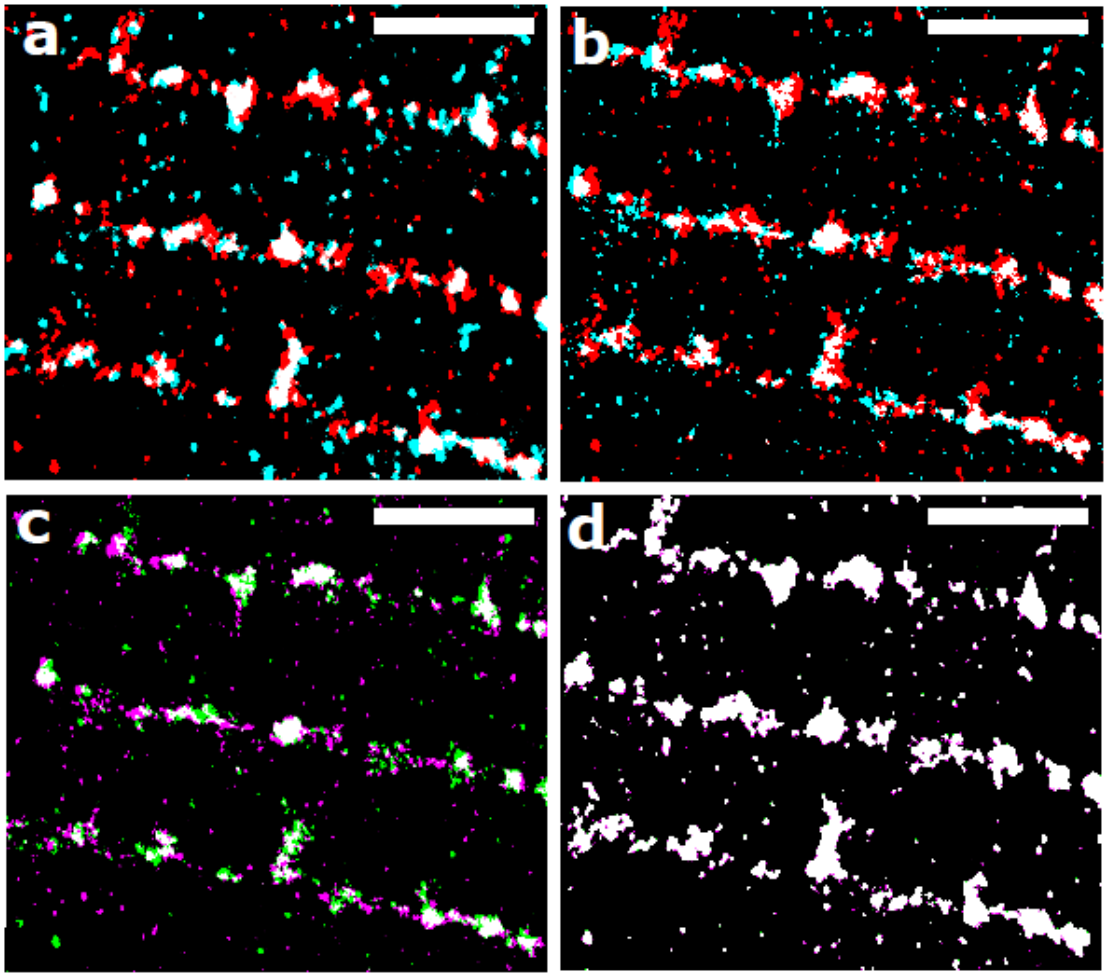


**Figure 5.5. Matrix-PAINT images for RyR2 and pRyR2-S2808 labelled tissue section. (a) Ratio-PAINT image of ATTO 700 RyR2 (red) and ATTO 655 pRyR2-S2808 (cyan). (b) Self-PAINT image after quenching of pRyR2-S2808 signal of RyR2 ATTO 700 (red) and ATTO 655 (cyan). (c) Exchange-PAINT image combining the ATTO 655 channels from ratio-PAINT (magenta, 5a,) and self-PAINT (green, 5b). (d) Internal reference comparing ATTO 700 channels from the first half (ratio-PAINT, magenta) and second half (self-PAINT, green). Scale bars = 2 µm.**

The Matrix-PAINT protocol allows for assumptions made in SMLM experimental set ups to be tests. Most notably, these are the assumptions of adequate drift correction for exchange-PAINT and successful chromatic aberration correction in ratio-PAINT or dual STORM. With the aid of quencher systems this protocol can be extended to an n x n matrix of channels stepping through sequential imager targets. For simplicity it has been demonstrated as a 2 x 2 matrix consisting of two channels and two imager targets. The data set demonstrate in figure 5 was obtained using P1 and P5 imagers.

The P1 ATTO 700 channel was selected to act as the reference channel. To set up the reference channel, P1 ATTO 700 was added at sufficient concentration to produce a comparable event rates to that observed in test series for 1 nM P1 ATTO 655 (circa 50 – 100 events per frame). After stabilisation of event rate, 1 nM P5 ATTO 655 was added to produce a ratio-PAINT image. This was imaged for sufficient frames (approximately 25,000) before the quencher for P5 was added at 5-fold concentration (Q5). This had been previously tested to be more than sufficient to quench the events and the event rate observed returned to the original levels. Importantly, only 1 – 2 µL of imagers and quenchers were added to a well of nearly 800 µL of imager solution, which did not dilute the reference channel or affect the tracking system. After several thousand frames 1 nM P1 ATTO 655 was added to obtain a self-PAINT image.

Here, the ATTO 655 channel results in an exchange-PAINT image that can be used in direct comparison to the ratio-PAINT image of the same ROI. For the first time, this protocol allowed this direct comparison, whereas STORM

would require parallel experiments. Figure 5.5 highlights the benefits of matrix-PAINT. The reference channel for P1 ATTO 700 first half and second half (5.5d) agreed well, as did the self-PAINT images. There are subtle differences observed between the ATTO 700 and ATTO 655 RyR2 images, however my judgement was that they were sufficiently similar to assess that the signal was likely originating from the same clusters, and so chromatic correction was of sufficient quality for ratio-PAINT.

As such either exchange-PAINT or ratio-PAINT were deemed reliable on this system and sample type. I decided to perform the experiments in the ratio-PAINT configuration as once the imager concentrations were established a sufficient number of images could be recorded keeping the event sampling the same. Exchange-PAINT is a very useful protocol, however each mage can take as long as 2 hours to obtain, compared to approximately 45 mins for ratio-PAINT. Additionally, exchange-PAINT requires excessive washing after each series in order to remove the quenchers that are added in excess and reset the concentrations needed to achieve exchange-PAINT images. Matrix-PAINT could be used on every image in certain scenarios, for example if a known effect size is to be observed. However, for the purposes of this thesis and these experiments, the aim was to replicate the type of experiments detailed in chapter 4 and assess the spatial distribution and abundance of Ser-2808 phosphorylation of RyR2 in tissue sections. As such ratio-PAINT is sufficient. Having validated this using matrix-PAINT supports this approach and I recommend this be adopted for each experimental paradigm, if not necessarily for all acquisition.

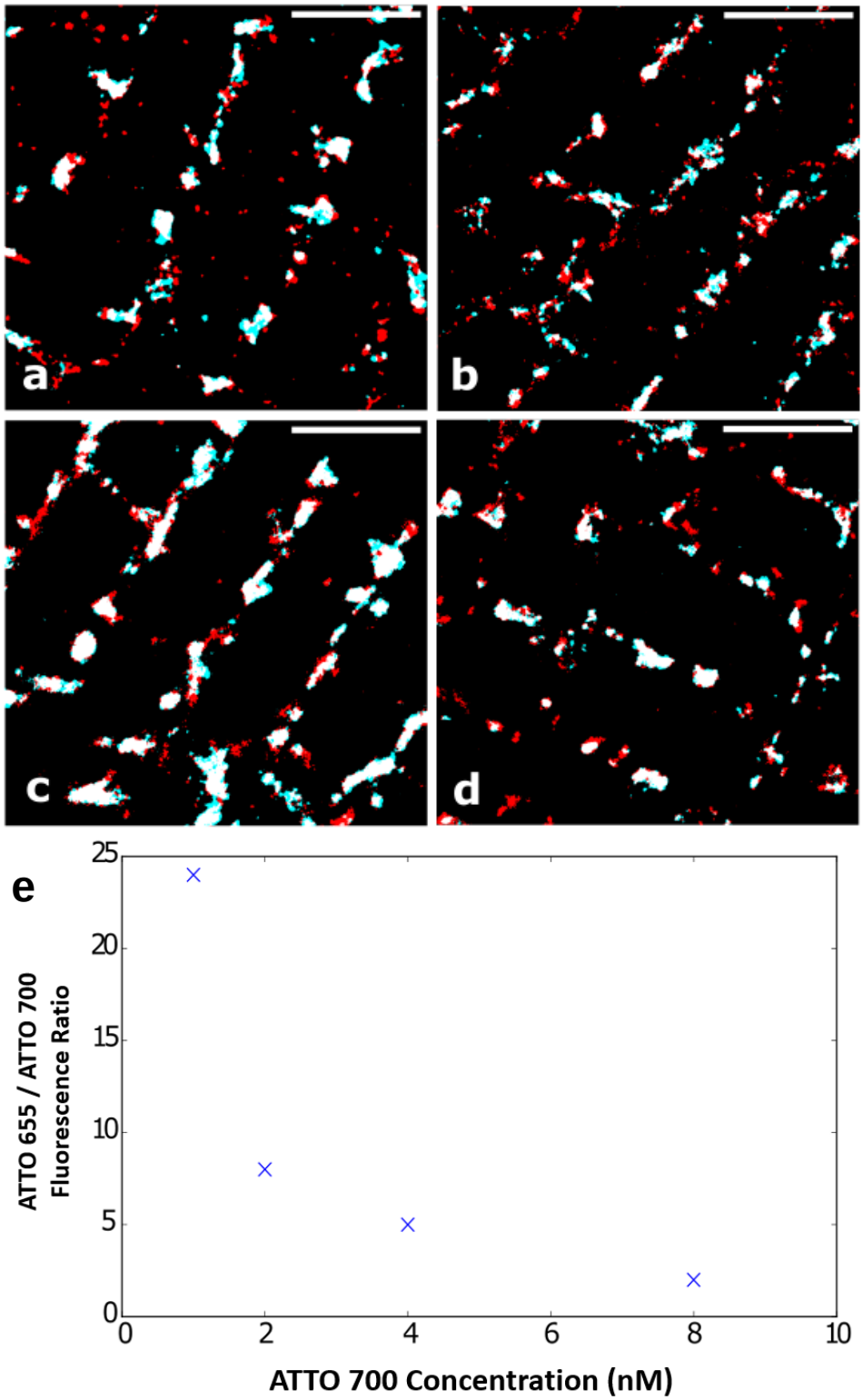


**Figure 5.6. Titration of self-PAINT events versus concentration. P1 ATTO 655 (red) was set to 1 nM and circa 30,000 frames were acquired from the same tissue section with sequential doubling of P1 ATTO 700 (cyan) imager strands. Corresponding images are shown. (a) 1 nM P1 ATTO 700. (b) 2 nM P1 ATTO 700. (c) 4 nM P1 ATTO 700. (d) 8 nM P1 ATTO 700. (e) Total numbers of events accepted for image rendering were divided.**

DNA-PAINT allows the event rates to be highly tuneable. This is of great general benefit but it has been assumed this is entirely due to the imager – docking strand binding kinetics (Jungmann *et al.*, 2014; Lutz *et al.*, 2018). As such the assumption would be that it is the concentration of imager strand that dictates the event rate evenly across series or samples. Whilst this was observed to be broadly true, large differences became apparent when comparing the same imager strands with different dyes in self-PAINT experiments. For a given concentration, P1 ATTO 700 had far lower events than P1 ATTO 655 in the same image.

This relationship was tested by setting P1 ATTO 655 at 1 nM and then P1 ATTO 700 at the same concentration. Only P1 ATTO 700 was doubled between series up to 2 nM, 4 nM, and 8 nM. The ratios of event rates were seen to decrease with this addition of P1 ATTO 700 only. Visual inspection did not immediately show an increase in colocalisation with each image surprisingly only having a subset of the area colocalised (figure 6). This finding was surprising in that it appeared that nominally the same imager strand had differing affinities, or on/off rates at least partly based on the fluorophore attached. This observation outlines the open questions in dual channel SMLM microscopy. These differences could be due to imager-fluorophore interactions, event detection differences between channels, influences from the splitter device, or excitation/photobleaching differences between the two dyes. This requires further experiments to optimise the pairs used in matrix-PAINT and ratio-PAINT and is being investigated by my colleagues within the Soeller Laboratory.

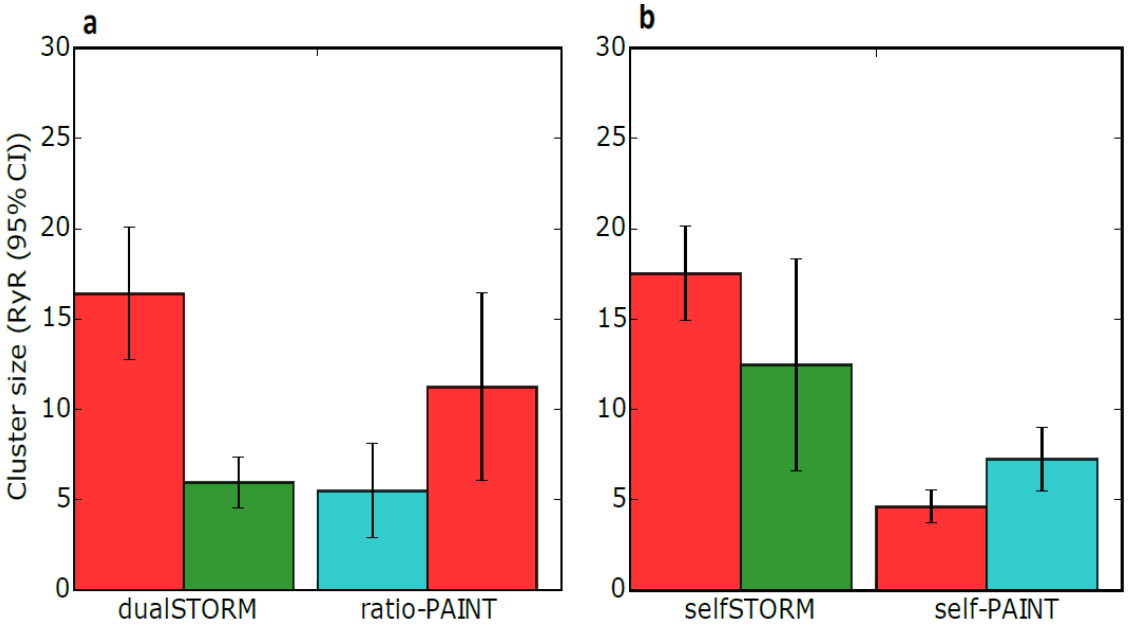


**Figure 5.7. Average (95% CI) super-resolved cluster sizes (RyRs) of all four experimental variants. Each experimental result is shown paired. Bar colours reflect image colours in figure 1: (a) DualSTORM (n = 29(4)) RyR2 Alexa 647 (red), pRyR2-S2808 Alexa 700 (green). Ratio-PAINT (n = 13(2)) RyR2 ATTO 700 (red) pRyR2-S2808 ATTO 655 (cyan). (b) SelfSTORM (n = 6(1)) mouse anti-RyR2 Alexa 647 (red) rabbit anti-RyR2 Alexa 700 (green). Self-PAINT (n = 7(2)) mouse anti-RyR2 P1 with P1-Atto 655 (red) P1-Atto 700 (cyan).**

RyR2 and pRyR2-S2808 cluster sizes were calculated for each type of experiment. All experiments were performed on the same type of rat ventricular tissue section and antibody incubations were identical between the experiment types. When comparing the mouse anti-RyR2 there appears to be a hierarchy of average median cluster sizes. Firstly, the mouse anti-RyR2 cluster sizes were very similar for the RyR-pssAb STORM experiment (figure 7a) when compared to the RyR-RyR dual primary selfSTORM experiments (figure 7b) at 16.4 ± 8.8 RyRs and 17.5 ± 2.7 RyRs respectively. This demonstrates that there is a high level of internal consistency for the mouse anti-RyR2 primary antibody in dual channel STORM experiments.

The ratio-PAINT experiments using the mouse anti-RyR2 and pRyR2-S2808 primary antibodies showed a reduction in average median RyR2 cluster size (5.5 ± 4.6 RyRs). This was likely due to the increased resolution and precision

afforded by the DNA-PAINT technology, despite being imaged with the long channel ATTO-700. When imaged in the short channel with ATTO-655 in the self-PAINT experiments, the mouse anti-RyR2 cluster sizes were reduced further to 4.6 ± 1.2 RyRs. These findings are consistent with the improvement in resolution for DNA-PAINT, and also the short channel's better performance due to greater amount of excitation (closer $\lambda_{exc}$ to the laser λ 642 nm) and shorter $\lambda_{em}$ used reflected in the photon yields in figure 3 and localisation precision in figure 2. This pattern is likely caused by increased resolution and the distinction of sub-clusters, resulting in finer detail of previously large puncta of signal as was demonstrated by this group (Jayasinghe *et al.*, 2018).

Rabbit anti-RyR2 was used for selfSTORM experiments (figure 7b). These were dual labelling experiments with both mouse and rabbit anti-RyR2 primary antibodies, labelled with Alexa 647 and Alexa 700 conjugated secondary antibodies respectively. The rabbit anti-RyR2 antibody had a similar value to the mouse anti-RyR2 and an average median cluster size of 12.5 ± 6.7 RyRs, more than double that of pRyR2-S2808 clusters (6.0 ± 3.4 RyRs, figure 7a). These data show that there was no limitation on applying two secondary antibody trees to the same clusters for pRyR2-S2808 and RyR2 as the rabbit anti-RyR2 clusters were larger than pRyR2-S2808. This showed that there was no spatial competition in the context of pRyR2-S2808 clusters.

The pRyR2-S2808 average median cluster sizes were consistently lower than mouse anti-RyR clusters. As phosphorylation of Ser-2808 is less than 100% this was not unexpected. Interestingly however, the average median cluster sizes for pRyR2-S2808 were very similar between the long channel in STORM experiments and the short channel in ratio-PAINT experiments. This

suggests that the pRyR2-S2808 antibody's reporting is robust and well sampled. It should be noted that whilst the cluster sizes appear the same, this will affect the other measures because the mouse anti-RyR2 puncta have reduced in median size. It is known that pRyR2-S2808 binding epitope approximates to the corner of an RyR2 monomer, and so will result in a possibility of one label per 30 nm. Even if that monomer is not phosphorylated, the neighbouring foot of the adjacent RyR2 channels may be phosphorylated at Ser-2808, effectively giving a possibly 30 nm separation. Once the 3-dimensional nature of these clusters are considered, it may be that DNA-PAINT is able to better resolve the RyR2 clusters, but not individual phosphorylation events in tissue sections. Antibody binding placement has been shown to be detectable in SMLM experiments, however this was in optically simpler samples (Leterrier *et al.*, 2015).

The 'self' experiments allowed us to assess any technical limitations that may occur from dual colour imaging. The selfSTORM relies on the fidelity of both primary antibodies and both sets of secondary antibodies, whereas the self-PAINT approach uses two different coloured imager strands to find the same secondary antibodies on only one primary antibody. The average median cluster sizes for self-PAINT were reduced in both channels compared with the mouse anti-RyR2 STORM data from either selfSTORM or STORM with RyR2 and pssAb to 4.6 ± 1.2 RyRs (ATTO 655) and 7.25 ± 2.4 RyRs (ATTO 700).

The ATTO 655 channel had a lower median compared with the ATTO 700, most likely due to an increase in resolution as this channel had far greater number of events (more than 3-fold). These data show the error produced by using two colours, however ATTO 700 still resulted in lower average median

cluster sizes (as a proxy for resolution) and so performed better than in optimal STORM conditions. Visual inspection suggests that sub-clusters become defined in DNA-PAINT experiments when compared to STORM. This could result in one STORM cluster of 10 RyRs now being resolved into three clusters or 2, 4, and 3 RyRs for example. This would agree with the observations recently published by our laboratory (Jayasinghe *et al.*, 2018).

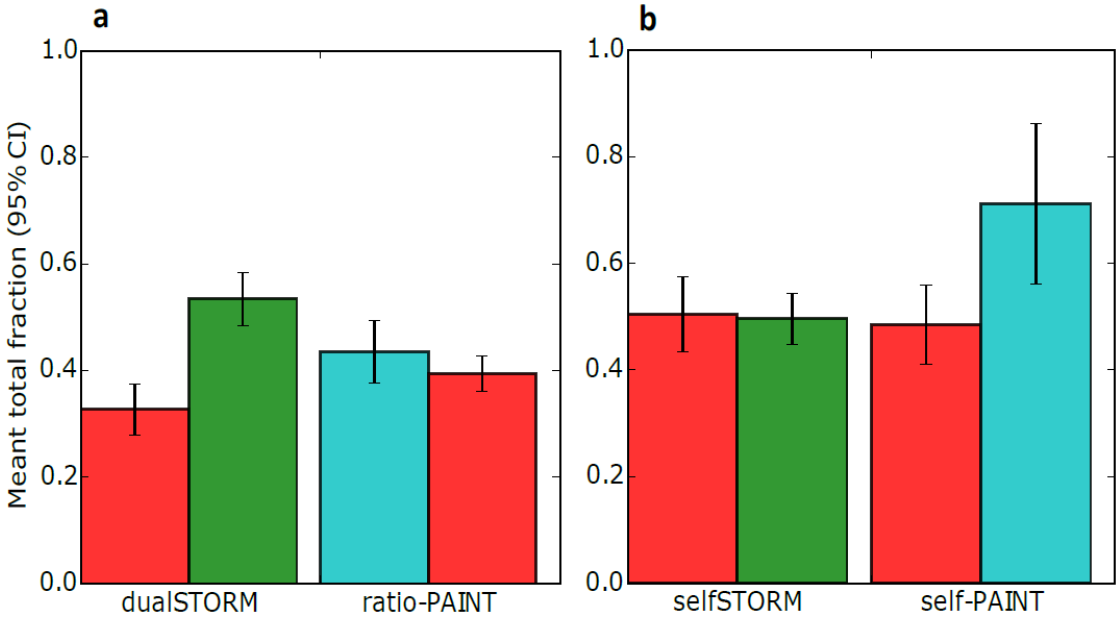


**Figure 5.8. Total fraction (Mean (95% CI)) of clusters colocalised across all clusters of all four experiments. Each experimental result is shown paired. Bar colours reflect image colours in figure 1: (a) DualSTORM (n = 29(4)) RyR2 Alexa 647 (red), pRyR2-S2808 Alexa 700 (green). Ratio-PAINT (n = 13(2)) RyR2 ATTO 700 (red) pRyR2-S2808 ATTO 655 (cyan). (b) SelfSTORM (n = 6(1)) mouse anti-RyR2 Alexa 647 (red) rabbit anti-RyR2 Alexa 700 (green). Self-PAINT (n = 7(2)) mouse anti-RyR2 P1 with P1-ATTO 655 (red) P1-ATTO 700 (cyan).**

Once cluster size had been assessed, the agreement between the two channels was quantified. The total fraction measure was used again to quantify how many of the clusters showed greater than 5% colocalisation. The inclusion criteria for this measure was binary, in that the amount of colocalisation was not taken into account other than the 5% threshold set. These data show a consistent pattern across the experiments.

The selfSTORM used two reliable and previously published total RyR2 antibodies (Baddeley *et al.*, 2009, 2011; Hou *et al.*, 2015; Munro *et al.*, 2016; Jayasinghe et a*l.*, 2018) and showed an approximately equal fraction of cluster colocalisation of approximately 0.5. It is important to remember the scales in operation here; an RyR tetramer is approximately 30 nm square, and antibody 'trees' are perhaps 10 – 20 nm based on the length of an IgG antibody (14.5 nm, (Tan *et al.*, 2015)) on the end of the primary antibodies in an unknown orientation. The localisation precision achieved in these images was similar to the physical error inherent to IHC techniques. When coupled with the projection through an approximately 900 nm optical section, individual proteins were flattened into 2D images. Events occurring from half this distance away in Z may be flattened together, whilst those on the edges of the optical section may only accept one channel due to differing chromatic aberration.

When the less than 100% occupancy of IHC labelling is also taken into account, the fraction of clusters colocalised would be expected to be less than 1, though it could increase in future 3D experiments as this removes the flattening effect due to diffraction limited optical sectioning. As such the total fraction measures gave an internal, experiment-specific consistency.

The self-PAINT data shows a higher fraction of ATTO 700 was within the ATTO 655 masks compared with the reverse comparison. This was likely due to the unequal event identification between the channels as highlighted in figure 5.6. This could be due to the lower excitation power of the 642 nm laser for ATTO 700, especially as the power drops off across the Gaussian beam profile. Images were cropped to where ATTO 700 appeared to still produce

sufficient events, however for the ratio-PAINT experiments the concentrations of ATTO 700 image strands were adjusted to provide a more similar event rate to that observed in single channel RyR2 DNA-PAINT experiments and then ATTO 655 imager added to a similar event density for pRyR2-S2808. More customised post-processing and event detection settings are required to optimise each channel individually, yet still process the data at the same time in order to fully alleviate this issue with ratio-PAINT, however in relation to what is currently available ratio-PAINT is currently the best approach to simultaneous dual channel SMLM imaging.

Ratio-PAINT experiments broadly agreed with the STORM experiments for RyR2 and pRyR2-S2808 labelled tissue sections. The ratio-PAINT total fractions were evened out for both channels in comparison to STORM. The RyR2 now in the long channel occupied 0.39 ± 0.03 of pRyR2-S2808 area, whereas the pRyR2-S2808 occupied 0.43 ± 0.06 of the RyR2 area. This was likely due to the relative improvement in resolution and more even performance between the two dyes afforded by ratio-PAINT compared with STORM.

The selfSTORM total fractions were remarkably even between the two primary antibodies. The mouse anti-RyR2 occupied 0.5 ± 0.07 of rabbit anti-RyR2 and the reciprocal fraction was 0.49 ± 0.05. The fraction of ATTO 655 RyR2 clusters that contained colocalisation was very similar to the selfSTORM figures, at 0.48 ± 0.07, whereas 0.71 ± 0.15 ATTO 700 RyR2 signal was colocalised. This data suggests that there is still some optimisation of the long channel event detection and post-processing when compared to the ATTO 655 channel in order to fully calibrate the ratio-PAINT event

detection for unequal dye properties using a single excitation laser and splitter device. This work is currently being considered by the Soeller Laboratory members. However, for purposes of analysis and comparison to dual channel STORM this was within an acceptable degree and was kept standard across all experiments.

The total fractions were lower in the RyR2 and pRyR2-S2808 experiments compared with the corresponding selfSTORM and self-PAINT approaches. These differences show that the corresponding labelling from pRyR2-S2808 is most likely a true subpopulation and not labelling like a total RyR2 antibody. SelfSTORM and self-PAINT total fractions also highlight the difficulties associated with antibody-based imaging at the nanoscale. Small clusters are more vulnerable to chromatic aberrations and sub-maximal IHC labelling of both antibodies or missed events due to insufficient STORM buffer performance or under sampling. Self-PAINT experiments showed consistent fractions for 20,000 – 50,000 frames rather than an upward relationship and so I am confident that sampling due to imager strand behaviour was satisfied. This was also confirmed in the tracking channel shown in figure 5.6. Sampling due to IHC labelling performances, how many secondary antibodies have lost their docking strands due to redox reactions (Blumhardt *et al.*, 2018), or never had them conjugated to begin with is a longer term and highly challenging question for the field to hope to address.

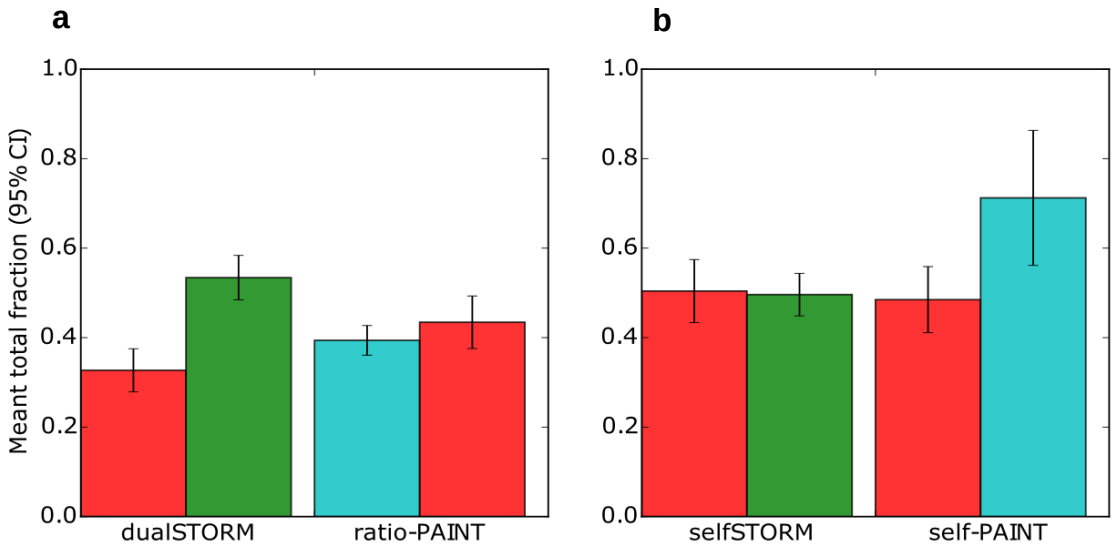


**Figure 5.9. Clusterwise fraction (Mean (95% CI)) of clusters colocalised across all clusters of all four experiments. Each experimental result is shown paired. Bar colours reflect image colours in figure 1: (a) DualSTORM (n = 29(4)) RyR2 Alexa 647 (red), pRyR2-S2808 Alexa 700 (green). Ratio-PAINT (n = 13(2)) RyR2 ATTO 700 (red) pRyR2-S2808 ATTO 655 (cyan). (b) SelfSTORM (n = 6(1)) mouse anti-RyR2 Alexa 647 (red) rabbit anti-RyR2 Alexa 700 (green). Self-PAINT (n = 7(2)) mouse anti-RyR2 P1 with P1-ATTO 655 (red) P1-ATTO 700 (cyan).**

The mean clusterwise fraction describes the mean area of colocalisation and so is sensitive to the resolution achieved. 0.39 ± 0.04 of RyR2 cluster area was colocalised with pRyR2-S2808 in STORM experiments and this was reduced to 0.14 ± 0.02 in ratio-PAINT experiments. The fraction of pRyR2-S2808 colocalised with RyR2 was 0.55 ± 0.05 in STORM experiments and 0.46 ± 0.06 in ratio-PAINT experiments. The drastic reduction in RyR2 area coverage is likely a combination of the reduced cluster sizes observed likely due to the ability to resolve sub-clusters in ratio-PAINT, and also the pRyR2-S2808 was imaged in the short channel in ratio-PAINT, further increasing the resolution. That the pRyR2-S2808 clusterwise fractions were more similar suggests consistent labelling and sampling of pRyR2-S2808, and so the real distribution of Ser-2808 phosphorylation.

Clusterwise fractions for selfSTORM experiments were very similar with 0.50 ± 0.05 of mouse anti-RyR2 being colocalised whilst 0.50 ± 0.07 of rabbit

anti-RyR2 was colocalised. This experiment represents the results of two primary antibodies bound to the same protein target. Median cluster sizes and visual inspection support the working assumption that there was no direct inhibition between the two antibody trees. Self-PAINT ATTO 655, which is analogous to the Alexa 647 labelled mouse anti-RyR2 of selfSTORM and STORM experiments. The clusterwise fraction for ATTO 655 was 0.48 ± 0.07 colocalised with ATTO 700, whereas the ATTO 700 clusterwise fraction was 0.71 ± 0.15. This increase reflects what was seen in the total fraction measures (figure 5.8) with ATTO 700. Whilst this may be in part explained by the unequal event detection as seen in figure 6, however the event rate was set for this set of experiments, not imager concentration to approximately equal events from both dyes. Visual inspection suggested that ATTO 655 produced more non-colocalised small puncta, which would result in more zeros being included in the mean calculations. Median cluster sizes and visual inspection suggest that ATTO 700 still adequately captured the RyR clusters (figures 5.1 – 5.5). That ATTO 655 produced a similar fraction to the selfSTORM experiments was initially surprising This suggests that the limitations of the microscope system or image processing procedures are being reached by both STORM and DNA-PAINT, as selfSTORM could still produce full occupancy with both primary antibodies within the localisation precision of one another too.

Whilst the increase in resolution has the potential to reduce the colocalisation, it is better to consider it as a tightening of the area of signal to the area of true location of the dye. It is not possible to resolve all individual RyR receptors at the resolutions achieved in these experiments (approximately 17 nm

localisation precision in ratio-PAINT). However, puncta that may have shown as clusters in STORM appear to have resolved into sub-clusters. Additionally, a cluster of equal size and shape in ratio-PAINT would have resolved to a smaller punctum in the rendered image than if imaged with STORM. As such, whilst the total fraction should be dictated by the biological sample and the resolution of sub-clusters, the mean clusterwise fractions is more sensitive to improvements in resolution.

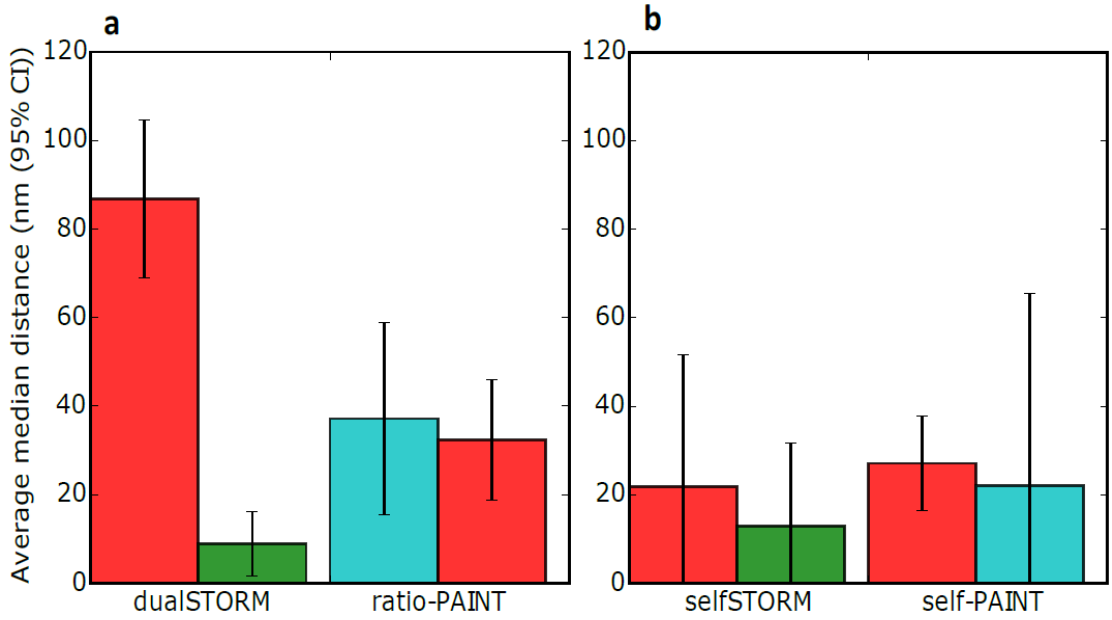


**Figure 5.10. Average median distances (nm (95% CI)) from reference mask to median pixel distance of coloured channel for all four experiments. Each experimental result is shown paired. Bar colours reflect image colours in figure 1: (a) DualSTORM (n = 29(4)) RyR2 Alexa 647 (red), pRyR2-S2808 Alexa 700 (green). Ratio-PAINT (n = 13(2)) RyR2 ATTO 700 (red) pRyR2-S2808 ATTO 655 (cyan). (b) SelfSTORM (n = 6(1)) mouse anti-RyR2 Alexa 647 (red) rabbit anti-RyR2 Alexa 700 (green). Self-PAINT (n = 7(2)) mouse anti-RyR2 P1 with P1-ATTO 655 (red) P1-ATTO 700 (cyan).**

Median pixel distances from the reference channel were used to compare the relationship of signals from both channels as described in chapter 4, in order to compare the techniques directly. The median distance of pRyR2-S2808 from RyR2 was 8.9 ± 7.17 nm whilst RyR2 were 86.8 ± 17.87 nm. The same measures in ratio-PAINT were 37.2 ± 21.80 nm from RyR2 and 32.4 ± 13.72 nm. These differences should be entirely due to the differences

in performance between STORM and ratio-PAINT. When also considering the change in appearance of RyR2 clusters to sub-clusters, these are effectively removed pixels to have a distance calculated for them, and brings a new, closer boundary in to the pRyR2-S2808 signal.

A proportion of the area of pRyR2-S2808 signal that could have lay within the boundary or closer to the boundary in the STORM experiments would now have an increased distance to the RyR2 sub-clusters observed in the ratio-PAINT experiments. This explains the perhaps unexpected increase in distance from pRyR2-S2808 observed. That this error is approximately one RyR distance means the likelihood of the signal being specific to that cluster is high. This essentially means that the mean colocalisation could be considered as the fraction stated as clusterwise fraction, plus 50% of the remainder. This correction factor is not directly possible in STORM experiments as the remaining jitter from having two antibody trees is an unknown variable.

The distance measures for the selfSTORM and self-PAINT experiments were broadly similar at 21.8 ± 29.73 from mouse anti-RyR2 and 13.0 ± 18.74 from rabbit anti-RyR2. This likely represents the residual chromatic aberration and unequal excitation and sampling of both dye pairs within our system. When compared to the localisation precision achieved these approaches, in particular the self-PAINT approach should help to better inform the limitations in image analysis on a system per system, and sample per sample basis. Although the measured distances had similar medians for selfSTORM and self-PAINT, when considered with the distances from pRyR2-S2808 to RyR2 (figure 5.10a) and the reduced median RyR cluster sizes in PAINT versus STORM experiments, these all point towards improvements in resolution for

RyR2 clusters. If the true resolution were equal between selfSTORM and self-PAINT, then one would expect the physical separation of primary and secondary antibodies in selfSTORM to become evident in the median distance measures. The fact that they are similar suggests that they happen to have a similar median distance despite a physically larger distance underlying the images. This suggests that there must be a loss of resolution and loss of sub-cluster resolution in the selfSTORM experiments compared to self-PAINT.

## Conclusion

Colocalisation analysis has been used as a useful approximation of proximity of two labelled proteins. In reality however, it is an aberration caused by the diffraction of light. SMLM addresses the majority of the distortion caused by light diffraction by improving the resolution achieved, whilst chromatic aberration correction collars on microscopy objectives minimise the chromatic aberrations that result in two wavelengths of light originating from different z-positions focusing onto the same image plane.

The self-PAINT experiments here represent, for the first time, an ability to assess only the remaining chromatic aberration as, in theory, the dye molecules attached to the imager strands were immobilised on the same docking strands. Prior to this the best situation was to apply two different primary antibodies onto the same target, and label them with different dyes, as demonstrated by the selfSTORM experiments. Similarly, the improvement in resolution afforded by ratio-PAINT compared with dualSTORM from the same antibody labelling systems and analogous dye pairs represents the

remaining inefficiencies inherent in STORM microscopy. These comparisons allow a more accurate quantification of the distribution of the antibody labels and so the protein(s) of interest.

DNA-PAINT has distinct advantages in the ability to multiplex as seen in exchange-PAINT, or fine tune the number of events between two channels to obtain optimal conditions. The additional benefit of an effectively limitless pool of imager strands available combines to offer the greatest control of event sampling compared to other SMLM techniques. The experiments detailed in this chapter demonstrate the open questions remaining about DNA-PAINT that arose once it was applied to a challenging biological question. Such as why the apparent inequality of event rate for two channels given the same imager strand concentrations, which should be the major influence. Whether this is excitation dependent, bespoke event detection is required per channel, or there are even dye-oligo interactions that have not been appreciated are currently being investigated by the Soeller Laboratory.

Self-PAINT experiments allow experimenters to test the quality of their own systems by testing both localisation precision and remaining chromatic aberrations. These tests will also prove useful for testing the event detection algorithms across dyes in controlled conditions. By combining the use of quenchers and ratio-PAINT technology to create the matrix-PAINT protocol, I created a protocol to assess which DNA-PAINT approach is the most appropriate as well as the ability to set the sampling criteria prior to experimentation. The data presented in this chapter show another example of DNA-PAINT technology being used to answer a biologically interesting question and provide its own solutions to questions around experimental

parameters. These data have also opened up the question of how to define an RyR cluster in SMLM experiments. Altogether, this chapter represents a stepwise change in the capability of SMLM microscopy and evidenced working examples compared with dual colour STORM microscopy.

# Chapter 6

## Discussion

The aim of this thesis was to apply the use of cardiac pssAb in fluorescence microscopy to assess the spatial distribution of phosphorylation in the context of cardiac ion channel distribution. Candidate antibodies were screened through diffraction limited microscopy and successful candidate targets progressed to validation in STORM and DNA-PAINT super-resolution microscopy.

The study of cardiac $Ca^{2+}$ handling is vital to understanding the causes of cardiac health and disease. PTMs, including phosphorylation control a wide range of cellular processes. Aberrant control of phosphorylation has been widely linked to cardiac dysfunction, but the study of phosphorylation events has been limited to *en masse* biochemical measures or indirect inference from electrophysiological recordings. The study of the spatial distribution of phosphorylation will provide new insights into a range of disease phenotypes, and more broadly general biological principles.

A range of pssAb were screened using diffraction limited confocal microscopy for the common proteins of interest in cardiac $Ca^{2+}$ handling RyR2, SERCA2a, and PLN. **Chapter 3** detailed the validation of pssAb in Western blot and diffraction limited confocal microscopy. PLN and RyR2 had two pssAb that gave a good agreement with the appropriate total protein antibodies. Whilst PLN phosphorylation is of interest to the field, total PLN distribution itself has not been quantified, in particular in relation to SERCA2a. This task was out of the scope of this thesis, however PLN, pPLN-s16, and pPLN-T17 have been

shown as a potential target for future work. RyR2 related pssAb were selected to progress to quantification.

**Chapter 4** quantified the spatial distribution of RyR2 phosphorylation at Ser-2814 and Ser-2808 in diffraction limited confocal microscopy. These experiments found two interesting differences. Tissue sections showed a fundamentally different pattern of phosphorylation, with Ser-2814 phosphorylation being punctate and accounting for just over half of the area of RyR2 signal. Ser-2808 phosphorylation appeared near continuous along the length of striations and accounted for 86% of the RyR2 signal area. Secondly, CM isolations were performed for the purpose of pharmacological modulation of phosphorylation levels.

Fundamental differences in Ser-2808 phosphorylation between tissue sections and CM were observed. Ser-2808 colocalisation are reduced towards 50% and became punctate, whereas there were approximately similar patterns of phosphorylation of Ser-2814 between CM and tissue sections. The phosphorylation of Ser-2808 in the context of total RyR2 clusters were then quantified between CM and tissue sections using dual channel STORM super-resolution microscopy. There are wide implications of these findings, not least that the phosphorylation sites were unequally affected by the CM isolation procedure. These differences were investigated in STORM microscopy data.

Tissue sections were shown to have a decreased fraction of phosphorylated RyR clusters compared with CM, which is opposed to the data from confocal microscopy. Artificial convolution of STORM microscopy images produced a continuous pattern of phosphorylation analogous to that observed in confocal microscopy. This highlights the investigative power of SMLM techniques.

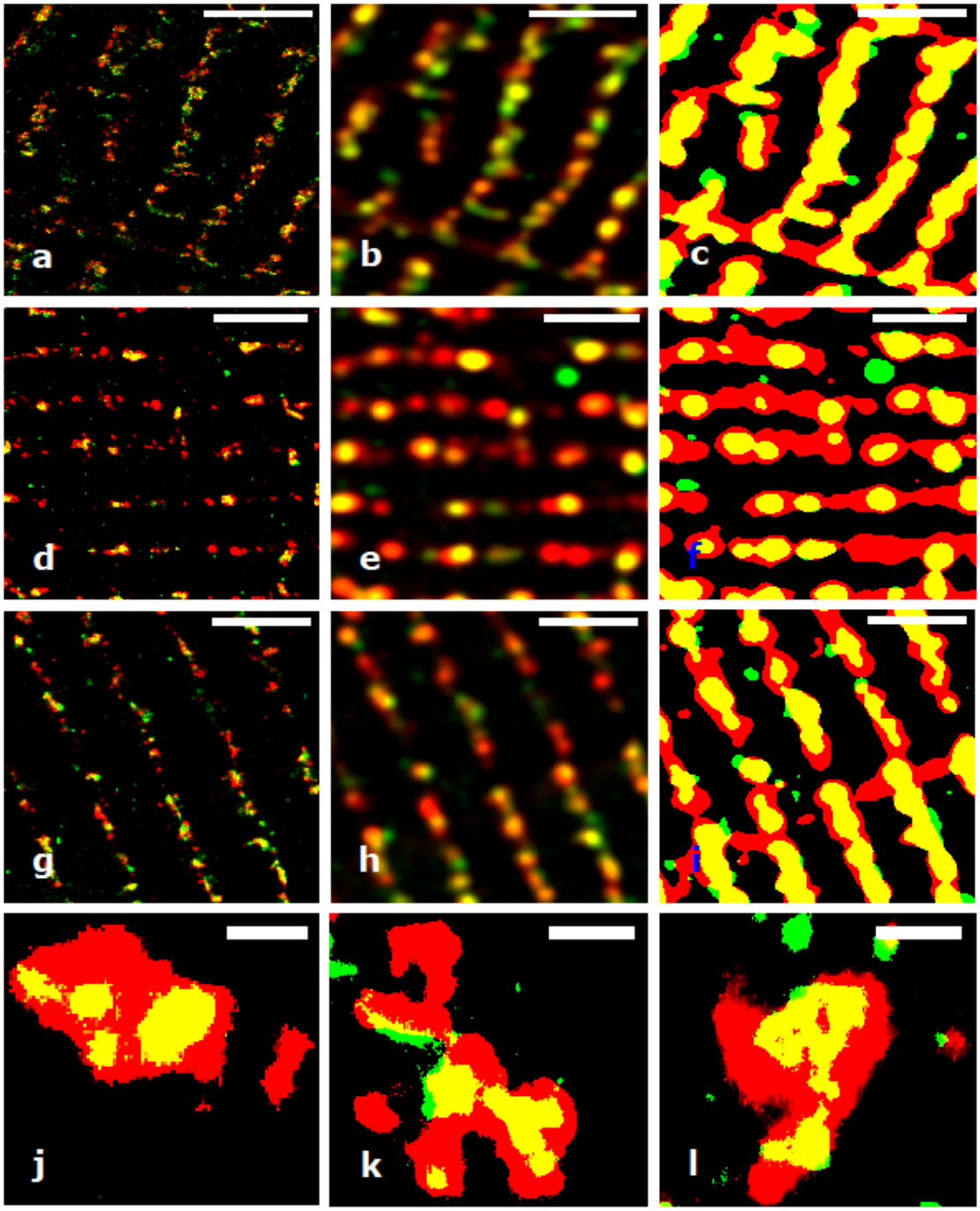


**Figure 6.1. Improved resolution led to greater detail observed about RyR2 Ser-2808 phosphorylation patterns in dual channel STORM experiments when compared to confocal microscopy. All images depict Alexa 647 labelled RyR2 (red) and Alexa 700 labelled pRyR2-S2808 (green). Each row displays a rendered dual channel STORM image, a Gaussian blurred pseudo-confocal microscopy image of the same data, and a binarised version of this image analogous to the confocal microscopy image processing detailed in chapters 2 – 4. Tissue sections (a – c), Contol CM (d – f), and 1 µM Calyculin A CM (g – i) are shown. Scale bars = 2 µm. Example representative STORM cluster for control CM (j), 1 µM Calyculin A CM (k) and tissue (l). Scale bar = 200 nm.**

The distribution of Ser-2808 phosphorylation was fundamentally altered by the CM isolation procedure (figure 6.1). The fraction of phosphorylated clusters

increased from 0.36 to 0.56 due to the isolation procedure, whereas the average fraction of phosphorylation coverage within the clusters went in the opposite direction, from 0.55 down to 0.33. These numbers represent a loss of Ser-2808 phosphorylation choreography and would be consistent with a spread of phosphorylation from tightly selected clusters with moderate levels of phosphorylation, to more clusters having less phosphorylation. It is somewhat difficult to unite these findings with that of the confocal microscopy data, where the coverage decreased from tissue sections to control CM and became more punctate after the isolation procedure. This reinforces the requirement of imaging modalities such as SMLM STORM and DNA-PAINT microscopy for molecular questions. In essence, to ask questions about physiology at the nanoscale, one must be able to observe the nanoscale.

This is an important discovery as when the potential role of specific phosphorylation sites has been studied previously, the CM experiments have been handled in apparent identical manners as is good scientific practice. However, if the phosphorylation levels are unequally altered by the phosphorylation procedure, this new information becomes of more importance considering the local variations in CM isolation procedures. I recommend all standard protocols be investigated with these methods for procedural effects as well as confirming variability for studies investigating the role of altered phosphorylation in CM disease states.

DNA-PAINT is a recent advance in SMLM technology and allows for greater experimental control and increased resolution. **Chapter 5** details a direct comparison of performance between STORM and DNA-PAINT in the context of a population and sub-population experimental paradigm. In this case,

Ser-2808 and RyR2 were imaged in rat cardiac tissue sections and open questions about the applicability of DNA-PAINT were highlighted. The introduction of the matrix-PAINT also demonstrates a simple method for scientists to set acquisition parameters prior to DNA-PAINT experiments. Figure 6.2 demonstrates the similar results between the two techniques, however the RyR2 sub-clusters become apparent in the ratio-PAINT image (figure 6.2).

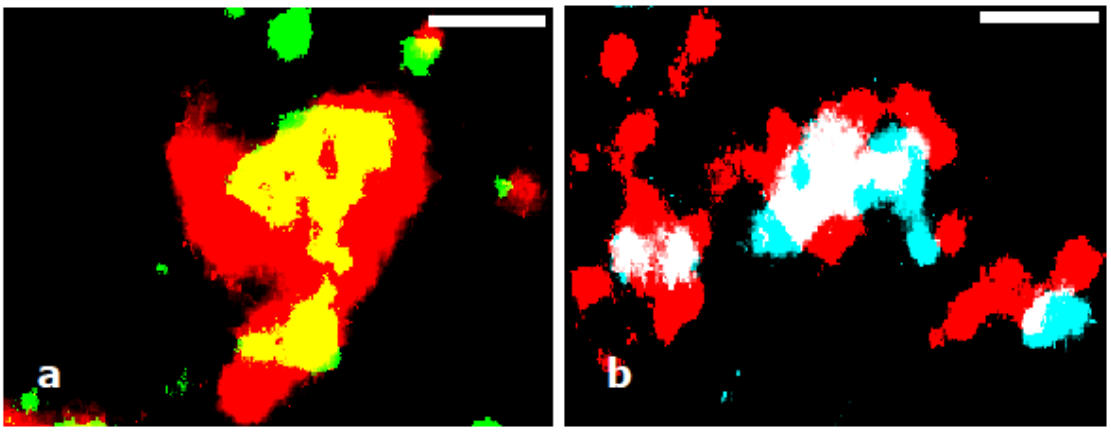


**Figure 6.2. Example dual channel super-resolution clusters. (a) STORM image of RyR2 (red) and pRyR2-S2808 (green). (b) Ratio-PAINT image of RyR2 (red) and pRyR2-S2808 (cyan). Scale bars = 200 nm.**

Cardiac diseases such as arrhythmia are a result of a loss of local $Ca^{2+}$ handling control within individual RyR clusters. Phosphorylation alters the open probability of RyRs (Carter *et al.*, 2011). The ability to measure how many RyRs within clusters are phosphorylated will help to understand the RyR cluster physiology. Additional parallel experiments for other modulatory factors, such as Ser-2814 phosphorylation or the previously published junctophillin-2 data (Munro *et al.*, 2016; Jayasinghe *et al.*, 2018a). DNA-PAINT has been used to demonstrate n = 10 exchange-PAINT on DNA origami and the data in this thesis shows the capacity of DNA-PAINT to describe an RyR 'clusterome'. Another important question I would have liked

to be investigated in future work is the cause of these differences due to the isolation procedure. Isolations in the absence of protease, and/or collagenase and then section these hearts. These experiments would begin to ask whether biochemical or mechanobiological (or both) factors are at play.

DNA-PAINT has the potential to allow SMLM experiments to be optimised to optimal sampling and resolution conditions for the question being answered. Currently, STORM microscopy has provided great insight, however resolution achieved and sampling conditions are inherent limits of the underlying mechanisms. The application of the matrix-PAINT protocol will allow experimentalists to define the acquisition criteria prior to each experimental paradigm, as well as providing a valuable test of microscope design. DNA-PAINT allows a controlled environment to test and refine the event detection and localisation algorithms, especially in dual channel imaging with unequal excitation of fluorophores. These further tests will refine the SMLM procedures.

These experiments hopefully lay the foundations of observing the cellular and molecular anatomy including physiological modifications of important subcellular structures. It is my hope that this type of experiment is adopted by those within and outside of the cellular cardiac field. This method is equally applicable to other types of subpopulations or heterogenous ion channel cluster populations to contextualise colocalisation experiments within cluster composition.

# Appendix 1

## Human and mouse neuromuscular junction SNAP25 active zone protein observed and compared with STORM super-resolution microscopy

### Introduction

Neurons are specialised cells that transmit information via electrical impulses. Neurons integrate signals from one or more inputs and gate the output signals. In general terms, neurons are a polar cell, with dendrites (that receive the signal) on one side of the cell body, and an axon (that transmits the signal) on the other. The AP is a propagation of a depolarising membrane potential. APs are all or nothing responses; when the depolarisation threshold is reached in the axon hillock (entrance), a full AP will result. APs can only travel in one direction.

The nervous system is broadly divided into the central nervous system (CNS) and the peripheral nervous system (PNS). The CNS comprises the brain and spinal cord, and has a range of conscious and subconscious functions. The PNS comprises sensory, motor, or mixed nerves that connect the CNS to the body. Motor neurons (MNs) can be classified as either upper MNs or lower MNs. The pyramidal cells of the cerebral cortex are upper MNs. They originate in the precentral gyrus and their axons travel down through the brainstem where they decussate at the medulla oblongata. Upper MN axons then travel down the contralateral corticospinal tract in the spinal cord. At every spinal level, upper MNs synapse with the lower MN cell bodies that lie within the ventral horn of the spinal cord gray matter. The lower MNs send

their axons out via the ventral root into the mixed spinal nerve and on to the muscle.

Neurons communicate at specialised connections between axons and dendrites called synapses. Chemical neurotransmitters are packaged into synaptic vesicles at the pre-synaptic terminal. Depolarisation activates synaptic vesicle exocytosis. The neurotransmitters released are spatially confined to the synaptic cleft. The pre- and post-synaptic membranes are approximately 100 nm apart, resulting in rapid activation of receptors in the post-synaptic membrane. This signal has the potential to then trigger a post-synaptic AP. The specialised synapse between a lower MN and its target - skeletal muscle; termed the neuromuscular junction (NMJ). The anatomy outlined above indicates the relative inaccessibility of most central synapses. Located in the PNS however, NMJs represent an experimentally accessible model synapse, as well as being of special interest in neurodegenerative disorders.

Jones *et al* (2016) described a robust ImageJ plugin, NMJ-morph, capable of quantifying 21 pre- and post-synaptic morphological variables. This was applied to the mouse NMJ. Principle components analysis revealed that the overall synaptic size and degree of synaptic fragmentation were key determinants of synaptic morphological variation. Differences across anatomically distinct populations of NMJs correlated to differences in synaptic function that were supported by physiological recordings. Taken together, these data supported the relationship between synaptic size and strength that has been demonstrated previously.

Preliminary experiments compared the mouse NMJ, a common model for human neurodegeneration and age-related weakness, to human NMJs obtained from surgical discard (analogous to a fresh biopsy) and found stark differences. This sampling approach utilising non-traumatic amputations (performed for vascular disease), with immediate fixation, prevents serious deterioration post-mortem. Initial qualitative differences were noted between human and mouse NMJs labelled with antibodies against the pre-synaptic synaptic vesicle protein 2 (SV2). To assess whether these qualitative observations reflected any underlying differences in pre-synaptic 'active zones' (housing the machinery responsible for neurotransmitter release), the active zone protein SNAP25 was assessed through STORM super-resolution microscopy. Additional proteomic studies were performed to assess the broader similarities and differences between the NMJ and muscle proteomes across species (human and mouse).

**Methods**

Muscle biopsies were acquired and fixed within 30 mins of dissection from mouse and immediately in human. Samples were fixed in 4% PFA for 1 hour and processed immediately. Samples were incubated with TRITC conjugated α-bungarotoxin (BTX) for 30 mins, permeabilised with 4% Triton-X for 90 mins, and blocked with 4% bovine serum albumen and 2% Triton-X for 30 mins. Mouse anti-SNAP-25 primary antibody was incubated in blocking solution for 3 nights at 4°C. Samples were washed 4 times for 30 mins with PBS and Alexa 680 conjugated goat IgG anti-mouse secondary antibody overnight at 4°C. Human samples underwent an additional 70 min treatment

with 1mM $CuSO_4$ in 50 mM ammonium acetate buffer, pH5.0 to remove lipofuscin-genic autofluorescence after immunolabelling (Schnell, Staines and Wessendorf, 1999). Samples were then washed 4 times for 30 mins in PBS and mounted in STORM imaging buffer (100mM MEA, 90% glycerol, 10% 10x PBS).

Imaging was performed on a customized Nikon Ti Eclipse inverted fluorescent TIRF microscope with a 642 nm laser. The lateral stage control was electronic and a piezo focuser (P-725, Physik Instrumente, Germany) precisely controlled the axial position. 30,000-65,000 frames were recorded with a 25 ms acquisition time, in a z-step format. Z-steps were repeatedly performed at z-intervals of 200 nm. Z-limits were set manually, slightly above and below the plane of interface between nerve terminal and motor endplate. Only switching events in the given focal plane were accepted by a thresholding filter as part of the PYME implemented jittered triangulation algorithm (Hou *et al.*, 2015). The same settings were used to capture a 550 nm LED illuminated widefield stack of TRITC-BTX labelled AChRs through a Texas Red filter set prior to STORM imaging. AChR stacks were used to produce a mean intensity projection image to act as a mask.

Super-resolution images were rendered in PYME software and saved as 16-bit tiff images. Mean intensity projections of the corresponding TRITC masks were also rendered as tiff images using ImageJ. These data sets were sent to Dr Ross Jones (University of Edinburgh) and Professor Tom Gillingwater (University of Edinburgh) and processed in ImageJ. Data were recorded semi-blind-anonymised samples were supplied with only the species plus identifying codes.

Composite images containing STORM SNAP25 and AChR mask images were used for quantification by Dr Ross Jones in ImageJ. The widefield component was traced manually and all STORM clusters were threshold in Image before being quantified. Density of SNAP25 puncta, average area of SNAP25 puncta, and fraction of bouton area covered by SNAP25 were measured for both human and mouse NMJs.

## Results

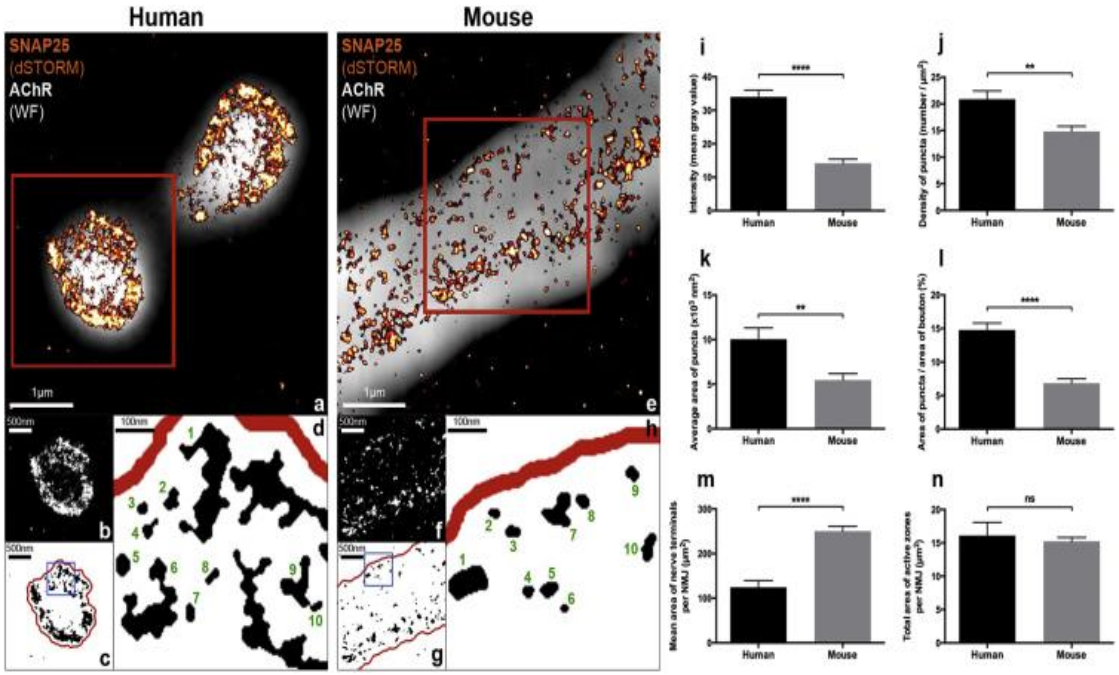


**Figure A1.1. Comparative Super-Resolution (STORM) Imaging of the Active Zone Protein SNAP25 at Human and Mouse NMJs. (A and E) Composite images of SNAP25-labeled nerve terminals (STORM, orange/red) overlaid on BTX-labelled AChRs of the motor endplate (wide-field, gray). Note that (A) only shows two single synaptic boutons from the human NMJ (not the whole NMJ), and (B) only shows a sub-region of one single synaptic bouton from the mouse NMJ (again not the whole NMJ). Scale bars, 1 µm. (B and F) 8-bit greyscale images of single boutons (representing the areas contained within the red boxes in A and E) used to quantify intensity of labelling (I). Note the increased intensity and density of SNAP-25 in the human NMJ. Scale bars, 500 nm. (C and G) Despeckled, binary versions of (B) and (F) used to quantify the remaining variables (J–L). The boxed areas have been enlarged (D and H) to depict individual SNAP-25 puncta; 10 discrete puncta have been labelled in each image. Scale bars, 100 nm. (I–L) Bar charts showing STORM image quantification of SNAP-25 intensity (I), density of SNAP-25 puncta (J), average area of SNAP-25 puncta (K), and the area of SNAP-25 puncta as a percentage of total bouton area (L), at human and mouse NMJs. All 4 measures of SNAP25 labelling were significantly greater in the human NMJs. For both human and mouse datasets, n = 50 boutons; bar charts depict mean (±SEM). Unpaired t test and Mann-Whitney test. (M and N) Bar charts comparing the average size of human and mouse NMJs (nerve terminal area, M) with the total size of their active zone material (SNAP-25 area per NMJ, N). Although the human NMJ is significantly smaller than the mouse NMJ (M), the total amount of SNAP25 labelling at the NMJ is the same when adjusted to reflect the total overall size of the synapse (N). Unpaired t test. ****p < 0.0001, **p < 0.01. Figure and legend from Jones et al., (2017) created by Dr Ross Jones.**

SNAP25 is a structural protein found in the SNARE complex of the active zone and responsible for synaptic vesicle release. It was selected as a robust marker for the active zone since it could be reliably labelled in both mouse and human samples. STORM microscopy was substantiated in the mouse

and then extended into the human samples. 2945 (human) and 10,666 (mouse) SNAP-25 puncta from 50 boutons, each from 10 NMJs from 3 specimens were quantified. The average area of individual SNAP-25 puncta, SNAP-25 puncta density per bouton (both **p<0.01), total area of SNAP-25 puncta per bouton and SNAP-25 labelling intensity (****p<0.0001) were all significantly greater in humans compared with mice.

Pre-synaptic motor nerve terminals at the human NMJ are significantly smaller than in mice (approximately 5 fold smaller). The total area of SNAP-25 labelling per NMJ was calculated and found to be identical in both humans and mouse: approximately 15 $\mu m^2$ of SNAP-25 per NMJ. Since the amount of active zone material is likely to reflect the amount of vesicle release, this finding suggested the possible presence of a conserved evolutionary homeostatic mechanism. When taken with existing data demonstrating extensive post-synaptic junctional folding at the human NMJ, the pre-synaptic specialism shown here predicts that neurotransmission in the smaller human NMJ can still be maintained effectively (Slater *et al.*, 1992).

Start-of-the-art tandem mass tagging proteomics was also used by the team at the University of Edinburgh to compare genome-wide protein levels between NMJ-enriched muscle biopsies and NMJ-devoid muscle biopsies, for mouse and human samples. Analysis of NMJ-devoid muscle biopsies showed 66 % of 200 known metabolic cascades were present in both species. NMJ-enriched biopsies however showed statistically significant differences in 36 nervous system signalling cascades. Some pathways were relatively stronger in each species across samples, and so were not an artefact of NMJ enrichment. Overall, these data support the finding that human and mouse

NMJs are fundamentally different at both the cellular and molecular level, which has important consequences for the translation of mouse models of NMJ disease to the human condition.

## Conclusion

These STORM data were acquired blind and analysed independently. The data corroborated the proteomics and cellular morphological experiments to show clear, distinct differences between human and mouse NMJs. These findings highlight the importance of careful model selection and data interpretation when using mouse models of the neuromuscular junction and motor neuron diseases. Careful interpretation of lower order animal studies in relation to human health and physiology is crucially important, as exemplified by this NMJ research.

## Publication

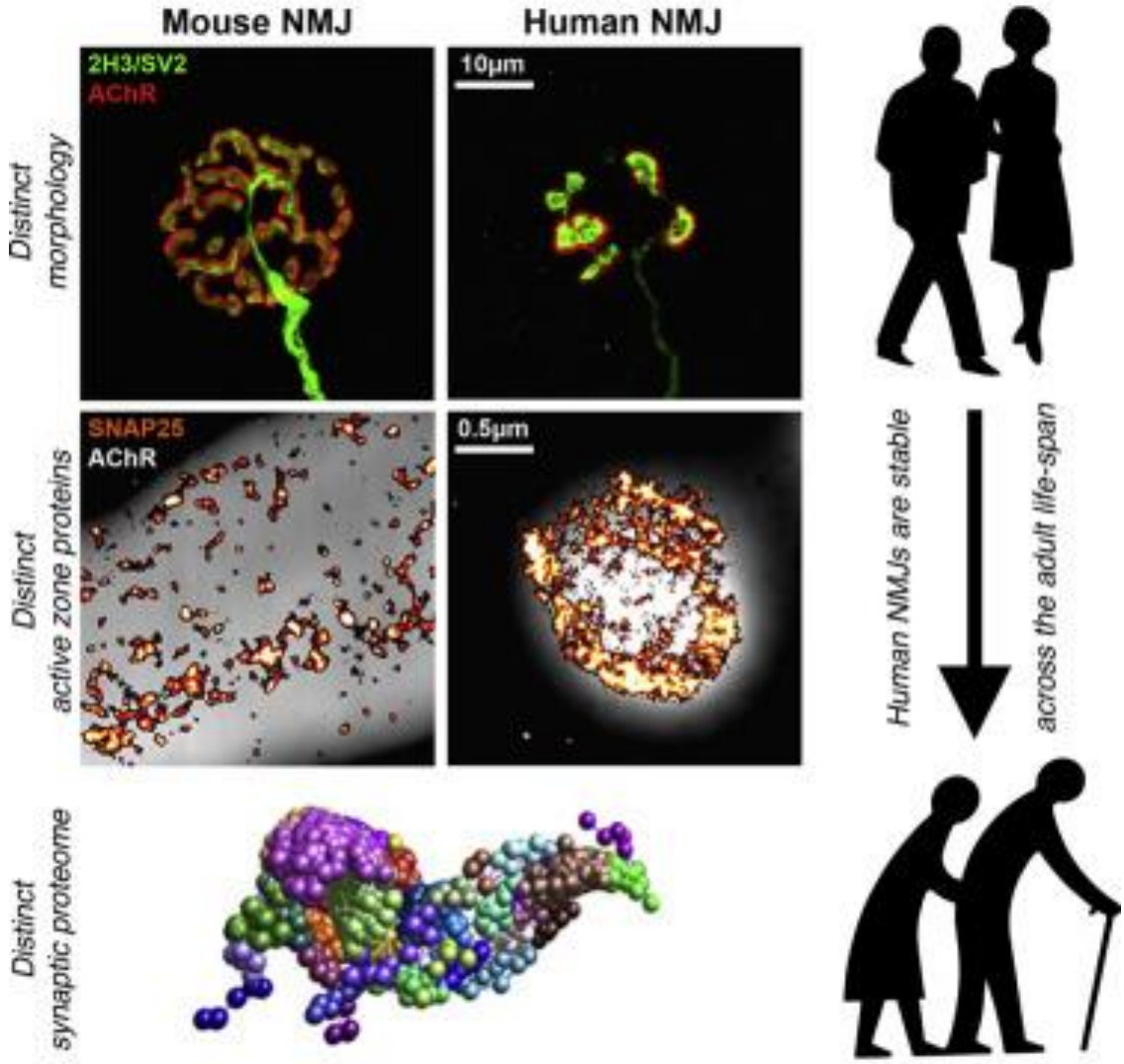


**Figure A1.2. Graphical abstract (adopted from Jones et al., 2017). Top panel: Maximum projection z-stack confocal microscopy images of 2HV/SV2 (green) and AChR (red) that label the pre- and post-synaptic neurons respectively. Middle panel: STORM super-resolution microscopy z-stack images of SNAP-25 in individual synaptic boutons (orange hot) and widefield mean intensity projection z-stack AChR masked images. Bottom panel: Proteomic results of enriched neuromuscular junction samples. Right panel: Proteomics and human samples were consistent across all age groups. (Jones *et al.*, 2017)**

# Appendix 2

## Permission of use of figure 1.5

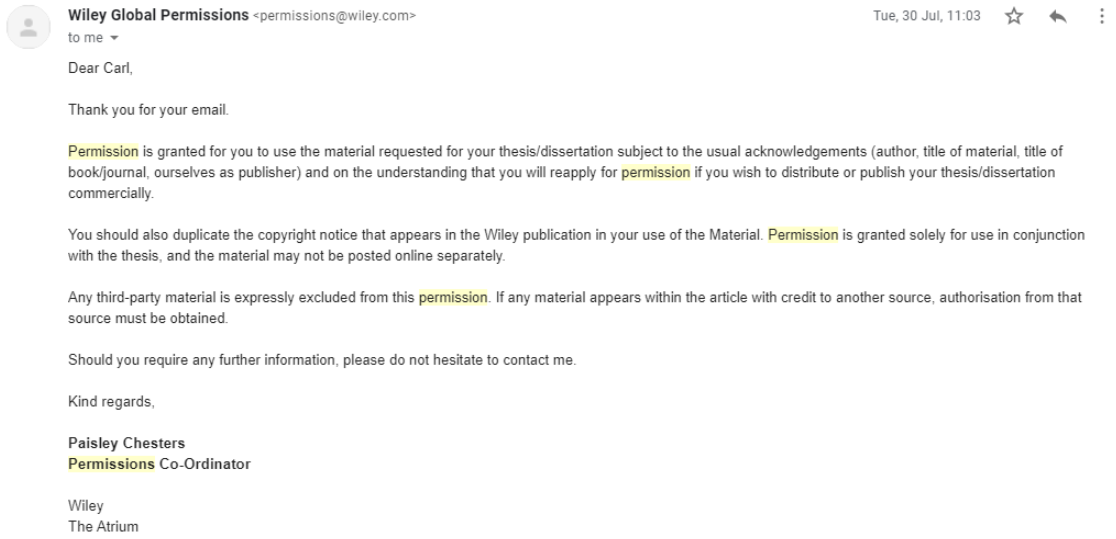

**Wiley Global Permissions** <permissions@wiley.com> Tue, 30 Jul, 11:03

to me

Dear Carl,

Thank you for your email.

Permission is granted for you to use the material requested for your thesis/dissertation subject to the usual acknowledgements (author, title of material, title of book/journal, ourselves as publisher) and on the understanding that you will reapply for permission if you wish to distribute or publish your thesis/dissertation commercially.

You should also duplicate the copyright notice that appears in the Wiley publication in your use of the Material. Permission is granted solely for use in conjunction with the thesis, and the material may not be posted online separately.

Any third-party material is expressly excluded from this permission. If any material appears within the article with credit to another source, authorisation from that source must be obtained.

Should you require any further information, please do not hesitate to contact me.

Kind regards,

**Paisley Chesters**
**Permissions Co-Ordinator**

Wiley
The Atrium

# References

Abbe, E. (1873) ‘Beiträge zur Theorie des Mikroskops und der mikroskopischen Wahrnehmung’, *Archiv für Mikroskopische*, 9, pp. 413–418.

Ai, X., Curran, J. W., Shannon, T. R., Bers, D. M., Pogwizd, S. M., (2005) ‘$Ca^{2+}$/Calmodulin-dependent protein kinase modulates cardiac ryanodine receptor phosphorylation and sarcoplasmic reticulum $Ca^{2+}$ leak in heart failure’, *Circulation Research*, 97, pp. 1314 - 1322.

Aoyama, H. *et al.* (2011) ‘Isoform-specific roles of protein phosphatase 1 catalytic subunits in sarcoplasmic reticulum-mediated Ca2+ cycling’, *Cardiovascular Research*, 89(1), pp. 79–88. doi: 10.1093/cvr/cvq252.

Ardito, F. *et al.* (2017) ‘The crucial role of protein phosphorylation in cell signaling and its use as targeted therapy (Review)’, *Int J Mol Med*, 2(40), pp. 271–280.

Asghari, P. *et al.* (2018) ‘Phosphorylation of the Type 2 Ryanodine Receptors Plays a Role in the Organisation of their Array’, *Biophysical Journal*, 114(3), p. 622a.

Baddeley, D. *et al.* (2009) ‘Optical single-channel resolution imaging of the ryanodine receptor distribution in rat cardiac myocytes’, *Proceedings of the National Academy of Sciences*, p. pnas.0908971106. doi: 10.1073/pnas.0908971106.

Baddeley, D. *et al.* (2011) ‘4D Super-Resolution Microscopy with Conventional Fluorophores and Single Wavelength Excitation in Optically Thick Cells and Tissues’, *PLOS One*.

Baddeley, D., Cannell, M. B. and Soeller, C. (2010) ‘Visualisation of localisation microscopy data’, *Microscopy and Microanalysis*, pp. 64–72. doi: 10.1017/S143192760999122X.

Baruscotti, M., Bucchi, A. and DiFrancesco, D. (2005) ‘Physiology and pharmacology of the cardiac pacemaker (“funny”) current’, *Pharmacology & Therapeutics*, 107(1), pp. 59–79.

Bates, M. *et al.* (2012) ‘Multicolor Super-Resolution Fluorescence Imaging via Multi-

Parameter Fluorophore Detection', *Chemphyschem*, 13(1), pp. 99–107.

Belevych, A. E. *et al.* (2011) 'MicroRNA-1 and -133 Increase Arrhythmogenesis in Heart Failure by Dissociating Phosphatase Activity from RyR2 Complex', *PLOS One*, 6(12), p. e28324.

Benkusky *et al.,* (2007) 'Intact β-adrenergic response and unmodified progression towards heart failure in mice with genetic ablation of a major protein kinase A phosphorylation site in cardiac ryanodine receptor', *Circulation Research*, 101, pp. 819-829

Berthet, J., Rall, T. and Sutherland, E. (1957) 'The relationship of epinephrine and glucagon to liver phosphorylase. IV. Effect of epinephrine and glucagon on the reactivation of phosphorylase in liver homogenates', *J Biol Chem*, 224(1), pp. 463–475.

Betzig, E. *et al.* (2006) 'Imaging Intracellular Fluorescent Proteins at Nanometer Resolution', *Science*, 313(5793), pp. 1642–1645.

Bers, D. M., (2012) 'Ryanodine receptor S2808 phosphorylation in heart failure', *Circulation Research,* 110, pp. 796 - 799.

Bers, D.M., Eisner, D. A., and Valdivia, H. H., (2003) 'Sarcoplasmic reticulum Ca2+ and heart failure: roles of diastolic leak and Ca2+ transport', *Circulation Research* 93(7), pp. 592 - 594

Blumhardt, P. *et al.* (2018) 'Photo-Induced Depletion of Binding Sites in DNA-PAINT Microscopy', *Molecules*, 23(12), p. 3165.

Bossi, M. *et al.* (2006) 'Breaking the diffraction resolution barrier in far-field microscopy by molecular optical bistability', *New Journal of Physics*, 8.

Bovo, E., Huke, S., Blatter., L. A., Zima, A. V., (2017) 'The effect of PKA-mediated phosphorylation of ryanodine receptor on SR $Ca^{2+}$ leak in ventricular myocytes', *Journal of Molecular and Cellular Cardiology*, 104, p 9 - 16

Brandenburg, S. *et al.* (2016) 'Axial tubule junctions control rapid calcium signaling in atria', *Journal of Clinical Investigation*, 126(10), pp. 3999–4015.

Brown, H. F., DiFrancesco, D. and Noble, S. J. (1979) ‘How does adrenaline accelerate the heart?’, *Nature*, 280, pp. 235–236.

Burnett, G. and Kennedy, E. (1954) ‘The enzymatic phosphorylation of proteins’, *J Biol Chem*, 11(2), pp. 969–980.

Cairns, S. P. and Borrani, F. (2014) ‘β-adrenergic modulation of skeletal muscle contraction: key role of excitation-contraction coupling’, *The Journal of Physiology*, 593(21) pp 4713-4727.

Camors, M. and Valdivia, H. H. (2014) ‘CaMKII regulation of cardiac ryanodine receptors and inositol triphosphate receptors’, *Front Pharmacol*, 101(5).

Cannell, M. B., Cheng, H. and Lederer, W. J. (1994) ‘Spatial non-uniformities in [Ca2+]i during excitation-contraction coupling in cardiac myocytes’, *Biophysical Journal*, 67(5), pp. 1942–1956.

Carter, S. *et al.* (2011) ‘Ca2+-dependent phosphorylation of RyR2 can uncouple channel gating from direct cytosolic Ca2+regulation’, *Journal of Membrane Biology*, 240(1), pp. 21–33. doi: 10.1007/s00232-011-9339-9.

Chelu *et al.,* (2009) ‘Calmodulin kinase II-mediated sarcoplasmic reticulum Ca2+ leak promotes atrial fibrillation in mice’, *J Clin Investigation*, 119(7) pp 1940 - 1951.

Chen *et al.,* (2015) ‘Expansion Microscopy’, *Science*, 347(6221) pp 543-548.

Chen-Izu, Y. *et al.* (2006) ‘Three-Dimensional Distribution of Ryanodine Receptor Clusters in Cardiac Myocytes’, *Biophysical Journal*, 91(1), pp. 1–13.

Cheng, H., Lederer, W. J., and Cannell, M.B. (1993) ‘Calcium sparks: elementary events underlying excitation-contraction coupling in heart muscle’, *Science*, 262(5134), pp. 740–744.

Cheng, H., Lederer, M. R., Lederer, W. J., and Cannell, M.B. (1996) ‘Calcium sparks and [Ca2+]i waves in cardiac myocytes’, Am J Physiol, 270(1), pp. 148–159.

Colyer, J. and Wang, J. H. (1991) ‘Dependence of cardiac sarcoplasmic reticulum calcium pump activity on the phosphorylation status of phospholamban’, *Journal of Biological Chemistry*, (266), pp. 17486–17493.

Cori, G. T. and Green, A. A. (1943) 'Crystalline muscle phosphorylase', *J Biol Chem*, 151, pp. 31–38.

Curran, J. *et al.* (2007) 'β-Adrenergic Enhancement of Sarcoplasmic Reticulum Calcium Leak in Cardiac Myocytes Is Mediated by Calcium/Calmodulin-Dependent Protein Kinase', *Circulation research*, 100, pp. 391–398.

Denniss, A., Dulhunty, A. F. and Beard, N. A. (2018) 'Ryanodine receptor Ca2+ release channel post-translational modification: Central player in cardiac and skeletal muscle disease', *The International Journal of Biochemistry & Cell Biology*, 101, pp. 49–53.

Dobrev, D. and Wehrens, X. H. T. (2014) 'Role of RyR2 phosphorylation in heart failure and arrhythmias: Controversies around ryanodine receptor phosphorylation in cardiac disease', *Circulation Research*, 114(8), pp. 1311–1319. doi: 10.1161/CIRCRESAHA.114.300568.

Fabiato, A.. (1983) Calcium-induced release of calcium from the cardiac sarcoplasmic reticulum', Am J Physiol, 245(1). pp 1-14.

Fawcett, D. W. and McNutt, N. S. (1969) 'THE ULTRASTRUCTURE OF THE CAT MYOCARDIUM I. Ventricular Papillary Muscle', *Journal of Cell Biology*, 42(1), pp. 1–45.

Fleischer, S. *et al.,* (1985) 'Localisation of Ca2+ release channels with ryanodine in junctional terminal cisternae of sarcoplmic reticulum of fast skeletal muscle', PNAS, 82(21), pp7256-7259.

Franzini-Armstrong, C., Protasi, F. and Ramesh, V. (1999) 'Shape, size, and distribution of Ca2+ release units and couplons in skeletal and cardiac muscles', *Biophysical Journal*, 77(3), pp. 1528–1539.

Gadeberg, H. C. *et al.* (2016) 'Heterogeneity of T-tubules in pig hearts', *PLOS One*, 11(6).

Galice, S. *et al.* (2018) 'Size Matters: Ryanodine Receptor Cluster Size Affects Arrhythmogenic Sarcoplasmic Reticulum Calcium Release.', *J Am Heart Assoc*,

7(13), p. e008724.

Glushonkov, O. *et al.* (2018) 'Optimised protocol for combined PALM-dSTORM imaging', *Scientific Reports*, 8, p. 8749.

Goodman, L. *et al.* (2017) 'N-terminal SAP97 isoforms differentially regulate synaptic structure and postsynaptic surface pools of AMPA receptors', *Hippocampus*, 27(6).

Gray, H. and Carter, H. V. (1858) *Anatomy: Descriptive and Surgical*. 1st edn. Edited by J. W. Parker. London: John William Parker.

Hagemann, D. and RP, X. (2002) 'Dual site phospholamban phosphorylation and its physiological relevance in the heart', *Trends Cardiovasc Med*, 12(2), pp. 51–56.

Harrison, C. (2018) 'Nanoscopy in Cardiac Physiology', *Physiology News*, pp. 38–38.

Hazra, A. (2017) 'Using the confidence interval confidently', *Journal of Thoracic Disease*, 9(10), pp. 4125–4130.

Heilemann, M. *et al.* (2008) 'Subdiffraction-resolution fluorescence imaging with conventional fluorescent probes', *Angew Chem Int Ed Engl*, 47(33), pp. 6172–6176.

Heilmeyer Jr, L. M. G. *et al.* (1970) 'Control of phosphorylase activity in a muscle glycogen particle. II activation by calcium', *J Biol Chem*, 245, pp. 6649–6656.

Hell, S. W. *et al.* (2015) 'the 2015 super-resolution microscopy roadmap', *Journal of Physics D: Applied Physics*, 48(44).

Herzog, W. *et al.* (2014) 'The role of titin in eccentric muscle contraction', *Journal of Experimental Biology*, 217 pp. 2825-2833.

Hill, A. V. (1949) 'The abrupt transition from rest to activity in muscle', *Proc Royal Soc B* 136(884).

Hoeper, M. M., *et al.,* (2013) 'Definitions and diagnosis of pulmonary hypertension', *J Am Coll Cardiol*, 62, pp. D42-D50.

Hou, Y. *et al.* (2015) 'Nanoscale analysis of ryanodine receptor clusters in dyadic couplings of rat cardiac myocytes', *Journal of Molecular and Cellular Cardiology*, 80, pp. 45–55. doi: 10.1016/j.yjmcc.2014.12.013.

Houser, S. R.. (2014) 'Role of RyR2 phosphorylation in heart failure and

arrhythmias', *Circulation Research*, 114, pp 1320 - 1327

Huke, S. and Bers, D. M. (2008) 'Ryanodine receptor phosphorylation at Serine 2030, 2808 and 2814 in rat cardiomyocytes', *Biochem Biophys Res Commun*, 376(1), pp. 80–85.

Hunter, T. (1995) 'Protein Kinases and Phosphatases: The Yin and Yang of Protein Phosphorylation and Signaling', *Cell*, 80, pp. 225–236.

Huxley, A.F. (1971) 'The activation of striated muscle and its mechanical response', *Proc R Soc Lond B Biol Scil*, 178(1050) pp. 1-27.

Ibrahim, M *et al.,* (2011) 'The Structure and Function of Cardiac T-Tubules', Proc Biol Sci, 278(1719), pp. 2714–2723.

Jayasinghe, I. D. *et al.* (2012) 'Comparison of the organization of T-tubules, sarcoplasmic reticulum and ryanodine receptors in rat and human ventricular myocardium', *Clin Exp Pharmacol Physiol*, 39(5), pp. 469–76.

Jayasinghe, I. *et al.* (2018) 'Shining New Light on the Structural Determinants of Cardiac Couplon Function: Insights From Ten Years of Nanoscale Microscopy', *Frontiers in Physiology*.

Jayasinghe, I. D. *et al.* (2018a) 'True molecular scale visualisation of variable clustering properties of ryanodine receptors', *Cell Reports*.

Jayasinghe, I. D. *et al.* (2018b) "Shining new light on the structural determinants of cardiac couplon function: insights from ten years of nanoscale microscopy", *Frontiers in Physiology*, 9, pp. 1472-1481.

Jones, R. A. *et al.* (2016) 'NMJ-Morph reveals principal components of synaptic morphology influencing structure - function relationships at the neuromuscular junction', *Open Biology*, 6.

Jones, R. A. *et al.* (2017) 'Cellular and Molecular Anatomy of the Human Neuromuscular Junction', *Cell Reports*, 21(9), pp. 2348–2356. doi: 10.1016/j.celrep.2017.11.008.

Jungmann, R. *et al.* (2014) 'Multiplexed 3D cellular super-resolution imaging with

DNA-PAINT and Exchange-PAINT', *Nature Methods*, 11(3), pp. 313–318. doi: 10.1038/nmeth.2835.

Kranias, E. (1985) 'Regulation of Ca2+ transport by cyclic 3',5'-AMP-dependent and calcium-calmodulin-dependent phosphorylation of cardiac sarcoplasmic reticulum', *Biochim biophys Acta*, 844(2), pp. 193–199.

Krzywinski, M. and Altman, N. (2014) 'Visualising samples with box plots', *Nature Methods*, 11, pp. 119–120.

Kurien, B. T. and Scofield, R. H. (2006) 'Western blotting', *Methods*, 38(4), pp. 283–293.

Kushnir, A. *et al.* (2010) 'role of CaMKII delta phosphorylation of the cardiac ryanodine receptor in the force frequency relationship and heart failure', *Proceedings of the National Academy of Sciences*, 107(22), pp. 10274–10279.

Lerner, R. A. (1982) 'Tapping the immunological repertoire to produce antibodies of predetermined specificity', *Nature*, 299593–596.

Leterrier, C. *et al.* (2015) 'Nanoscale Architecture of the Axon Initial Segment Reveals an Organized and Robust Scaffold', *Cell Reports*, 13(12), pp. 2781–2793.

Levy, D. *et al.* (1996) 'The progression from hypertension to congestive heart failure', *JAMA*, 275(20), pp. 1557–1562.

Levick, J. (20X03An Introducion to Cardiovascular Physiology, 4th Edition', CRC Press (4th Edition) ISBN-10: 0340809213

Levy, D. *et al.* (1996) 'The progression from hypertension to congestive heart failure', *JAMA*, 275(20), pp. 1557–1562.

Li, L. *et al.* (1998) 'Cardiac myocyte calcium transport in phospholamban knockout mouse: relaxation and endogenous CaMKII effects', *Am J Physiol Heart and Circ Physiol*, 274(4), pp. 1335–1347.

Liu, J. *et al.* (1991) 'Calcineurin is a common target of cyclophilin-cyclosporin A and FKBP-FK506 complexes', *Cell*, 66(4), pp. 807–815.

Lutz, T. *et al.* (2018) 'Versatile multiplexed super-resolution imaging of

nanostructures by Quencher-Exchange-PAINT', *Nano Research*, pp. 1–14. doi: 10.1007/s12274-018-1971-6.

MacDonnell *et al.,* (2008) 'Adrenergic regulation of cardiac contractility does not involve phosphorylation of the cardiac ryanodine receptor at serine 2808', *Circulation Research*, 102, pp. e65-e72.

MacPhee, D. J. (2010) 'Methodological considerations for improving Western blot analysis', *Journal of pharmacological and toxicological methods*, 61(2), pp. 171–177.

MacQuaide, N. *et al.* (2015) 'Ryanodine receptor cluster fragmentation and redistribution in persistent atrial fibrillation engance calcium release', *Cardiovascular Research*, 108(3387–398).

Mahmood, T. and Yang, P. (2012) 'Western Blot: Technique, Theory, And Trouble Shooting', *N Am J Med Sci*, 4(9), pp. 429–434.

Marx, S. *et al.* (2000) 'PKA phosphorylation dissociates FKBP12.6 from the calcium release channel (ryanodine receptor): defective regulation in failing hearts.', *Cell*, 101(4), pp. 365–376.

Mattiazzi, A. *et al.* (2005) 'Role of phospholamban phosphorylation on Thr17 in cardiac physiological and pathological conditions', *Cardiovascular Research*, pp. 366–375.

Mattiazzi, A. and Kranias, E. (2014) 'the role of CaMKII regulation of phospholamban activity in heart disease', *Front Pharmacol*.

Meissner, G., Darling, E. and Eveleth, J. (1986) 'Kinetics of rapid Ca2+ release by sarcoplasmic reticulum. Effects of Ca2+, Mg2+, and adenine nucleotides', *Biochemistry*, 25(1), pp. 236–244.

Munro, M. *et al.* (2016) 'Junctophilin-2 in the nanoscale organisation and functional signalling of ryanodine receptor clusters in cardiomyocytes', *Journal of Cell Science*, 129, pp. 4388–4398.

Park, W. J. and Oh, J. G. (2013) 'SERCA2a: a prime target for modulation of cardiac contractility during heart failure', *BMB Reports*, 46(5), pp. 237–243.

Park, S-J., *et al.* (2019) 'Insights into the pathogenesis of catecholaminergic polymorphic ventricular tachycardia from engineered human heart tissue', Circulation, 140, pp. 390-404.

Rayleigh F.R.S, Lord (1879) 'Investigations in optics, with special reference to the spectroscope', *Philosophical Magazine*, 5(8 (49)), p. 261 274.

Respress, J. L., *et al.* (2012) 'Role of RyR2 phosphorylation at S2814 during heart failure progression', *Circulation Research*, 110, pp. 1474 - 1483.

Richards, M. A. *et al.* (2011) 'Transverse tubules are a common feature in large mammalian atrial myocytes including human', *Am I Physiol Heart Circ Physiol*, 301(5), pp. 1996–2005.

Rodriguez, P., Bhogal, M. S. and Colyer, J. (2003) 'Stoichiometric Phosphorylation of Cardiac Ryanodine Receptor on Serine 2809 by Calmodulin-dependent Kinase II and Protein Kinase A', *Journal of Biological Chemistry*, 278(40), pp. 38593–38600.

Rodriguez, P., Jackson, W. A. and Colyer, J. (2004) 'Critical evaluation of cardiac Ca2+-ATPase phosphorylation on serine 38 using a phosphorylation site-specific antibody', *Journal of Biological Chemistry*, 279, p. 17111 = 17119.

Rust, M. J., Bates, M. and Zhuang, X. (2006) 'Sub-diffraction-limit imaging by stochastic optical reconstruction microscopy (STORM)', *Nature Methods*, 3(10), pp. 793–795. doi: 10.1038/nmeth929.

Sage, D., Neumann, F. R. and Hediger, F. (2005) 'Automatic tracking of individual fluorescence particles: application to the study of chromosome dynamics', *IEEE Transactions on Image Processing*, 14(9), pp. 1372–1383.

Sahl, S. J., Hell, S. W. and Jakobs, S. (2017) 'Fluorescence nanoscopy in cell biology', *Nature Reviews Molecular Cell Biology*, 18, pp. 685–701.

Salvage, S. C., Gallant, E. M., Beard, N. A., Ahman, S., Valli, H., Fraser, J. A., Huang, C. L. H., Dulhunty, A. F., (2019) 'Ion channel gating in cardiac ryanodine receptors from the arrhythmic RyR2-P2328S mouse', Journal of *Cell Science* 132,

Savio-Galimberti, E. *et al.,* (2008) Novel features of the rabbit transverse tubular

system revealed by quantitative analysis of three-dimensional reconstructions from confocal images', *Biophys J*, 95(4), pp2053-2062.

Schnell, S., Staines, W. and Wessendorf, M. (1999) 'Reduction of lipofuscin-like autofluorescence in fluorescently labeled tissue', *J Histochem Cytochem*, 47(6), pp. 719–730.

Schnitzbauer *et al.,* (2017) 'Super-resolution microscopy with DNA-PAINT', *Nature Protocols,* 12 pp 1198-1228

Schwinger, R. H. G. *et al.* (1999) 'Reduced Ca2+ sensitivity of SERCA2a in failing human myocardium due to reduced serine-16 phospholamban phosphorylation', *Journal of Molecular and Cellular Cardiology*, 31(3), pp. 479–491.

Shan, J. *et al.* (2010) 'Phosphorylation of the ryanodine receptor mediates the cardiac fight or flight response in mice', *Journal of Clinical Investigation*, 120(12), pp. 4388–4398.

Shan, J. *et al.* (2010) 'Role of chronic ryanodine receptor phosphorylation in heart failure and β-adrenergic receptor blockade in mice', *Journal of Clinical Investigation*, 120(12), pp. 4375 - 4387

Siddiqui, A. (2011) 'Effects of vasodilation and arterial resistance on cardiac output', *Journal of Clinical & Experimental Cardiology*, 2(11).

Skoestad, J Aronsen, J M. (2018) 'Hypokalemia-induced Arrhythmias and Heart Failure: New Insights and Implications for Therapy', *Frontiers in Physiology*, 9 pp1500-1504.

Slater, C. *et al.* (1992) 'Structure and function of neuromuscular junctions in the vastus lateralis of man. A motor point biopsy study of two groups of patients', *Brain*, 155(2), pp. 451–478.

Smymias, I. *et al.* (2010) 'Comparison of T-tubule system in adult rat ventricular and atrial myocytes, and its role in excitation-contraction coupling and inotropic stimulation', *Cell Calcium*, 47(3), pp. 210–223.

Soliman, H., *et al.,* (2019) 'ROCK2 promotes ryanodine receptor phosphorylation and

arrhythmic calcium release is diabetic cardiomyocytes', *International Journal of Cardiology*, 281, pp. 90-98.

Soeller, C. and Cannell, M. B. (1997) 'Numerical simulation of local calcium movements during L-type calcium channel gating in the cardiac diad', *Biophysical Journal*, 73, pp. 97–111.

Soeller, C. and Cannell, M. B. (1999) 'Examination of the transverse tubular system in living cardiac rat myocytes by 2-photon microscopy and digital image-processing techniques', *Circulation Research*, 84(3), pp. 266–275.

Sparrenberger, F. *et al.* (2009) 'Does psychosocial stress cause hypertension? A systematic review of observational studies', *Journal of Human Hypertension*, 23, pp. 12–19.

Sparrow, C. M. (1916) 'On spectroscopic resolving power', *ApJ*, 44, p. 76.

Stantchev, R. I. *et al.* (2018) 'Subwavelength hyperspectral THz studies of articular cartilage', *Scientific Reports*, 8, p. 6294.

Sperelakis, N. and Rubio, R. (1971) An orderly lattice of axial tubules which interconnect adjacent transverse tubules in guinea-pig ventricular myocardium', *J Mol Cell Cardiol.* 2(3) pp. 211-220.

Stange, M., Xu, L., Balshaw, D., and Yamaguchi, N. (2003) 'Characterization of recombinant skeletal muscle (Ser-2843) and cardiac muscle (Ser-2809) ryanodine receptor phosphorylation mutants', *Journal of Biological Chemistry*, 278, pp. 51693-51702

Stern, M. D. *et al.* (1999) 'Local Control Models of Cardiac Excitation-Contraction Coupling: A Possible Role for Allosteric Interactions between Ryanodine Receptors', *Journal of General Physiology*, pp. 469–489.

Swoboda, M. *et al.* (2012) 'Enzymatic oxygen scavenging experiments for photostability without pH drop in single-molecule experiments', *ACS NANO*, 6(7), pp. 6364–6369.

Tada, M. *et al.* (1974) 'The stimulation of calcium transport in cardiac sarcoplasmic

reticulum by adenosine 3':5'-monophosphate-dependent protein kinase', *The Journal of Biological Chemistry*, 249(19), pp. 6174–6180.

Tada, M., Kirchberger, M. A. and Katz, A. M. (1975) 'phosphorylation of a 22,000-dalton component of the cardiac sarcoplasmic reticulum by adenosine 3':5'-monophosphate-dependent protein kinase', *The Journal of Biological Chemistry*, 250, pp. 2640–2647.

Tam, J. and Merino, D. (2015) 'Stochastic optical reconstruction microscopy (STORM) in comparison with stimulated emission depletion (STED) and other imaging methods', *Journal of Neurochemistry*, 135(4).

Tan, Y. H. *et al.* (2015) 'A Nanoengineerng Approach for Investigation and Regulation of Protein Immobilization', *ACS NANO*, 2(11), pp. 2374–2384.

Taylor, C. W. and Tovey, S. C. (2010) 'IP3 receptors: Toward understanding their activation', *Cold Spring Harb Perspect Biol*, 2(12).

Terentyev, D. *et al.* (2003) 'Protein Phosphatases Decrease Sarcoplasmic Reticulum Calcium Content by Stimulating Calcium Release in Cardiac Myocytes', *The Journal of Physiology*, 552(1), pp. 109–118. doi: 10.1113/jphysiol.2003.046367.

Tokunaga, M. Imamoto, N. and Sakata-Sogawa, K. (2008) 'Highly inclined thin illumination enables clear single-molecule imaging in cells', *Nature Methods,* 5, pp. 159-161.

Valdivia, H. H. (2012) 'Ryanodine receptor phosphorylation and heart failure: phasing out S2808 and "criminalizing" S2814.', *Circulation research*, 110(11), pp. 1398–402. doi: 10.1161/CIRCRESAHA.112.270876.

Valverde, C. A., *et al.* (2018) 'Ablation of phospholamban rescues reperfusion arrhythmias but exacerbates myocardium infarction in hearts with $Ca^{2+}$/calmodulin kinase II constitutive phosphorylation of ryanodine receptors', *Cardiovascular Research,* 115(3), pp. 556-569.

Vangheluwe, P. *et al.* (2003) 'Ca2+ transport ATPase isoforms SERCA2a and SERCA2b are targeted to the same sites in the murine heart', *Cell Calcium*, 34(6),

pp. 457–464.

Van Oort *et al.* (2010) 'Ryanodine receptor phosphorylation by calcium/calmodulin-dependent protein kinase II promotes life-threatening ventricular arrhythmias in mice with heart failure', *Circulation,* 122, pp. 2669 - 2679.

Vega, A. L. *et al.* (2011) 'Dynamic changes in sarcoplasmic reticulum structure in ventricular myocytes', *Journal of Biomedicine and Biotechnology*, 2011.

Venetucci, L., Trafford, A. and Eisner, D. (2007) 'Increasing ryanodine receptor open probability alone does not produce arrhythmogenic calcium waves: threshold sarcoplasmic reticulum calcium content is required', *Circulation research*, 100(1), pp. 105–111.

Vogelsang, J. *et al.* (2008) 'A Reducing and Oxidizing System Minimizes Photobleaching and Blinking of Fluorescent Dyes', *Angewandte, Chemie*, 47(29).

Vogelsang, J. *et al.* (2010) 'Make them blink: probes for super-resolution microscopy.', *Chemphyschem*, 11(12), pp. 2475–2490.

Wagenknecht, T. *et al.* (1989) 'Three-dimensional architecture of the calcium channel/foot structure of sarcoplasmic reticulum', *Nature*, 338.

Walweel, K. *et al.* (2017) 'Ryanodine receptor modification and regulation by the intracellular Ca2+ and Mg2+ in healthy and failing human hearts', *Journal of Molecular and Cellular Cardiology*, 104, pp. 53–62.

Walweel, K., *et al.* (2019) 'Calmodulin inhibition of human RyR2 channels requires phosphorylation of RyR2-S2808 or RyR2-S2814',*Journal of Molecular and Cellular Cardiology*, 130, pp. 96-106.

Wang, W. *et al.* (2014) 'Reduced junctional Na+/Ca2+-exchanger activity contributes to sarcoplasmic reticulum Ca2+ leak in junctophilin-2-deficient mice', *AJP Heart and Circulatory Physiology*, 307(9), pp. H1317–H1326.

Weber, M. A., Tackland, D. T., (2016) 'Cardiovascular benefits of lowering blood pressure', *Nature Reviews Nephrology*, 12, pp. 202-204.

Wehrens, X. H. T. *et al.* (2004) 'Ca2+/Calmodulin-Dependent Protein Kinase II

Phosphorylation Regulates the Cardiac Ryanodine Receptor', *Circulation Research*, 94(6), pp. e61–e70. doi: 10.1161/01.RES.0000125626.33738.E2.

Wehrens, X. H. T., Lehnart, S. E., Reiken, S., Vest, J. A., Wronska, A., Marks, A. R. (2006) Ryanodine receptor/calcium release channel PKA phosphorylation: A critical mediator of heart failure progression', PNAS, 103(3), pp. 511 - 518.

Weir, W. and Beuckelmann, D. (1989) 'Sodium-calcium exchange in the mammalian heart: current-voltage relation and intracellular calcium concentration', *Mol Cell Biochem*, 89(2), pp. 97–102.

Weiss, J N. and Zhilin, Q. (2017) 'electrophysiology of Hypokalemia and Hyperkalemia', *Circulation: Arrhythmia and Electrophysiology*, 10

Wescott, A. P. *et al.* (2016) 'Ryanodine receptor sensitivity governs the stability and synchrony of local calcium release during cardiac excitation-contraction coupling', *Journal of Molecular and Cellular Cardiology*, 92, pp. 82–92.

White, F. M. and Wolf-Yadlin, A. (2016) 'Methods for the Analysis of Protein Phosphorylation-Mediated Cellular Signalling Networks', *Annual Review of Analytical Chemistry*, 9, pp. 295–315. doi: 10.1146/annurev-anchem-071015-041542.

Williams, D. B. and Carter, C. B. (1996) *The transmission electron microscopy*, *Transmission Electron Microscopy*.

Witcher, D. R., Kovacs, R. J., Schulman, H., Cefali, D. C., Jones, L. R., (1991) Unique phosphorylation site on the cardiac ryanodine receptor regulates calcium channel activity', *Journal of Biological Chemistry*, 266, pp 11144 - 11152

Wong, J. *et al.* (2013) 'Nanoscale Distribution of Ryanodine Receptors and Caveolin-3 in Mouse Ventricular Myocytes: Dilation of T-Tubules near Junctions', *Biophysical Journal*, 104(11), pp. L22–L24.

Woodbury, L. A., Woodbury, J. W. and Hecht, H. H. (1950) 'Membrane resting and action potentials of ingle cardiac muscle fibers', *Circulation*, 1(2), pp. 264–266.

Wu, A. Z. *et al.* (2016) 'Phospholamban is concentrated in the nuclear envelope of cardiomyocytes and involved in perinuclear/nuclear calcium handling', *Journal of*

*Molecular and Cellular Cardiology*, 100, pp. 1–8.

Wulllschleger, M. *et al.* (2014) 'High Incorrect Use of the Standard Error of the Mean (SEM) in Original Articles in Three Cardiovascular Journals Evaluated for 2012', *PLOS One*, 591, pp. 2103–2111.

Xiao, B. *et al.* (2005) 'Characterization of a novel PKA phosphorylation site, serine-2030, reveals no PKA hyperphosphorylation of the cardiac ryanodine receptor in canine heart failure.', *Circulation research*. American Heart Association, Inc., 96(8), pp. 847–55. doi: 10.1161/01.RES.0000163276.26083.e8.

Xiao, B., *et al.,* (2006) 'Ser-2030, but not Ser-2808, is the major phosphorylation site in cardiac ryanodine receptors responding to protein kinase A activation upon β-adrenergic stimulation in normal and failing hearts', *Biochemical Journal,* 396(1), pp. 7 - 16.

Yin, C. C. and Lai, F. A. (2000) 'Intrinsic lattice formation by the ryanodine receptor calcium-release channel', *Nature Cell Biology*, 2, pp. 669–671.

Zalk, R. and Marks, A. R. (2017) 'Ca2+ release channels join the "resolution revolution"', *Trends Biochem Sci*, 42(7), pp. 543–555.

Zhao, W. *et al.* (2004) 'Threonine-17 phosphorylation of phospholamban: a key determinant of frequency-dependent increase of cardiac contractility', *Journal of Molecular and Cellular Cardiology*, 37(2), pp. 607–612.

Zissimopoulos, S., Selfan, S., Maxwell, C., Williams, A. J., Lai, F. A., (2011) 'Disparities in the association of the ryanodine receptor and the FK506-binding proteins in mammalian heart', *Journal of Cell Science*, 125, pp. 1759-1769.